DIFFRACTION STUDIES OF THE STRUCTURAI PHASE TRANSITION IN THE HIGH TEMPERATURE SUPERCONDUCTOR YBCO

Bahram KHOSHNEVISAN

A thesis submitted in partial fulfillment of
The requirement of the degree of
Doctor of Philosophy

Neutron Scattering and Material Physics Group
Joule Physics Laboratory
Institute for Materials Research
UNIVERSITY OF SALFORD

October 2002

In The Name Of Allah

To My Beloved Wife

And

Shakiba , Shamim

List of Publications

Observation of twinning in $YBa_2Cu_3O_{6+x}$, $0<x<1$, at high temperatures
B Khoshnevisan, D K Ross, D P Broom and M Babaeipour ; J.Phys.: Condens. Matter **14**(2002) 9763- 9778

Observation of OrthorhombicII in YBCO
B Khoshnevisan, D K Ross; " Superconductivity Group Annual Conference" (Poster), University of Cambridge (Jan. 2002)

YBCO: Phase transition and Twining
D K Ross, B Khoshnevisan; ISIS Experimental Report (2001)

We would note that we have recently completed a full analytical study of the diffraction from narrow twins, which it is not included in this thesis.
D K Ross, B Khoshnevisan; to be Published

Contents

Acknowledgements

Thanks my Lord for every thing I've got

I would like passionately to thank Professor D.K. Ross for his supervision, enthusiasm and ideas through the project and Dr H. Arabi for his advice. I am grateful to "The ministry of Research and Technology" in Iran, which allowed me to study for a Ph.D in The University of Salford.

I would like to thank my fellow members of the Neutron Scattering and Marerial Physics Group; D.J.Bull, D.P.Broom, M.Babaeipuor, G.Rowsell, P.Georgiev, D.Roach, J.Liu, G.Abdolrashidy, A.Esmaeilian.

Thanks to Dr M.Mercer for her advice and her thesis was a great help in this work; also I like to thank Dr I.Morrison for setting the access to the computational physics facilities.

The Instrument Scientist in ISIS and ILL, Dr K.Anderson and Dr E.Suard were very kind to me and thanks to J.Dreyer and P.Cross for their help when I was in ISIS and ILL, and also thanks to Mr R.Thompson for help with running the XRD measurements.

I would like to thank Dr T.Shamekhi the previous Chancellor and all of my colleagues in the University of Kashan (Iran) specially Mr B.Jazi for keeping me in touch with the physics group in there.

Finally my special thanks go to my wife and daughters, my parents and my brother and sister for their continual love and support. I apologise to my sister and her husband Reza, because I couldn't attend their wedding ceremony, when I was in Salford.

Bahram Khoshnevisan Oct. 2002

Abstract

In-situ x-ray and neutron diffraction combined with computation modeling have been used to elucidate the details of the structural phase transitions in $YBa_2Cu_3O_{6+x}$ for $0<x<1$.

In this study it is found that in the elevated temperature range [200 - 300°C], with increasing oxygen content, the structure changes from the well known tetragonal (Tet.) to the orthorhombic II (OII) superlattice phase (under thermodynamical equilibrium condition). This transition is found to be first order (a matter of considerable controversy) with the expected linear change in the volume fraction of each phase across the corresponding two phase mixed region (Gibbs phase rule). The possibility of the existence of a stable entirely OII phase region at 300°C around $x \approx 0.7$ is perhaps the most notable result of this study, which this result implies a substantial correction on the YBCO's structural phase diagram. From the full analyses of the data, the possibility of the formation of a superstructure along the "c" direction under the aforementioned conditions cannot be ruled out

At higher temperature [500 – 600°C] the measurements relate to the second order Tet. to orthorhombic I (OI) phase transition. The interesting issue here is the nature of the twining microstructure that forms just after the transition. The computation modeling and peak broadening analyses of the data, reveals the interference effect on the diffracted peak shapes from the thin stripe twinned sample at the early stages of transition from the Tet. to OI phase.

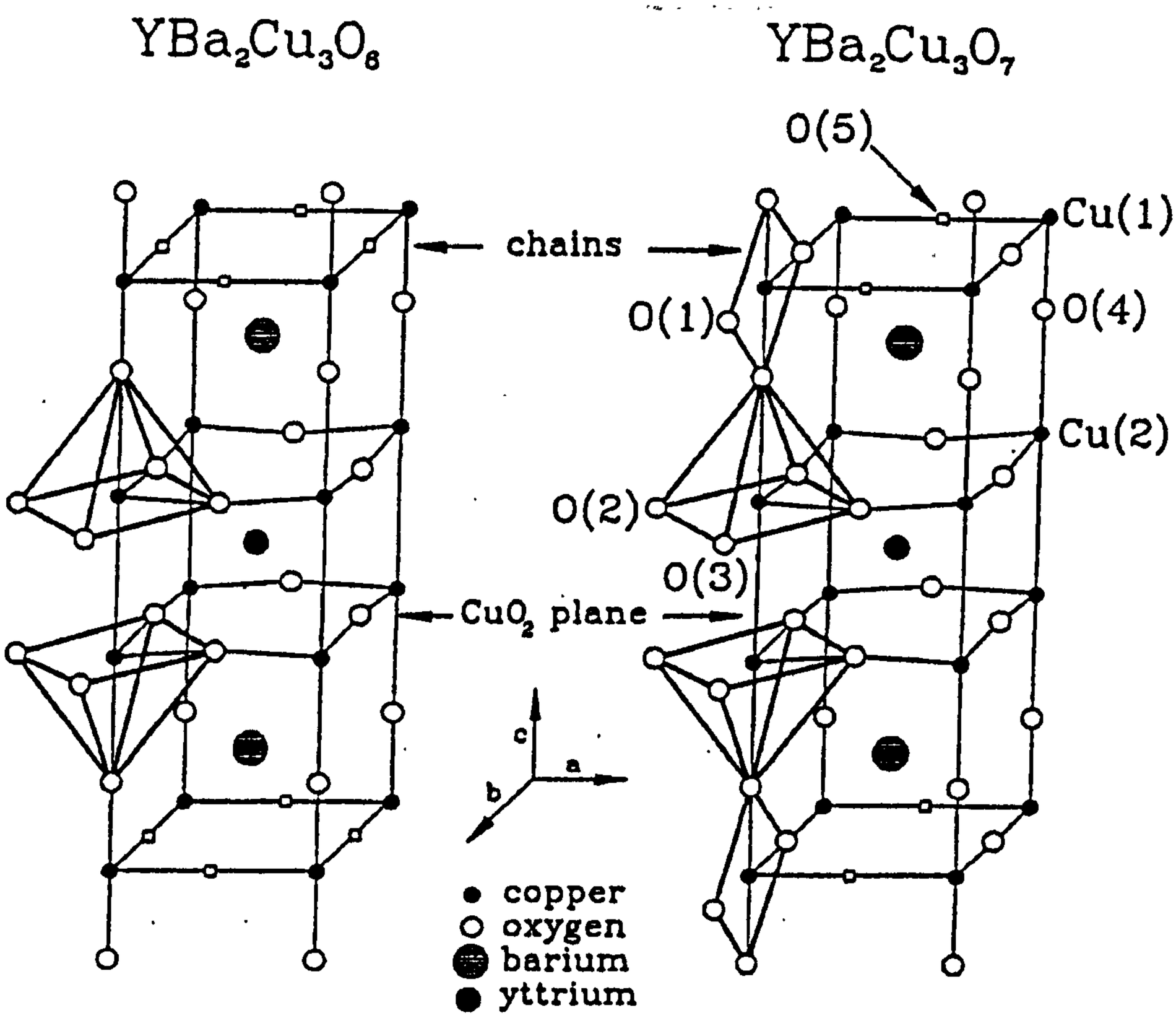

A representation of the structures of a) the tetragonal phase at x=0, b) the orthorhombic I phase at x=1, of $YBa_2Cu_3O_{6+x}$. All equivalent oxygen and copper sites are labeled according to the standard convention. The open squares indicate unoccupied sites. When x=0 both O(1) and O(5) are unoccupied, when x=1 the O(1) site is filled and o(50 site is empty. Notice, that the Cu(1) has two fold co-ordination when x=0 and four co-ordination when x=1 (Fig. taken from Mercer's thesis1997).

Chapter I

INTRODUCTION

The result for a general search in the web about YBCO shows:

Searched the web for YBCO: Results ..... Of about 15,400 !!

$YBa_2Cu_3O_{6+x}$ is perhaps the most the most heavily studied compound among the superconducting cuprates as the above phrase shows. Since the discovery of the compound in 1987 many physical aspects of this high T_c cuprate material have been studied and published. One of the reasons is that the relatively simple synthesis route, and the very good intrinsic superconducting behavior in an applied field, has been viewed as promising for practical applications. Also it became the archetype of a family of compounds with the same basic structure, obtained by substitutions of one or more ionic species, which allowed the effect of ionic size, point and extended defects etc [Radaelli; 1998] to be examined.

YBCO ($YBa_2Cu_3O_{6+x}$; $0<x<1$) was discovered in an attempt to replace La in LBCO with another rare earth, the 4d transition element Y. A much higher transition temperature was observed at 93°K [Wu et al; 1987]. This was the first compound discovered to have a T_c above the temperature of liquid nitrogen. Like doped LBCO, YBCO has an unusual crystal chemistry [Bourdillon et al; 1994]. This is apparent from a consideration of charge balance. The unit cell contains one trivalent ion, Y, while all other atoms, whether anions or cations, are typically divalent. When $x<0.5$ or $x>0.5$, the charges can be balanced by a change in atomic valence, by site vacancies, or by the creation of holes.

A considerable proportion of the publications on YBCO have been concerned with structural effects. From this point of view, one of the most interesting properties of this compound is its ability to support a large oxygen nonstoichiometry. The compound undergoes a structural phase transition which is compositionally involving a change in

oxygen content. Certainly the subject of this thesis, **"Diffraction study of the structural phase transition in YBCO"**, is not unprecedented but here the main concern will be over i) the formation of the intermediate oxygen content ($x \approx 0.5$ 0) superstructure which is called "orthorhombic II" (OII), at elevated temperature range [200-300°C] , ii) the early stages of creation of twin stripes at high temperature range [500-600°C].

In the present study, *in-situ* x-ray and neutron powder diffraction measurement are combined with computational modeling to investigate these areas of interest. Utilizing the knowledge gained from previous volumetric and gravimetric studies [Mercer, 1997; Schleger, 1991; Meuffels 1989], *in-situ* diffraction experiments were performed, to produce conditions under which the above interesting phenomenon had been observed and to allow the measurement of any structural changes associated with these points of interest. Neutron is an excellent probe of the structures as they are sensitive to the oxygen in a high atomic number lattice.

Chapter II contains a very general survey of superconductivity in cuprates including YBCO. Chapter III reviews the structural and microstructural (twins & tweeds) aspects of YBCO. Monte-Carlo simulation has always been as an efficient method for studying the structural transitions in YBCO and Appendix **A** provides a detailed study of this approach. Chapter IV provides a background to the theory of diffraction and especially of the neutron techniques, neutron sources (Pulsed Spallation & High-Flux Reactor). In this Chapter, the Rietveld Method (R.M.), as the most powerful method for structural analysis of diffraction data, is reviewed also. Chapter V presents and discusses results obtained from *in-situ* powder x-ray and neutron diffraction about the formation of OII phase. The quantitative results extracted from the Rietveld refinements indicate the existence of a mixed phase region which means that there is a **first order** structural phase transition between tetragonal(Tet.) and OII phases in the temperature range of [200-300°C].

Chapter VI introduces the theory of "peak broadening analyses", as a practical method for analyzing microstructures and other crystal defects which may cause highly anisotropic (*hkl* dependent) line broadening effect on diffraction patterns. In this chapter

the benefit of the Williamson-Hall (W-H) plot due to a qualitative analysis of the anisotropic line broadening, is emphasized. Chapter VII is dedicated to the **second order** Tet. to Orthorhombic I (OI) phase transition at higher temperatures [500-600°C]. The formation of twins during this phase transition is the main concern in this chapter. With the aid of a computation modeling and the W-H plots, the collected *in-situ* diffraction data are analyzed. The prominent point in the results of this Chapter is the effect of interference from very thin twin stripes (which are formed just after the T/OI phase transition) on the shape of some diffraction peaks [*h00 & 0k0*].

Chapter II

AN OVERVIEW OF HIGH T_c SUPERCONDUCTIVITY IN CUPRATES

Introduction

Introduction

The cuprates have been the subject of a great number of diffraction studies and many other experimental investigations. These results imply that there is a high defect concentration in such complex materials, but only a few of these defects are electrically active and therefore are associated directly with superconductivity (S.C).

Their layered structure makes it possible to reduce the interplanar strain energy by changing the concentration of some native defects in each plane, such as anionic vacancies and interstitials [Shi; 1996]. What makes the cuprates so special is the high oxygen mobility, that suggest small activation energy for diffusion and high densities of oxygen vacancies or interstitials.

Another characteristic feature of layered cuprates is the resistivity tensor which is very anisotropic, with the *c*-axis resistivity, ρ_c, being two to three orders of magnitude larger than the planar resistivity, ρ_{ab} .Because the layers are alternately metallic and semiconductive, this anisotropy is not surprising. The system exhibits a sharp metal-semiconductor transition in sufficiently homogeneous single crystal (powder) cuprates, and much more dramatic changes can be achieved by modifying the semiconductive barriers between the metallic CuO_2 planes by varying the oxygen concentration.

To understand the microscopic mechanism responsible for S.C., it is important to study properties near and just below T_c. Contrary to the BCS theory, H-T_c

materials are in the strong-coupling limit. Mean field theories fail to describe the phenomena, because they ignore the internal degrees of freedom connected with impurities or defects. This anomaly can be considered not only as a small correction $\Delta\rho(T)$ to $\rho(T)$ at low temperature, but instead to the entire scattering process of current carrying particles, the character of which can no longer be described in terms of perturbed wave pockets, (Fermi liquid model). For example Sr in the (La $_{1-x}$ Sr $_x$) Cu O_4 not only donates metallic properties to La $_2$ Cu O_4, but it may also act as a defect that breaks the crystal symmetry by occupying a La site and by rearranging the O atoms in its nearest neighbour co-ordination shell [Shi; 1996].

Considering an atomic model of defect configurations, if defects are formed in the semiconductive layers, they can provide some deep trapping centres that pin E_f to within $K_b\theta$ range (E_f: Fermi level; θ: Deby temperature; K_b : Boltzmann const.). These resonant pinnings might be essential for providing current paths if there are insulating domain walls in the otherwise metallic CuO_2 planes. So the resonant pinning states can change the character of conduction from insulating to metallic across insulating atomic planes.

II.1) STRUCTURAL VIEWPOINTS

Physical and structural information shows that superconducting properties appear in cuprates if:

1) Cu and O atoms form square planes with Cu atoms at the center and four O atoms at the corners (CuO_2). So the allowed co-ordination number for the Cu atoms in this planes can be V or VI, according to the additional binding with off-plane oxygen atoms. The heart of the electronic properties causing S.C are these CuO_2 and they are present in all cuprate superconductors.

(i) In the CuO_2 planes, for the majority of cuprates holes are responsible for carrying current[1].

(ii) The critical temperature, T_c, will be maximal by the appropriate doping process (oxygen, Rare Earth or Earth Alkaline element substitutions); the optimum concentration of holes per Cu atom in the CuO_2 planes falls in the [0.15-0.2] range.

Apart from these important features, there are some other remarkable points like: Each of the four Cu-O bonds in the CuO_2 planes has lengths between 1.89Å to 1.97Å, whereas the length of the off-plane Cu-O bond (bonding with apical oxygen) is between 2.2Å to 2.9Å.

All the superconducting cuprates are non-stoichiometric compounds (except for $YBa_2Cu_4O_8$ [Rao et al; 1993]). Carriers are imposed on the CuO_2 planes by the charge transfer process after doping foreign ions or oxygen vacancies in the intermediate block structures between CuO_2 planes. These blocks are usually call ***Charge Reservoirs***.

It is well known that the ordering and oxidation states of atoms in these charge reservoirs are the most important factors influencing T_c and J_c. Provided that the radius difference between cations is not more than 15%, at room temperature a wide range of cation substitutions can be expected. On the other hand, cations with larger radius prefer to occupy sites with higher co-ordination numbers like Ba, r= 1.52 Å and Y, r=1.019 Å, in YBCO. If the co-ordination number for Alkaline-Earth or Rare-earth ions or the oxidation state of Cu atoms is too large, according to the neutrality rule, one or more oxygen sites in the reservoir's structure must be vacant (vacancies).

In the majority of cases (including YBCO compounds) apical oxygen is one of the crucial parts of the charge reservoirs. As already been mentioned, the binding between such oxygen atoms and the Cu atoms is weaker than the in-plane Cu-O bounds, but their presence causes the stability of the doped holes concentration in CuO_2 planes because, in the absence of apical O atoms, the repulsion forces on the electronic states in CuO_2 planes will be reduced. So with decreasing distance between apical oxygen atoms and CuO_2 planes, the electrostatic stability of doped holes should be increased.

---

[1] Electron-doped cuprates are synthesised of the type $Ln_{2-x}M_xCuO_{4-\delta}$ (Ln=Nd, Pr, Sm, Eu and M=Ce,Th)

II.2) Cu-CHARGE STATE

Atomic copper has an [Ar]3d(10) 4s(1) electron configuration and in the solid's electronic state, the weakest bound is for the 4s(1) electrons. In La CuO_4, the formal valence of the ionic Cu is +2, Cu (+2), thus the Cu ion has a 3d (9) configuration. There are few compounds with Cu (+3) ions.

The Cu ions in YBCO have charge states that vary with doping. The insulator (semiconductor) $YBa_2Cu_3O_6$ ($x = 0$) has two four co-ordinated Cu(+2) ions in the CuO_2 planes and a single two co-ordinated Cu(+1) ion on the CuO planes. However the $YBa_2Cu_3O_7$ (superconductor) has three Cu (+2.33) ions if the charge is divided equally among the Cu ions and still assuming that the excess charge resides only on the Cu ions [Burns; 1992]. The Cu valency in the $YBa_2Cu_3O_{6+x}$ has been extensively investigated by x-ray absorption spectroscopy (XAS) and it has been observed that the structure contains both monovalant and divalent Cu atoms referred to as Cu(I) and Cu(II). Cu(I) is assigned to the linearly co-ordinated Cu(1) sites and Cu(II) is present on both Cu(1) and Cu(2) sites, depending upon the doping factor, x. In a fully depleted sample ($x = 0$), all Cu in Cu(1) sites are monovalant, corresponding to the complete filling of the Cu's 3d orbitals; Cu is divalent in Cu(2) sites, corresponding to a formal 3d(9) filling. Under oxygen uptake, the Cu in Cu(1) sites acts as a reservoir of charges giving its 3d electrons to the neutral oxygen while, in the Cu(2) sites, the formal Cu valancy remains unchanged. In a fully oxidised sample ($x = 1$), no evidence of a 3d (8) filling for Cu ions has been founded (the formal trivalent Cu). Actually the complete charge balance implies an injection of holes into oxygen's 2p bands. These doping holes which are responsible for high-Tc S.C. are injected in different O's 2p bands formed by orbitals with X,Y,Z symmetries [Tolentonio et al;1992].

The O-Cu-O chains do participate in the electrical conductivity of YBCO and do become superconducting by proximity effect [Radaelli; 1998], but the structural backbone of the superconducting cuprates is the strongly covalent CuO_2 planes. Each Cu ion in the plane is surrounded with 5 oxygen ions, so that four Cu-O bonds are in plane $(Cu\text{-}O)_p$ and one Cu-O bond is along Z axis $(Cu\text{-}O)_z$, but, for the in-plane bonds the distance is about 1.9Å whereas the out of plane bond the distance is about 2.4Å. Thus, the $(Cu\text{-}O)_z$ is largely nonbonding compared to the

in-plane bonds. These bonds are consisted of 3d and 2p orbitals on the Cu ions and 2p orbitals on the surrounding oxygen ions. We will focus on the in-plane bonding, and consider the two planar O atoms with p orbitals that are directed toward the central Cu atom. On the central Cu atom, we only use the $d(X^2-Y^2)$ orbitals, since it is correctly oriented for σ bonding with its neighbouring oxygen.

Figure (2.1a) shows the CuO2 plane with $d(X^2-Y^2)$ orbitals attached to Cu atoms, and with p_x and p_y orbitals attached to the O atoms. The orbitals on Cu are all the same and those of the O atoms are same in *a* and *b* directions. Bonding between charge lobes of the orbitals occurs when the orbitals have the same phase (shaded-shaded or white-white). Antibonding occurs between orbitals with opposite phase (a shaded and a white orbital).

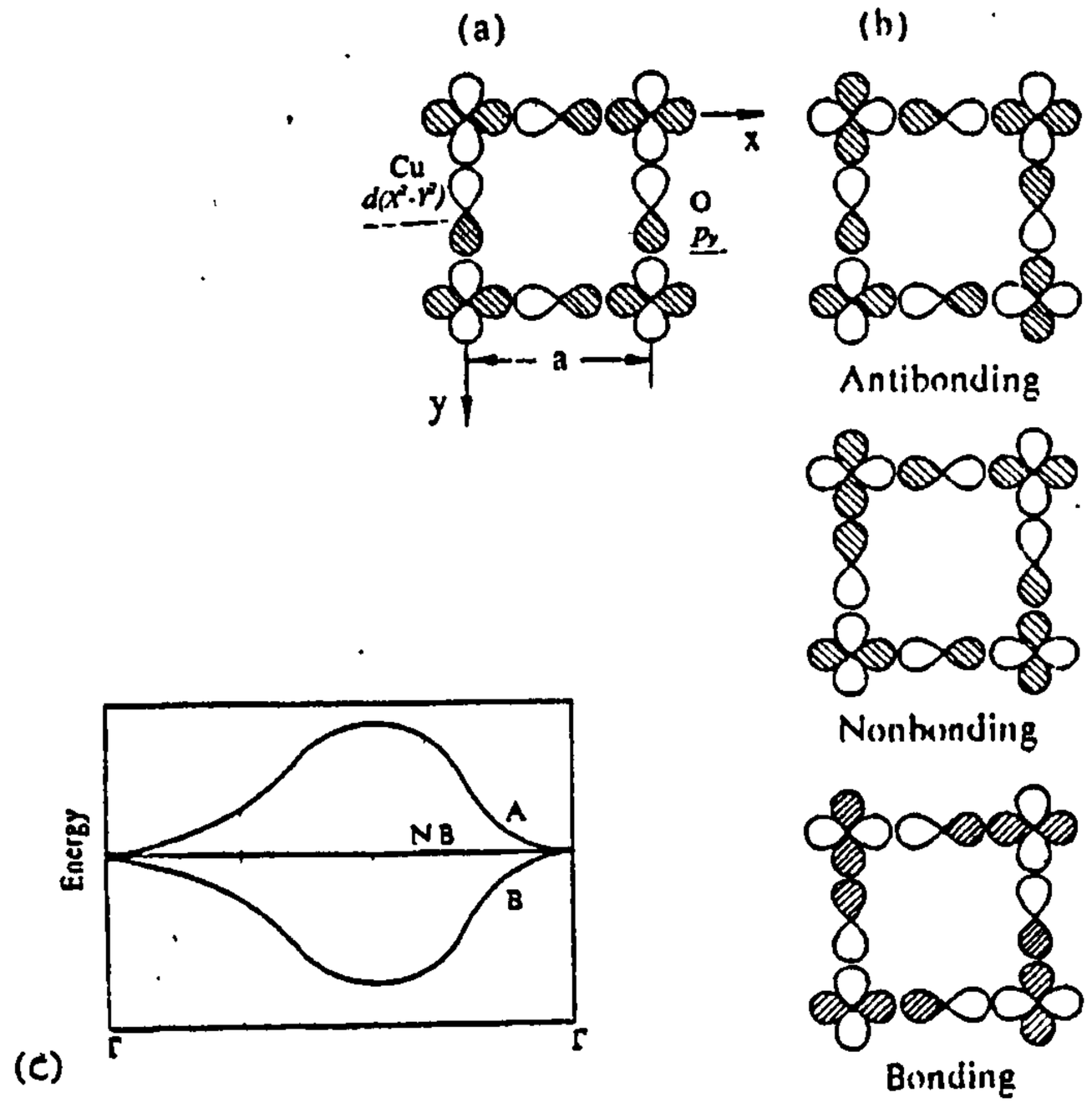

Fig.(2.1) a_ the CuO2, plane viewed from above, shows a hybrid bonding between the Cu[d] and O[p] orbitals. k = 0 refers to Γ point in the Brillouin zone. b_ is the same for M point in the Brillouin zone. c_ E vs. k for bonding (B) , antibonding (A) , and nonbonding (NB) orbitals (from Burns; 1992).

For the molecular orbitals in Fig.(2.1a), there are as many bonding as antibonding overlaps. Since the bonding and antibonding energies are approximately the same but opposite in sign, this molecular orbital is nonbonding. The bonding molecular orbital (B) has maximum amount of overlap and hence the lowest energy. The

antibonding molecular orbital (A) has minimum amount of overlap and hence the highest energy. The nonbonding molecular orbital (NB) has as many bonding as antibonding overlapping orbitals, hence the overlap causes little energy change from atomic case [Burns; 1992].

Superconductivity is believed to occur in the CuO_2 planes. The conductivity in the CuO_2 planes is on the basis of the formation of a narrow band, because of tight-bonding effects on hybrid bonds. If for some reason a hole or an electron is induced on the central Cu(+2) on each square of oxygen atoms in the CuO_2 planes, this excess charge moves through the lattice in a similar way as a charge (hole or electron) in the single-bond effective Hamiltonian, and a further hole or electron, created by under doping, feels a strong repulsion, so it is highly mobile [Zhang et al; 1988].

In YBCO the basal planes (Cu-O sheets), act as a charge reservoir. Each variation in the ordering of oxygen in the basal plane causes a redistribution of charges (holes) in this plane and in turns a hole transferring to the CuO_2 larger. A proper understanding of S.C. phenomena in $YBa_2Cu_3O_{6+x}$ system requires a detailed analyses of the simultaneous effects of the electronic correlation and the oxygen ordering

When the interchange between the localised linear chain states (basal plane) and extended states of CuO_2 plane reaches equilibrium, this electrical equilibrium between the 1D (chains) and the 2D (CuO_2 planes) parts of system regulates the variation of T_c as a function of x. Because of highly localised electronic states of the 1D chains, it is rational to consider that they do not have the necessary backgrounds to form Cooper pairs on them, but they regulate the number of holes on the CuO_2 planes [Latage et. al; 1990].

It is believed that the charge transfer mechanism is therefore:

In each chain, there is a strongly correlated system due to a hybridisation between O(p) orbitals and Cu(d) orbitals. A chain, $Cu_{n+1}O_n$, consisted of (n+1), Cu (1+) ions and, n, neutral oxygen (because of bonding between Cu and apical oxygen). Charge transferring is completed in two stages. First, a new charge redistribution over the chain takes place as:

Cu(+) — O....— Cu(+) — O — Cu(+)....— O — Cu(+) → Cu(2+) — O(-)....— Cu(2+) — **O(2-)** — Cu(2+)....— O(-) — Cu(2+)

So there would be just one O(2-) in each chain.

Second, charges from O(-) transfer to CuO_2 and the remained chain, have a composition like : $Cu(2+)_{n+1}\ O(2-)_m\ O(-)_{n-m}$ where n is the number of Cu-O bonds and m is the number of O(2-) ions in each chain. As is shown, m holes are transferred from the chained O(2-) ions in the basal plane to the CuO_2 sheet. It is established experimentally for long chains [Hagerud et al; 1997]:

$$\frac{m}{n > 4} = 0.7$$

For the majority of cuprates (including YBCO) Hall effect studies shows that the Hall Constant is positive, so carriers are holes, and $R_H \propto 1/T$ where:

$$(R_H)^{-1} \propto \textit{Density of carriers}$$

The density of carriers generally decreases with decreasing x, which is consistent with decreasing negative charge from fewer O(2-) ions [Burns; 1992].

II.3) SUPERCONDUCTING STATE

Some of the H-T_c material parameters are compared with conventional superconductors (metals) in table 1:

Table II.1

Quaantity	Conventional (metals)	High T_c Materials
Effective mass (m*)	1-15 Me (Me: mass of electron)	~ 5 Me
E_f (Fermi level)	5-10 ev	Order : 0.1 ev
Coherence Length (ζ)	Order : 1000 Å	Order : 10 Å
$\Delta(0)$ (the energy gap at 0°K)	Order : 10^{-4} E_f	Order : 0.1 E_f

As a result of the S.C. transition and of electron pairing (BSC theory), the Fermi surface undergoes a reconstruction within a layer of thickness Δ. Therefore the parameter $\Delta(0)/E_f$, shows what fraction of the electronic states are directly involved in pairing.

The large value of the above ratio corresponds to a significant fraction of the carriers being paired up, so naturally this implies a short coherence length. The possibility of having a large value of Δ/E_f and a short coherence length is directly related to the quasi two-dimensional structure of cuprates. Indeed in conventional superconductors, pairing can occur only near the Fermi surface, but in cuprates the

states on the Fermi surface form a two dimensional system in momentum space. This is important because in two dimensions any attraction (for example coming from magnetic interactions) will lead to the formation of a bound state [Kersin & Wolf; 1990].

From the band theory point of view, $YBa_2Cu_3O_{6+x}$ contains two different energy bands, of a quasi two-dimensional (CuO_2 planes) and a quasi one-dimensional (O-Cu-O chains) nature. So one should observe two energy gaps in the system as each band has its own density of carriers and other characteristics.

The superconducting state in the chains is caused by weak interband coupling, whereas that in the planes is characterised by strong coupling. Coherence length in planes is about 10Å and in the chains is about 7Å and the effective mass for chains is much heavier than it is for planes, $m^*_{ch} >> m^*_{pl}$, [Hagerud et al; 1997].

Origin of High T_c: Many experimental data indicate that the high T_c oxides display many features of the BSC theory, such as carrier pairing and the presence of an energy gap, Δ.

The pairing is caused by some intermediate field. In the BCS theory, this field comes from electron-phonon interactions. Generally speaking, attraction can be mediated by other excitations, such as plasmons, excitons, magnons, but which of these are responsible for interelectronic attraction is still an open question. As a result of BCS theory, the critical temperature, T_c, is determined by the strength of the coupling between electron and one of the aforementioned excitations, λ, and by the energy scale of the excitations, ω.

$$T_c = T_c(\lambda, \omega)$$

What is the role of phonons in these materials?

If the coupling is weak, then the observed high T_c can be provided by a large value of the energy scale, so much greater than the phonon energies, and so the phonon contribution will not be important. Otherwise phonons must play an essential role.

Chapter III

STRUCTURAL DEFECTS IN $YBa_2Cu_3O_{6+x}$

Introduction

Some defects in superconducting materials destroy or deteriorate superconductivity, S.C., while others promote it. For example, defects of an appropriate size can act as flux-pinning centres in a crystal (promoting). On the other hand, doping some impurities (like Pr) destroy S.C, but some other defects like "large-angle grain boundaries", which often act as weak links in the cuprate oxides (i.e. they subdivide the sample in regions, grains, of strong S.C. by weak S.C. interfaces because of missing the bulk ordering in the surface of the grains, walls). Therefore the existence and the size of structural defects, are the key elements limiting the use of these materials.

Thus an understanding of interfacial structure of grain boundaries is needed in the search for possible engineering processes to eliminate the bad grain boundaries in the H-T_c materials.

It is important to note that the range of the superconducting coherence length, ξ[1], in the cuprates is less than 20Å and the pertinent geometrical scale of importance for local structural is therefore of the same order. Hence, characterisation of the microstructure by using a near ξ scale and high resolution techniques are often required to study the relevant defects.

[1] - Coherence length

III.1) OXYGEN ORDERING

The equilibrium oxygen content of $YBa_2Cu_3O_{6+x}$ varies in a continuous way depending on the conditions of temperature and oxygen partial pressure. For the minimum oxygen content (x=0), the Cu atoms in basal planes, Cu(1), with +1 average charge are in the neighbourhood of two off-plane O atoms and so the structure is tetragonal (P4/mmm , a= 3.864Å , c= 11.849Å). Upon oxygen doping up to $x < 0.45$, the structure remains in a quasi tetragonal phase, which means that O atoms occupy (0,0.5,0) and (0.5,0,0) sites with the same random probability, and therefore the random distribution of short O-Cu-O chains along *a* and *b* directions make a texture like-structure, the **tweed** structure (locally orthorhombic strips randomly along *a* or *b* directions, which they preserve the total tetragonal symmetry of the system), where the Cu ions with unfavourable co-ordination number of 3 are just at the end of these chains. Basically it is well known that the oxygen ordering in the basal plane varies so as to ensure that the number of Cu(1) ions with co-ordination number of 3 is minimised.

When x=1 there is no oxygen deficit, (corresponding to the fully oxygenated state) and each Cu(1) atom is surrounded by four O atoms (two additional in-plane oxygen atoms) and the long ...O-Cu-O... chains form along the *b* directions, the structure should be orthorhombic (Pmmm, $a \approx 3.82$Å, $b \approx 3.89$Å, $c \approx 11.65$Å). The presence of oxygen vacancies in this structure at intermediate concentrations gives the possibility of vacancy ordering. This ordering process proceeds by the formation of superstructures consisting of mono or multi filled and empty oxygen chains (Fig.3.1) correspond to each superstructure unit cell in the basal plane. In diffraction experiments, diffuse superstructures intensitie are observed along the *a* direction which is perpendicular to the chains.

For concentrations near x= 0.5, some results indicate the formation of orthorhombic II (OII) phase, characterised by alternation of filled and empty oxygen chains (chapter V). This OII phase is assumed to have a superconducting T_c of 60°K and therefore to be responsible for the 60°K plateau in T_c which is observed in this concentration range (Fig.3.2).

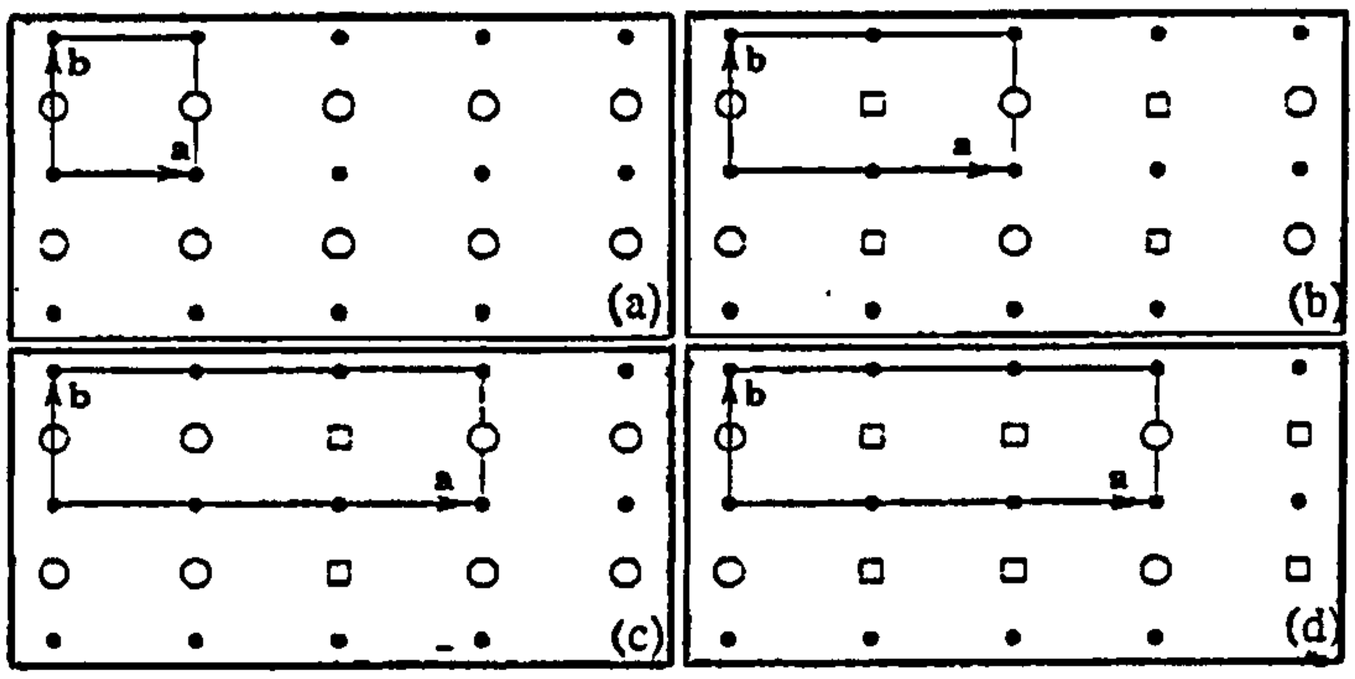

Fig.(3.1) a_Schematic representation of the basal (Cu-O) plane for the OI ordering; circles show the oxygen atoms and squares show the vacancies.
b_ model of the OII ordering ; c & d representations of ordering leading to triplet *a*- parameters, where c represent the OIII phase.
(Figure from Browning et al; 2000)

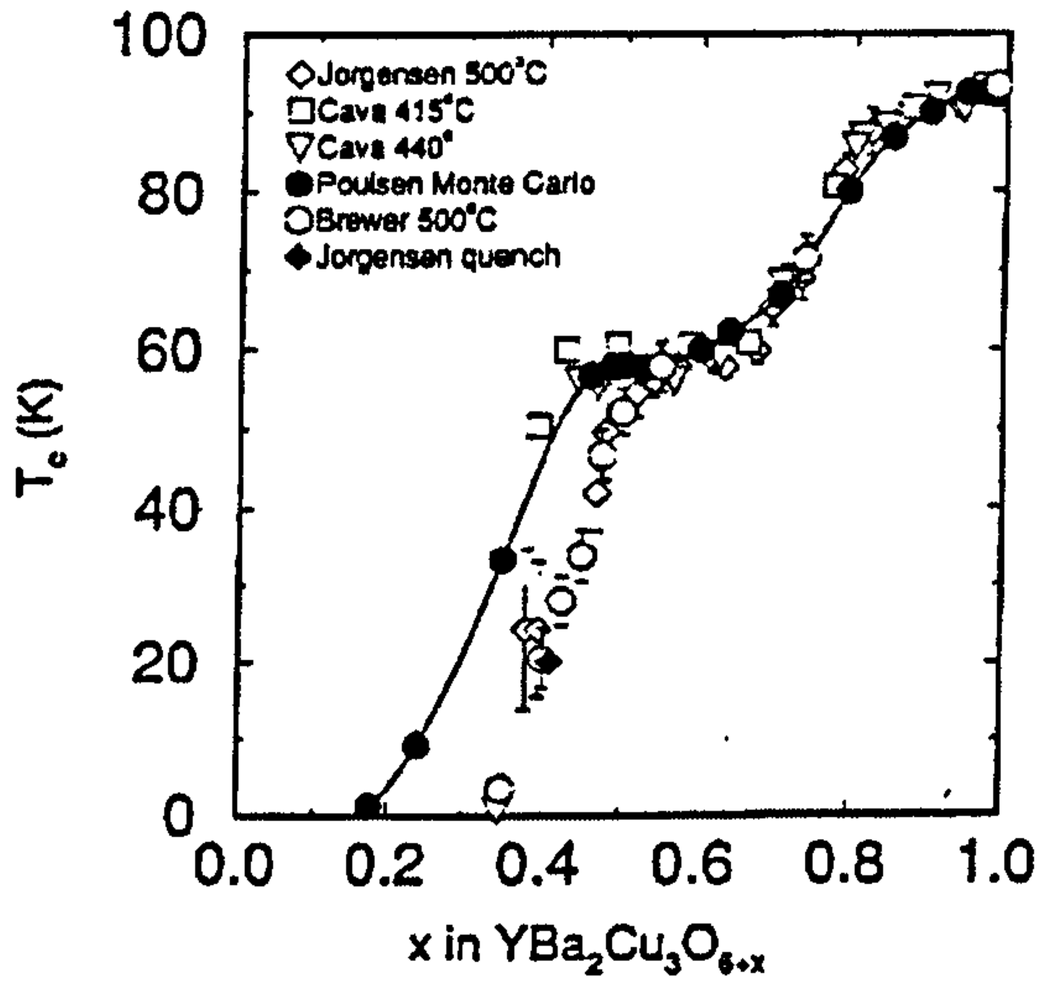

Fig.(3.2) A plot of T_c versus oxygen stoichiometry for $YBa_2Cu_3O_{6+2}$. (Figure taken from Schleger's thesis 1992)

At higher concentrations $0.55<x<0.75$, some peaks are observed at (2/5, 0, 0) and (1/3,0,0) by electron diffraction. These peaks are attributed to arrangements of filled and empty oxygen chains exhibiting a longer periodicity, e.g. two filled chains followed by an empty one (OIII structure) corresponding to $x= 2/3$.

Theoretical investigations of the phase diagram predict the stability of the OII phase up to a temperature of 400°C [de Fontaine et al; 1990], some also account for other ordered structures like the OIII stoichiometric at x=2/3 [Semenoskaya and Khachaturyan; 1992].

Besides the electron microscope results, the diffraction investigations of oxygen ordering and of the associated mesoscopic state as a function of the concentration and temperature are quite limited. Diffuse neutron scattering offers the possibility of investigating the state of oxygen order at the microscopic level. The microscopic ordering corresponds to correlation on the unit cell length scale and therefore leads to diffuse intensities at superlattice positions for single crystal samples. The results confirm the stability of the OII structure in a large range of x below 150°C [Schwarz et al; 1993].

III.2) TWINS

The most prominent structural defects in $YBa_2Cu_3O_{6+x}$ ($x>0.5$) are **twins** and twin layers are easily revealed in the (001) observation plane by electron microscopy methods [Moodie et al; 1988, Due et al; 1988 and Roy et al; 1991]. Below 750°C, the sample undergoes a tetragonal to orthorhombic I (T/OI) structural phase transition, resulting in twinning on the (110) or perpendicular planes. Splitting of long-range order reflections in the Electron Diffraction Pattern (EDP) beginning from third-order peaks, proves the existence of twin symmetry [Shekhtman; 1993].

Twins are formed to reduce strain energy due to the change in shape and volume of the unit cell resulting from the phase transformation. During the orthophase-tetraphase transformation the splitting of long-range-order spots disappears and the image of microtwin layers becomes blurred. It was possible to reversibily thermocycle the same transformation with repeated occurrence of a twin structure several times, though a detailed picture of the twin boundary localization was not reproduced. The twin layers become narrower, overlapped more often and disappeared completely after several cycles [Goncharov; 1993]. *Van Tendeloo* et al (1987), believed that the mechanism of Tet./OI phase transition is the disordering-ordering of vacancies in the oxygen sublattice.

Figure (3.3) shows a schematic representation of the strain field caused by the tetragonal to orthorhombic transition in the basal plane. The walls along the <110> directions are coherent. Walls along the <100> directions are also possible but at the cost of increasing the twin's surface energy. Here φ is the spontaneous rotation angle:

$$\varphi = \pi/4 - tg^{-1}(a/b) \qquad (3.1)$$

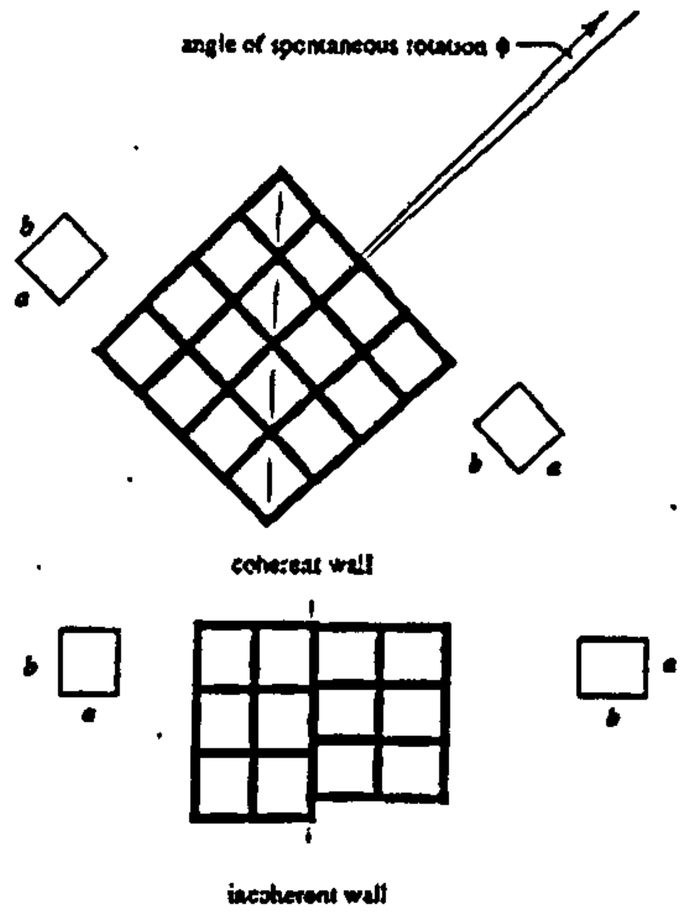

Fig.(3.3) Two possible twining arrangements in the basal plane (Fig. from Locherer et al; 1996)

Observations imply that there are two different types of twin boundaries in fully oxygenated and oxygen-deficient sample. For stoichiometric $YBa_2Cu_3O_7$, the twin boundaries appear to be centred on the (110) planes passing through the O atoms in the basal planes accompanied by a displacement of the cation sublattice along the boundaries (Fig.3.4a); for oxygen-deficient $YBa_2Cu_3O_{6+x}$, the twin boundaries are centred through the cations, and the cation sublattice displacements thus reduced or eliminated (Fig.3.4b). The structure of these two types of twin boundaries can transform one into an other. Such transition can be accomplished by the motion of the twinning dislocation and the associated twinning steps [Shi; 1996]. Electron microscopy also shows that two kinds of coherent walls can be formed:

i) In the Y $Ba_2Cu_3O_7$ samples, in addition to a rotation of φ , there is a lattice displacement given by:

$$\vec{R} = (1/2 - 1/3).2d_{110} \qquad (3.2)$$

at each boundary.

ii) In contrast with oxygen saturated samples, for Y $Ba_2Cu_3O_{6+x}$, $0.5 < x < 0.9$ there is no displacement at the boundary, just a rotation, φ, [Zhu et al; 1995].

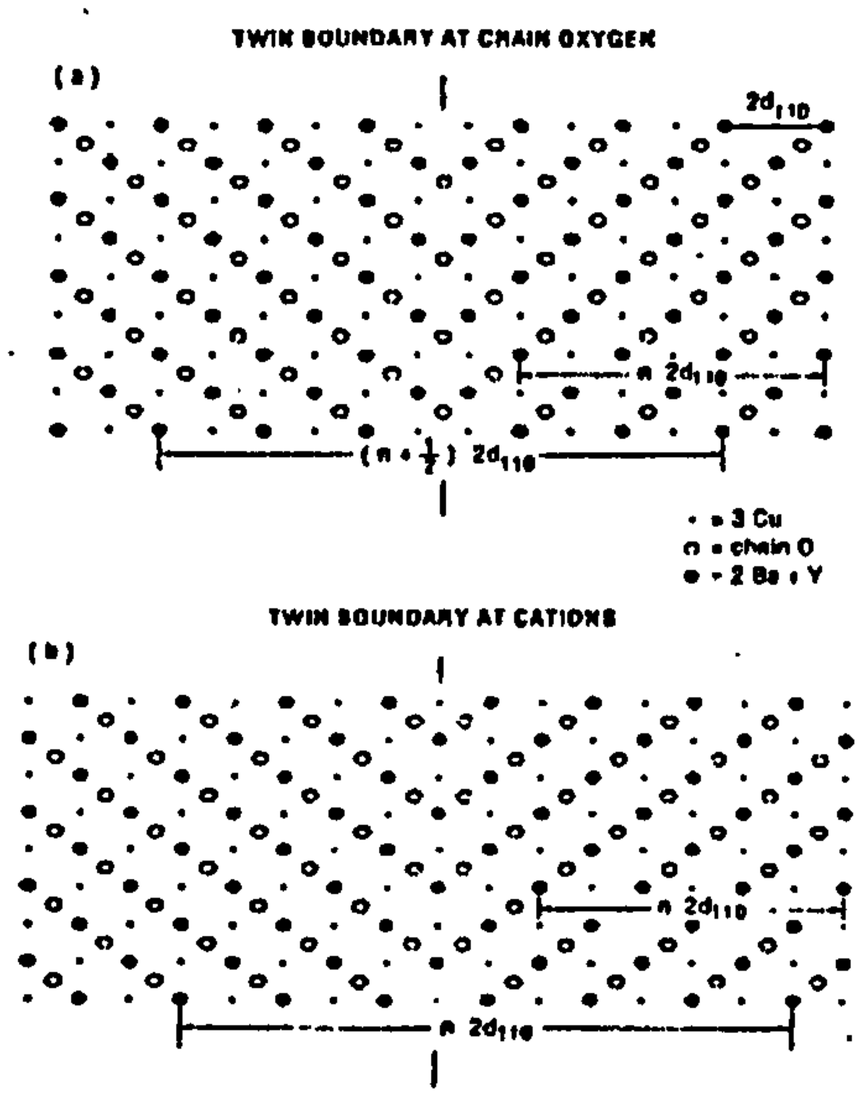

Fig.(3.4) Idealized drawing of the twin boundary region ; a) boundary at oxygen chains with displacement of cation sublattice along the boundary ; b) boundary centered at cations without local displacements of cation sublattice (Fig. from Shi; 1996).

Twinning destroys translational invariance in the direction normal to the twin boundaries, while the translational symmetry is preserved along the boundaries. The atoms lying on the boundaries are in a specific position, as compared with the other bicrystal atoms, and form a crystal with a dimension one less then that of the initial crystal.

All the boundary atoms lie more or less on the extension of the crystallographic planes, so that lattice distortion in crystallites forming a twin are minimum and drop rapidly with increasing distance from the boundary. Some recent accurate measurements suggest that there are very thin boundary walls (~ 7Å) between twined regions strips [Locherer et al; 1996]. This is why the excess energy due to a twin boundary is very low (the distortion is a small percentage of volume).

Twinning often occurs during plastic deformation, owing to defects formed during crystal growth and during the annealing of cold worked (hardened) specimens. Another effect caused by low excess energy of a twin boundary is that twinning can proceed in small particles of size, <1000 Å [Khlyustikov et al; 1987].

From the point of view of S.C. theory, a twin boundary is of interest, since near this plane, the conditions of Cooper Pairing may be quite particular. Correspondingly the

critical temperature of the superconducting transition in a twin boundary is higher than the T_c for the surrounding crystal, a phenomenon known as "critical-temperature enhancement" [Fang et al; 1988].

Fig.(3.5) shows a typical twinning morphology in a particle with whole grains. Usually in each particle several grains with their own twins strips can be seen. The platelet images show twin lamellae.

In practice, twining is of great importance because there is reason to believe that twin boundaries affect flux pinning. Figure (3.6) displays a vortex line going through a YBCO crystal with twin boundaries in different orientations. It may be speculated than when twin boundaries are perpendicular to the direction of the vortex, they might inhibit vortex motion; whereas with twin boundaries parallel to the vortices, they might move easily along the boundaries, but not across them.

Fig.(3.5) Scanning electron microscope image of twining (thanks to A.E.O. Lab. in IRAN).

all the chains are in <010> direction compared to the first one (so in resemblance to the ferromagnetic systems this phase is called **Ferroelastic** being opposite to the tetragonal phase which is called the **Paraelastic** phase) and then to build a stress free wall between them. The twin boundary will be parallel to the crystallographic (110) plane.

Several computational models (based on elastic strains) to describe the development of microstructure have been introduced [Parlinski et al; 1993, Salje et al; 1991, Semenovskaya & Khachaturyan; 1993]. They find that the microstructure forms clusters of oxygen order. The size of the clusters is dependent on the competition between the short-range oxygen order (the affinity for oxygen chains that are formed to minimise the number of 3 co-ordinated Cu ions) and the ferroelastic strain produced due to the ordering of the oxygen. The tendency for the oxygen to form chains will be reduced at high temperatures due to the entropy term in the free energy. It has been shown in some simulations of the evolution of the microstructure during the passage from the tetragonal to the orthorhombic phase that just below the phase transition temperature, the domain boundaries are rough and mobile, due to the energy of lattice strain deformation still being small [Salje & Parlinski; 1991]. Therefore, cooling just below the phase transition temperature leads merely to coarsening of perpendicular domains along the two possible directions <110> & $<\bar{1}10>$ in the basal plane. However a domain wall between two perpendicular domains is energetically unfavourable, compared with a domain wall between two parallel domains. The energy difference between these two allowed types of domain wall increases as the temperature decreases, and therefore the development of twin domains with only one preferred domain wall orientation is observed. The domain walls were observed to become immobile when there was an equal and opposite force due to strain in the domain's boundary.

Khachaturyan et al (1983) have shown that the distance separating twinning walls, T, is determined by the ratio of oxygen-oxygen interactions across the twinning plane and the strain energy that is proportional to the orthorhombicity which is due to the difference in the *a* and *b* lattice parameters:

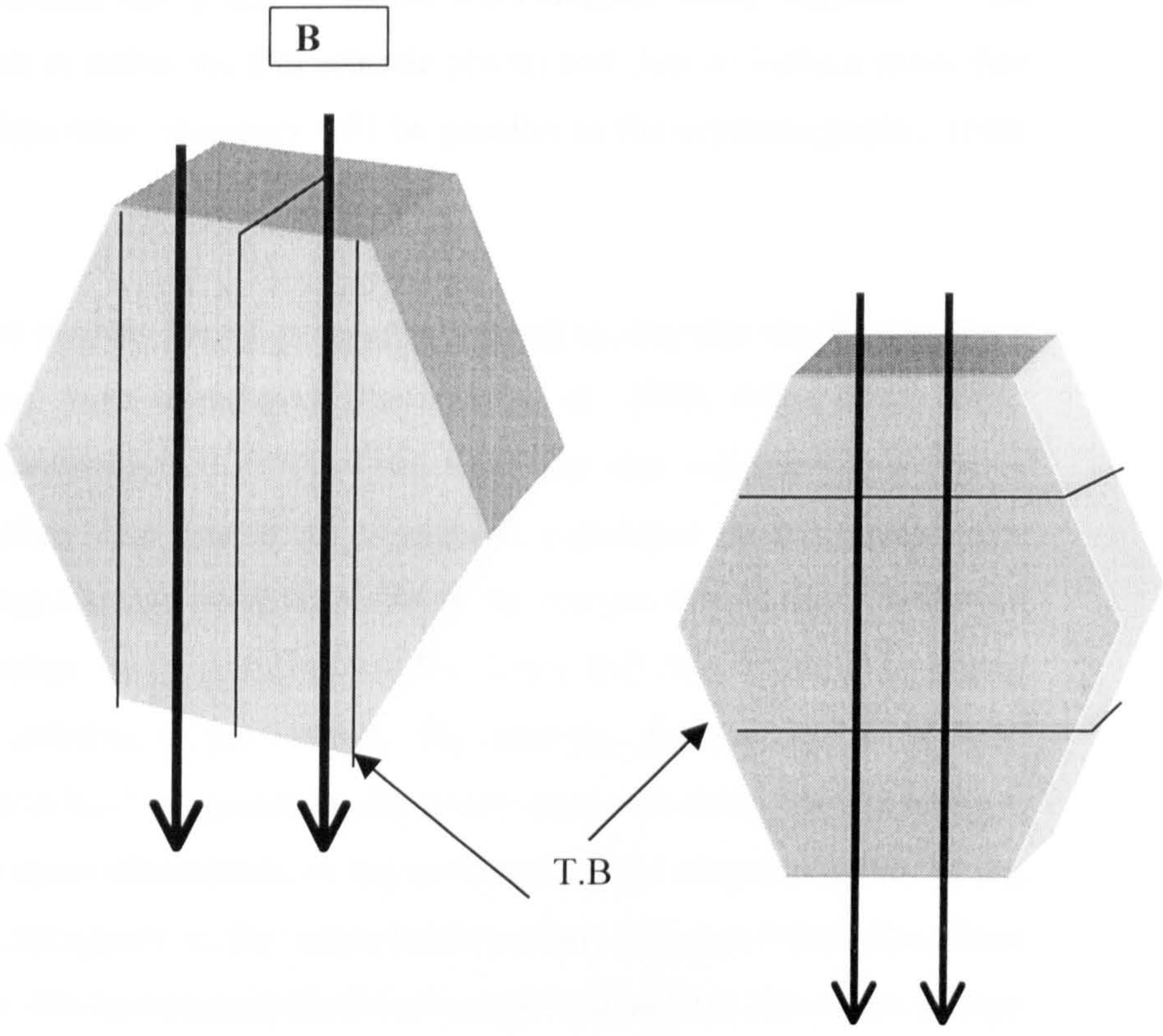

Fig.(3.5) A vortex line (B) penetrating YBCO crystal with Different twin boundaries (T.B) orientations.

Two groups [Welp et al; 1989] & [Wong-Ng et al; 1990] checked this idea experimentally by removing the twin boundaries from a single crystal (without losing oxygen) when it was heated up to about 400°C under 10^7 or 10^8 Pa pressure. This is because, under pressure, a slight rearrangements of the atoms take place, in particular the oxygen atom along the cell edge in the *b* direction will jump diagonally across the unit cell, relocating in the other position and the result is to change the *b* to the *a* direction.

With a sample in which flux pining was greatly enhanced [Cival et al; 1991], measured a superconductive critical current, J_c, up to 10^5 A/cm^2 for several Tesla magnetic field. It is rational for twining process if it is supposed in OI phase all the …O-Cu-O… chains at one lamellae are in the <100> direction and in other lamellae,

III.3) TWEEDS

Interestingly there are plenty of states and junctions of twin systems available under ordinary growth conditions for single and poly crystals of $YBa_2Cu_3O_{6+x}$, a so called ***tweed texture,*** that is, an equally probable overlapping of narrow microtwins, is always observed after exposure of a foil to an electron beam to an electron beam or after heating *in-situ*. The microtwins do not cause splitting of Bragg order reflections in electron diffraction patterns but show the average tetragonal symmetry by cross-shaped diffuse-reflection spots. The formation of tweed texture *in-situ* occurs when there is an oxygen deficiency, so the tweed structure is the ideal realization of homogeneous short-range ordering of oxygen atoms under oxygen-poor conditions.

Local oxygen ordering also occurs when a small fraction of Cu atoms in the basal plane is replaced by certain trivalent cations. In samples as follow:

$$YBa_2(Cu_{1-\delta}M_{\delta})_3O_{6+x}$$

(M= Fe, Co, Al), when $\delta<0.02$, the substitution causes the reduction of twin spacing. For $\delta>0.025$, it generates a homogeneous structural modulation with an overall tetragonal symmetry of the Bravais lattice.

The appearance of tweeding in HREM images shows a roughly periodic mutually perpendicular overlapping domains with somewhat diffuse boundaries positioned approximately parallel to the trace of $(1\bar{1}0)$ and (110) planes, associated with streaks of diffuse scattering as seen in electron diffraction patterns [Goncharov et al; 1993]. Although substitution did not enhance flux pinning as originally expected, the oxygen ordering related to the substructure has attracted much attention. In the aforementioned compounds several observations suggest that tweeding may not be directly caused by the presence of these trivalent ions. First, tweeds were also observed in the pure YBCO ($YBa_2Cu_3O_{6+x}$). Second, the extra positive charge that results from replacing a divalent or monovalent Cu ion with trivalent ions, the dopant M element, may attract an additional negative oxygen ion to form a short Cu-O chain along the *a*-axis, thus forming local " cross-links" around the dopant. Therefore the

$$T = \sqrt{\frac{G\gamma}{ES^2}} \tag{3.3}$$

Here the orthorhombicity, S=2(b-a)/(a+b), is a measure of transformation strain and G is the grain size, γ is the twin boundary energy per unit area and finally E is the elastic modulus of the material. Similar expressions have been derived using methods by Saikaya et al (1988), Barsch et al (1987), Xu et al (1989) and Mitchel et al (1990).

We should note here that the micrographs of samples showing twinned domains at ambient temperatures [Schmhal et al; 1989, Xu et al; 1989 and Goncharov et al; 1993], normally show quite large and rather uniform values of T. However, at high temperatures, we would expect that entropy effects would introduce fluctuations in the value of T about some mean value predicted from the above equation.

Now, if we adopt a Mean Field approach, i.e. if we give each O site on the a and b directions the appropriate occupation probability and calculate the twin boundary energy from the number of extra near-neighbour repulsions, we must conclude that γ is proportional to S^2, from which we would conclude that T is independent of S [Sarikaya et al; 1988]. However, the functional form of γ(S) is probably more complex than this because, clearly, with so many vacant O sites, the local arrangement of oxygen atoms can produce a lower internal energy than that predicted by MF theory, by minimizing the number of n.n. interactions and by some depletion in oxygen content near the twin plane [Moodie et al; 1988 and Goncharov et al; 1993]. This flexibility will be greatest at lower values of S so that we would expect γ(S) to increase as a higher power of S than S^2 and hence we would expect that the mean separation of the twin planes would tend to zero as S tends to zero. It is therefore of considerable interest to investigate the resulting diffraction pattern as S and T both tend to zero.

overall oxygen content in $Y Ba_2(Cu_{1-\delta} M_{\delta})O_{6+x}$ can be more than 7; every two trivalent ions incorporate approximately one oxygen. Third, oxygen reduction and low-temperature re-oxidation experiments of substituted samples show that the tweed appearance can be changed substantially. The disorder of the oxygen atoms occupying the unpermitted *a* direction sites nearest to the dopant changes the local symmetry of the lattice [Shi; 1996].

In the Salje and Parlinski's Monte-Carlo study, no spontaneous twinning was observed before the Tet./Orth. phase transition, but fluctuating tweed patterns always appear in the tetragonal phase (at all temperatures and $x< 0.4$). In fact the majority of the volume of the sample in the tetragonal phase was filled by small clusters having orthorhombic short-range order, extending over several unit cells (tweeding). Obviously, an equal number of small clusters must be ordered in the in the *a* and *b* directions, in order to maintain the macroscopic tetragonal symmetry, producing the characteristic "tweed" pattern, thus showing that a purely random distribution of oxygen vacancies is never achieved. To some extent the distribution of twin separation is dependent on the initial size and distribution of the embryonic ordered clusters in the tetragonal phase.

It is thus the oxygen configuration in the basal plane that is responsible for the formation of the tweed. The interstitial oxygen atoms in the basal planes cause the lattice to expand in the direction of Cu-O chains and to contract perpendicular to the Cu-O chains, resulting in a displacement modulation along the <110> direction. Furthermore, the correlation of the oxygen ordering between the Cu-O planes possibly generates a modulation along the <001> axis. The strain-induced, long-range O-O interactions and the nearest-neighbour dopant-oxygen attraction can account for the tweeding in the $YBaCu_3O_{6+x}$.

Chapter IV

NEUTRON TECHNIQUES

Introduction

Introduction

X-ray and neutron diffraction techniques provide quantitative information on crystal structures and defects averaged over volumes from about 10^{-3} to a few cm^3, respectively.

Electron diffraction and microscopy, probe volumes many orders of magnitude smaller than x-rays or neutrons (10^{-19}- 10^{-17} cm^3). This fact is important in correctly interpreting the nature of the information provided by the different diffraction techniques.

The results presented in Chapters V & VII utilise the experimental technique of neutron diffraction. In this chapter the theory of neutron scattering and of diffraction will be briefly described, along with the relative advantages of neutrons as a probe compared to other forms of radiation. An account of the neutron source and the instrument at which the data were attained will also be given.

IV.1) WHY NEUTRONS?

The neutron has certain advantages as a probe as compared with other sources of radiation utilised in solid state science. Neutrons interact predominantly with the nuclei of atoms in their path. Other commonly used radiation probes (x-ray and electrons) interact with the electrons of atoms in their path. One of the assumptions made during the discussions of scattering and diffraction theory was that the scattering centre is a point and has no finite size. Clearly the process of neutron nuclear scattering is closer to this assumption than the other probes which scatter from the electrons. It has also been mentioned that due to the point scatterer moving (having a spatial "thermal cloud") instead of being rigidly bound, an effect is observed called the "Debye Waller" factor which reduces the ideal intensity of diffraction peak (the factor decreases exponentially with increasing d-spacing). Clearly this effect is far more profound in data measured using probes which interact with electrons i.e. atomic size.

Another advantage of the neutron arises from the nature of its interaction with matter. The neutron interacts via the strong nuclear force. This force is very short range and causes the neutron to interact weakly with matter. Due to this weak interaction, the neutron is a highly penetrating probe, having the advantage that the bulk properties of a sample are measured and that large samples can be used. It also allows complex sample environment equipment to be utilized during experiments. The other common forms of radiation mentioned interact strongly via the electromagnetic force and thus are easily attenuated. Due to the fact that neutrons scatter from the nucleus, the strength of the scattering is not a function of the atomic number as it is with electrons and x-rays. This means that light atoms, for example, hydrogen and oxygen, can scatter neutrons much more strongly in comparison with other heavier atoms than x-rays. This is of great importance when attempting to study structures containing light atoms in high atomic number matrices, such as oxygen in the cuprate superconductors as studied in this

thesis. This fact also allows neutrons to differentiate between atoms of close adjacent atomic numbers as found in compounds like metallic alloys.

The neutron's major disadvantage is the expense involved in producing neutrons in a sufficient quantity to perform scattering studies as described. Even the most intense sources to date are less intense than laboratory x-ray kits and many orders of magnitude lower than the new large synchrotron facilities like the European Synchrotron Radiation Facility.

So in summary:

- Wavelength (~ Å for thermal neutron) , good for structural & phonon spectrum studies.
- Neutrality (high penetration ability with minimal multiple scattering).
- Magnetic moment (good probe for magnetic systems).
- Independence of its cross-section with the element's atomic number (suitable for detecting light elements and distinguishing different isotopes).

Properties of the neutron

Table VI.1[1]

mass	m= 1.008664924(14)u
spin	1/2
Magnetic moment	μ=1.91304275(45)μn
Electric charge	$Qn \leq (-0.04 \pm 1.1) \times 10^{-21}$ e
Mean square radius	Rn = 0.11± 0.02 fm
Electric dipole moment	$Dn \leq (-0.7 \pm 0.4) \times 10^{-21}$ e cm
Life time	$\tau = 888 \pm 3$ s

[1] From "Neutron And Synchrotron Radiation For Condensed Matter studies" Vol. I Hercules 1994

β decay of a free neutron $n \rightarrow p^+ + e^- + \nu$

IV.2) THERMAL NEUTRON SCATTERING

Thermal neutron scattering has become an important technique utilised by solid state scientists. The use of thermal neutrons as a probe of condensed matter dates back to the late fifties when research reactors of sufficiently large fluxes became available. Thermal neutrons are a useful probe due to the fact that they possess wavelengths which are comparable with inter-atomic separations in solids. This allows the study of ordered structures using diffraction techniques. A second most useful property of thermal neutrons is the fact that they have energies in a range which allows exchange of quanta of vibrational energy with the solid, therefore allowing the study of phonons. Thermal neutrons can also be used to study diffusive processes, where the neutron exchanges energy with the migrating atom. Due to the fact that the neutron has a magnetic moment, it can also be utilised to study magnetic structures and magnetic excitations. During the course of the studies described in this thesis only elastic neutron scattering techniques were utilised.

IV.2.1) *The Basic Theory of Neutron Scattering*

The neutron is an uncharged nucleon with a mass essentially the same as the proton, a spin of a half and a magnetic moment of $-1.913\mu_B$, nuclear Bohr magnetons. An overview of the theory follows. This theory is fully described in a number of text books [Bacon; 1975, Squires; 1978] to which the reader should refer for a more detailed derivation.

Thermal neutrons have wavelengths of the order of angstroms which are over four orders of magnitude greater than the size of the nucleus. The neutron is therefore unable to resolve the detailed nuclear structure and views the nucleus as a point scattering centre. The incident neutrons can therefore be regarded as a plane wave of the form

$$\Psi(\vec{r}) = e^{i\vec{k}_0 \cdot \vec{r}} \qquad (|\vec{k}_0| = 2\pi/\lambda) \qquad (4.1)$$

where $\mathbf{k_0}$ is the incident wave vector and is related to the wavelength, λ.

The perturbing scattterer, for instance a nucleus at the center, is:

$$V(\vec{r}) = (2\pi h^2/m) b\delta(\vec{r}) \qquad \text{(Fermi pseudo potential)} \qquad (4.2)$$

The scattered neutron at large distances compared with the radius of the nucleus:

$$\Psi'(\vec{r}) = -\frac{b}{r} e^{i\vec{k}_1 \cdot \vec{r}} \qquad (4.3)$$

where: b is called the " scattering length", and $\mathbf{k}_1$ is the scattered wave vector. In the above equations, b is a measure of the strength of scattering at a particular nucleus for a given total spin state, J (J=I+/-½, where I is the nuclear spin). The minus sign is conventionally inserted so as to make b positive in the expression for the scattered wave for the majority of nuclei.

The scattering length is in principle complex and describes how the wave functions from the incident wave matches the wave function in the compound nucleus (neutron and nucleus). The imaginary part signifies absorption of the neutron. In a small fraction of cases, the compound nucleus lies close to a resonant state and can give a value that varies widely both positive and negative for b.

IV.2.2) *Scattering Cross-Section*

The probability of a neutron interacting with a nucleus is defined in terms of the cross section, σ, which this is the rate of reaction per nucleon in unit incident flux.

The scattering of the neutrons may then be defined experimentally by the double differential cross-section:

$$\frac{d^2\sigma}{d\Omega dE} = \frac{R}{N\Phi d\Omega dE} \qquad (4.4)$$

Where R is the number of neutrons scattered per unit time into the solid angle dΩ in the direction (2θ,φ) with final energy E_f in the range E_i-E to E_i-(E=dE), E_i is the monochromatic beam of neutron's energy. Generally, a scattering event can result in a change in the direction and energy of the incoming neutron. The following discussion shall therefore be limited to the angular dependence of elastically scattered neutrons.

After an integration over the possible range of energies, the angular scattering cross section, $\frac{d\sigma}{d\Omega}(\theta,\varphi)$, is defined as the rate of scattering from unit incident flux, into a unit solid angle about the scattering angle, θ. Therefore,

$$\int_{4\pi}\frac{d\sigma(\theta,\varphi)}{d\Omega}d\Omega = \sigma_s \qquad (4.4)$$

Thermal neutron scattering from a nucleus is of s-wave type and therefore isotropic. Therefore for an isolated fixed nucleus, under elastic condition (diffraction) which the energy of neutron remains unchanged during the scattering process:

$$\sigma_s = 4\pi r^2 v\frac{\left|\left(-b/r\right)e^{ik_1\cdot r}\right|^2}{v\left|e^{ik_0\cdot r}\right|^2} = 4\pi\, b^2 \qquad (4.5)$$

where v is the neutron velocity, So: $\frac{d\sigma}{d\Omega} = \frac{\sigma}{4\pi} = b^2$ (4.6)

IV.2.3) *Scattering from a set of fixed nuclei*

Now consider the scattering from a set of N nuclei fixed at positions $\mathbf{R}_i$ each having nuclear scattering lengths b_i. The amplitudes of the scattered waves can be added in a given scattering direction.

The neutron wave functions are written for the incident and scattered plane waves each normalised to unit neutron density, so from the first Born approximation and the Fermi Golden role:

$$\left(\frac{d^2\sigma}{d\Omega dE}\right)_{\vec{k}_0\to\vec{k}_1} = \frac{1}{N}\frac{k_1}{k_0}\left(\frac{m}{2\pi h^2}\right)^2\sum_{\lambda_0}P_{\lambda_0}\sum_{\lambda_1}\left|<\vec{k}_1\lambda_1|V|\vec{k}_0\lambda_0>\right|^2\delta[E-(E_{\lambda_1}-E_{\lambda_1})]$$

where the states of the scattering system changes from λ_0 to λ_1 and the wave vector of neutrons changes from $\mathbf{k}_0$ to $\mathbf{k}_1$.

P_{λ_0} is the probability of the scattering system being in the λ_0 state and <...> indicates the thermal average.

With proper replacement (the δ function has been replaced by an integral representation over time):

$$\frac{d^2\sigma}{d\Omega dE} = \frac{1}{N}\frac{k_1}{k_0}\frac{1}{2\pi h}\int_{-\infty}^{\infty}\sum_{ii'} < b^*_i b_{i'} e^{-i\vec{Q}.\vec{R}_i(0)} e^{i\vec{Q}.\vec{R}_{i'}(t)} > e^{-i\omega t} dt \qquad (4.7)$$

where: $\vec{Q} = \vec{k}_1 - \vec{k}_0$ & $E = \hbar\omega$

also, $\vec{R}_i(t)$ is the actual instantaneous position of scattering centers with reference to some arbitrary origin.

With the assumption that there is no correlation between b values (random phase approximation), the matrix of the above equation can be simplified by averaging over the diagonal terms (i=j), yielding $<b^2>$ and over the non-diagonal terms. If the diagonal terms are reinserted as $<b^2>$, So:

$$b^*_i b_{i'} = \begin{cases} |\bar{b}|^2 \; if \; i \neq i' \\ |\bar{b^2}| \; if \; i = i' \end{cases}$$

$$\sigma_{coh} = 4\pi|\bar{b}|^2$$

and by definition : $\{$

$$\sigma_{inc} = 4\pi[|\bar{b^2}| - |\bar{b}|^2]$$

Therefore:

$$(\frac{d^2\sigma}{d\Omega dE})_{coh} = \frac{\sigma_{coh}}{4\pi}\frac{k_1}{k_0}\frac{1}{2\pi h}\sum_{ii'}\int_{-\infty}^{\infty} < e^{-i\vec{Q}.\vec{R}_{i'}(0)} e^{i\vec{Q}.\vec{R}_i(t)} > e^{-i\omega t} dt$$

Coherent partial differential Cross_section (4.8)

$$(\frac{d^2\sigma}{d\Omega dE})_{inc} = \frac{\sigma_{inc}}{4\pi}\frac{k_1}{k_0}\frac{1}{2\pi h}\sum_{i}\int_{-\infty}^{\infty} < e^{-i\vec{Q}.\vec{R}_i(0)} e^{i\vec{Q}.\vec{R}_i(t)} > e^{-i\omega t} dt$$

Incoherent partial differential Cross_section (4.9)

In general for elastic scattering (ΔE=0 or $|\mathbf{k}_1| = |\mathbf{k}_0|$) from a rigid lattice ($\vec{\vec{R}}_i(0) = \vec{\vec{R}}_i(t)$) :

$$(\frac{d\sigma}{d\Omega})_{inc} = N\{<|b_i|^2> - |<b_i>|^2\} = N<|b_i - <b_i>|^2>$$
$$(\frac{d\sigma}{d\Omega})_{coh} = \frac{\bar{b}^2_i}{N}\sum_{ii'} <e^{-i\vec{Q}.\vec{R}i} e^{i\vec{Q}.\vec{R}_{i'}}> \quad (4.10)$$

The scattering cross section has thus been separated into two terms, the first term, is the incoherent scattering and is isotropic, containing only information about a particular tagged atom. The incoherent term arises from deviations from the mean scattering length of different atoms, due to isotope and nuclear spin effects.

The second term is the coherent scattering, which is determined by the relative positions of the atoms taken in pairs. The coherent term arises from correlations between the same nucleus at different times as well as correlations between different nuclei at different times. This term includes the interference effects which are used to gain information on the structure in diffraction experiments.

Scattering function, $S(\vec{Q},\omega)$

From Van Hove(1954):

$$(\frac{d^2\sigma}{d\Omega dE}) = \frac{k_1}{k_0}\frac{\sigma_s}{4\pi}S(\vec{Q},\omega) \quad (4.11)$$

$S(\vec{Q},+\omega)$: *Neutron loses Energy in the scattering process*

$S(\vec{Q},-\omega)$: *Neutron gains Energy in the scattering process*

where: $S(\vec{Q},-\omega) = \exp\{-h\omega/k_B T\}S(\vec{Q},\omega)$ ***(principle of detailed balanced)***

$S(\vec{Q},\omega)$ contains all the physical information of the structure and dynamics of the scattering system , particularly useful when diffusion is involved. It can be related to the time dependent "pair correlation function", G(**r**, t).

$$S_{coh}(\vec{Q},\omega) = \frac{1}{2\pi}\iint G(\vec{r},t)e^{i(\vec{Q}.\vec{r}-\omega t)}d\vec{r}dt \quad (4.12)$$

$$S_{inc}(\vec{Q},\omega) = \frac{1}{2\pi}\iint G_s(\vec{r},t)e^{i(\vec{Q}.\vec{r}-\omega t)}d\vec{r}dt \quad (4.13)$$

Gs(**r**, t): The probability that if a particle at time, t=0 is at some origin then **the same particle** will be at **r** relative to that origin at some later time, t, **(self correlation function).**
G(**r**,t): The probability that if a particle at time, t=0 is at some origin then **any** particle will be at **r** relative to that origin at some later time, t, **(total correlation function).**

Otherwise we can interpret Gs as a measure of a single particle behavior averaged over all particles in the system, whereas G gives information on the pair correlations which is averaged over all pairs in the system.

IV.3) NEUTRON DIFFRACTION

The neutron diffraction technique utilizes the properties of coherent elastically scattered neutrons. As in other methods of diffraction, the aim is to study the structure of a material. A neutron diffraction instrument only measures the angular dependence of the scattered neutrons. Therefore, a reasonable starting point would be the angular differential cross-section expression discussed in the previous section,

$$d\sigma/d\Omega = [\langle b^2\rangle - \langle b\rangle^2] + (\langle b\rangle^2/N)\sum_{ij} \exp[i\mathbf{Q}.(\mathbf{R}_j - \mathbf{R}_i)] \qquad (4.14)$$

From this equation it can be seen that the incoherent part produces an isotropic background (other factors have an influence i.e. Debye-Waller factor) onto which the features due to the coherent interference effects produced by the structure of the probed lattice are added.

It is obvious therefore that the right-hand side (r.h.s) of the above equation is responsible for information concerning the structure.

The r.h.s can be expressed in terms of **G**, the lattice vector of a given unit cell and ρ, the position of the atom within the unit cell, to give

$$(d\sigma/d\Omega)_{coh} = |\sum_{ii} \exp(i\mathbf{Q}.\mathbf{G})|^2 \times |\sum_{ij} \langle b_\rho\rangle \exp(i\mathbf{Q}.\rho)|^2 \qquad (4.15)$$

where, n refers to the summation over all unit cells and ρ to the summation over all atoms within the unit cell.

It can be shown that the first term in the above equation has a sharp maxima at points where the wave vector transfer **Q** corresponds to a reciprocal lattice vector τ. Integrating over the region of space surrounding each lattice point, it can be shown that the magnitude of this term is $8\pi N_o/V$, where N_o is the total number of unit cells in the crystal and V is the volume of the unit cell.

Therefore:

$$(d\sigma/d\Omega)_{coh} = (8\pi^3 N_0/V) \sum_\tau |F_\tau|^2 \delta(Q-\tau) \quad (4.16)$$

where the Dirac delta function expresses the condition that the wave vector transfer is equal to the reciprocal lattice vector. The expression,

$$F_\tau = \sum_\rho <b_\rho> \exp(i\tau.\rho)\exp(-W_\rho) \quad (4.17)$$

is known as the structure factor of the unit cell for the reciprocal lattice vector τ. The structure factor depends on the atomic position in the unit cell form factors and temperature factors.

The form factor for neutrons is simply the scattering length for the particular scatterer isotope, whereas for x-ray it depends on the atomic Z number and the diffraction angle ($\sin\theta / \lambda$).

The W_ρ is called the Debye-Waller factor, and is a damping term which depends upon the thermal atomic displacements. A complete treatment of the Debye-waller factor is beyond the scope of this thesis but its general behavior is well illustrated by: $2W = \frac{1}{3} Q^2 \langle u^2 \rangle$, where $<u^2>$ is the mean square thermal displacement of an atom from its equilibrium position.

For elastic scattering the magnitude of Q is $2k_o \sin\theta_B = 4\pi \sin\theta_B/\lambda$ where θ_B is the Bragg angle. If adjacent *hkl* planes are separated by a distance d, $|\tau| = 2\pi/d$ and since $|Q|=|\tau|$ for elastic scattering, this implies that $1/d = 2\sin\theta/\lambda$, satisfying Bragg's Law.

As with x-rays, with neutron diffraction, the symmetry and separation (lattice constants) of the unit cell are found from the positions of the observed maxima, whilst the unit cell structure is determined form the measurement of the integrated intensities of the maxima. Several other factors exist which influence the data measured during a neutron diffraction experiment.

IV.4) THE RIETVELD REFINEMENT METHOD

The Rietveld refinement method was extensively used in the analysis of the neutron diffraction patterns presented and discussed in Chapters V and VII. An excellent book on the subject has been complied by Young (1993), with help from many prominent researchers in the field. Rietveld introduced this method to the public domain by publishing two papers, (1969,1967). The technique was initially ignored but now is a fundamental technique in the area of powder diffraction.

The Rietveld refinement method differs from previous powder diffraction analysis techniques by its use of all available data; the whole pattern is used. A model pattern is calculated and compared to the observed pattern. The parameters of the model are varied until the best least squares fit is obtained. Parameters contained in the model define the crystal structure and instrumental setup. In this study the method has been utilized to gain accurate lattice parameters and oxygen contents of $YBa_2Cu_3O_{6+x}$ throughout the phase diagram. It has also been used to highlight the hkl dependency of the peak widths in this material.

IV.4.1) Fundamentals of the Rietveld Method

For a powder with well-resolved Bragg reflections, it can be written:

$$y_i = \sum_H I_H \, \Omega \, (T_i - T_H) + D_i + B_i$$

where y_i is the number of counts, the subscript " i " represents a discrete observation at the scattering variable T_i . Here we adopt the variable T to describe either the scattering angle 2θ, the time of flight *t* (TOF, if a neutron pulsed source is used) or the scattering vector Q.

H corresponds to Bragg peaks contributing to the channel 'i'. I_H is the integral intensity of the reflection H, $\Omega(T_i-T_H)$ is the value of the normalized profile function of the Bragg reflection at the position T_i due to the reflection H at the position T_H. D_i is the diffuse scattering due to defects. Finally, Bi is the background coming from other sources (TDS, incoherent scattering, inelastic, sample environment, etc.)

The diffuse term D_i can be approximated by an expression like:

$$D_i = \sum_j \alpha_j \sin[Q_j] / (QR_j) \qquad (4.18)$$

The number of terms to be considered in the sum, and the interpretation of the coefficients α_j and the distances R_j, depends on the particular defect model. To obtain the maximum information from the powder diffraction data experimentally, absolute values (corrected for inelasticity and sample environment) of the intensities have to be collected in order to be able to separate the different contributions to the inelastic background. Only under these conditions can the diffuse scattering term be handled quantitatively.

The information about the average crystal structure is contained in $I_H(\sim F^2)$ and T_H (through the cell parameters). The size and shape of the reflection domains as well as the strains produced by the defects contribute to the profile function $\Omega(T)$.

In Rietveld method, the weighted sum of squared difference between y_{iobs} and y_{ical} is minimized. If the set of model parameters is $\xi = (\xi_1, \xi_2, \ldots \xi_p)$, the RM tries to optimize the chi-square function:

$$\chi^2_p = \sum_I w_i \{ y_{iobs} - y_{ical} \}^2 \qquad (4.19)$$

where w_i is the inverse of the variance associated to the observation 'i' ($\sigma^2(y_{iobs})$).

The functions I, Ω, D and B, are calculated on the basis of a particular structural model and some empirical functions depending on a number of adjustable parameters.

The integrated intensity for a Bragg reflection is given by:

$$I_H = \{ jL\, A\, O\, E\, F^2 \}_H \qquad (4.20)$$

Where j is the multiplicity, $L = 1/(2 \sin^2\theta \cos\theta)$ is the Lorentz factor for constant wavelength neutrons, in the case of TOF we have $L = d^4 \sin\theta$, A is the absorption correction, O is a function to correct, if needed, for preferred orientation, E is the primary extinction and F is the structure factor of the average unit cell.

Recently the RM has been used for the study of crystalline materials with defects, usually handling only average structure. This can be done in cases where the interaction of the defects does not have a big effect on the shape of Bragg reflections the profile function and where the half-width parameters are not very different from the instrumental ones.

IV.5) NEUTRON SOURCES

There are two ways in which neutrons can be produced in sufficient quantities to perform neutron scattering experiments. One is to use a nuclear fission reactor, the second is to use a pulsed spallation source in which protons are accelerated into a heavy metal target, and neutrons come out.

IV.5.1) ISIS

The ISIS neutron source is a proton spallation source. Three stages are required to produce protons with enough energy to produce efficient spallation. First, H^- ions are produced in an ion source and accelerated in a pre-injector column to 665KeV. Secondly the ions pass through a linear accelerator and reach an energy of 70MeV. At this, the third stage, the ions are stripped of their electrons using a thin (0.25mm) alumina foil, producing protons which are then injected into a synchrotron ring. The proton synchrotron has a diameter of 52m and accelerates 2.5×10^{13} protons per pulse to 800MeV. Here, the proton beam is extracted and sent to the target station. This process is repeated 50 times per second. The target at ISIS is either depleted uranium or tantalum. Many neutrons are produced from the spallation interaction of the protons with the nucleus of the heavy metal target material. This results in a pulsed beam of neutrons of sufficient flux to perform the type of investigations previously discussed in this chapter.

The neutron pulse which results from the spallation reaction has very high energies and must be slowed down to be of the correct range of wavelengths and energies for condensed matter neutron scattering studies. This is performed in a process called moderation. Moderation is achieved by allowing the beam of neutrons to pass through an hydrogenous medium such as water. Hydrogenous media are used in moderators due to the large scattering cross section of hydrogen. The neutrons passing through the moderator collide with the hydrogen nuclei and exchange energy and thus slow down until thermal equilibrium is achieved. At thermal equilibrium the neutrons will have a Maxwellian energy distribution characteristic of the temperature of the moderator. In this manner, moderators of different temperatures will produce neutrons with different

distributions of energies. ISIS uses three different moderators, ambient temperature water (316K, H_2O), liquid methane (100K, CH_4) and liquid hydrogen (20K, H_2).
As has already been noted, ISIS is a pulsed neutron source. This fact is exploited by using time-of-flight techniques on the white neutron beams to directly determine the energy and wavelength of each neutron. As time-of-flight is utilized to characterize the neutrons, it is important to determine the exact time of creation of the neutron and therefore the neutron pulse should be sharp. The initial width of the pulse is 0.4μs. This sharpness is preserved by the use of small moderators, which also gives a rich epithermal (high energy) component to the under-moderated spectrum. Due to the fact that white beams are utilized, the instruments can be of fixed geometries which reduces errors due to positional uncertainty.

Neutron Powder Diffractometer (OSIRIS)

This section gives a brief description of OSIRIS, the high resolution neutron powder diffractometer employed to obtain the results discussed in Chapter VII. An introduction to the instrument and its attributes will be presented. The technical information has been pasted from the site: http://www.isis.rl.ac.uk/molecularspectroscopy/osiris/

The OSIRIS Spectrometer

ISIS is not a continuous source of neutrons, as is a nuclear reactor. Neutrons are produced in pulses by letting a burst of protons hit a target (at present tantalum) whereby neutrons are produced by spallation. At ISIS, neutrons are produced every 20 ms (i.e. with a frequency of 50Hz). The neutrons released are however far too fast and have to be slowed down. This is done in a series of hydrogenous moderators at different temperatures, arranged around the target. The OSIRIS guide views the liquid H_2 moderator at 22 K. This means that the Maxwellian distributions of velocities/wavelengths has its maximum around 6 Å. The actual maximum is slightly lower, since there also exists a wing from the high energy (short wavelength) epithermal neutrons which moves the maximum towards shorter wave lengths.

Here we compare the neutron flux at OSIRIS, IRIS and HRPD. The increased intensity on OSIRIS compared to IRIS is due to the use of a supermirror guide. The flux on HRPD, though much lower for cold neutrons, extends to shorter wavelengths. HRPD views the liquid methane (CH_4) moderator at 100K, which gives an intensity maximum around 2 Å.

OSIRIS and IRIS share a beamport in the shielding around the target station. After the main shutter, the beamline is split and two neutron guides bring the neutrons to the instruments. The OSIRIS guide is a curved *m*=2 supermirror guide which avoids direct line-of-sight with the moderator and thus eliminates a large fraction of the fast neutrons and other background components coming from the spallation target.

Two disk choppers at 6 and 10 m from the moderator, select an appropriate range of wavelengths from the moderator and prevent frame overlap which can occur when fast neutrons from one pulse arrive at the detector simultaneously with slow neutrons from a previous pulse.

This time-distance diagram illustrates how frame overlap is eliminated by the choppers. In this example, they are running at 50 Hz and are set for 2 Å as the shortest wavelength. On the second pulse the opening times of the 6.3 and 10 meter choppers are marked. TCB marks the time channel boundaries for the detectors.

Most of the time, the choppers are run at 25 Hz, eliminating one ISIS pulse in two, and doubling the range of wavelengths which reach the sample. In this configuration, neutron wavelengths up to about 35 Å can be selected without significant frame overlap. To go to longer wavelengths, the choppers must be run at 10Hz and slightly dephased relative to each other. In this way, neutron wavelengths of up to 70 Å can be accessed.

Due to the curvature of the guide, wavelengths below about 1.5 Å do not reach the sample. This gives the lower limit to d-spacings accessible in the diffractometer. At the end of the curved guide, a converging guide focuses the beam onto a 22×44 mm (W×H) spot, increasing the flux on the sample.

Immediately before the converging guide, the Polariser Interchanger allows the insertion of a polarising supermirror bender to polarise the incident beam. This is followed by a current-sheet flipper and a series of guide fields to bring the incident beam polarisation up to the sample. In the non-polarised configuration, the polariser and flipper are replaced by a section of straight *m*=2 supermirror guide.

The incident beam monitor is placed immediately after the Polariser Interchanger. There is also a transmitted beam monitor in the 'get-lost' tube after the detector tank. Both are glass bead monitors. There are five beads horizontally and 6 vertically and the active component is ^{6}Lithium. The monitor efficiencies are wavelength-dependent, but always less than 1% over the range of wavelengths accessible on OSIRIS.

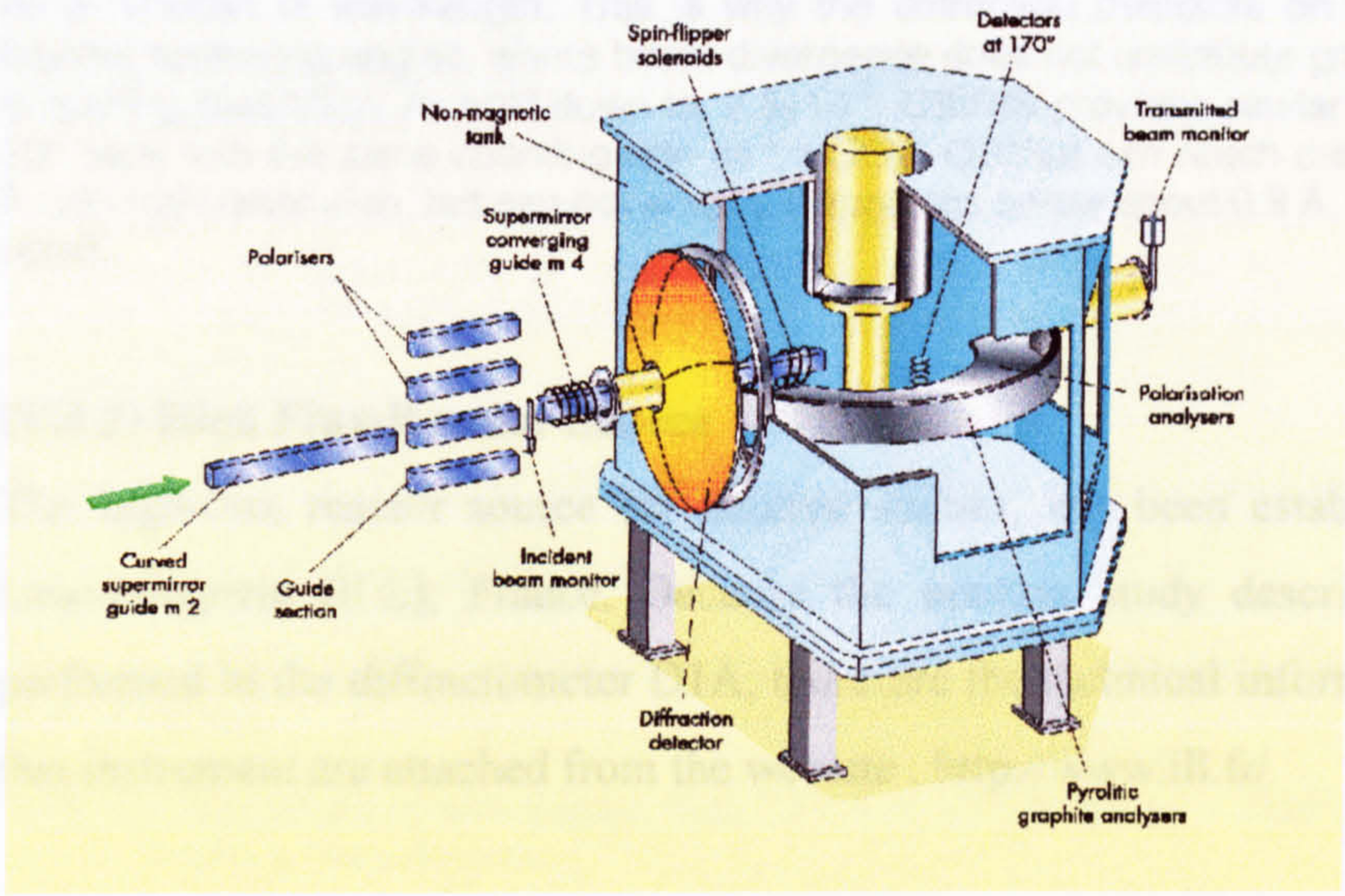

A schematic picture from OSIRIS

Technical Description of OSIRIS: Diffractometer

The diffraction detectors are placed in a ring around the incident beam. They cover the full range of scattering angles 2θ from 150° to 171°, providing a total solid angle coverage of 0.67 steradians.

The detectors are shown schematically here, seen from the sample position. They are scintillators and the full detector bank contains 8 modules, numbered according to the order in which they were installed. Each module consists of 120 detector elements. The first 20 are single detectors. Between 21 and 120 the even numbered detectors are still single but the odd numbered are physically composed of one detector above and one below the central strip, hardwired together, as shown for module 1 below.

The choppers typically run at a frequency of 25 Hz, which allows a 4 Å wide wavelength range to reach the sample with minimal contamination from other wavelengths.
The d-spacings measured are given by Bragg's law: $\lambda=2d\sin\theta$ and since the diffraction detectors are close to backscattering ($\Rightarrow \sin\theta \approx 1$) the d-spacing is about half the neutron wavelength. The range of d-spacings measured with the choppers at 25Hz is thus about 2 Å wide. In order to measure a full range of d-spacings to properly characterise the sample, a series of runs are usually performed with an incremental increase of the chopper phasing. The data from these runs are then merged in software to create a data set which spans the full range of d-spacings of interest in a continuous manner.
The combination of a cold moderator and a supermirror guide provides a high flux of cold neutrons on OSIRIS. Neutron wavelengths of up to 70 Å can be used.

The reduction in flux at long wavelengths is partly compensated for by the λ^4 form factor which applies to Bragg peak intensities. The use of a supermirror guide significantly enhances the neutron flux at all wavelengths, but at a price in beam divergence, which increases substantially

as a function of wavelength. This is why the diffraction detectors on OSIRIS only cover the highest scattering angles, where beam divergence does not contribute greatly to the instrumental d-spacing resolution. At $\Delta d/d$ down to 2.5×10^{-3}, OSIRIS provides similar resolution to the HRPD 90° bank with the same counting rate as on GEM. OSIRIS can reach d-spacings in excess of 30 Å with high resolution, but can not access d-spacings below about 0.9 Å, due to the curved guide cutoff.

IV.5.2) High Flux-Reactor Source

The high-flux reactor source for neutron studies, has been established in the "Institute Laue-Langevin (ILL); France. Because the neutron study described in the chapter V, performed in the diffractometer D1A, therefore the technical information corresponding to that instrument are attached from the website : http://www.ill.fr/

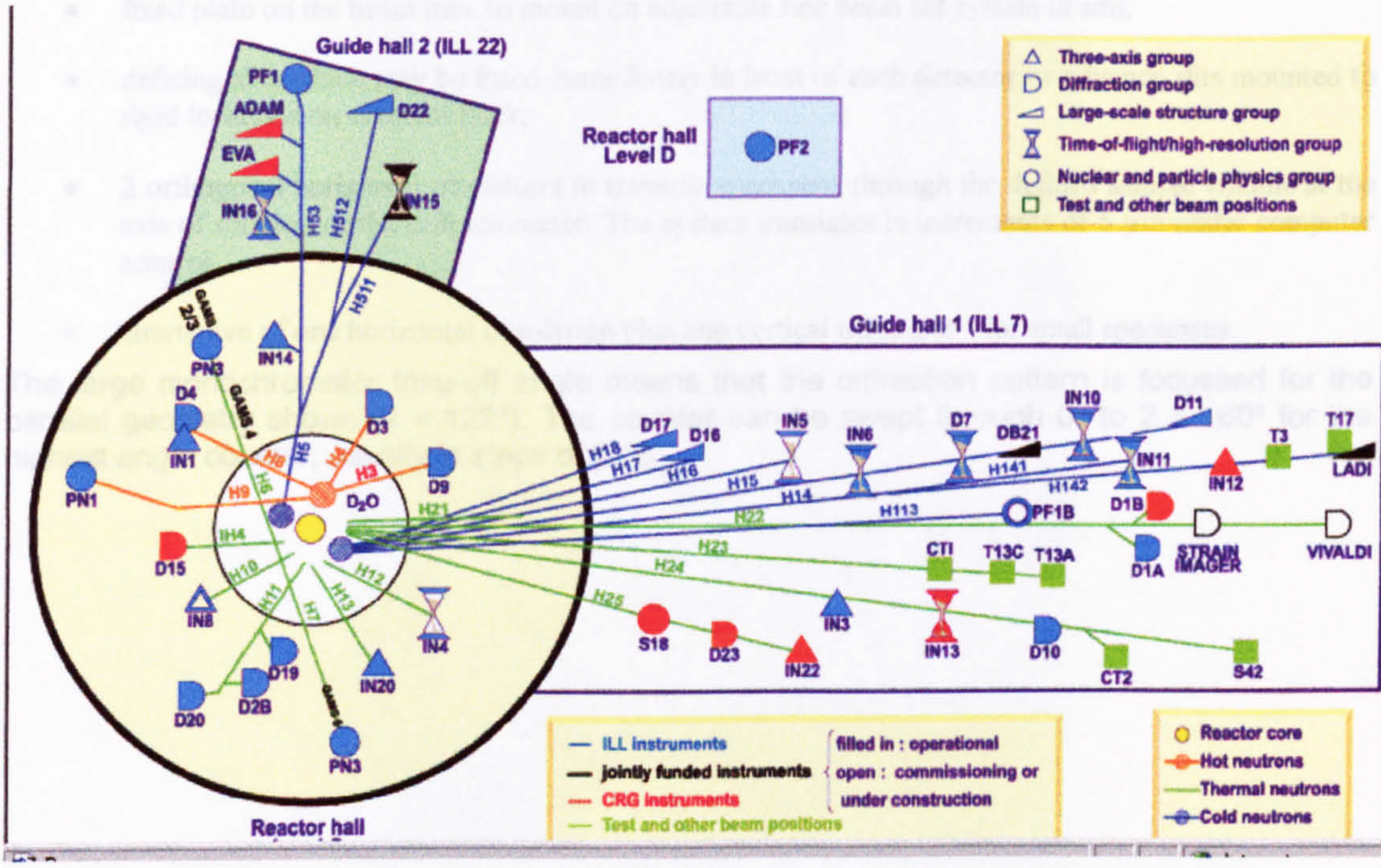

A schematic picture from the reactor neutron source in ILL

high-resolution two-axis diffractometer

D 1A is a reliable instrument for standard crystallographic problems. It gives excellent results with the Rietveld method owing to its near perfect Gaussian peak-shape in the 2-range 30° to 150°.

Complete scans take 2 to 10 hours. Crystal structures with low-symmetry unit cells and with cell volumes up to about 1000 $Å^3$ may be satisfactorily refined. The high reso-lution over a wide range of scattering angles permits the refinement of up to 150 structu-ral parameters by the Rietveld method.

special features include:

- a high take-off angle of 122°, giving high resolution at large scattering angles (up to 160°);
- a bank of 25 high efficiency collimators and counters;
- an anisotropically squashed germanium monochromator focussing a 250 mm high beam onto only 30 mm;
- a wide choice of wavelengths, from 1.39 Å to 2.99 Å, quickly available by simple rotation of the focussing monochromator;
- programmed temperature control for cryo-stats and furnaces.

the engineering package consists of:

- rigid fixed wall plate to mount a catheto-meter for precision location of sample to within 100 μm;
- fixed plate on the beam tube to mount an adjustable fine beam slit system in situ;
- defining slits which may be fitted immediately in front of each detector or advance slits mounted to rigid locations on detector bank;
- 2 orthogonal horizontal translators to traverse specimens through the defined sample volume at the axis of rotation of the diffractometer. The system translates in increments of 5 μm under computer control;
- alternative of one horizontal translation plus one vertical translator - for small specimens.

The large monochromator take-off angle means that the diffraction pattern is focussed for the parallel geometry shown (2 = 122°). The counter can be swept through 0° to 2 = 160° for the highest angle counter, usually in steps of 0.05°.

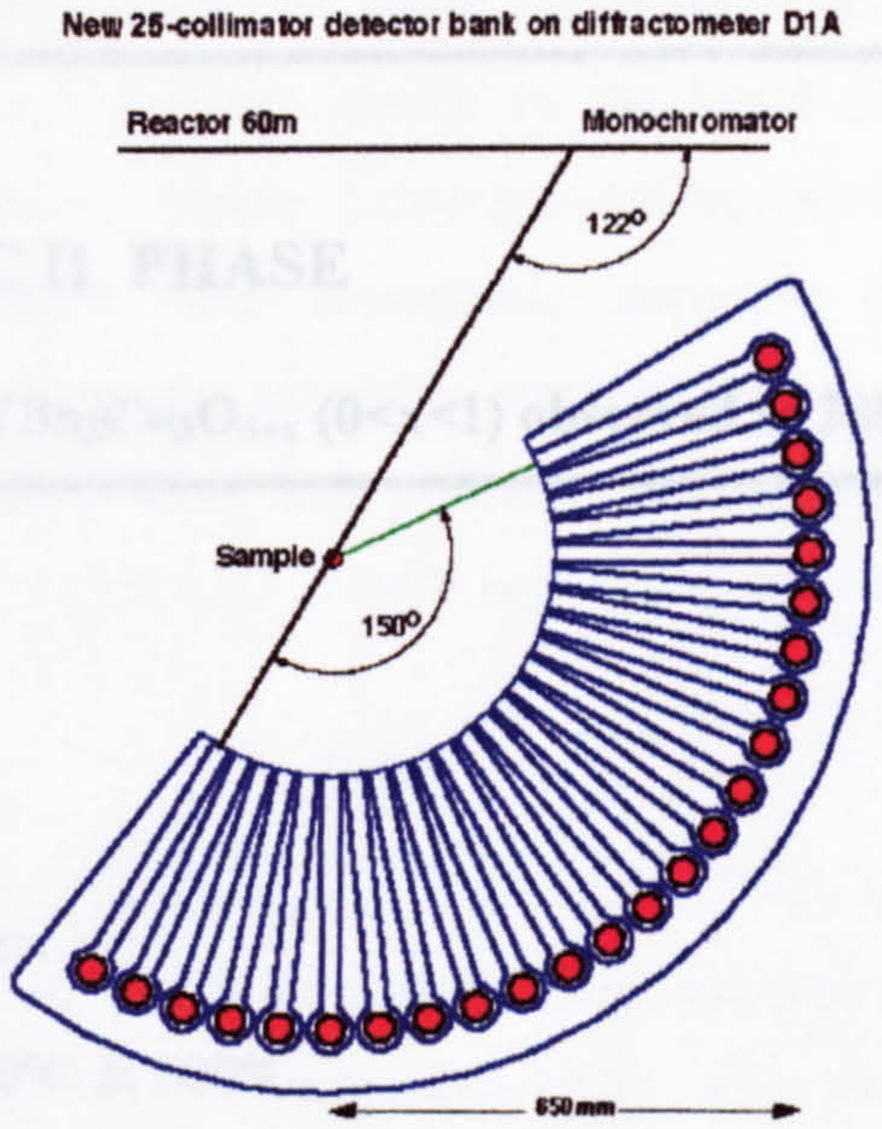

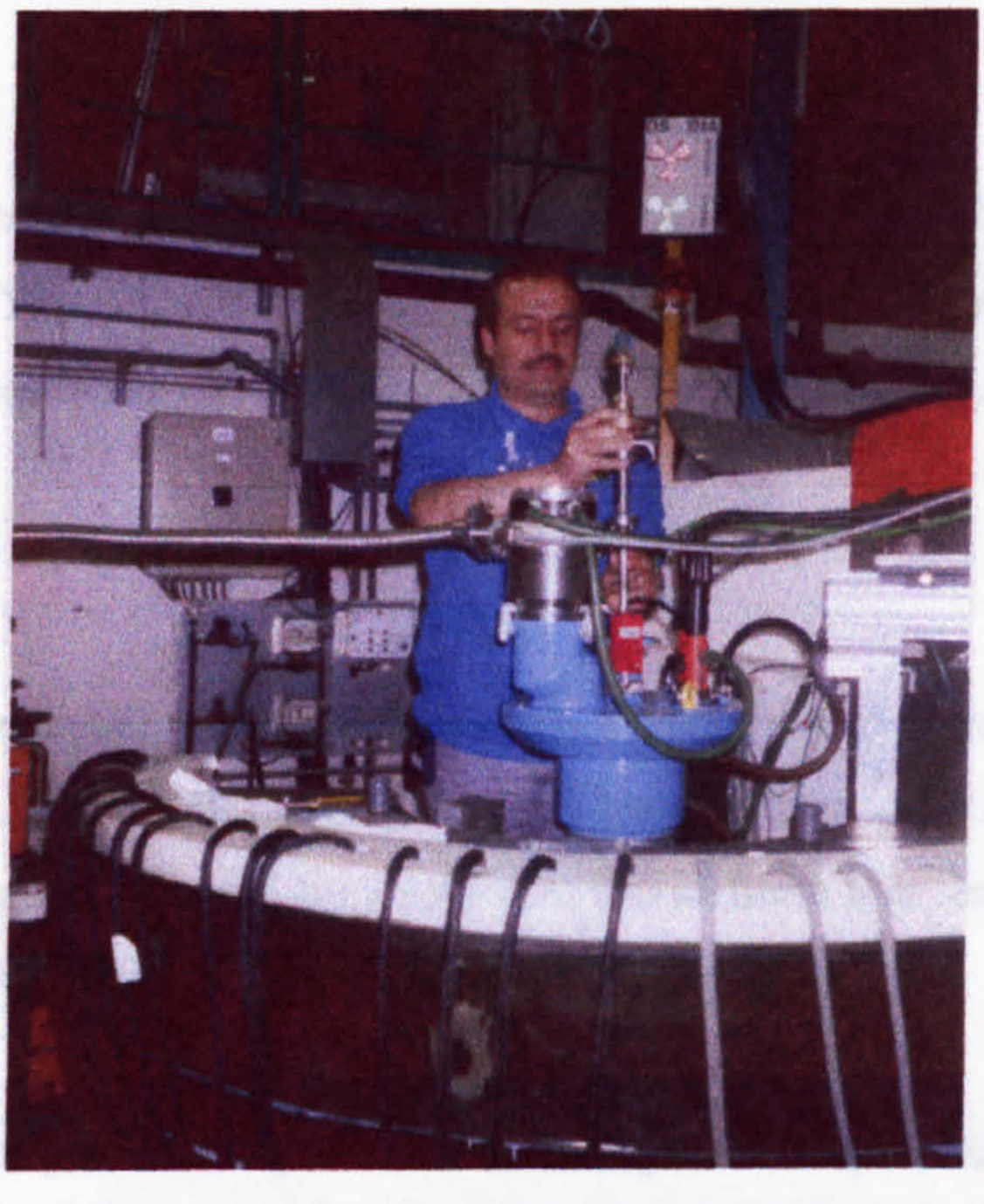

Diffractometer D1A ; ILL

Chapter V

The ORTHORHOMBIC II PHASE

A superstructure phase in $YBa_2Cu_3O_{6+x}$ ($0<x<1$) observed at 200 °C & 300 °C

Introduction

A large number of studies have been carried out on samples of the H-Tc superconductor, YBCO ($YBa_2Cu_3O_{6+x}$ where $0<x<1$) to elucidate the microstructure caused by dynamic changes in the oxygen content during the fabrication of the sample (normal state).

There are two motives for studying the phases of YBCO:

i) A complete understanding of the concentration/ temperature/ time behaviour of this system is important to control the microstructure produced during fabrication. This must be based on data collection at finite temperature under equilibrium conditions (*in situ* study).

ii) This system is a good example of a lattice gas with particular nearest neighbour interactions, which are strongly influenced by lattice microstrain effects. The development of techniques for modelling such effects at finite temperature is essential to efforts aimed at simulating "virtual materials".

In YBCO, the essential forces driving the phase transition behaviour are the O-O interactions that tends to form O-Cu-O chains in the basal (*a-b*) plane. These interactions, when inserted into a Monte Carlo simulation, determine the general features of the phase diagram with remarkable accuracy [Salomons et al; 1990]&[Selke et al; 1993]. Despite the extensive previous works on this topic, very limited experimental investigations have been performed on the phase structure in the lower range of temperature (200°C & 300°C) because of the relatively sluggish oxygen dynamics.

According to previous reports [Salomons (1990), Ceder (1990), Gerdanian (1993)] up to about 200°C, YBCO is stable in three structural phases (depends on the oxygen content, x), tetragonal (Tet) or orthorhombic (OI) and the superstructural orthorhombic (OII) phases (Figs. 5.1_a,b).

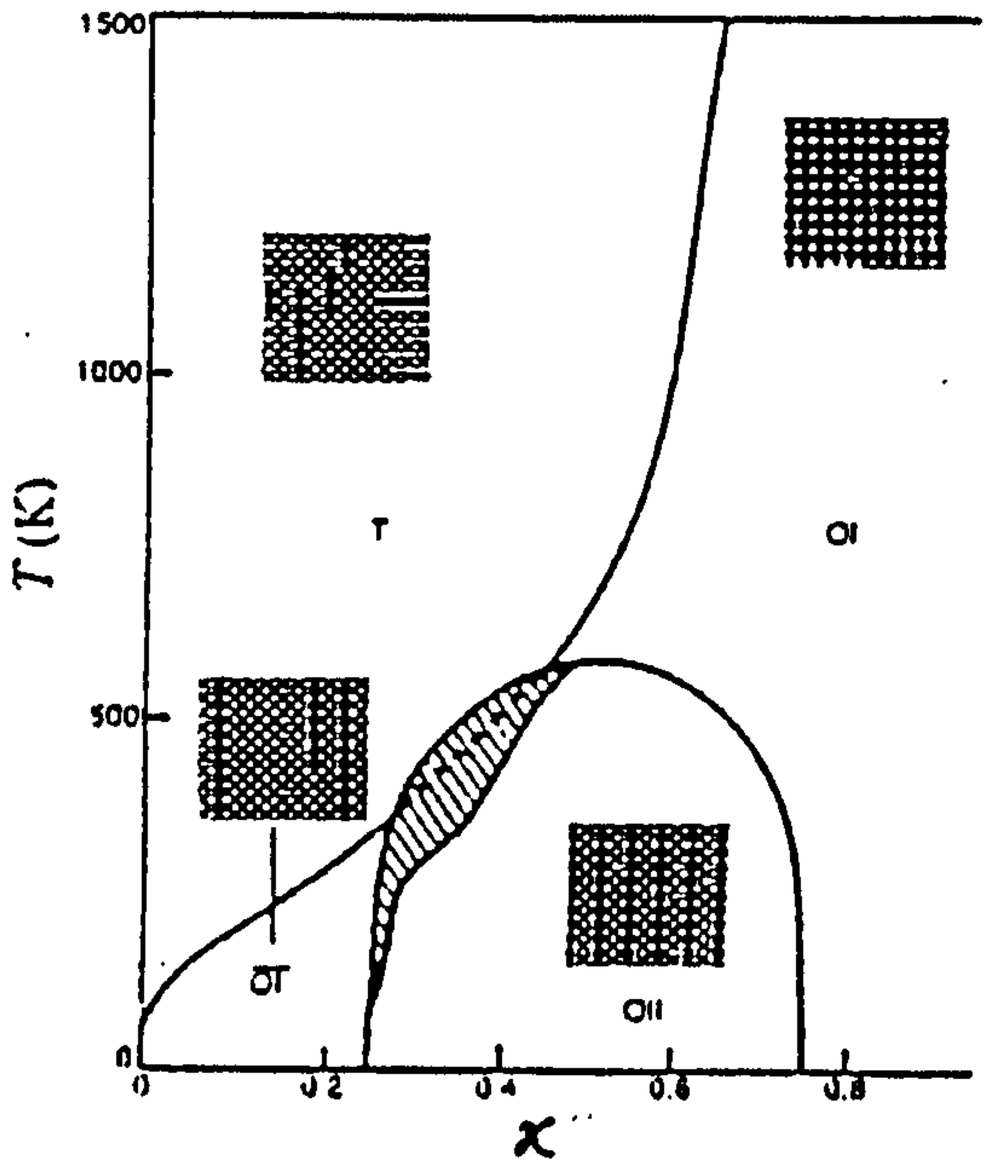

Fig.(5.1_a) Calculated phase diagram of YBCOx. T and OI stand for normal tetragonal and orthorhombic phases. OII is an ordered orthorhombic phase with a supercell doublet along the *a* direction. For each phase the pattern of oxygen occupation on the basal plane is given. Filled and open circles denote O atoms and vacant O sites (from Ceder et al; 1990).

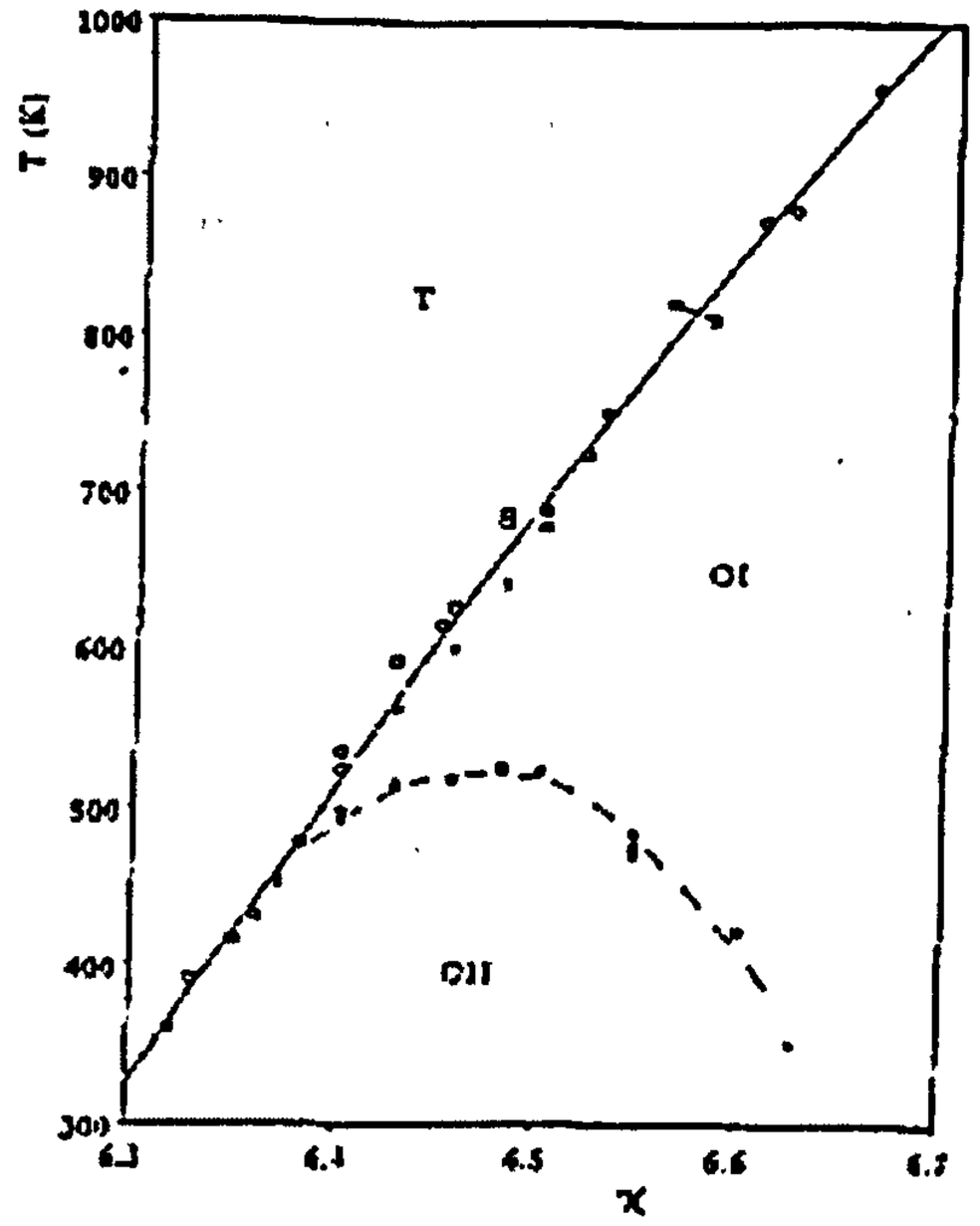

Fig.(5.1_b) Structural phase diagram based on thermo power measurements , T stands for tetragonal while OI and OII refer to orthorhombic I and orthorhombic II respectively. Crosses and Open circles or squares refer to experimental data basically gathered from single crystal samples. (from Gerdanian & Picard, 1993)

In the tetragonal phase at low oxygen concentration (x<0.2) short segments of the O-Cu-O chains form in both *a* and *b* directions (tweed patterns) maintaining, on average, the four-fold symmetry of the unit cell around the *c* axis. In this low oxygen concentration region, some models predict a small probability of forming fairly long O-Cu-O chains along *b* with many empty columns between them and, in some literature this unlikely structure is known as antiorthorhombic I phase ($\overline{OI}$), but generally this region is dominated by tetragonal phase at low oxygen concentration [Poulsen et al; 1991] & [Van Tendeloo et al; 1987].

The OI phase is characterized by the chains all lying the *b* direction, whereas in the OII phase, chains form in that direction in every other column. By changing the oxygen stoichiometry, x, starting from the Tet. phase, it is possible to enter the other phases (OI or OII) directly or through an intermediate two phase mixed phase region

and vice versa, depending on whether the phase transition is **second order** or **first order.**

This procedure is performed by adjusting the oxygen partial pressure in an isothermal *in situ* process. It should be mentioned that the question of the first or second order characteristic of the phase transition at low(≥ room temp.) and elevated temperature region (<450°C) of the YBCO's structural phase diagram has been a very controversial issue so far [there is a brief review in Poulsen et.al; 1996].

The OII phase, on the other hand,corresponds to an orthorhombic structure consisting of two adjacent tetragonal cells along *a* direction with a common oxygen-vacant *b* side in the basal plane, so there are long O-Cu-O chains in every other column and it is only stoichiometric at x=0.5. Fig.(5.2a) and Table (5.1) show the superstructure OII cell and the atomic coordination. Using a crystallographic package called "CarIne", the corresponding calculated structure factor, shows the relative peak intensities (Fig. 5.2b). For lower values of x, this modulation would exist over a part of the sample giving rise to a mixed phase structure (with Tet. phase) which makes the structural analysis more complicated.

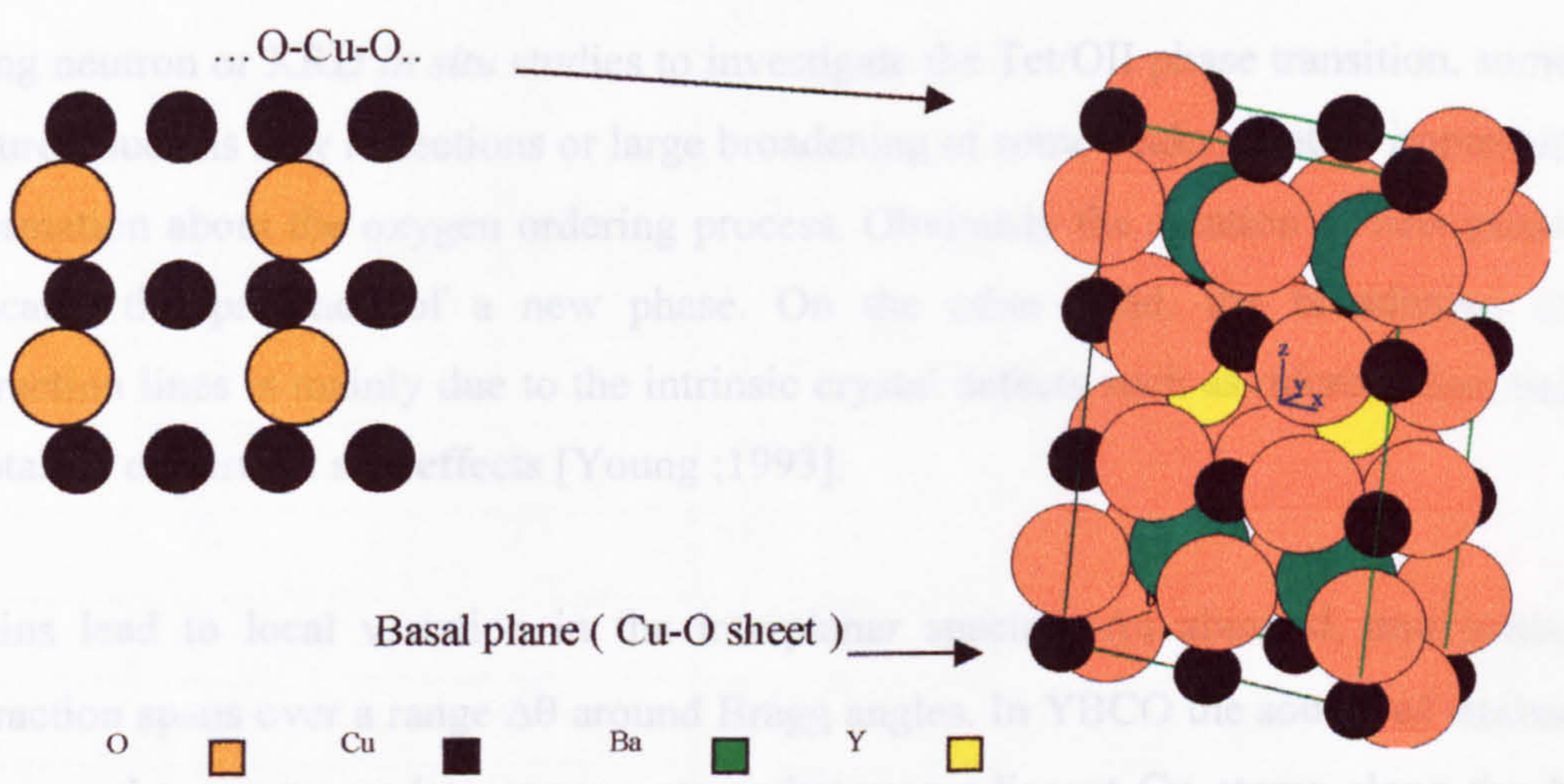

Fig.(5.2a) Orthorhombic II (x=0.5)

$Y Ba_2 Cu_3 O_{6.5}$

This is a superconducting phase (T_c=60 °K). This phase is easily recognized in electron diffraction patterns , because the superstructure spots appear at the (h+1/2, k,l) positions.

The every other line O-Cu-O chains in the basal plane are shown on the left (Figure from Radaelli; 1998)

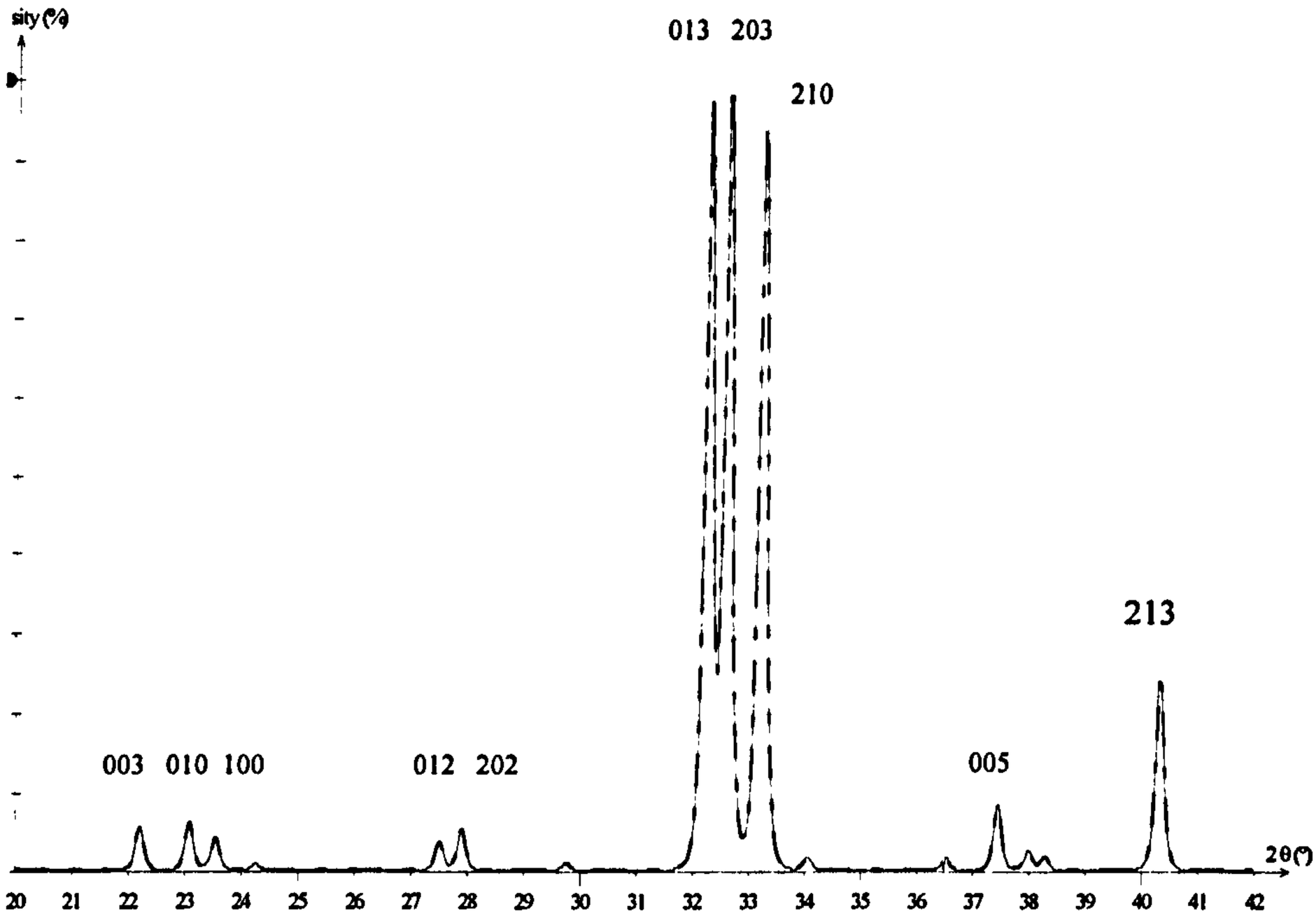

Fig (5.2b) A typical calculated x-ray fractional intensity ($|\text{structure factor}|^2$) for the OII phase (using "CarIne")

Using neutron or XRD *in situ* studies to investigate the Tet/OII phase transition, some features, such as new reflections or large broadening of some peaks, contain important information about the oxygen ordering process. Obviously the creation of new peaks indicates the presence of a new phase. On the other hand, the broadening of diffraction lines is mainly due to the intrinsic crystal defects such as microstrains and crystallite or particle size effects [Young ;1993].

Strains lead to local variation in the interplanar spacing, Δd about d, and hence diffraction spans over a range $\Delta\theta$ around Bragg angles. In YBCO the source of strains is the need to accommodate oxygen atoms between adjacent Cu atoms along the *b* direction in the basal plane, therefore pushing the Cu atoms away and increasing the *b* parameter. The size of the crystal's coherent diffracting microstructure region (crystallite-size), on the other hand (by analogy with the broadening of diffracting lines from an optical grating with a limited numbers of lines), tends to an appreciable broadening independent of the order of reflection.

atom	x ‖ *a*	y ‖ *b*	z ‖ *c*
Y	1/4	1/2	1/2
Y	3/4	1/2	1/2
Ba	1/4	1/2	0.185
Ba	3/4	1/2	0.185
Ba	1/4	1/2	0.825
Ba	3/4	1/2	0.825
Cu	0	0	0
Cu	1/2	0	0
Cu	0	0	0.355
Cu	1/2	0	0.355
Cu	0	0	0.6451
Cu	1/2	0	0.6451
O	0	1/2	0.355
O	1/2	1/2	0.355
O	1/4	0	0.355
O	3/4	0	0.355
O	0	0	0.185
O	1/2	0	0.185
O	0	1/2	0
O	0	1/2	0.6451
O	1/2	1/2	0.6451
O	1/4	0	0.6451
O	3/4	0	0.6451
O	0	0	0.815
O	1/2	0	0.815

Table (1) The atomic positions in the super cell (OII), calculated from modelling by "CarIne".

Generally speaking, in the orthorhombic phases the oxygen ordering process generates a synchronised shear stress in the structure, resulting in twinning along the (110) planes. These twin lamellas (microstructures) are typically a few hundred Å wide and several microns long in the basal planes [Van Tendeloo et al; 1987].

Chapter VII is dedicated to studies of the twining structure and the effect of this on the line broadening in YBCO, but at lower oxygen concentration region (< 0.4), the case in here, the main line broadening source could be local micro strains and stacking faults, (section 3 in this chapter).

In this chapter the first section deals with the experiment procedure, the results of in-situ x-ray measurements, illustrated in section 2, and finally the supplementary neutron diffraction results will be presented (section 3).

V.1) EXPERIMENTAL PROCEDURE

The powder sample used in this work was purchased with high purity and high stoichiometry (x> 0.96), i.e. $YBa_2Cu_3O_{6.96}$ (in the OI phase), and the particle size range was 1-5 μm' (Fig 5.3a_b). The value of stoichiometry, i.e. the value of x, has been confirmed by full x-ray profile refinement (GSAS) and the TGA method (Thermogravimetric Analysis) [2].

Experiments have been performed using the x-ray diffractometer unit in the University of Salford (D5000, SIEMENS). The unit is equipped with a sample environment chamber which operates up to 300°C, in which the oxygen partial pressure ,p.p., could be controlled up to 1 bar manually.

To remove adsorbed moisture from the sample, it was left under vacuum at 200°C for about 2 hours. It is of course crucial for neutron measurements to avoid incoherent hydrogen scattering. This treatment was known not to remove the lattice oxygen atoms [Mercer; 1997].

Because the oxygen diffusion process in this interesting relatively low temperature range is rather slow (it is determined by the quantity called "diffusion time constant", t_s, which can be extracted form the volumetric or gravimetric measurements [3] [Mercer; 1997]), before starting each data collection the sample had to be left for several hours under the desired oxygen atmosphere at the required temperature to allow oxygen atoms diffuse to the sample particles. The range of pressure variation was between 0.07 to 1000 mbar (for more than this pressure the chamber might be damaged). The data collection lasts about 6 hours at each isobaric step. After the run was completed the sample was cooled quickly to the ambient temperature by switching off the furnace.

1- PI-KEM
2 - Appendix 2
3- Appendix 3

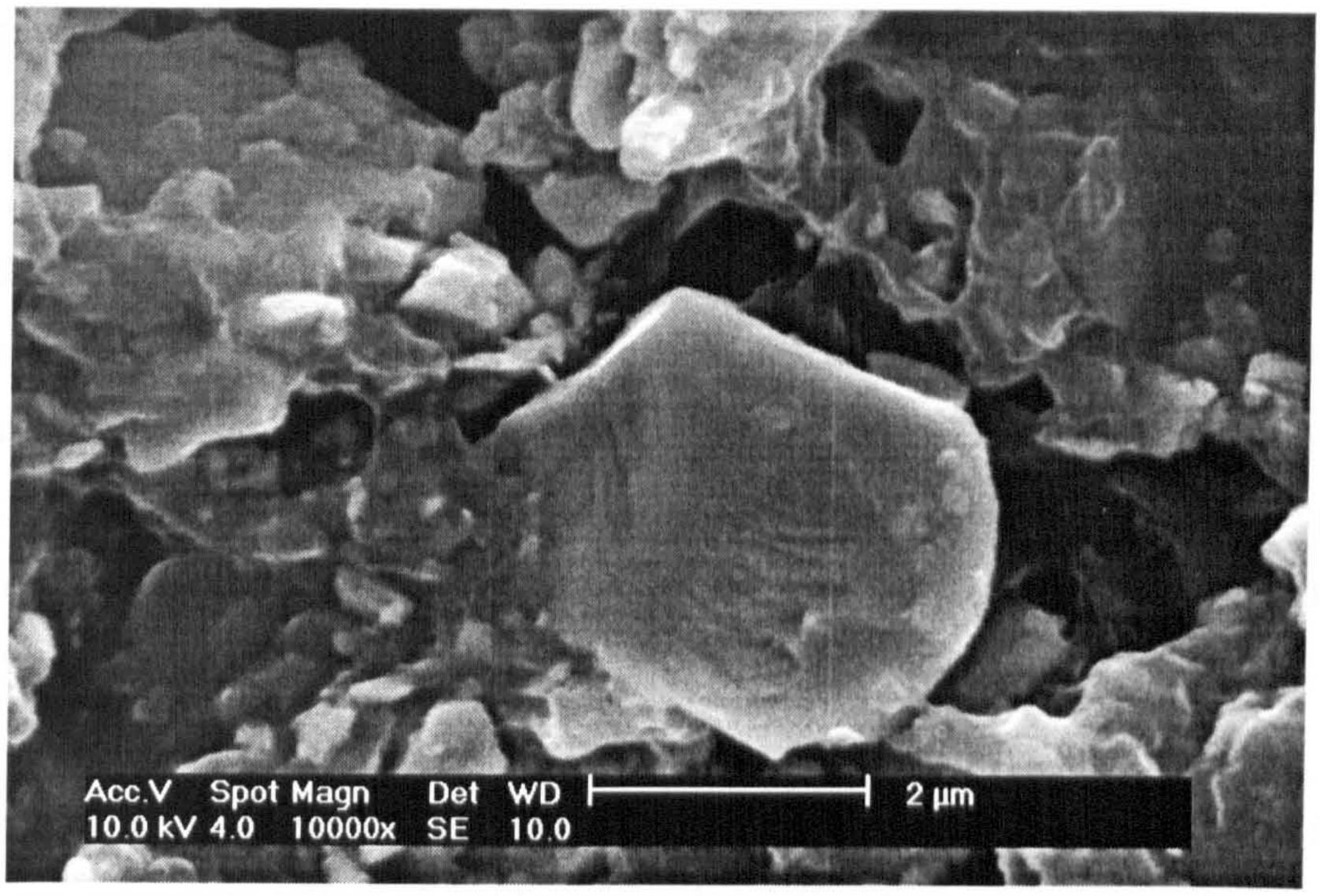

(a)

(b)

Fig (5.3) S.E.M. images of the purchased powder sample to show the particle dimensions

The reproducibility of the data from repeated measurements shows that there is no change in the oxygen stoichiometry due to the thermal cycling [Poulsen et al; 1996]. In this study, contrary to many previous studies, the sample was taken to the tetragonal phase first, by outgassing under vacuum (0.01 mbar) at 650°C for at least 3 hours, so that the oxygen content was less than 6.20, ($x < 0.20$). Here the [010] and [020] peaks have completely merged with the [100] and [200] peaks respectively (the main diffraction features of transition to the tetragonal phase). Then the sample was dosed up to cross the phase boundaries, by changing the ambient oxygen partial pressure at the desired temperatures.

Because thermal neutrons are more sensitive than x-rays to light atoms such as oxygen, an extensive series of neutron powder diffraction measurements using D1A in Institute Laue-Langevin (ILL) has been carried out. Due to the strict limitation on the available beam time, in this measurements a set of samples with expected oxygen concentration was prepared beforehand by the Sievert method[4] and during the measurement, the furnace was brought to the desired temperature. Since the sample cell was sealed and the dynamic of gas diffusion is low, it could be assumed that the oxygen concentration was left unchanged.

[4] Appendix B

V.2) XRD IN-SITU MEASUREMENTS

V.2.1) 200°C isotherm x-ray measurements_ Figs.(5.4a_b) shows clear modifications in the x-ray diffraction pattern as a function of oxygen p.p. and hence various oxygen concentration, x, at 200°C (a room temperature pattern from a pre-prepared sample with oxygen content, x~0.2, has been attached as a reference. For this graph, because the exposure time is lower, the intensity is reduced). The generation and growth of some new peaks definitely indicate the presence of a new phase after absorbing oxygen. This absorbed oxygen, in turns creates the local strain fields which lead to the broadening of the initial phase peaks. More investigations, using GSAS and an alternative crystallographic software package (CarIne), suggested the existence of a mixed-phase (Tet+OII) region. The peaks with prefix 'S' (attributed to the suprelattice OII phase) are at the expected positions consistent with the OII model. For instance, the superstructural [S.006] peak grows between the matrix tetragonal [T.200]&[T.006] peaks which demonstrates that the average c_{OII} parameter is less than c_T, in agreement with the contraction in the c direction with increasing concentration of the ordered oxygen atoms in the basal plane [Jorgensen et al; 1987]. The notable point is the reduction of the intensity of the tetragonal peaks against the increasing intensity trend of the OII peaks (the vacuum data were collected at room temperature and with a lower exposure time to the others, so the other patterns are shifted at elevated temperature). The 200°C patterns show a slight shift due to the residual strains caused by the oxygen absorption process, presumably because the samples had not completely reached thermodynamical equilibrium.

Fig.(5.5a_b) shows the same behaviour for the interesting superstructure, OII, peaks [S.213]&[S.300]. As is obvious, the lessening of the tetragonal [T.112] peak intensity is much lower than the other tetragonal peaks due to the fact that it overlaps the [S.300] peak. It should be noted that [S.213] is effectively a superstructure reflection, i.e. there is no equivalent line from the tetragonal lattice in the corresponding d-spacing (index 2,1/2,3 on the original lattice unit cell).

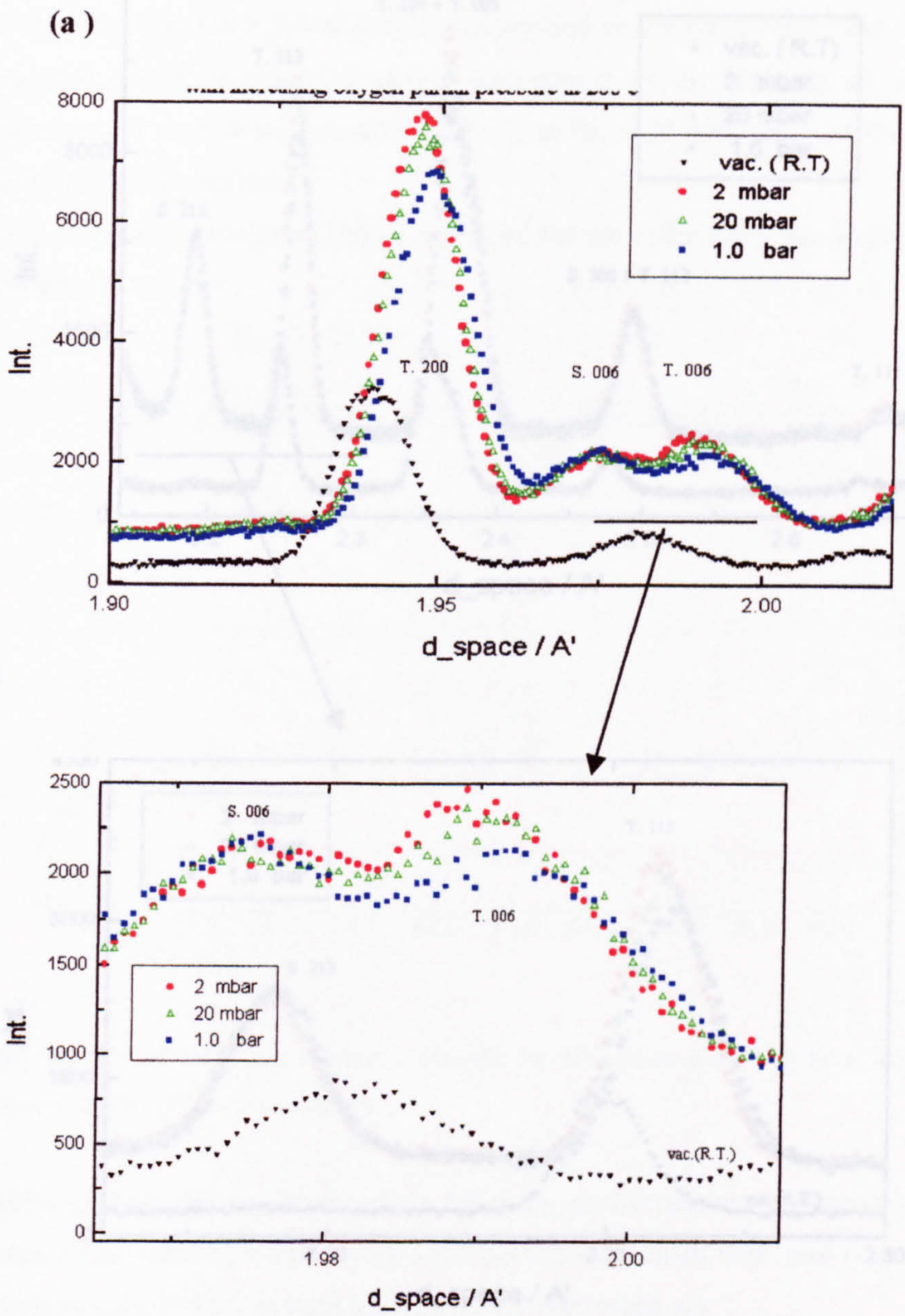

Fig.(5.4) Growing the OII peak (S.006), against the Tet.peaks (T.200 & T006) with increasing oxygen partial pressure at 200°C

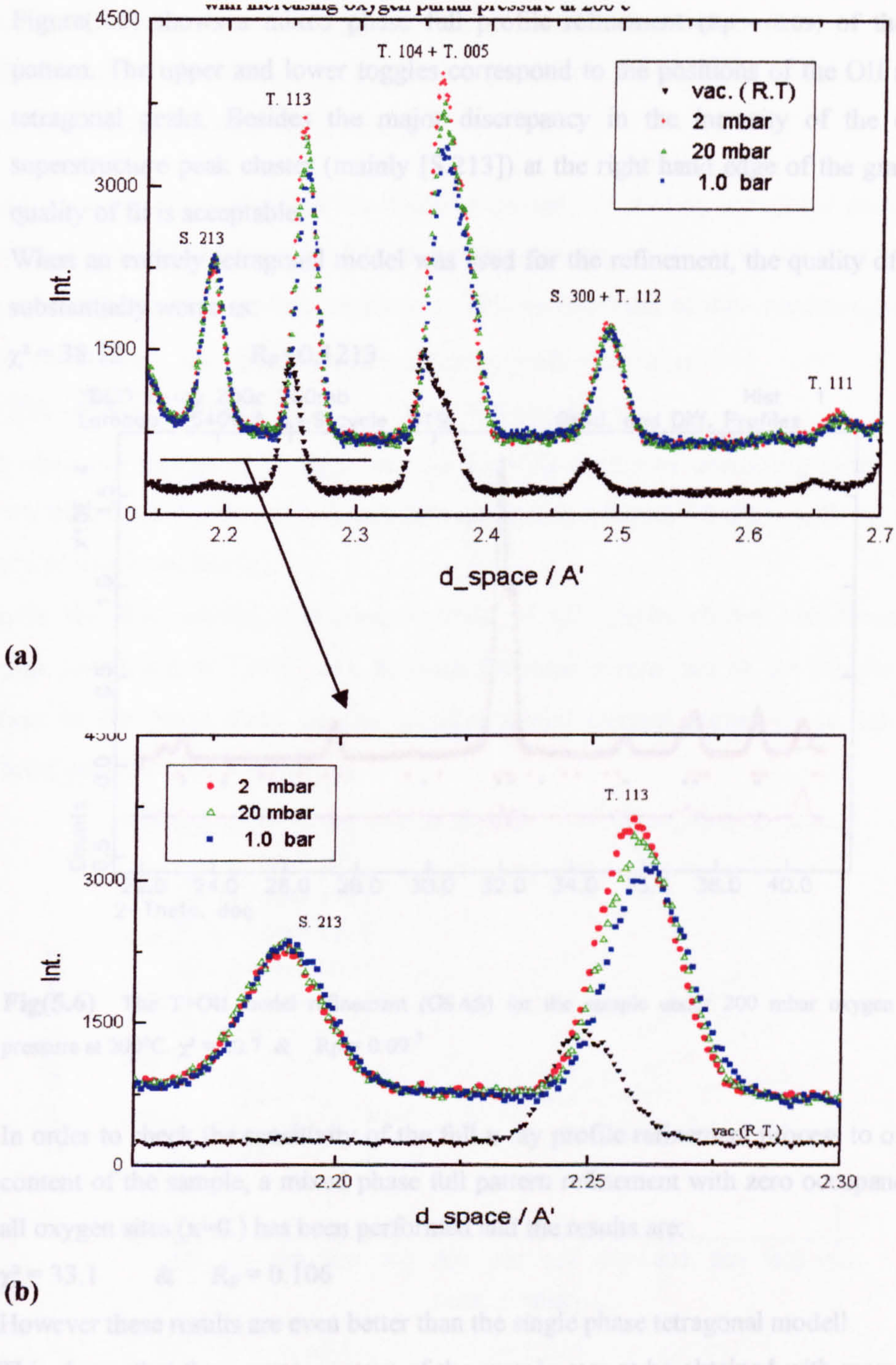

Fig.(5.5) a_ Growing the OII peaks [S.213] & [S.300] against Tet. peaks (T.113 etc.) with increasing oxygen partial pressure, at 200°C.

Figure(5.6) shows a mixed phase full profile refinement (R_p = 0.09) of the x-ray pattern. The upper and lower toggles correspond to the positions of the OII and the tetragonal peaks. Besides the major discrepancy in the intensity of the entirely superstructure peak cluster (mainly [S.213]) at the right hand edge of the graph, the quality of fit is acceptable.

When an entirely tetragonal model was used for the refinement, the quality of fit got substantially worse as:

$\chi^2 = 38.13$ $R_p = 0.1213$

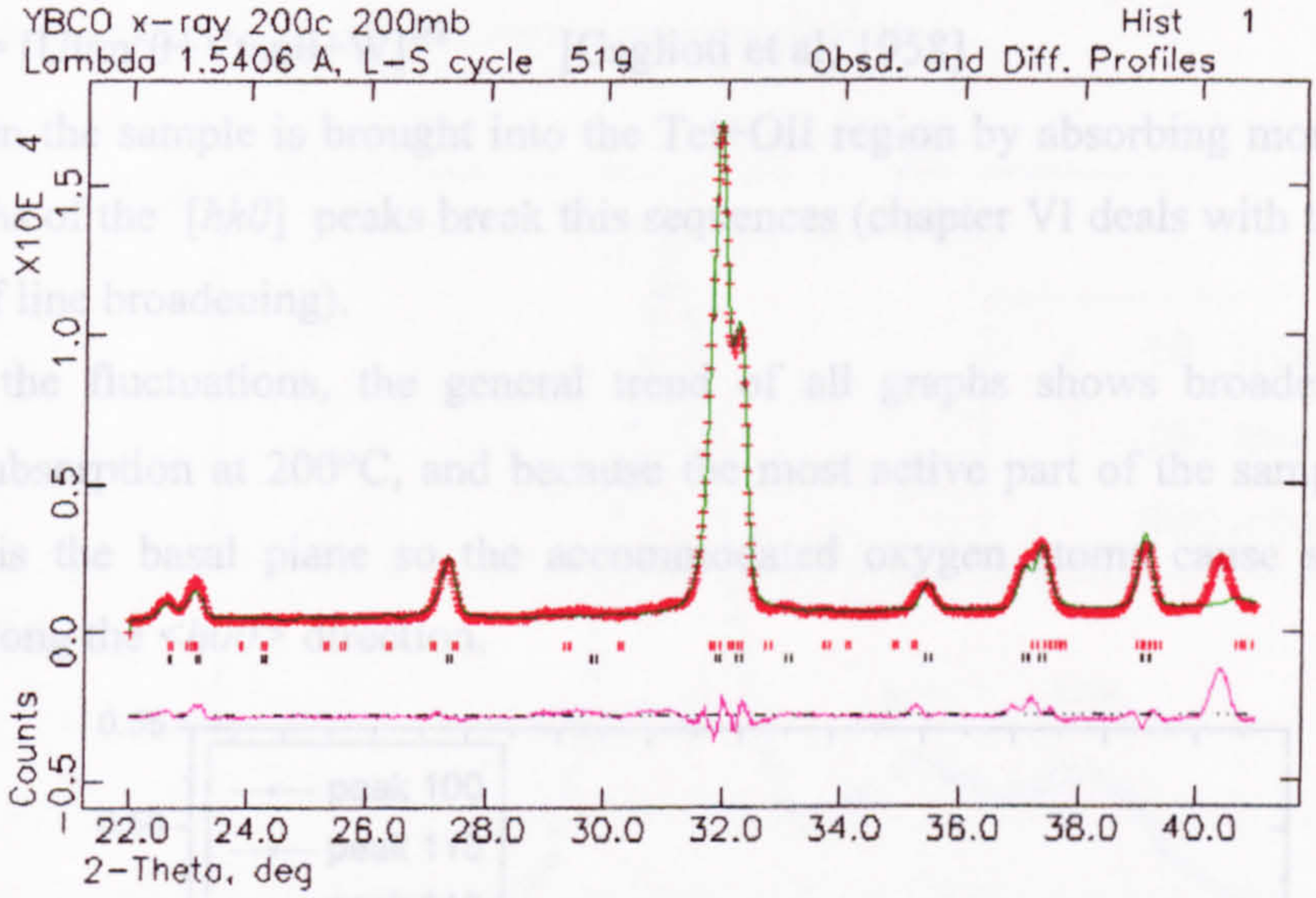

Fig(5.6) The T+OII model refinement (GSAS) for the sample under 200 mbar oxygen partial pressure at 200°C. $\chi^2 = 20.7$ & $Rp = 0.09$ [5]

In order to check the sensitivity of the full x-ray profile refinement process to oxygen content of the sample, a mixed phase full pattern refinement with zero occupancy for all oxygen sites (x=0.) has been performed and the results are:

$\chi^2 = 33.1$ & $R_p = 0.106$

However these results are even better than the single phase tetragonal model!

This shows that the oxygen content of the sample cannot be obtained with reasonable accuracy from site occupancy fractions even after a good x-ray profile refinement.

---

[5] In the '**Least Squares Theory**'; $R_p=(\sum|I_o-I_c|)/\sum I_o$; where I_o and I_c are the observed and calculated intensities and the summation runs over all the Bragg reflections in the pattern and $\chi^2=\sum w(I_o-I_c|)^2/(N-P)$ where w is the weight, N is the number of observations and P the number of parameters.

Therefore, the estimated oxygen content was extracted indirectly from the extrapolation of the change in the lattice parameters (*b-a*) by comparison to some previous studies [Poulsen et al; 1996].

Fig.(5.7) shows the changes in the widths of some pre-existing tetragonal peaks versus the oxygen partial pressure. In the low oxygen p.p. region (close to the pure tetragonal phase at beginning), the width sequences follows the order of their scattering angles,θ. This is because of the instrumental resolution profile function:

$$FWHM = [U\tan^2\theta + V\tan\theta + W]^{1/2} \qquad \text{[Caglioti et al; 1958]} \qquad (5.1)$$

but when the sample is brought into the Tet+OII region by absorbing more oxygen, the widths of the [*hk0*] peaks break this sequences (chapter VI deals with the general theory of line broadening).

Despite the fluctuations, the general trend of all graphs shows broadening with oxygen absorption at 200°C, and because the most active part of the sample in this process is the basal plane so the accommodated oxygen atoms cause substantial strains along the <*h00*> direction.

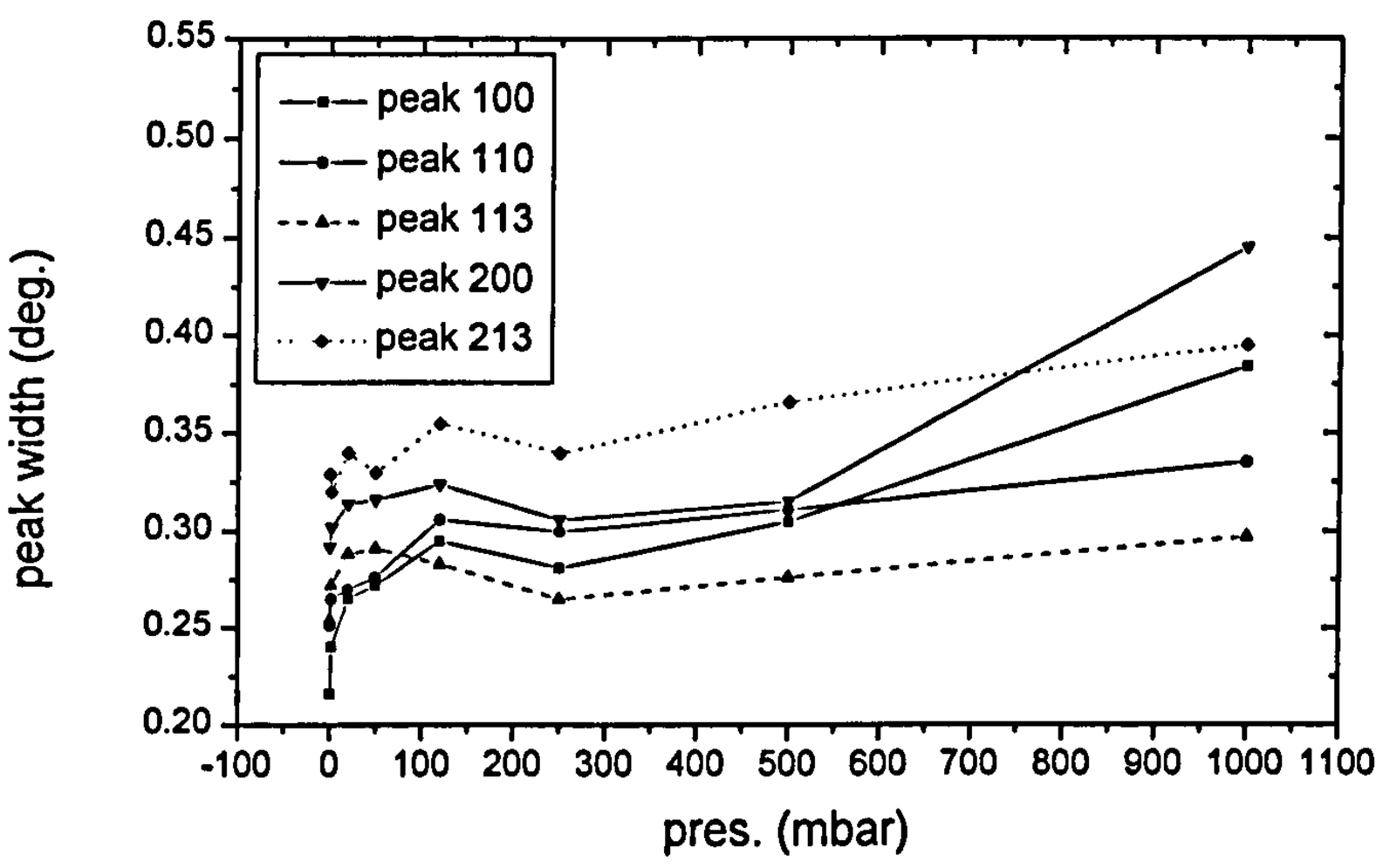

Fig.(5.7) Peak width vs. oxygen p.p. at 300°C (x-ray data)

V.2.2) 300°C isotherm x-ray measurements

After the 200°C uptake cycles, the same sample was heated up to 300°C, and the ambient pressure was increased up to 600 mbar. Here, there is a little notable change in the patterns at 10,160 and 600 mbar. The OII peaks grow slightly as compared to the tetragonal peaks (Fig 5.8). This means presumably that, there was a temporary saturation, maybe a feature of a metastable state after the 200°C cycles, as has been pointed by other authors [Khachaturyan; 1988], because in the vicinity of a local stable point the phase concentration changes very slow.

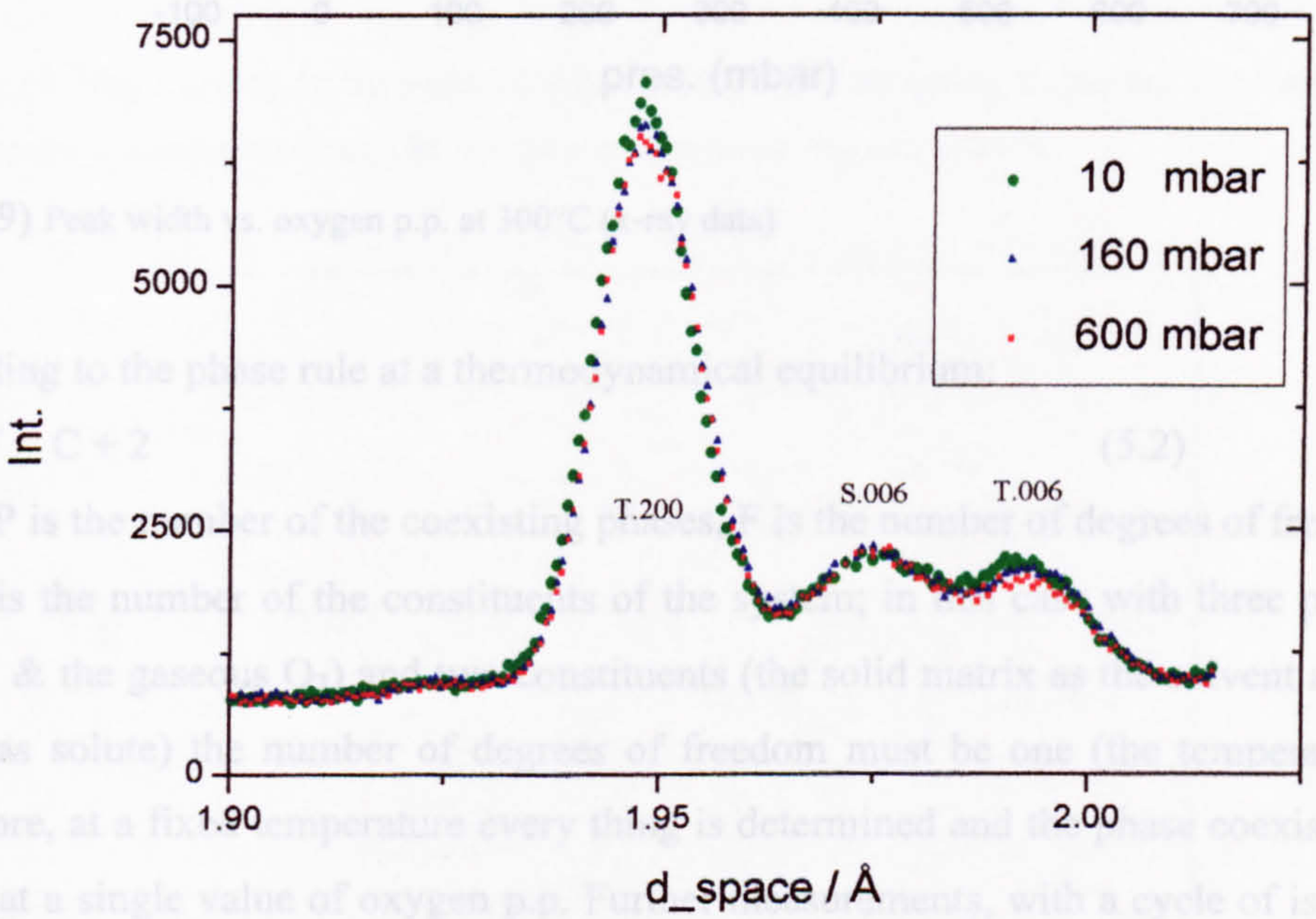

Fig (5.8) Growing the OII peak (S.006), against the Tet.peaks (T.200 & T006) with increasing oxygen partial pressure at 300°C

Figure (5.9) shows that besides the very sluggish gas absorption at 300°C, up to 600 mbar oxygen p.p., the long-range ordering driving forces are more active and therefore the trend of the all the tetragonal peak widths are more or less downward and they return to the accepted sequence, so it is concluded that during these isotherm studies, an annealing process has occurred.

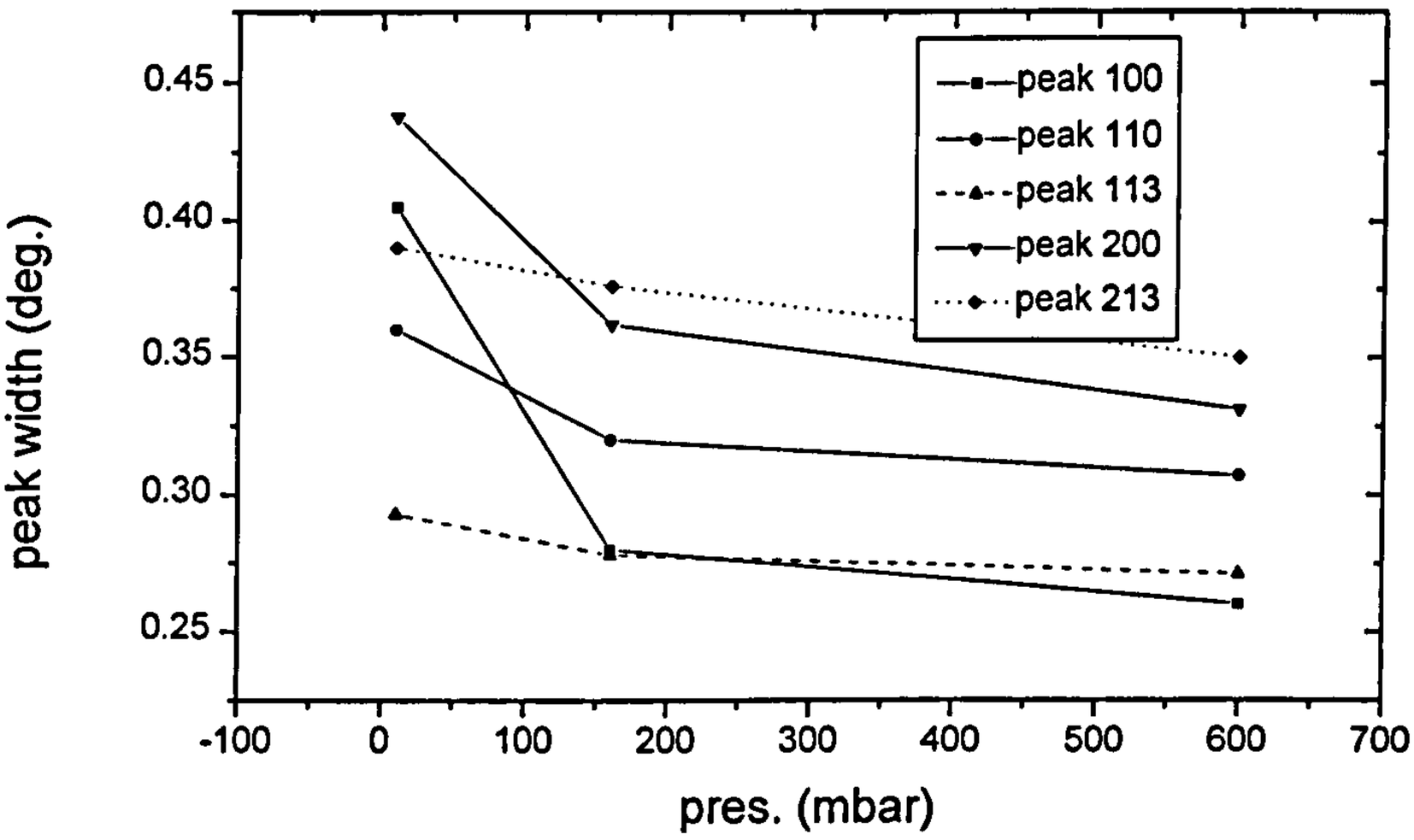

Fig (5.9) Peak width vs. oxygen p.p. at 300°C (x-ray data)

According to the phase rule at a thermodynamical equilibrium:

$$P + F = C + 2 \qquad (5.2)$$

where P is the number of the coexisting phases, F is the number of degrees of freedom and C is the number of the constituents of the system; in this case with three phases (T, OII & the gaseous O_2) and two constituents (the solid matrix as the solvent and O atoms as solute) the number of degrees of freedom must be one (the temperature). Therefore, at a fixed temperature every thing is determined and the phase coexistence occurs at a single value of oxygen p.p. Further measurements, with a cycle of isobars (1.0 mbar) at 300°C against annealing time, just before the diffraction measurement, have been performed on a new sample with initial oxygen concentration x~0.2.

In Figs.(5.10), although the beam exposure time for each step of the annealing time is different, it shows again a higher intensity growth rate for the superstructure reflections, and it means the sample is on the way to reach an equilibrium condition in the mixed phase region.

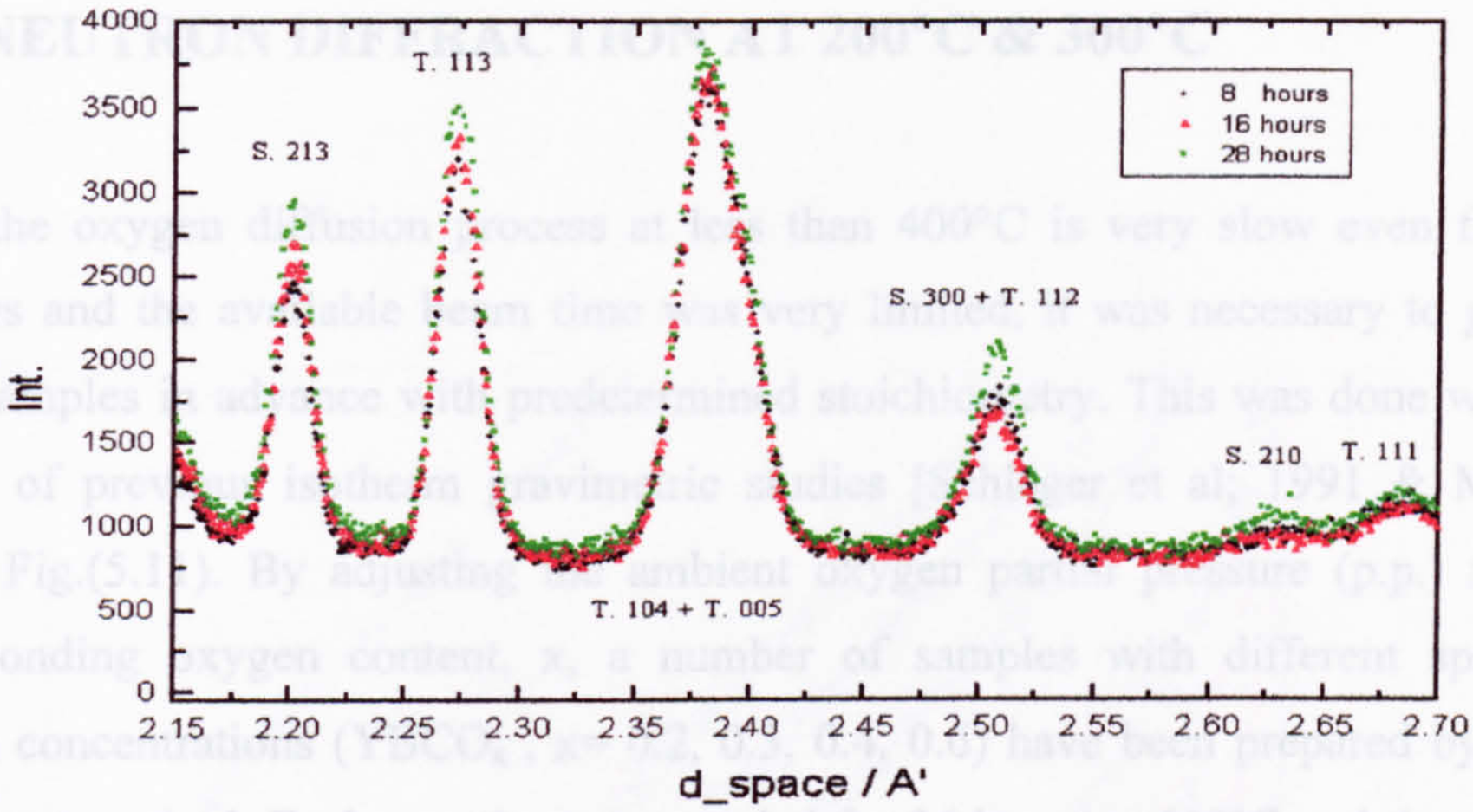

Fig.(5.10a) Growing the OII peaks [S.213] & [S.300] & [S.210] against Tet. peaks (T.113 etc.) with increasing the annealing time under 1.0 mbar oxygen partial pressure, at 300°C.

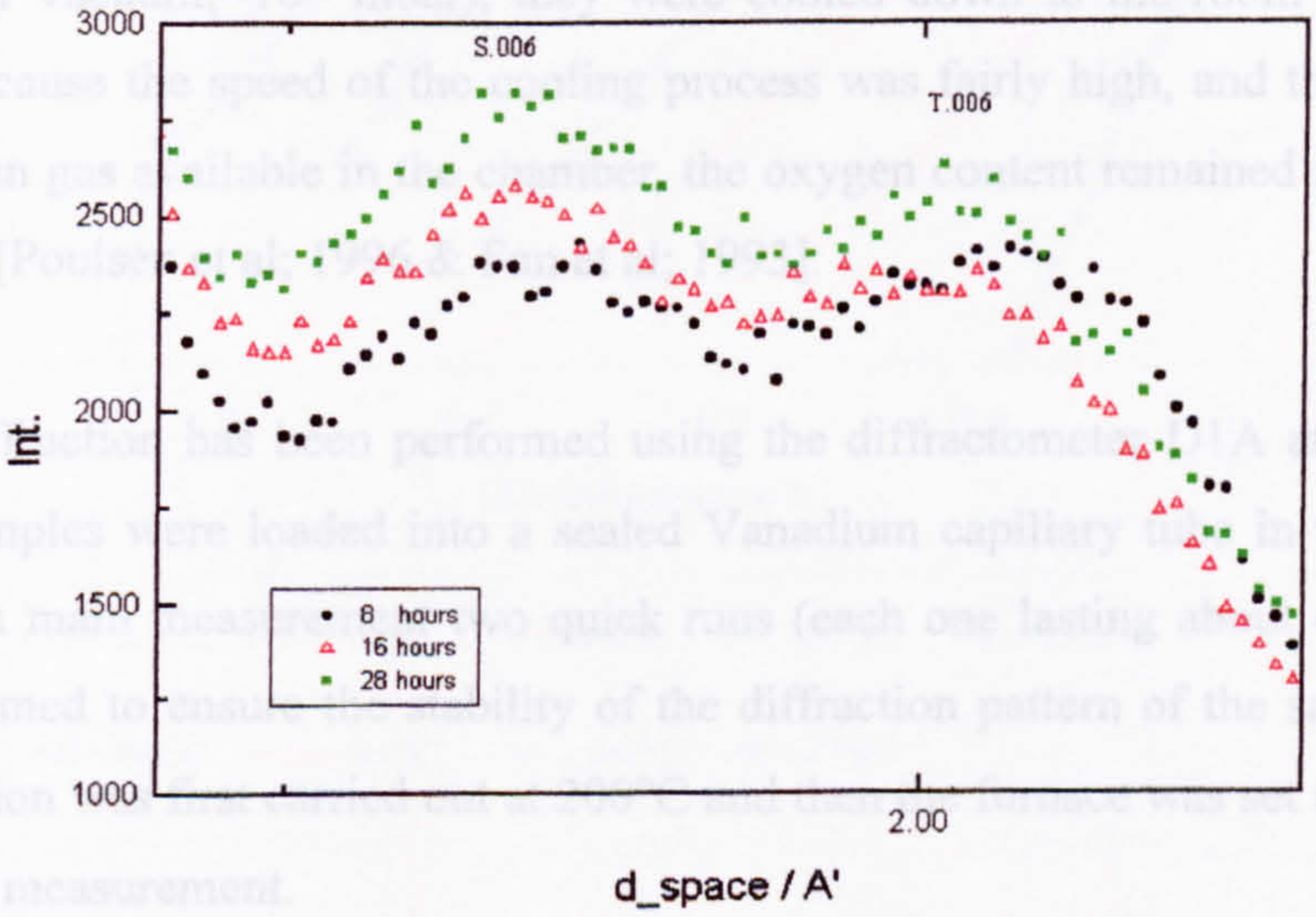

Fig.(5.10b) Growing the OII peak [S.006] against Tet. peak [T.006] with increasing the annealing time under 1.0 mbar oxygen partial pressure, at 300°C. The beam exposure time for 8 & 18 hours steps was same but for the last step the beam exposure time was higher.

V.3) NEUTRON DIFFRACTION AT 200°C & 300°C

Since the oxygen diffusion process at less than 400°C is very slow even for fine powders and the available beam time was very limited, it was necessary to prepare some samples in advance with predetermined stoichiometry. This was done with the benefit of previous isotherm gravimetric studies [Schleger et al; 1991 & Mercer; 1997], Fig.(5.11). By adjusting the ambient oxygen partial pressure (p.p.) for the corresponding oxygen content, x, a number of samples with different specified oxygen concentrations ($YBCO_x$, x= 0.2, 0.3, 0.4, 0.6) have been prepared by using the Sievert method. Each sample was annealed for 36 hours at 603°C and the desired oxygen p.p., to reach the equilibrium condition. This time is much greater than the diffusion time constant for oxygen at that temperature(~3 min., [Mercer; 1996]). Then, under vacuum(~10^{-3} mbar), they were cooled down to the room temperature rapidly. Because the speed of the cooling process was fairly high, and there was not more oxygen gas available in the chamber, the oxygen content remained more or less unchanged [Poulsen et al; 1996 & Fan et al; 1993].

Neutron diffraction has been performed using the diffractometer D1A at the "ILL"; France. Samples were loaded into a sealed Vanadium capillary tube in the furnace. Before each main measurement two quick runs (each one lasting about 45 minutes) were performed to ensure the stability of the diffraction pattern of the samples. The data collection was first carried out at 200°C and then the furnace was set up to 300°C for the next measurement.

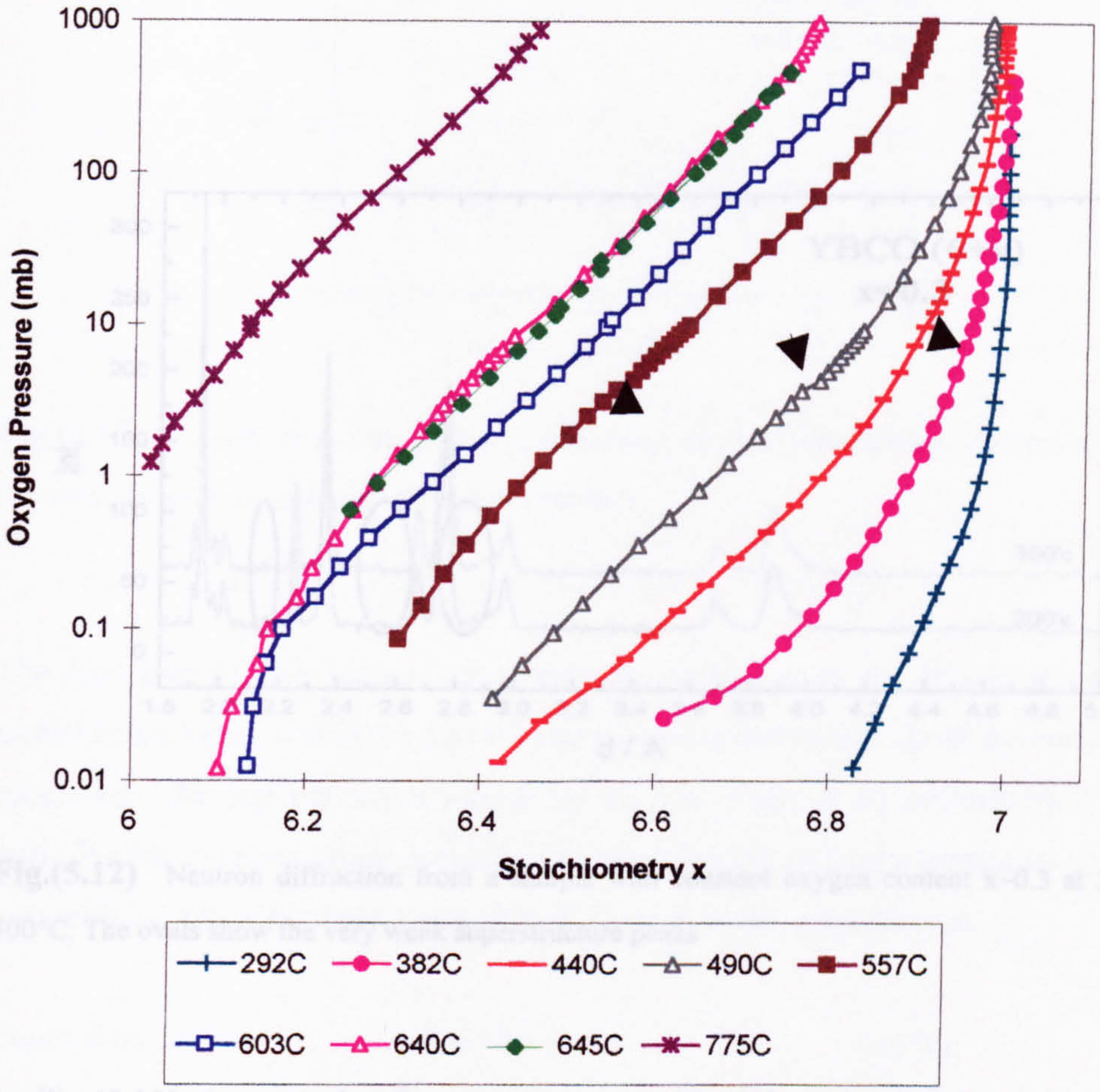

Fig (5.11) Oxygen partial pressure vs. oxygen stoichiometry isotherms of YBCO in the temperature range 292°c to 775°c and stoichiometry range 6.0 to 7.0 .

The isotherms were measured using the intelligent gravimetric analyses (IGA) method. Arrows indicate small plateaux in the isotherms (from Ph.D thesis Michelle Mercer; 1997)

A comparison of the 200°C and 300°C diffraction patterns, shows that they are very close together, for example at x ~ 0.3 the pattern for 300°C shows a slightly stronger features due to the OII phase, than does the pattern at 200°C (Fig. 5.12).

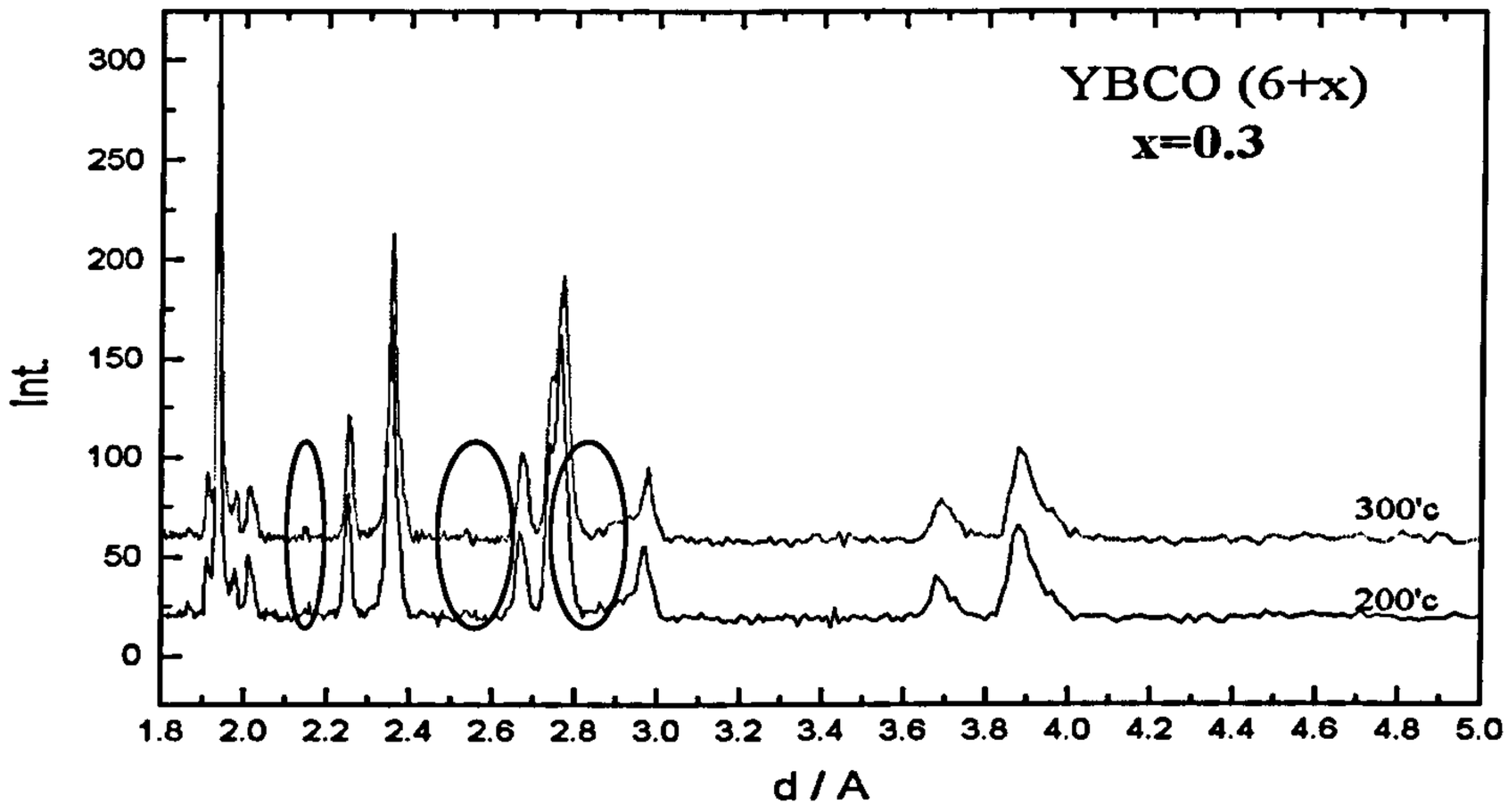

Fig.(5.12) Neutron diffraction from a sample with constant oxygen content x~0.3 at 200°C and 300°C. The ovals show the very weak superstructure peaks

In Fig.(5.13) the growth of a superstructure [S.102] peak with increasing oxygen content is obvious. This peak is important because there is no tetragonal phase peak at this relatively high d-spacing range (it would be indexed 1/2,0,2 on the original lattice unit cell). The results in this series of neutron diffraction measurements are consistent with the aforementioned x-ray data.

Because of a technical fault during the last measurement, the furnace had to be shut down so the data for x~0.6 was collected at room temperature. Refinement of this measurement suggests the coexistence of the OII and OI phases around the boundary between the OII & OI phases in the T-x structural phase diagram. If so, this could mean that the OII/OI phase transition is also first order, but more accurate data collection in this region is needed.

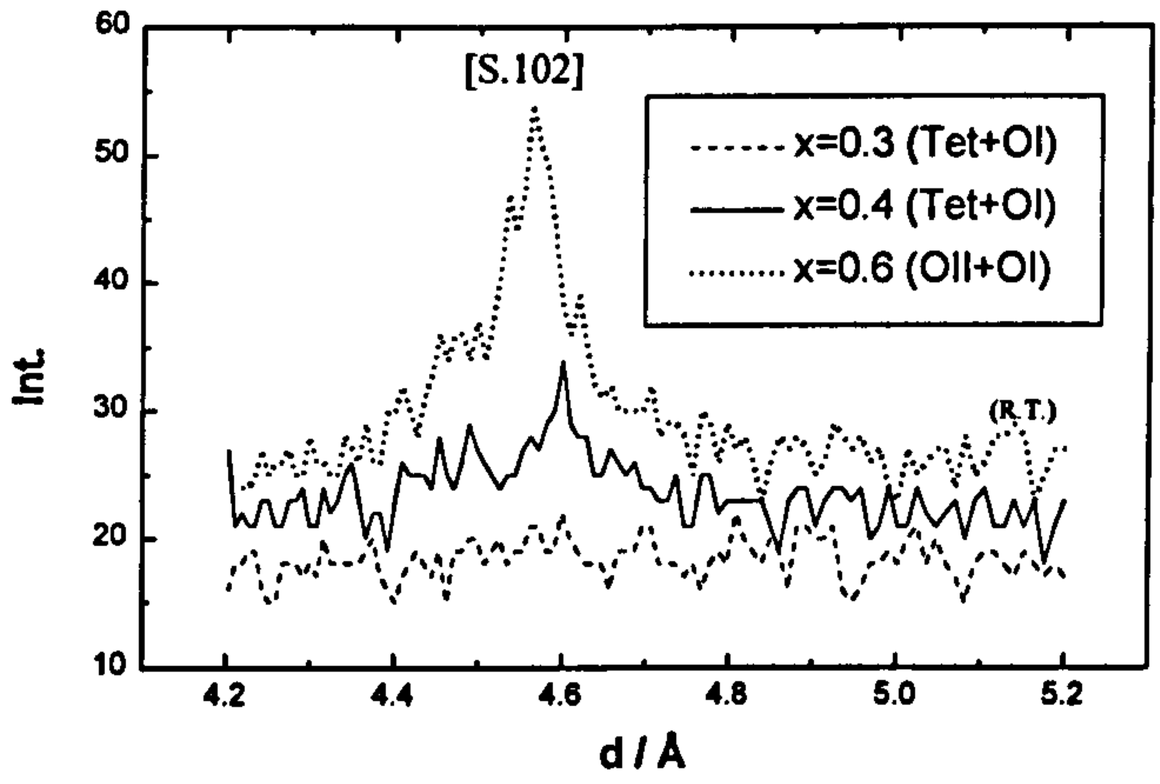

Fig.(5.13) Growth of an OII peak with increasing oxygen concentration (neutron diffraction) . The data at x ≈0.6 was collected at room temperature

The first part of this section deals with the results from the mixed-phase (T+OII) model refinements and in the second part a general discussion about the results will be presented. The superstructure model for the OII phase is an orthorhombic unit cell with P m m m space group consisting of two adjacent ordinary tetragonal cells with a common *b-c* plane between them (Fig. 5.2), with lattice parameter as:

$a_{OII} = 2a_T$, $b_{OII} = b_T$, $c_{OII} = c_T$,

V.3.1) The Results

A mixed-phase (T+OII) profile refinement for the sample with x~0.2 at 200°C is presented in Fig.(5.14), that the upper toggles come from the OII phase (using a refinement program called GSAS ; **G**eneral **S**tructure **A**nalysis **S**ystem).

The goodness of the refinement shows by :

$\chi^2 = 3.322$ and $R_p = 0.092$

The volume fraction of the OII phase is about 15% and the oxygen site occupancy fractions are:

Tetragonal : O1 ~ 0.05±0.0046 & O5 ~ 0.05±0.0046

Orthorhombic II : O1 ~ 0.55±0.05 ; $O1_p$ ~ 0.32±0.029 & O5 ~ 0.05±0.0046

(where $O1_p$ is the counterpart of the O1 site in the middle vertical plane of the OII super cell)

Therefore, with regards to each site multiplicity and phase volume fraction, the average oxygen concentration in the basal plane for each phase is:

$\overline{O_T} \approx 0.085 \pm 0.015$

$\overline{O_{OII}} \approx 0.1455 \pm 0.026$

So the total oxygen content in the sample is :

$\bar{x} \approx 0.23$ (close to the expected value ~ 0.2)

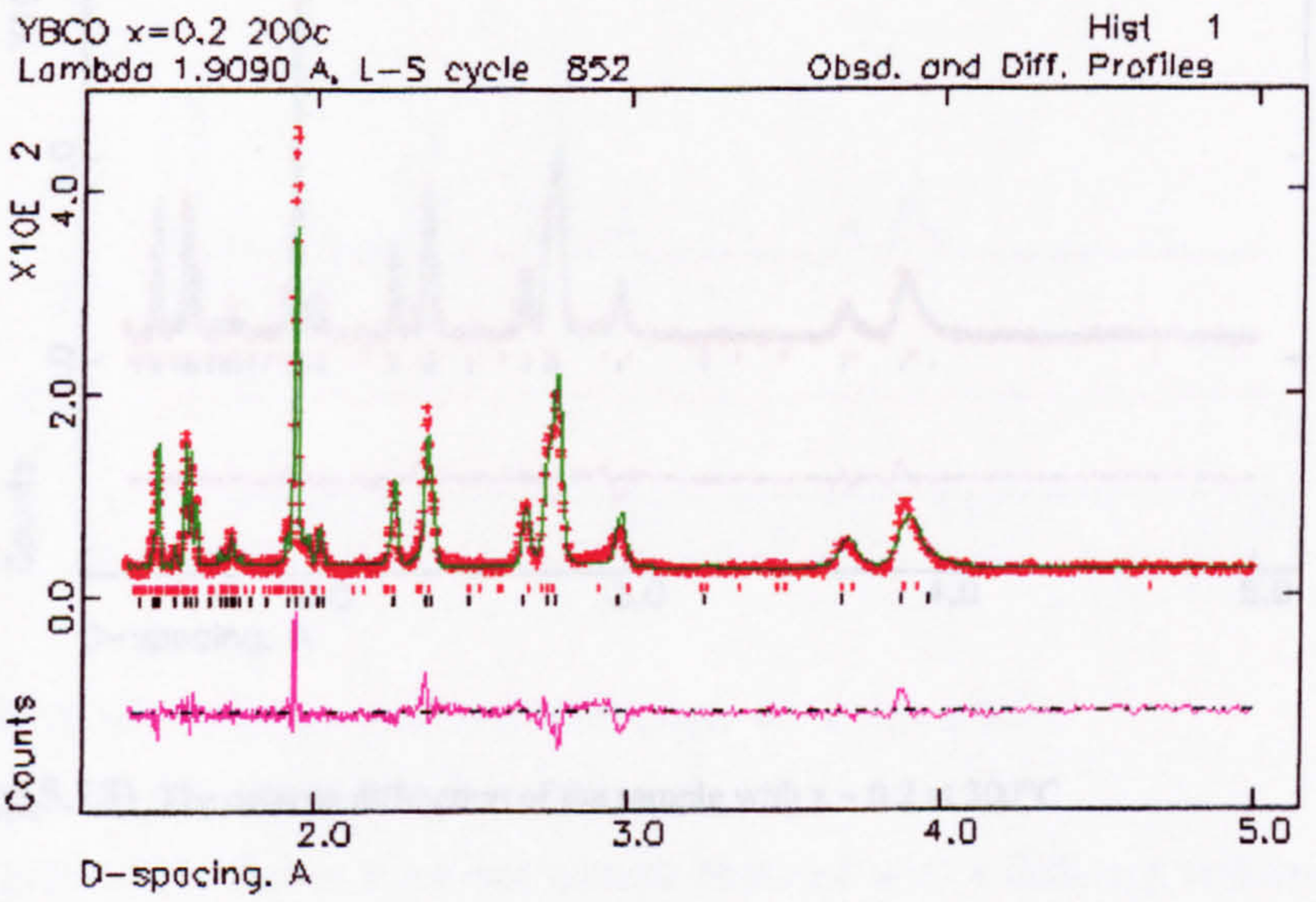

Fig.(5.14) The neutron diffraction of the sample with x ~ 0.2 at 200°C

Figure (5.15) shows a mixed-phase (T+OII) profile refinement for the same sample (x~0.2) at 300°C.

The goodness of the refinement is shown by :

$$\chi^2 = 3.508 \text{ and } R_p = 0.0981$$

The volume fraction of the OII phase is about 8 % and the oxygen site occupancy fractions are:

Tetragonal: O1 ~ 0.085±0.0083 & O5 ~ 0.085±0.0083

Orthorhombic II: O1 ~ 0.48±0.047 ; $O1_p$ ~ 0.21±.02 & O5 ~ 0.017±0.0016

Therefore with regards to each site multiplicity and the phase volume fraction the average oxygen concentration in the basal plane for each phase is:

$\overline{O_T} \approx 0.156 \pm 0.03$

$\overline{O_{OII}} \approx 0.058 \pm 0.011$

So the total oxygen content in the sample is :

$\bar{x} \approx 0.214$ (quite close to the expected value ~ 0.2)

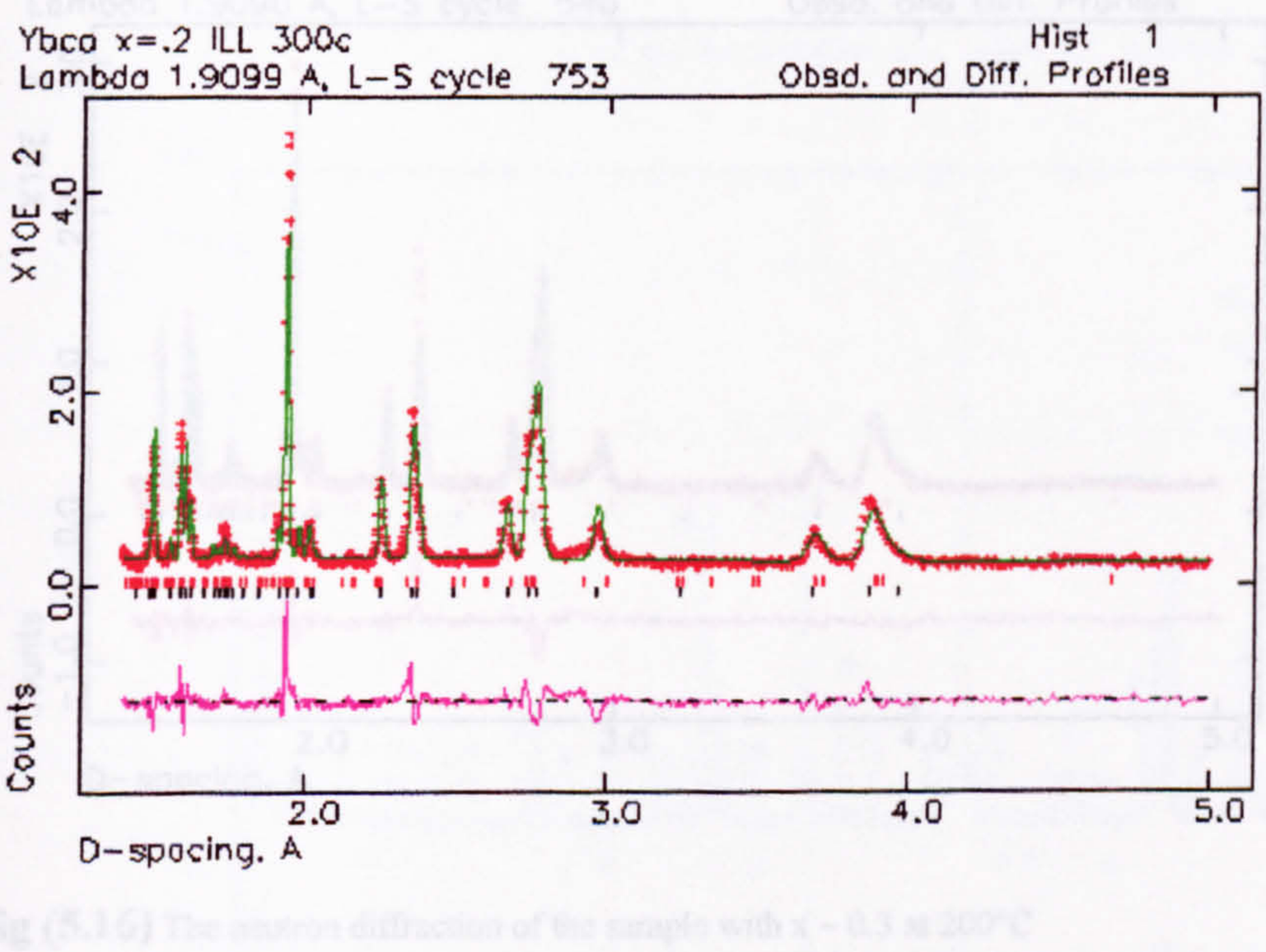

Fig(5.15) The neutron diffraction of the sample with x ~ 0.2 at 300°C

For the sample with x~0.3, Fig.(5.16) shows a mixed-phase (T+OII) profile refinement for the same sample at 200°C. Goodness of the refinement is shown by :

$$\chi^2 = 3.064 \text{ and } R_p = 0.088$$

The volume fraction of the OII phase is about 36.5% and the oxygen site occupancy fractions are:

Tetragonal : O1 ~ 0.052±0.0045 & O5 ~ 0.052±0.0045

Orthorhombic II : O1 ~ 0.47±0.041 ; $O1_p$ ~ .10±0.0088 & O5 ~ 0.064±0.0016

Therefore with regards to each site multiplicity and the phase volume fraction the average oxygen concentration in the basal plane for each phase is:

$$\overline{O_T} \approx 0.066 \pm 0.01$$

$$\overline{O_{OII}} \approx 0.231 \pm 0.037$$

So the total oxygen content in the sample is :

$$\bar{x} \approx 0.297$$ (close to the expected value ~ 0.3)

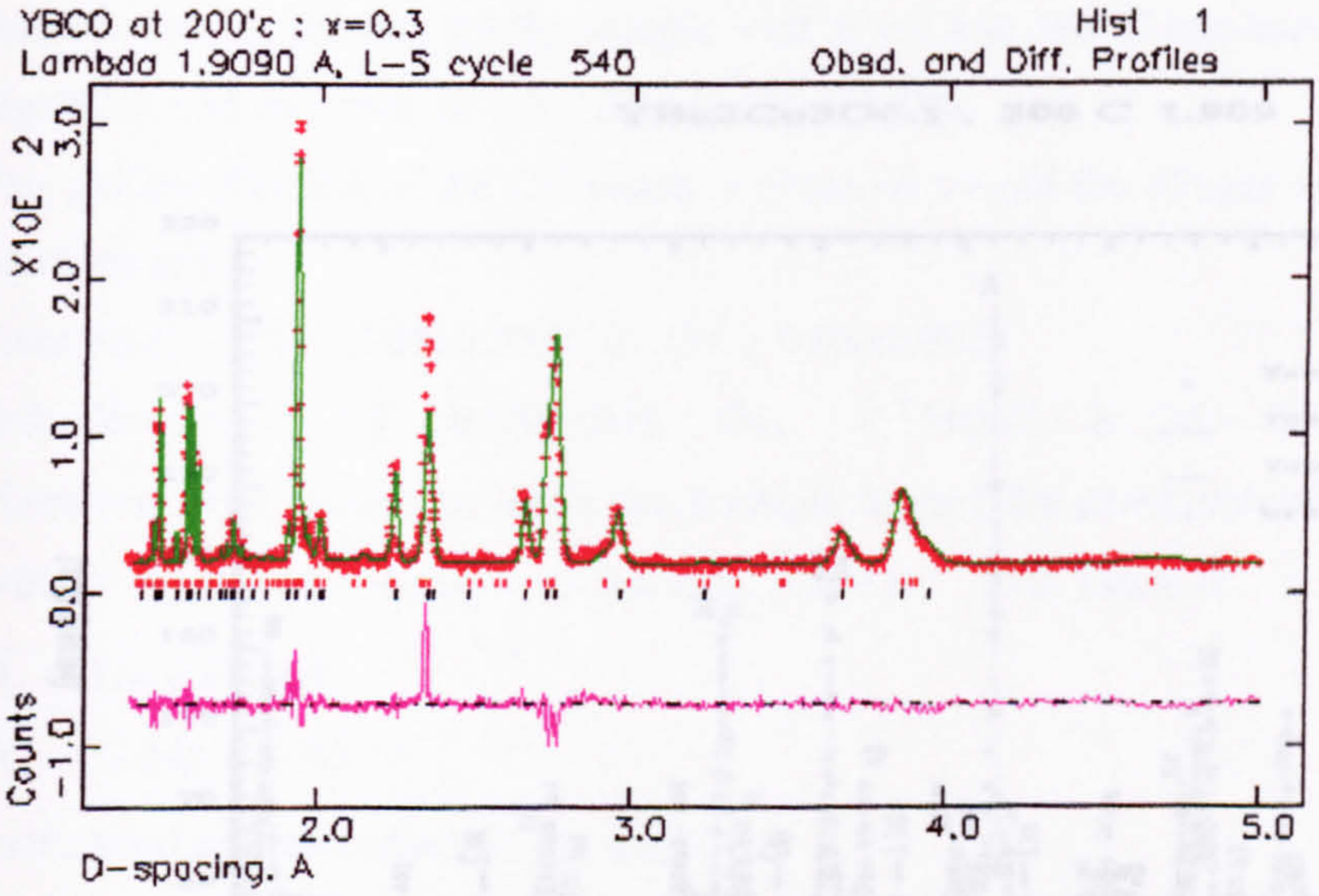

Fig (5.16) The neutron diffraction of the sample with x ~ 0.3 at 200°C

Figure (5.17) shows a refined pattern obtained with a different refinement program called "FULLPROF" (usually used in ILL) for the sample with x ≈ 0.3 at 300°C, with

respect to just one phase (tetragonal) structure. The fit is not very good because of the presence of the OII component.

When again the same mixed-phase model for the refinement was performed used GSAS, a much better results has been obtained (Fig. 5.18), as:

Goodness of the refinement shows by : $\chi^2 = 3.19$ and $R_p = 0.091$

The volume fraction of the OII phase is about 35 % and the oxygen site occupancy fractions are:

Tetragonal : O1 ~ 0.061±0.055 & O5 ~ 0.061±0.055

Orthorhombic II : O1 ~ 0.43±0.039 ; $O1_p$ ~ 0.145±0.0131 & O5 ~ 0.052±0.0047

Therefore with regards to each site multiplicity and the phase volume fraction the average oxygen concentration in the basal plane for each phase is:

$$\overline{O_T} \approx 0.0793 \pm 0.014$$

$$\overline{O_{OII}} \approx 0.219 \pm 0.039$$

So the total oxygen content in the sample is :

$\bar{x} \approx 0.298$ (quite close to the expected value ~ 0.3)

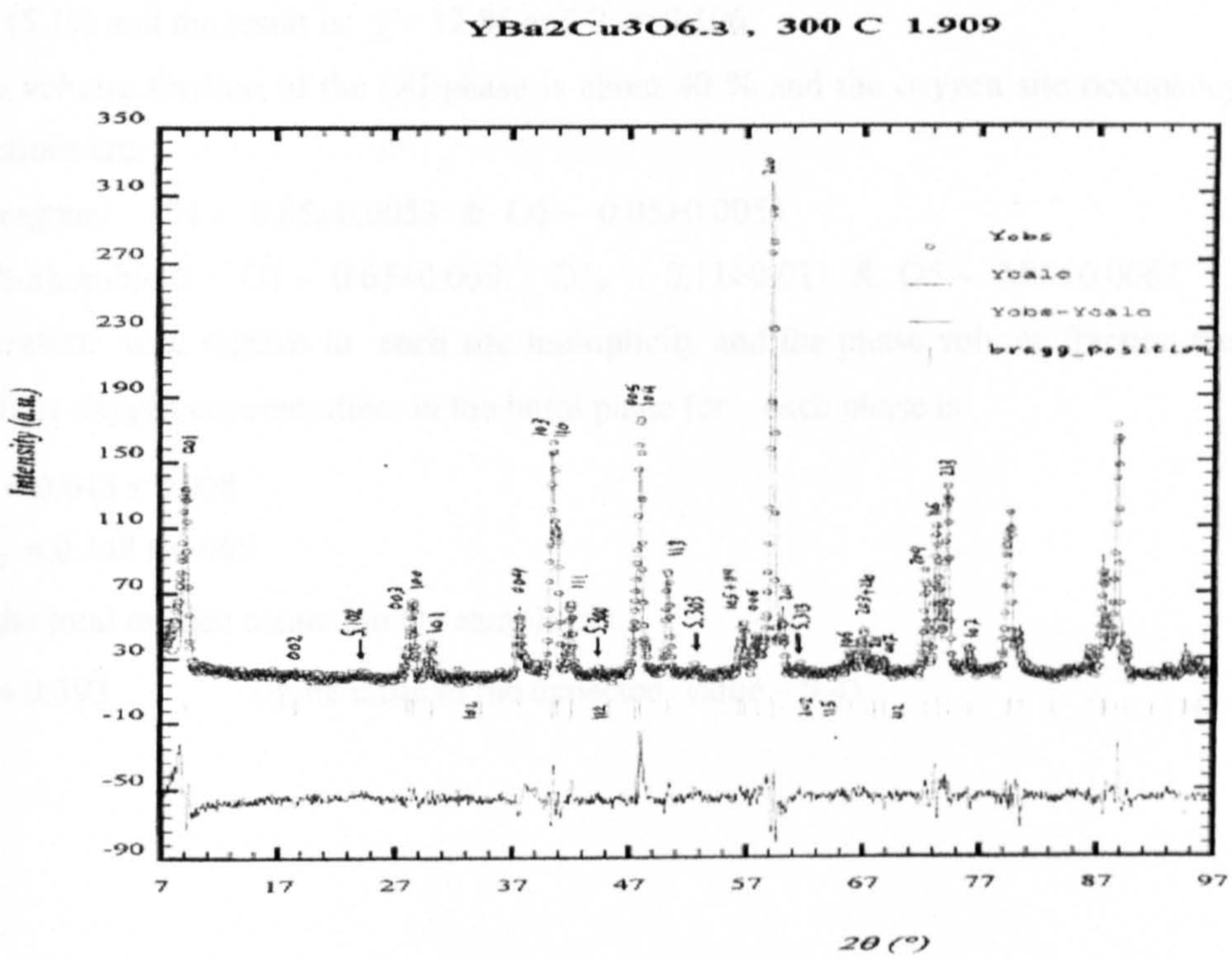

Fig(5.17) The neutron diffraction of the sample with x ~ 0.3 at 300°C using just the tetragonal model (FULLPROF, with assistance of Juan Rodrigues-Carvajal)

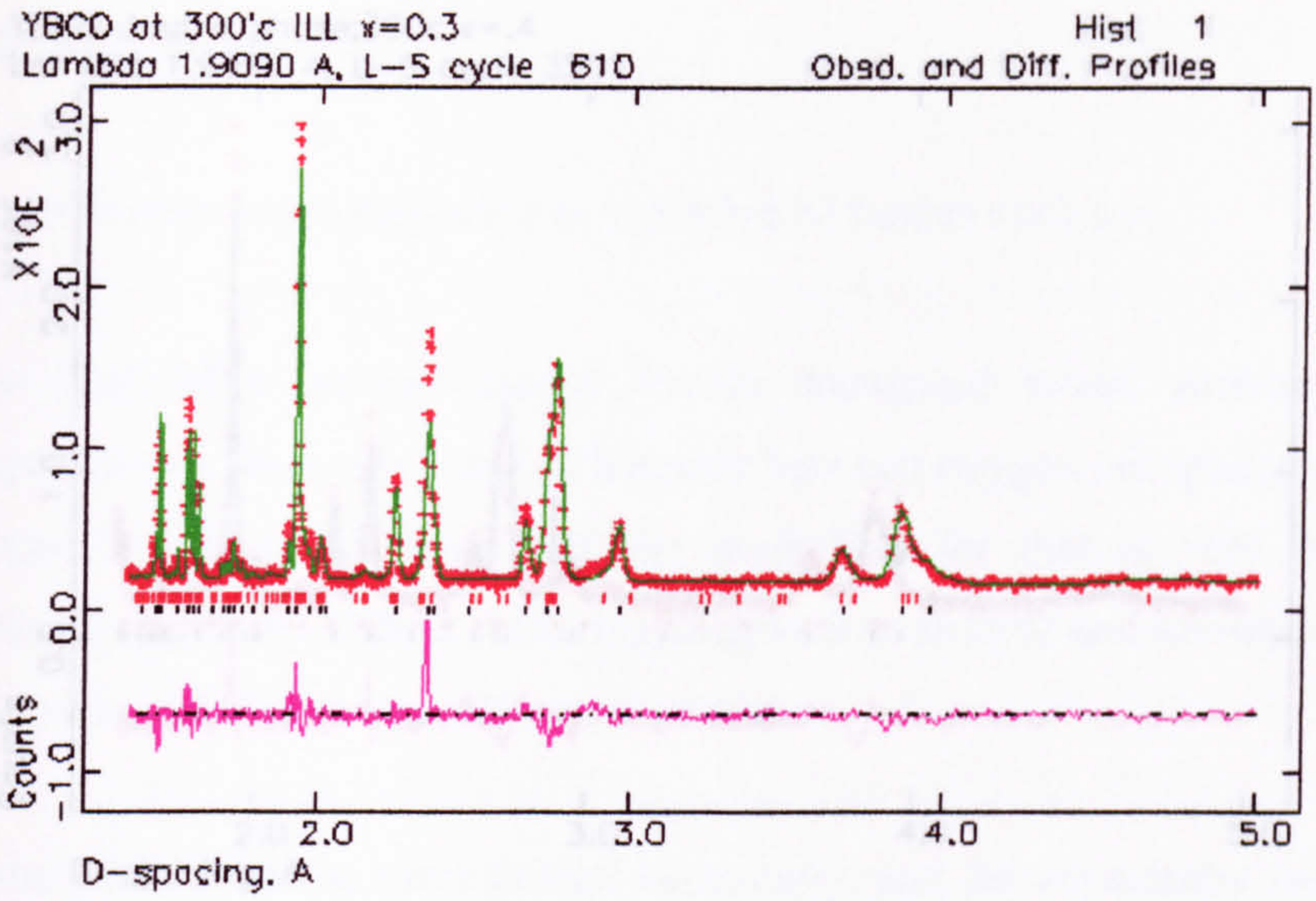

Fig(5.18) The neutron diffraction of the sample with x ~ 0.3 at 300°C

Another refined pattern for the sample with x ~ 0.4 at 300°C has been presented in Fig.(5.19) and the result is: $\chi^2 = 12.85$ and $R_p = 0.106$

The volume fraction of the OII phase is about 40 % and the oxygen site occupancy fractions are:

Tetragonal : O1 ~ 0.05±0.0053 & O5 ~ 0.05±0.0053

Orthorhombic II : O1 ~ 0.65±0.069 ; $O1_p$ ~ 0.11±0.011 & O5 ~ 0.06±0.0063

Therefore with regards to each site multiplicity and the phase volume fraction the average oxygen concentration in the basal plane for each phase is:

$\overline{O_T} \approx 0.045 \pm 0.008$

$\overline{O_{OII}} \approx 0.348 \pm 0.065$

So the total oxygen content in the sample is :

$\bar{x} \approx 0.393$ (quite close to the expected value ~ 0.4)

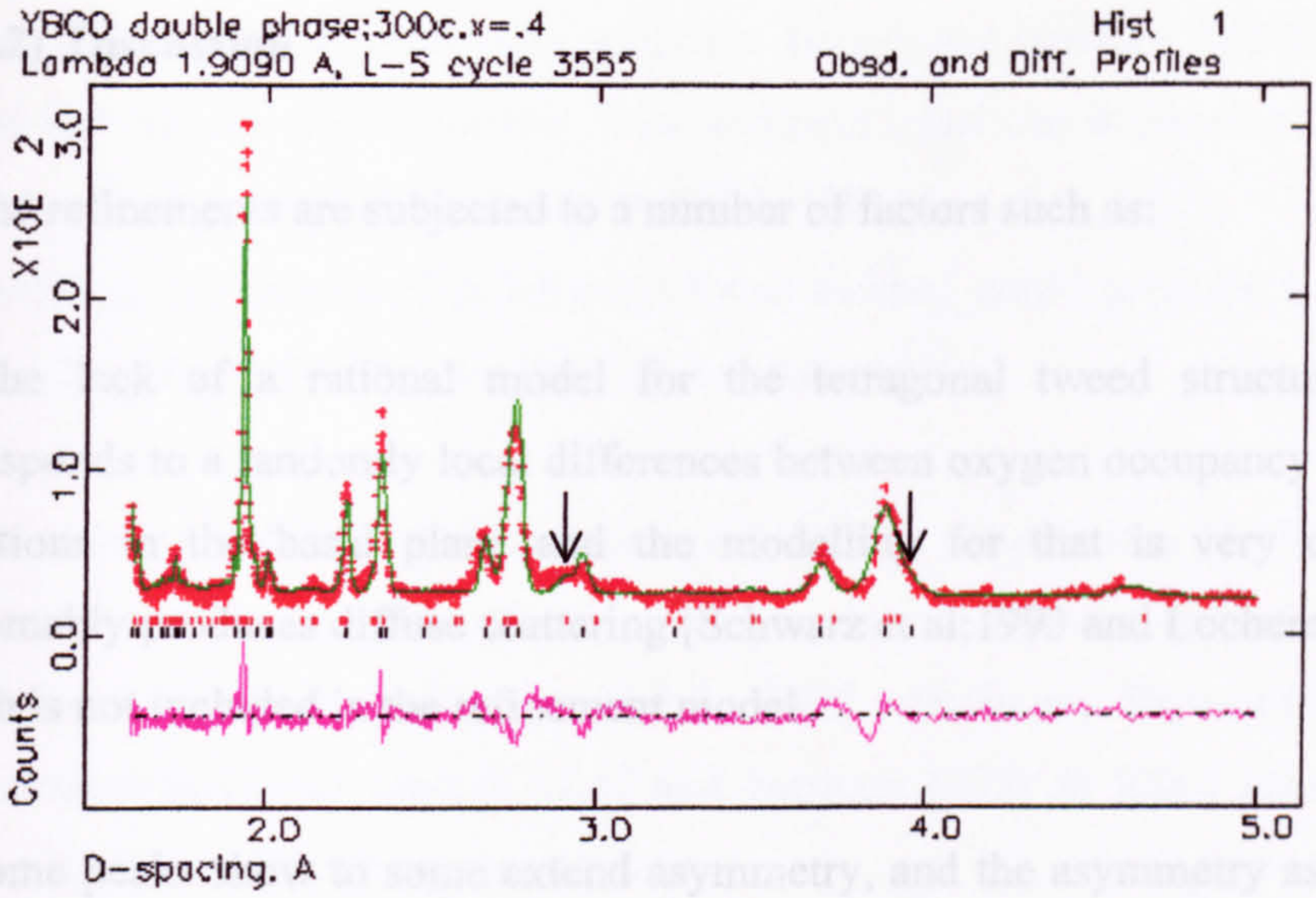

Fig(5.19) The neutron diffraction of the sample with x ~ 0.4 at 300°C The thin arrows show the very broad [*00l*] lines for the OII phase.

An entirely OII phase model has been used to refine this sample as well and the results deteriorated:

$\chi^2 = 16.72$ & $R_p = 0.208$

In the next section some possible explanations are presented.

V.3.2) Discussion

All the refinements are subjected to a number of factors such as:

a- The lack of a rational model for the tetragonal tweed structure because it corresponds to a randomly local differences between oxygen occupancy along *a* and *b* directions in the basal plane and the modelling for that is very difficult. This presumably produces diffuse scattering [Schwarz et al;1993 and Locherer et al; 1996], which is not included in the refinement model.

b- Some peaks show to some extend asymmetry, and the asymmetry associated with the *c* axis might be attributed to an oxygen concentration gradient through the grains of powder [David; 1989]. This, in turn, would indicate that the sample has not reached prefect thermodynamical equilibrium condition. If so, because the cell volume increases as oxygen is removed, the average cell volume in the outer shells of grains would differ from the inner concentric shells. Since there is more material in the outer shells, thus produces the asymmetry.
On the other hand, "Stacking faults" along the *c* direction are a very common cause of broadening and asymmetry in layered cuprate superconductors, especially for [*hk0*] lines (Fig. 5.20) [Mercer; 1997]

c- Large broadening of the [*00l*] reflections in the OII phase, especially as indicated by the arrows in Fig.(5.19), for the sample with higher oxygen content and OII phase volume fraction. The main reason for this effect could be the possibility of "antiphase boundaries" between adjacent layers along the *c* direction.
For an ideal OII suppercell, the oxygen site on the middle vertical plane (along *b* direction) in the supercell basal plane, O1p, must be empty and in the side vertical planes there are full oxygen sites, O1. This will leads to some expansion along the *c* direction in the supercell's middle vertical plane[6] (Fig. 5.21a) but for an oxygen deficient OII phase (the case in here) there are some other possibilities (meshes) that some of them are shown schematically in the Figs. (5.21b_d). The anti phase boundary can happen between two domains, each one consisting of a couple of

[6] In absence of the oxygen in the basal plane the O4p can move further away from the CuO2 sheet, therefore the *c* parameter for tetragonal phase is always a bit longer than the *c* in the orthorhombic phases

columns of one mesh wide. The antiphase boundaries between OII domains do not anneal out and the reason for this is the intrinsic quasi one dimensional nature of the system, possibly coupled with a random field [Schleger et al; 1995].

In addition, the mismatches between these meshes could produce a vast range of strains along the *c* direction for the OII structure.

d- The other possibility which cannot be ruled out is the presence of a kind of periodic structure among each couple of unit cells along the *c* direction (a kind of modulation which would produce satellites around the [*00l*] reflections). Figures (5.22a_b) show two unidentified lines around [004] and between [005] & [006] reflections which grow with increasing the oxygen content.

According to the relative instability of the z component of atoms in the middle vertical plane, $Cu(2)_p$; $O(3)_p$ and $O(4)_p$, (the suffix, p, used for atoms in the middle vertical plane) during the refinement procedure, and some reports based on the formation of a super structure along the *c* direction [Marshal et al; 1988]&[Pandey et al; 1990], it seems the above assumption could be rational, although it is still controversial [Liang et al; 2000].

Fig.(5.23) shows the suggested atomic displacements in the supercell, but the GSAS program is not able to deal with the modulation effect, so it will need more accurate structural analyses in future.

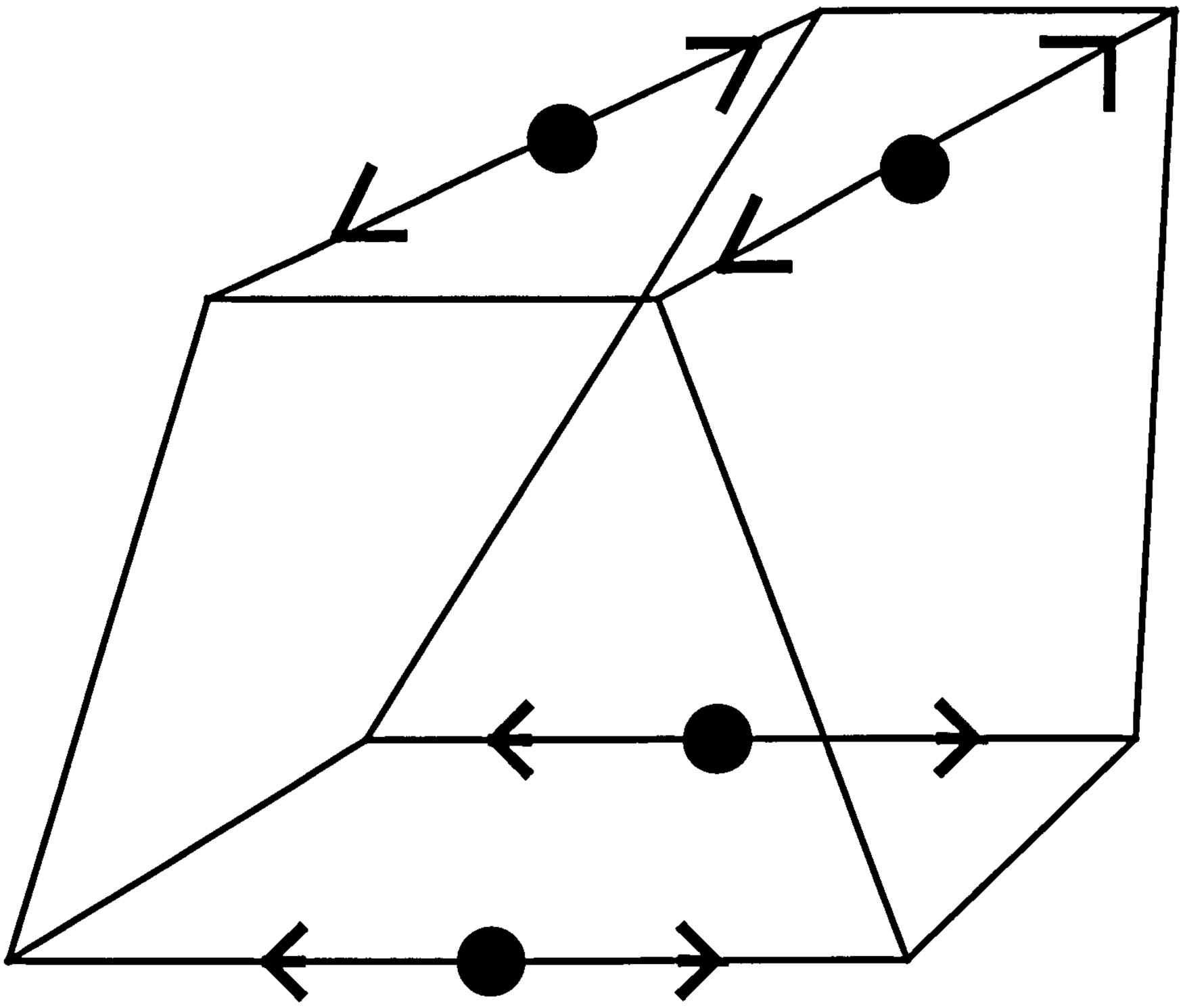

● Oxygen atom

← Forces

Fig.(5.20) A representation of a stacking fault in *c* direction , produced by a mismatch in oxygen order . Forces are shown as arrows. The oxygen atoms will resist any contraction and therefore the cell edge in which no oxygen are present will suffer more deformation (expansion).

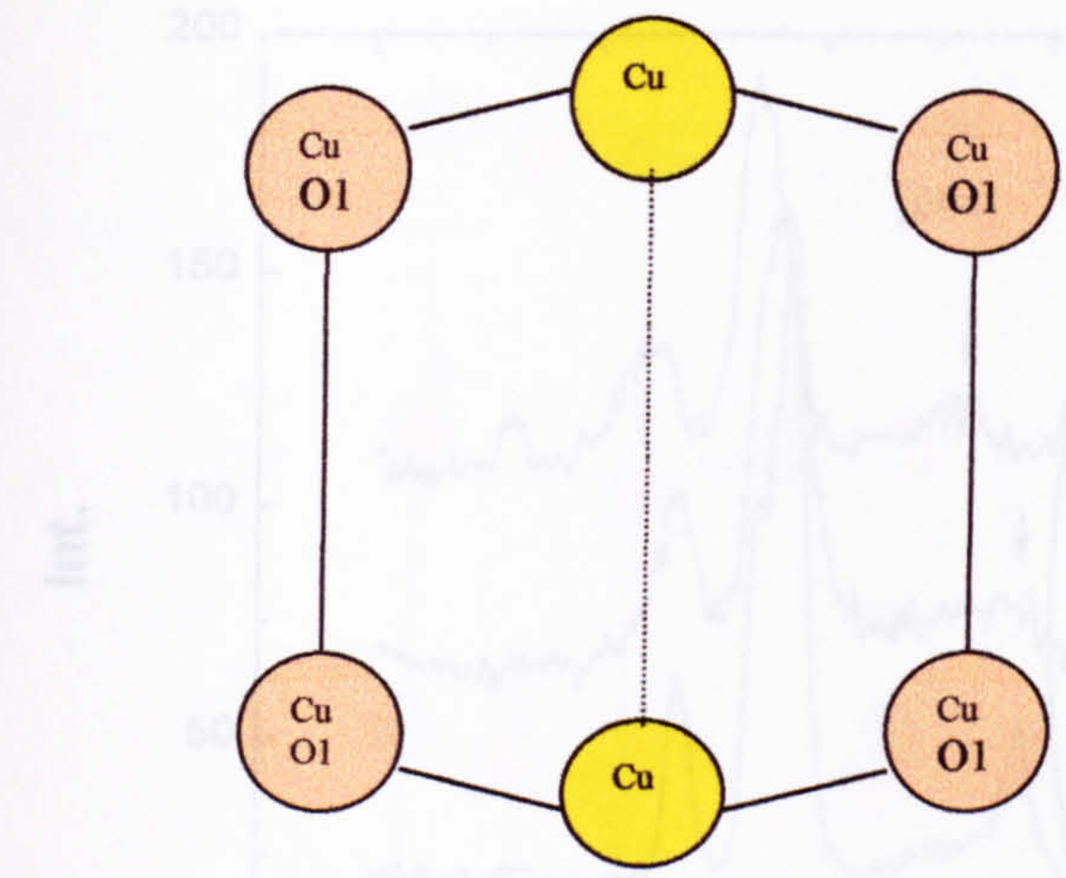

(a)

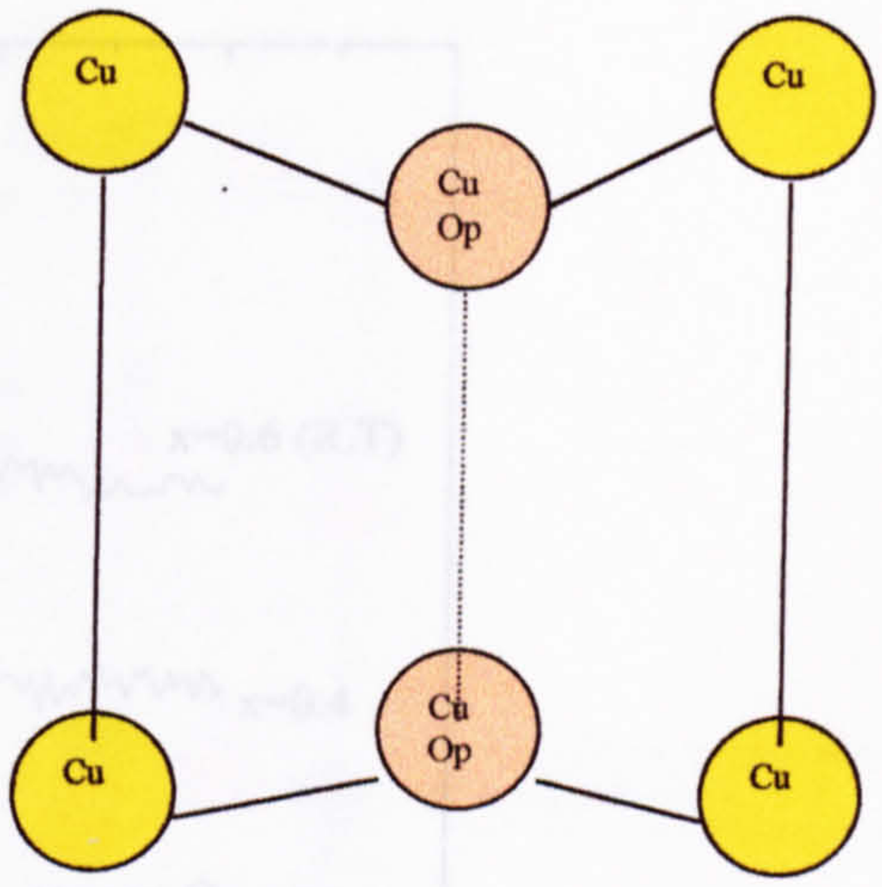

(b)

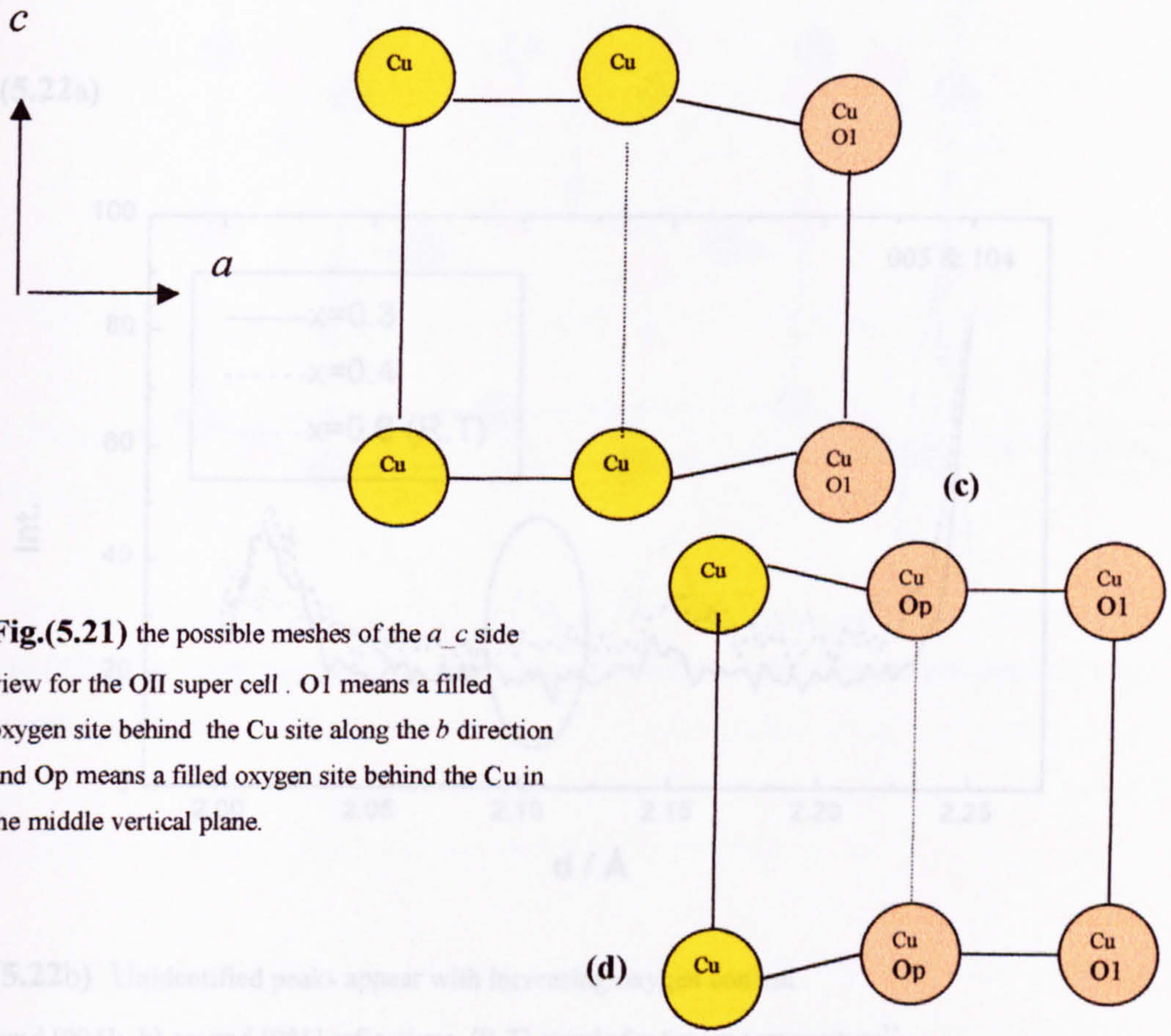

(c)

(d)

Fig.(5.21) the possible meshes of the *a*_*c* side view for the OII super cell . O1 means a filled oxygen site behind the Cu site along the *b* direction and Op means a filled oxygen site behind the Cu in the middle vertical plane.

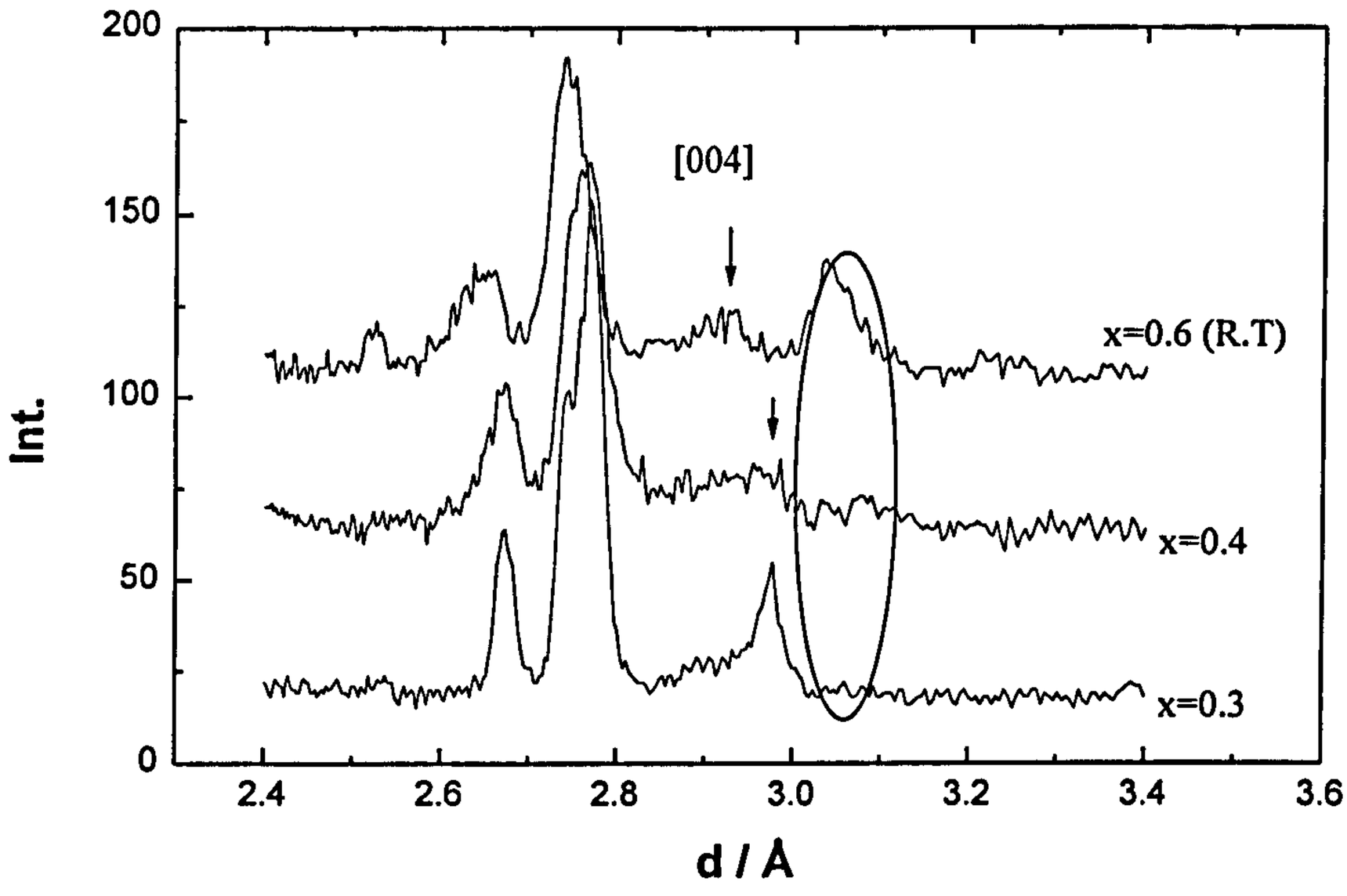

Fig.(5.22a)

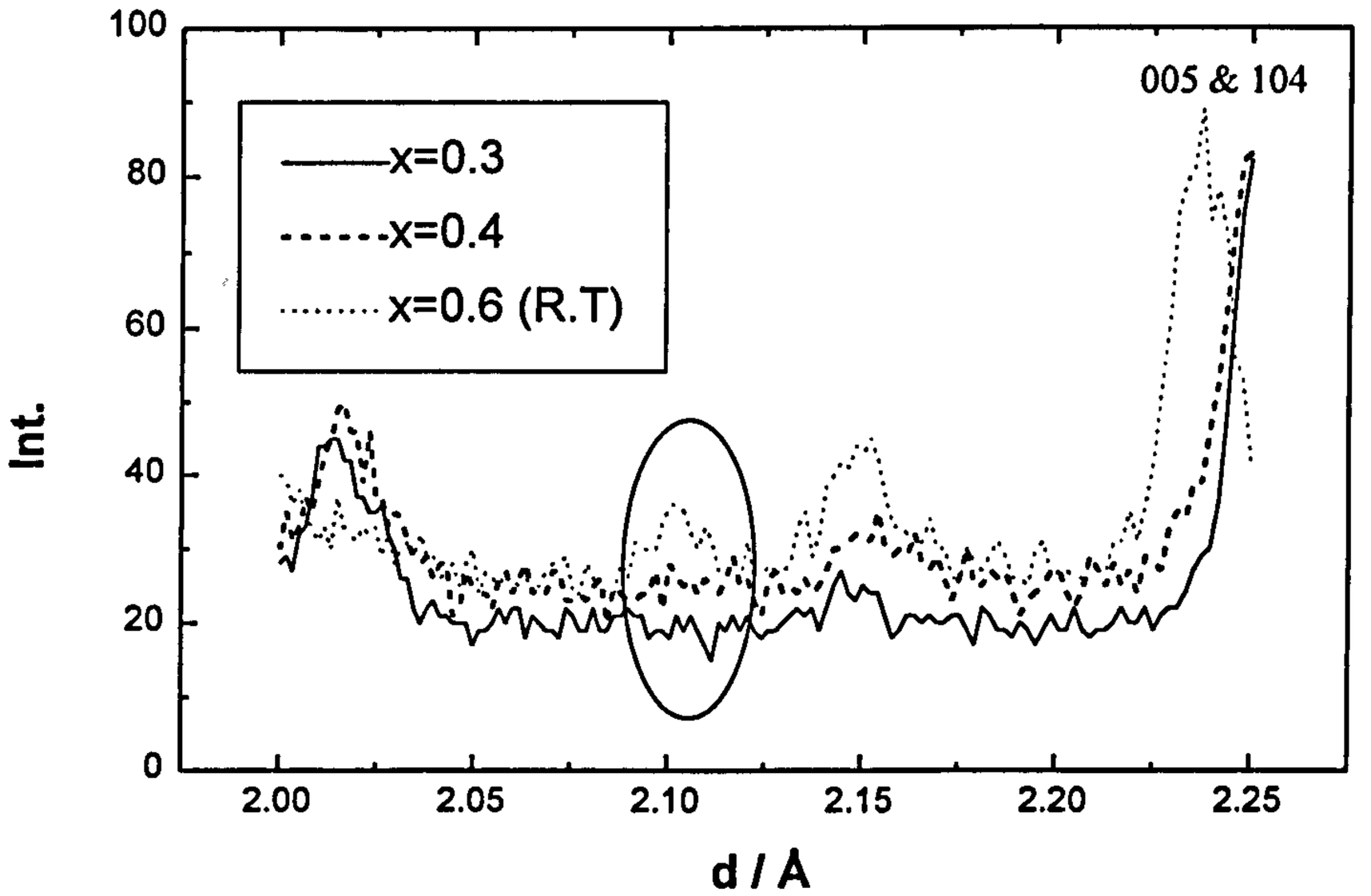

Fig.(5.22b) Unidentified peaks appear with increasing oxygen content .

a) around [004]; b) around [005] reflections. (R.T) stands for "room temperature"

Despite the above factors which create some uncertainty in the quantities extracted from the refinement, the general trend of the measurements is in agreement with a mixed phase region behaviour, for instance the intensity of the entirely OII phase peaks grow with increasing oxygen content (Figs. 5.13 and 5.24).

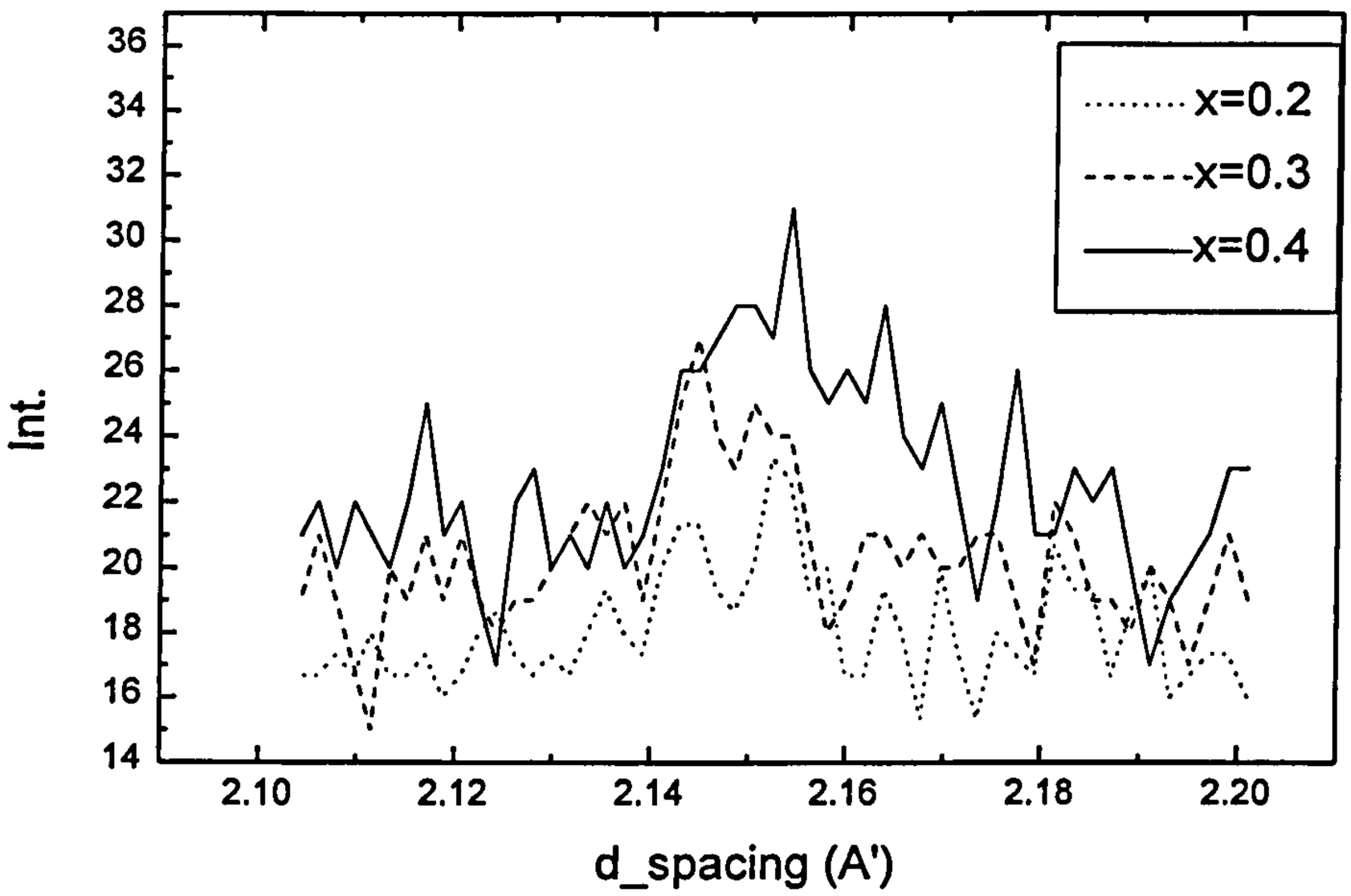

Fig (5.24) Growth of the [S.213] peak with increasing the oxygen concentration at 300°C

In addition, the OII volume phase fraction and the average share of the basal plane's oxygen for this phase grows with increasing the x values (Figs. 5.25a_b).

At 200°C although the oxygen content in the tetragonal phase drops slightly, the tangent of the increasing rate for the oxygen content in OII phase is remarkably higher, this is perhaps because the calculated oxygen content of the Tet. phase is not accurate enough (tweeding effect). Finally, Figs.(5.26a_b) show the variation of the lattice parameter in both phases vs. the oxygen concentration, x.

A roughly linear extrapolation of the data suggests that the pure OII phase at 300°C(200°C) corresponds to x≈0.7 (≈0.62), and this is consistent with some other studies [Fleming et al; 1989 and Blagoev et al; 1993]. But since theoretically the OII phase is stoichiometric only for x=0.5, it seems that the stability of the OII phase at elevated temperatures [200-300°C] demands more repulsive O-O forces by absorbing

more oxygen atoms, 0.5<x<0.7. These extra oxygen atoms can distribute randomly between the O-Cu-O chains in this phase.

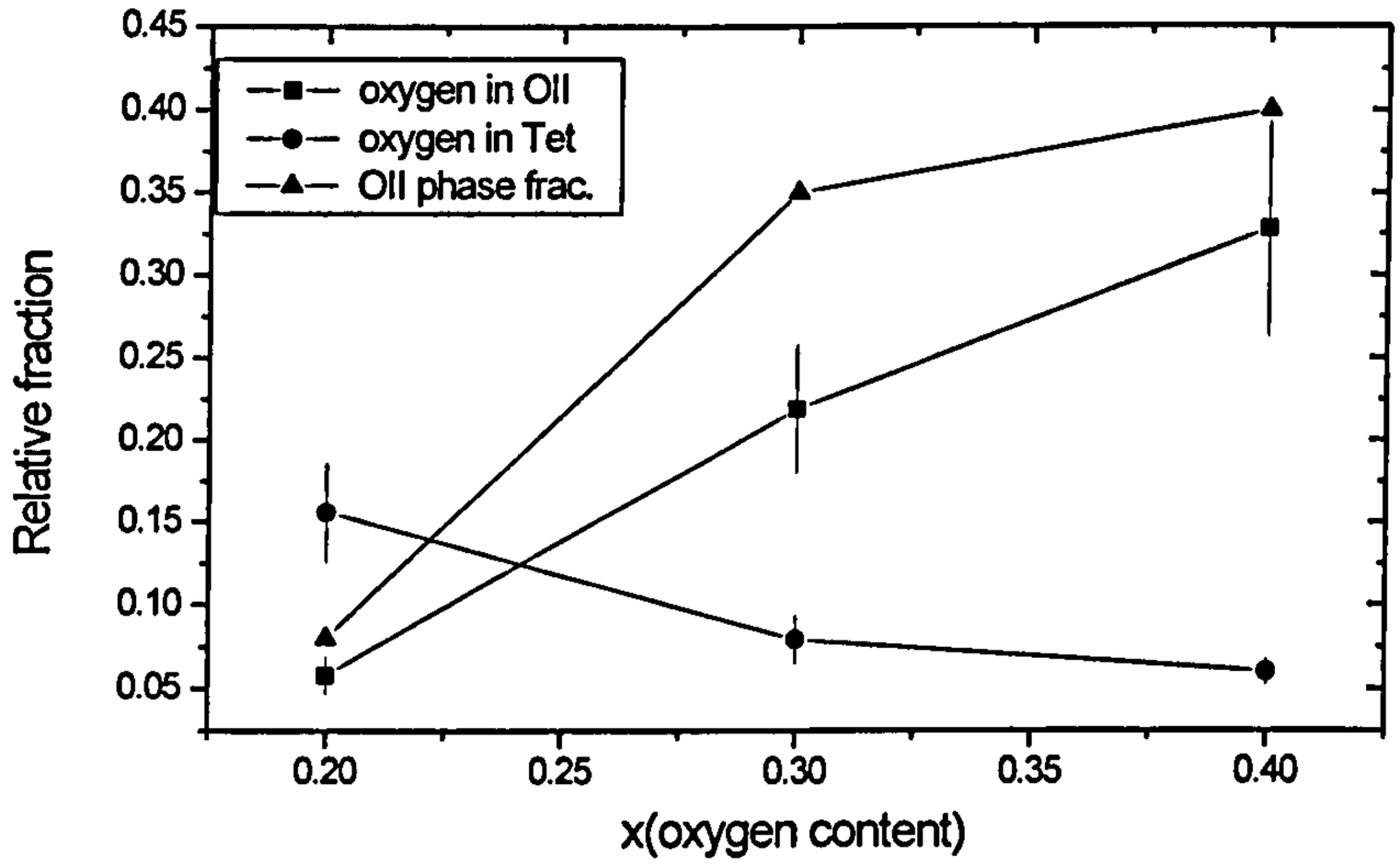

Fig (5.25a) The relative phase fraction vs. x at 300°C

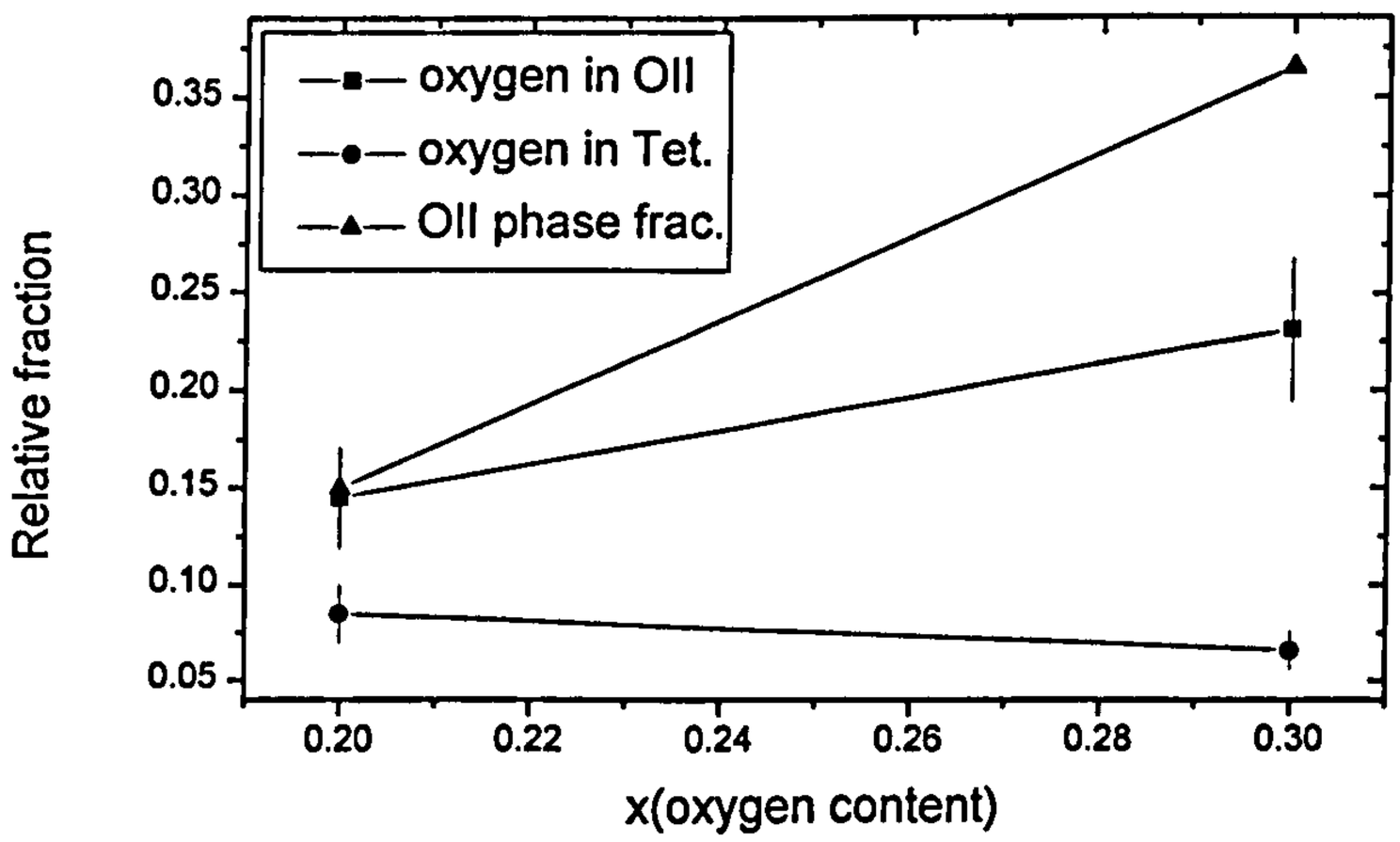

Fig.(5.25b) The phase relative fraction vs. x at 200°C

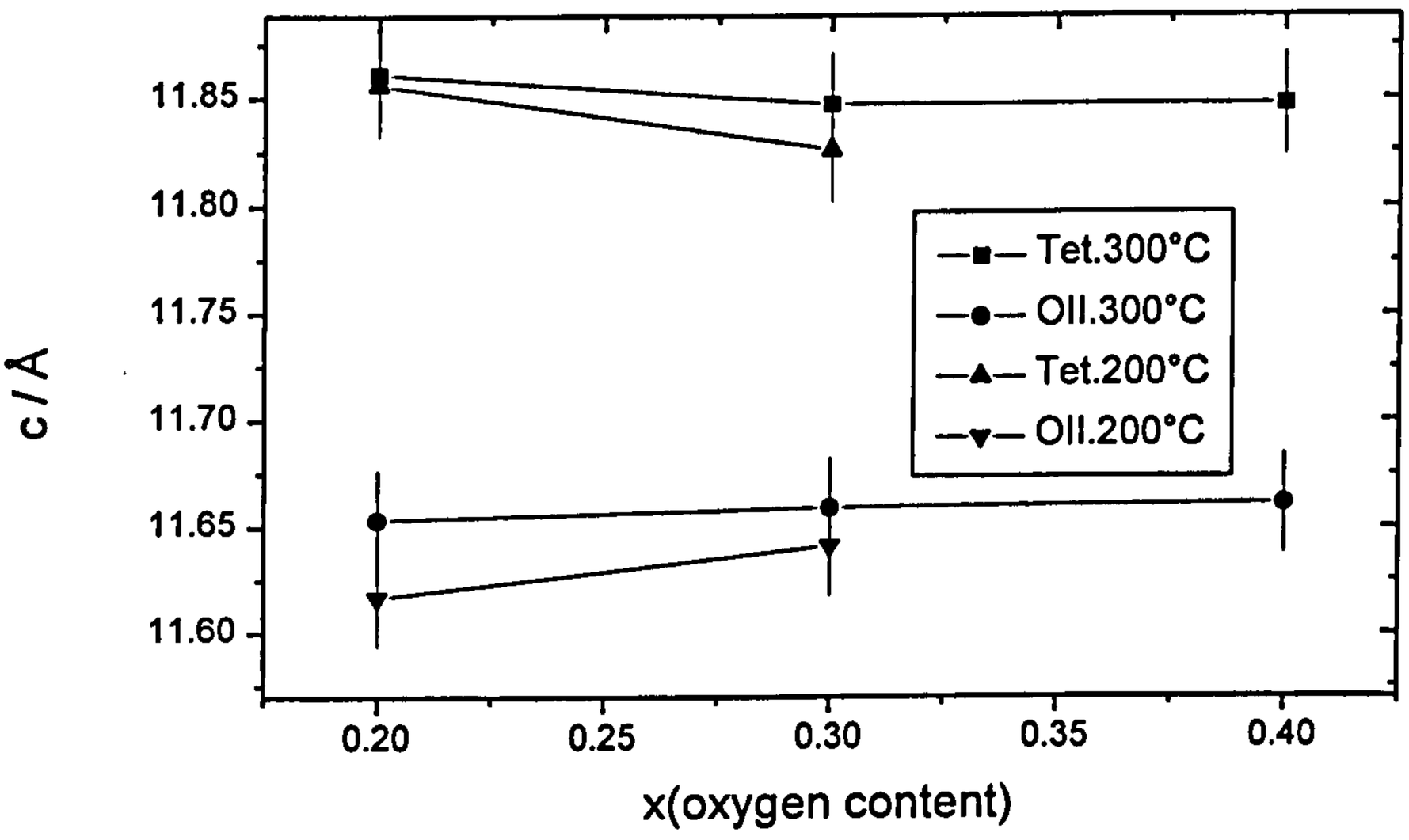

Fig.(5.26a) Variation of the *c* (lattice parameter) vs. x

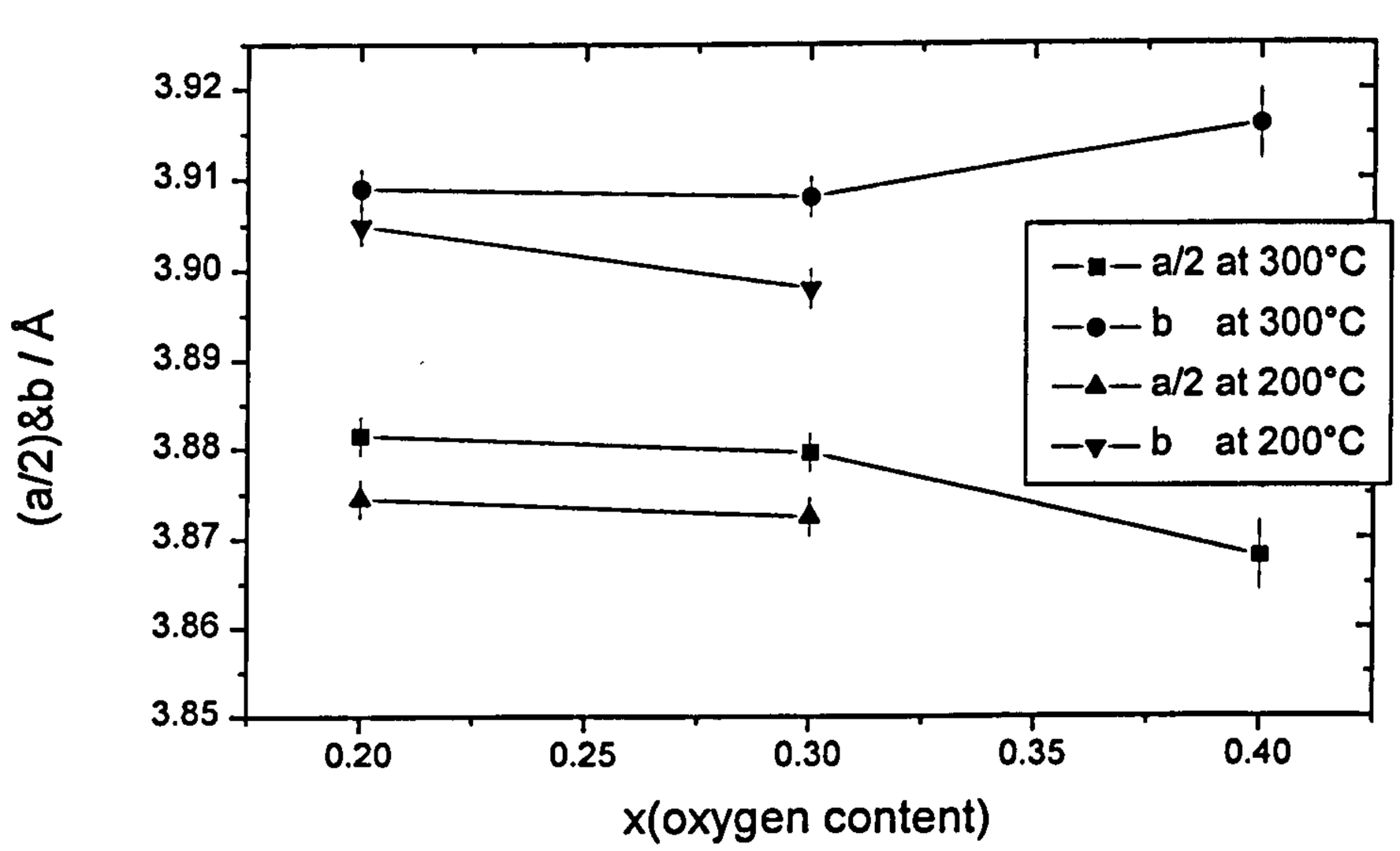

Fig . (5.26b) Variation of *a/2* and *b* vs.x

V.4) CONCLUSION

The character of the YBCO's OII superstructure section in the structural phase diagram at elevated temperature (200°C-300°C) has been studied by powder x-ray *in situ* and complementary neutron powder diffraction, whereas the majority of the previous experimental data comes from electron microscopy (E.M), or single crystal neutron diffraction. The popular *ASYNNNI* lattice-gas model which has successfully explained the majority of the high-temperature features, here predicts a second order phase transition for Tet/OII consistent with screened Coulomb repulsion potential [Algia et al; 1990] model, but the other calculations based on the de Fontaine model [Wille & de Fontaine; 1988] and [Khachaturyan et al; 1988] predicts a first order transition in here. The modelling improvement for this part of the phase diagram is still active [Poulsen et al; 1996], [Liang et al; 2000]. In this work is presented some strong experimental evidences in support of the **first order** characteristic transition between tetragonal and OII phase. It has also been seen some evidences of first order transition feature for the other part of the low and elevated temperature zone of the structural phase diagram between OII and OI phases, but it still needs more study.

The other interesting point in this work was the existence of the OII components at 300°C in contrast to the other reports for 150°C [Poulsen et al; 1996] & [Schwartz et al;1993], so it seems the boundary of the OII phase region in the YBCO's structural phase diagram must be corrected at least up to 300°C.

Chapter VI

Powder Diffraction Microstructure Analysis (P.D.M.A.)

Introduction

Many samples show microstructure effects on line profile shape, width and position. The powder diffractometer resolution improvements no longer cause the sample effects to be obscured by instrumental effects.

The well known Rietveld Method (R.M.) is a crystal structure refinement method, from powder diffraction data. A diffraction pattern is calculated from a series of structural parameters (cell dimension, atomic co-ordinates, thermal motion, etc) and the peak shape (width parameters) plus background, Lorentz_polarization, etc. It is compared to the observed data, and then the parameters are adjusted by a least square process.

If the effects of sample imperfections on the distribution of intensity for individual reflections is negligible, the parameters which are introduced to account for the profile shape and the peak widths can be refined in the usual way in any R.M. program.

If, on the other hand, the effects of microstructure properties of the specimen are found to be significant, the natures of any imperfections present are first ascertained. The

relationship of the peak widths and the shape of the profiles as a function of *hkl* are then obtained and used to model these parameters in the R.M.

The R.M. is intrinsically unable to consider diffuse scattering, since it concentrates on the Bragg scattering (*hkl* based). Nevertheless, some defects can be described reasonably as leading to a mean statistical effect inside the average cell (if due to small and uncorrelated atomic displacement). Only these periodic defects can be seriously considered in a full profile approach depending on an *hkl* - based description of the diffracted intensity. If assimilation to a periodic effect is acceptable in the case of size line-broadening , this is much less evident for all the possible effects due to all kinds of dislocations or grain boundaries. Indeed, dislocations or grain boundaries are locally building some arrangements completely different from the mean unit cell, but they certainly do have statistical effects on the neighboring cells due to the displaced atoms trying to restore the faults.

In complex components, the single crystal Laue technique shows large diffuse effects (weak extra spots) for similar faults (for example: Locherer et al;1996), but on a powder pattern all information is in the one dimensional pattern, so in a pessimistic limit expression : ***the R.M. cannot cope with such imperfection effects which expecting the refined parameters to have physical meaning*** [Le Bail A; Sixth International School and Workshop of Crystallography, Jan.2000].

VI.1) DECONVOLUTION AND PEAK PROFILE SHAPE MODELS

From diffraction theory, the profile peak shape is determined by a function like:

$$y = \sin^2 Nx / \sin^2 x \qquad (6.1)$$

where along the a_i direction, $x_i = ½ (\mathbf{Q}.\mathbf{a}_i)$ and N is the number of unit cells in that direction (Warren; 1969).

Profile shape (and peak widths) of large well crystallized samples are due to the instrumental effects (denoted *g(x)*)[1]. The experimental pattern (denoted *h(x)*) is a convolution of the effect due to the sample structural profile (denoted *f(x)*) with the instrumental effect profile, *g*.

$$h = f * g \qquad \text{or}$$

$$h(x) = \int_{-\infty}^{\infty} f(y)g(x-y)dy \qquad (6.2)$$

The *h* and *g* profiles are the only data available from the diffraction recording (it is supposed that the *g* profile is determined from a standard sample data set, Fig.6.1).

To obtain *f*, equation (6.2) must be deconvoluted by knowing *h* and *g*. Since convolution of functions is equivalent to multiplication of the complex Fourier transforms of the respective functions, this deconvolution can be done by a simple division in the Fourier space :

$$F_n = H_n / G_n \qquad (6.3)$$

(n is the order and F_n , G_n , H_n are normalized coefficient of the Fourier expansion with $F_0=G_0=H_0=1$)

[1] Even in a prefect crystal the profile shapes are not ideally sharp (δ function) and it comes from a variety of causes such as divergence of the incident beam , the natural width of the beam's monochoromacity, the finite width of the slit of the counter ; these all contribute to the instrumental effect.

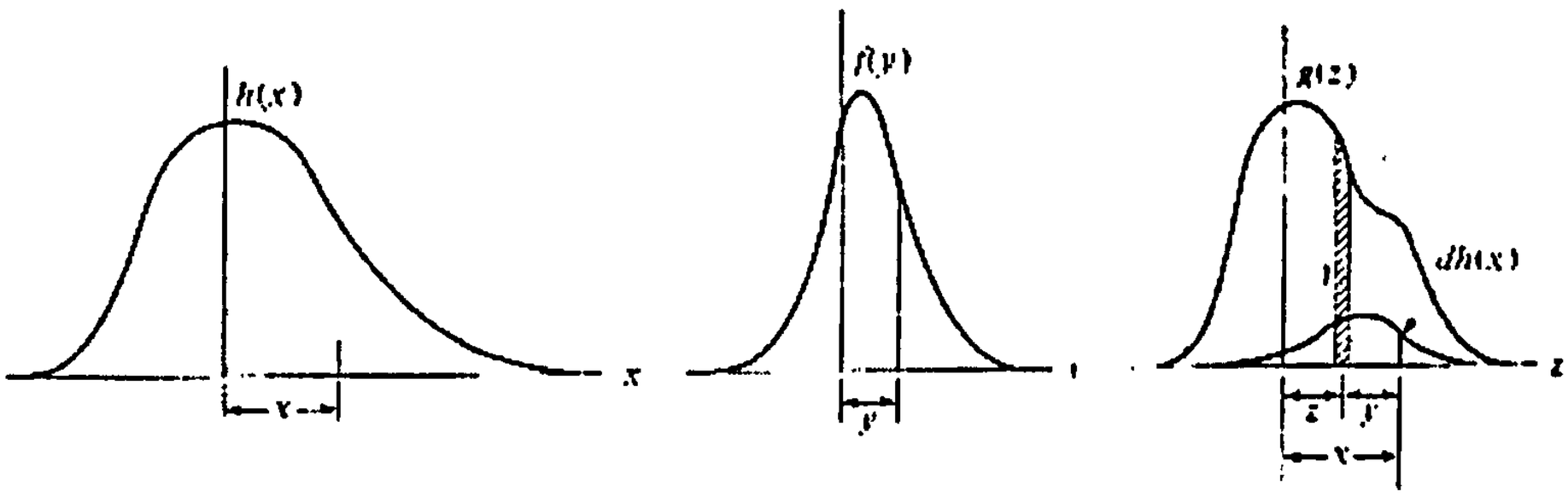

Fig. (6.1) The three curves which are involved in the correction for instrumental broadening. f(y) is desired curve which would be obtained if there were no instrumental broadening. g(z),z=x-y, is the curve representing instrumental broadening which is obtained from the standard. h(x) is the curve from the sample, containing both the desired broadening and the instrumental broadening (Fig. from Warren; 1969).

Deconvolution on the basis of Eq.(6.2) has been demonstrated first by Stokes [Stokes; 1984] for X-ray diffraction line profile analysis. The profile *f(x)* may be synthesized from the Fourier coefficients. For this, one has to designate a "cut-of" harmonic number : the Fourier coefficients with a harmonic number larger than the "cut-off" value are considered as unreliable. The result of a deconvolution should always be regarded with mistrust, and an arbitrarily small variations in *h(x)* may correspond to great changes in *f(x)* (unstable solution) [Delhez et al; 1982].

The other important method, which is employed in the next chapter is based on the basis of the "integral breadth", β , and the "full width at half maximum" (FWHM) , 2w.
The "integral breadth"; is defined as the breadth of a line with a square –topped profile of the same total area and peak height, it is obtained by dividing the total area by the peak intensity and 2w is the FWHM (full width at half maximum) which is the distance between the two points of the peak with half the its intensity, Fig.(6.2). In this method, it is generally assumed that the *h(x),f(x)* and *g(x)* profiles can be estimated by:

(I) Cauchy (Lorentzian) function

(II) Gaussian function

(III) Voigt function, which is the convolution of Cauchy and Gaussian functions.

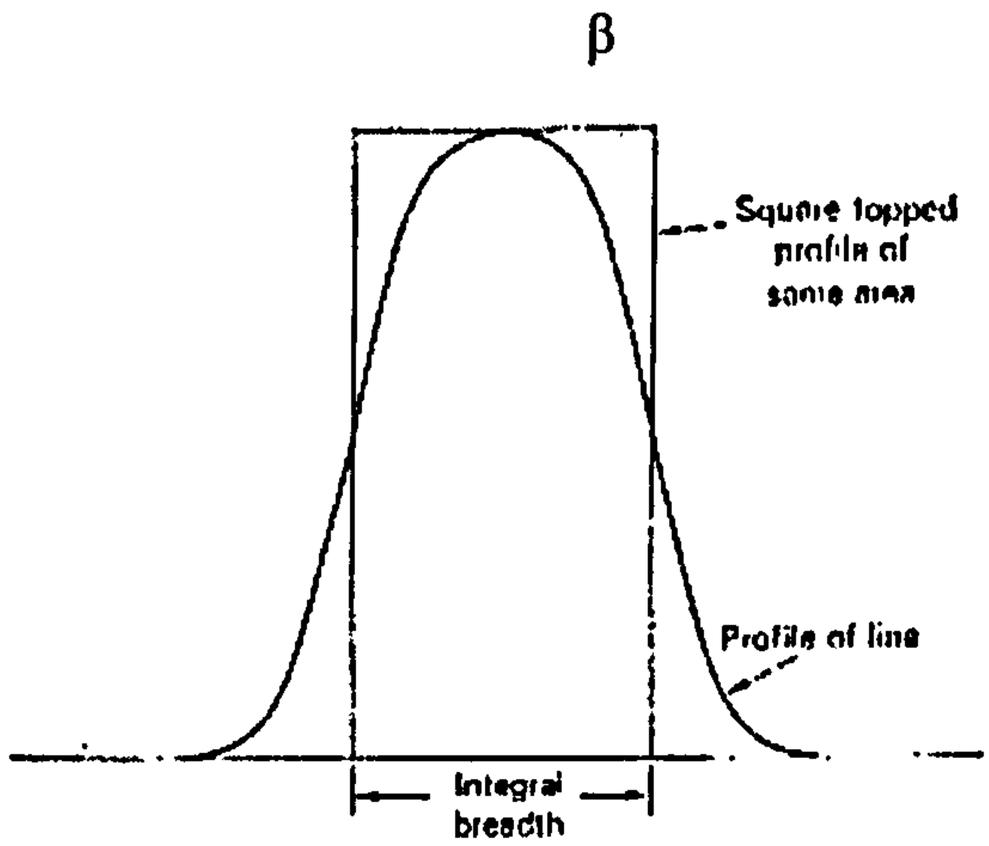

(a)

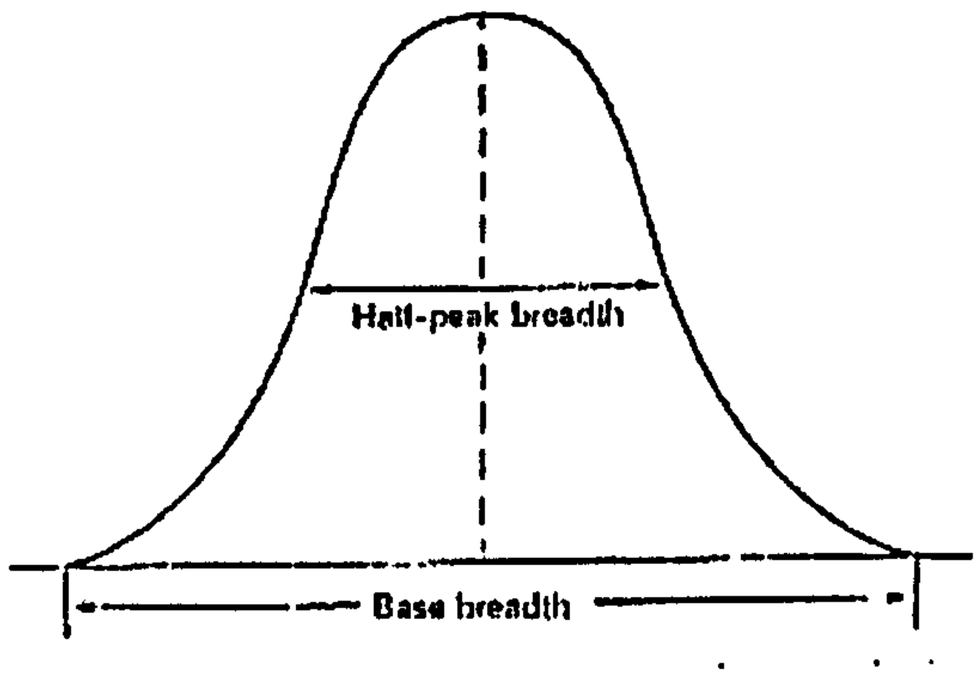

(b)

Fig. (6.2) a_ Integral breadth of a powder, β . b_ Half-peak breadth and base breadth for a powder line, FWHM (Fig. from Lipson & Steeple).

The Cauchy and Gaussian descriptions have been frequently used in the past.

Here deconvolution is accomplished by:

$\beta^f = \beta^h - \beta^g$; $2\,w^f = 2\,w^h - 2\,w^g$ (for the Cauchy case) (6.4)

$\beta^f = [\,(\beta^h)^2 - (\beta^g)^2\,]^{1/2}$; $2\,w^f = [(2\,w^h)^2 - (2\,w^g)^2\,]^{1/2}$ (for the Gaussian case) (6.5)

However, according to the present author's opinion the Voigt description is the more versatile and powerful one and should be preferred in practice. The necessary procedure for "deconvolution" is given below [Langford et al; 1978]. If *h*, *f* and *g* are assumed to

be Voigt functions then the Eqs. (6.4-5) follows for obtaining the Cauchy and Gaussian components of the deconvoluted f profile. The Cauchy and Gaussian constituents can be obtained from the ratios $2w/\beta$ ($= 2\Phi$; Φ is called the "Shape factor") for the h and g profiles by using the following empirical formulae:

$$\beta_c / \beta = 2.0207 - 0.4803 (2w / \beta) - 1.7756 (2w / \beta)^2 \qquad (6.6)$$

$$\beta_g / \beta = 0.6420 + 1.4187 (2w/\beta - 2/\pi)^{1/2} - 2.2043 (2w / \beta) + 1.8706 (2w / \beta)^3 \qquad (6.7)$$

where β_g / β and β_c / β are the Gaussian and Cauchy components of a Voigt function with the total integral breadth, β.

On the other hand :

$$2w/\beta = [(1+ k^2) / \pi]^{1/2} [-k\pi^{1/2} + (\pi k^2 + 4)^{1/2}] - (0.1889) \exp (-3.5) \qquad (6.8)$$

where $k = \beta_c / \pi^{1/2} \beta_g$

The maximum error induced by these equations is about 1 % [Delhez et al; 1982]. On the other hand, the R.M. needs a peak shape function to apply to each *hkl* reflection as well, and many brilliant Fourier coefficient description of diffraction profiles end up almost invariably as a pseudo-Voigt profile shape, certainly losing a bit of the original general sense by some assumption [Le Bail; 2000].

The pseudo-Voigt function is the sum of a Lorentzian, L(x), and Gaussian, G(x), in the ratio $\eta/ (\eta-1)$, where η is the " mixing factor". It is simpler to calculate than the true Voigt but the disadvantage is that the convolution of a pseudo-Voigt with another pseudo-Voigt is not itself a pseudo-Voigt.

$$\Phi(x) = A[\eta L(x) - (\eta-1) G(x)]$$

and $\beta = \eta\beta_l + (1-\eta) \beta_g = \eta \pi w_l + (1-\eta)(\pi \ln 2)^{1/2} w_g$

When modeling line profiles, w_l and w_g are usually made equal, but there is no reason a priori why they should not have different values. The pseudo-Voigt also includes the Lorentzian ($\eta = 1$) and Gaussian ($\eta = 0$) functions as limiting case [Wertheim et al;1974]. However, in pattern decomposition, parameters describing individual Bragg reflections are normally used, rather than the complete line profile [Langford; In *Defect and Microstructure* ...].

VI.2) CHARACTERIZATION OF MICROSTRUCTURES

Microstructural features which modify diffraction line profiles by a measurable amount have been broadly known to fall into three categories as "size effect", "microstrains" and "faults", so this approach will be followed here.

The size effects arise from the finite thickness in the direction parallel to Q_{hkl}, scattering vector, of domains over which diffraction is coherent. This can be the mean thickness of an individual crystallites (or grains, in a polycrystalline sample), but it can also related to a sub-domain structure, e.g. the mean distance between structural faults, the separation of the regions bounded by low angle grain boundaries.

The second category is based on a distortion of the crystal lattice, which amounts to a variation of *d*-space within (or possibly between) the domains. This can arise from microstrains, due to an applied or residual stress, or from a compositional gradient in the sample. In the terminology they are described as a "microstrain effect". It is not possible to distinguish these effects from each other by examination of the diffraction peak shape, and it needs some extra care and the use of some quite sophisticated methods.

Dislocations contribute to both categories of line broadening; there will be a "size" contribution due to their mean separation, inversely proportional to the dislocation density, and the microstrains effect arising from internal stress fields.

If structural "faults" are present, the arrangement of atoms varies in different regions of crystallite. This can arise during crystallization, or it can be introduced by some external influences, such as heat treatment, plastic deformation, adsorptions or radiation damages.

Strains can be expressed as ($\Delta d / d$) and the corresponding line broadening thus increased linearly with the order of reflections (section VI.2.2). Size and fault broadening, on the other hand, do not depend directly on Q_{hkl}, and this property can be used to identify and separate the contributions to the overall broadening arising from structural imperfections.

VI.2.1) Size broadening

In order to understand how the small crystallite size affects the width of powder lines, Bragg's Law has to be extended to cover the incomplete reinforcement of the waves scattered by successive lattice planes.

Bragg's law was deduced by finding the conditions under which the waves reflected from all planes in a crystal are in phase with each other. There will, however an appreciable amount of radiation scattered even when the law is not precisely obeyed. The possible deviation from the law is greater the smaller the crystal, and the reflections appear over a range of angle and are thus broadened.

This can be shown as:

A monochromatic beam falling on a set of *2m* lattice planes (Fig. 6.3) at an angle $\theta+\delta\theta$ and scattered at the same angle; $\delta\theta$ is the deviation from the correct Bragg angle θ for a particular reflection from the lattice planes. The path difference PBQ for waves scattered from successive planes is: $2d \sin(\theta + \delta\theta)$

The condition for total reinforcement of the waves is of course $\lambda = 2d \sin\theta$; but suppose that $\delta\theta$ is such that the plane *m+1* scatters 180° out of phase with the first; that is:

$$2md \sin(\theta+\delta\theta) = (m+1/2)\lambda$$

If this equation is true for the first plane and the plane *(m+1)*, it will also be true for any two planes with the corresponding separation, up to planes *m* and *2m*. Thus the crystal can be divided into two parts, the scattering from each of which will be 180° out of phase and so will cancel exactly. If $\delta\theta$ is small after expansion of the $\sin(\theta + \delta\theta)$ and using Bragg Law for *m* in-phase planes:

$$2md \sin\theta = m\lambda \qquad (6.9)$$

it is deduced:

$$\delta\theta = \lambda /(2t \cos\theta) \qquad (6.10)$$

where t (=2md) is the thickness of the crystal normal to the scattering vector.

This expression is not precise in view of assumptions made in deriving it (Warren & Stokes), but it gives the same order of magnitude as the expression obtained with rigorous assumption.

Von Laue (1926) has expressed the above equation in terms of the integral breadth, β_θ, of a line broadened only by small crystallite size:

$$\beta_\theta = K\lambda / (t \cos\theta) \quad (6.11)$$

where K is a numerical constant of the order of unity (Sherrer constant).

The broadening is particularly simple to express in terms of the reciprocal lattice. The reciprocal lattice is regarded as an array of points and since here the reflection condition is not met precisely so the reciprocal points must be considered as extended; for a spherical crystal with diameters, *t*, each reciprocal point will be a small sphere. Now distances from the origin in reciprocal space are equal to:

$$Q = 2\pi / d = (4\pi / \lambda) \sin\theta \quad (6.12)$$

so the diameter of the spots according to coherence thickness, *t* , is:

$$\delta Q = (4\pi / \lambda) \cos\theta \, \delta\theta \quad (6.13)$$

if $\delta\theta$ is replaced from Eq.(6.10):

$$\delta Q = \beta_c \, (\text{Å}^{-1}) = (4\pi / \lambda) \cos\theta \, [\lambda / (2t\cos\theta)] = 2\pi / t \quad (6.14)$$

This is independent of θ and therefore all reciprocal points will be broadened to the same extend (Fig. 6.4) shows by β_c (Å^{-1}).

It should be noted that all points, even zero order (0 0 0), are broadened and the broadness is inversely proportional to '*t*' [Lipson & Steeple; Interpretation of x-ray Powder Diffraction Patterns].

The mean thickness of a crystallite, measured for various directions [*hkl*], amounts to the generating of a 3-D representation of crystallites from 1-D diffraction data. If the domains are other than spherical, *t* will depend on the direction of the diffraction vector and the corresponding line breadths are then said to be "anisotropic", i.e. do not vary monotontically with 2θ or Q.

If the distribution of sizes is known, or can be ascertained, then the line profiles can be calculated for a given shape. However, this information is not normally available and individual reflections are approximated by fitting an appropriate analytical function. Thus, in order to determine the size and shape of domains over which diffraction is coherent, it is necessary to know the form of theoretical line profiles due to size effects and how well these are modeled by standard functions.

The shape factor, $\Phi = w / \beta$, gives an indication of the overall form of an intensity distribution, and it is always less than unity for diffraction line profiles. In fact, larger value indicate a rapid fall-off of intensity and smaller values are indicative of a slower decrease of intensity in the tails of line profile. In general, the frequently used Lorentzian model is not a good approximation unless $\Phi \approx 0.634$ [Langford; In *Defect and Microstracture...*].

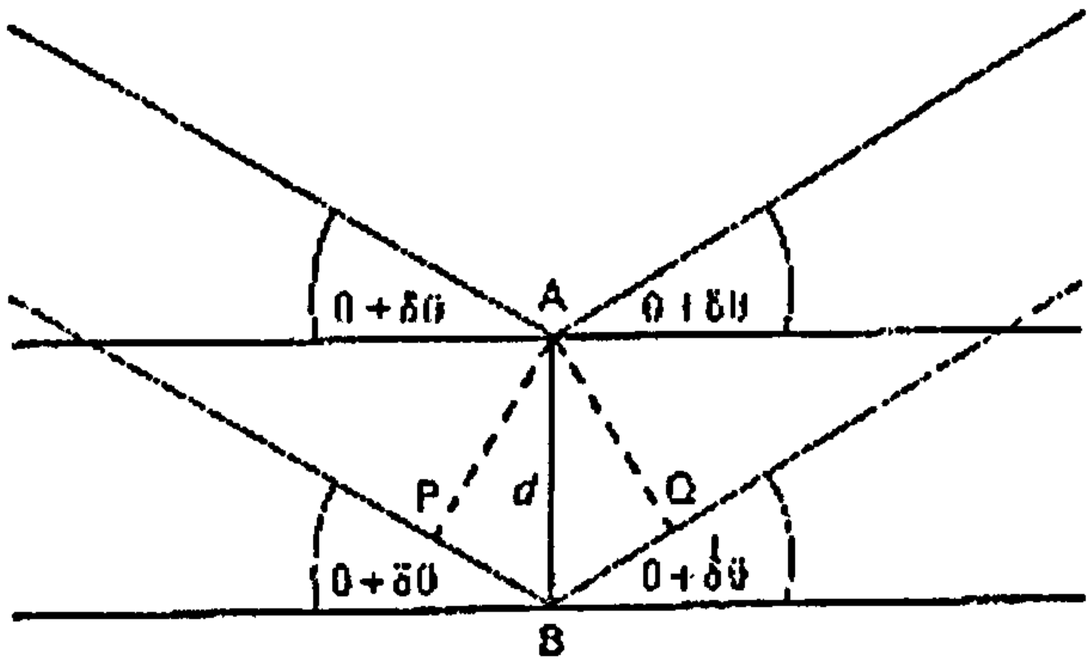

Fig. (6.3) Incident rays upon lattice planes with sight deviation from the true Bragg angle

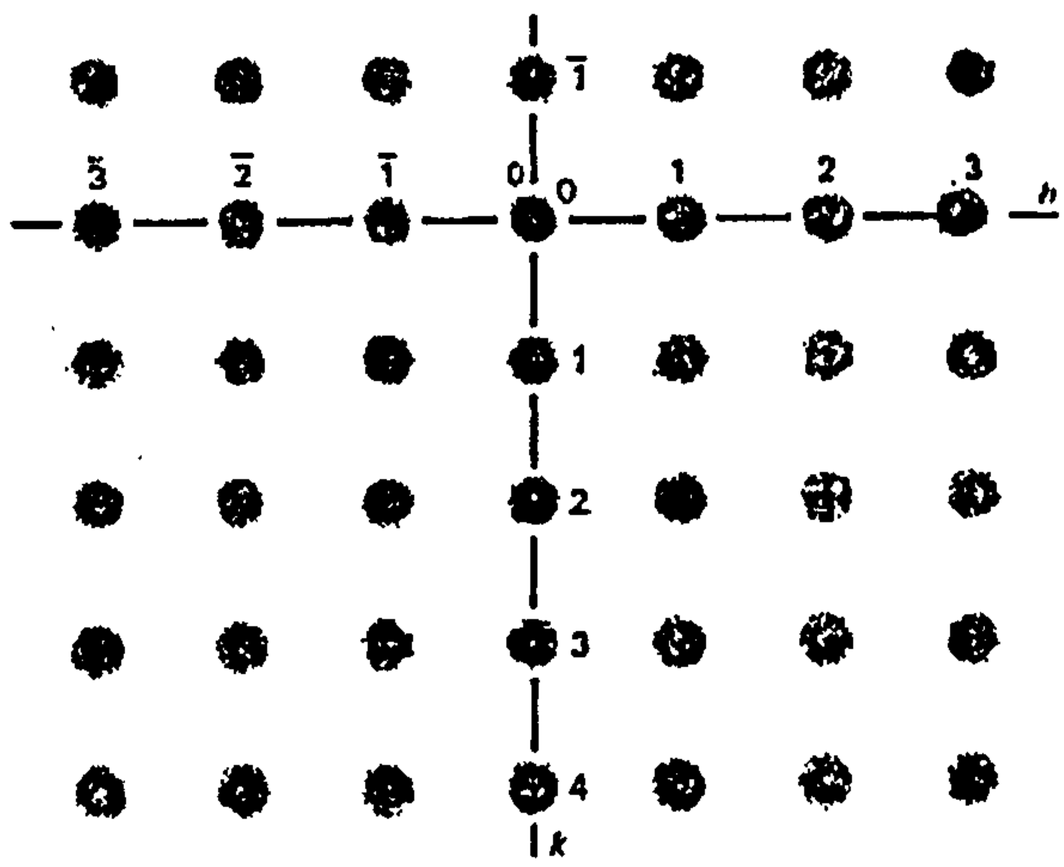

Fig. (6.4) Section of the reciprocal lattice of a small spherical crystal (Fig. from Lipson & Steeple).

VI.2.2) Strain broadening

To determine the diffraction broadening caused by lattice distortion, from Bragg's Law:

$$-(\delta d / d) = \delta\theta \ \mathrm{cotg}\theta \qquad (6.15)$$

so for one specified line, cotgθ may be regarded as constant and thus any measure of the spread of lattice spacing is equal to the product of cotgθ and the corresponding spread in the diffraction angle. Stokes and Wilson (1994) have shown that in this case:

$$\beta_\theta = K(\varepsilon) \tan\theta \qquad (6.16)$$

where $K(\varepsilon)= 2\eta$ (η called apparent strain) is a quantity that is independent of λ but which may be a function of h,k,l and $\varepsilon = \delta d/d$ which it is called "actual strain".

It is clear the strain broadening depends on the order of reflection (θ or d). Again in reciprocal space :

$$\delta Q = (4\pi/\lambda)\cos\theta \ \beta_\theta = (4\pi/\lambda)\cos\theta\,[K(\varepsilon)\tan\theta] = (4\pi/\lambda)K(\varepsilon)\sin\theta$$

so:
$$\delta Q = \beta_s\ (\text{Å}^{-1}) = K(\varepsilon)\,Q \qquad (6.17)$$

This is linearly dependent on Q.

Unlike the interpretation of diffraction effects from finite domain size, there is no general model to account for an observed apparent strain, η.

A common cause of lattice distortion is the presence of dislocations, but this is by no means the only source of microstrain. In so far as methods based on the integral breadth are concerned, it is customary to use the simple stress model considered by Stokes & Wilson (1944), in order to relate η to an actual strain, ε. In this model the strain is assumed to be isotropic on average and distributed according to a Gaussian error curve. Implicit in this model is that $\langle\varepsilon^2(n)\rangle$, denoting the average strain between two unit cells, n cells perpendicular to the diffracting planes, is equal to $\langle\varepsilon^2\rangle$, the mean square strain.

Diffraction is now considered as being coherent and: $\eta = 2\sqrt{2\pi}\left\langle\varepsilon^2\right\rangle^2 \approx 5\langle\varepsilon^2\rangle^{1/2}$, where $\langle\varepsilon^2\rangle^{1/2}$ is the root mean square [Langford; In *Defect and Microstructure*...,1999].

In general, lattice distortion is accompanied by, and must be separated from, other forms of structural imperfection. For this purpose, it is necessary to assume that the strain line profile has some analytical form. It is frequently to assume Gaussian, but as has been pointed out by Delhez et al (1993), in ***general there is no reason a priori why the line profile***

should be approximately Gaussian, or indeed any other particular shape. With an ideal powder, the statistical averages contain contributions from remote grains that are independent of each other. This allows one to reasonably assume that Gaussian distribution of strain at each crystal distance. The degree of column independence is likely to be more limited for deformed single crystals.

Strains in the vicinity of the grain boundaries become more intense. This is because the crystal periodicity is cut in this region and this can affect the higher order reflections (lower crystallographic plane distances) so if the ratio of the surface area of a crystallite to its bulk is high so can cause some remarkable deviation from the present Gaussian pre-assumption [Houska & Kuzel R; In *Defect and Microstructure*...,1999].

The approach to expressing the hkl dependence of the strain broadening as the generalized form, developed by Stephens (1996) which it is incorporated into GSAS recently. In this formulation the strain broadening represents as a multi-dimensional distribution of lattice metrics and the moments of this distribution determined the widths of each reflection. The anisotropic broadening contribution to the FWHM (in radians) of a diffraction line is given by:

$$\Gamma = [\sigma^2(M_{hkl})]^{1/2} \tan\theta / M_{hkl}$$

where M_{hkl} is the quantity that is dependent to the metric parameters and σ is the variance of M_{hkl}.

VI-3) WILLIAMSON-HALL PLOT

The first step in analyzing *f(Q)*, or parameters derived there from, in terms of sample microstructure in both Fourier and integral-breadth methods, is to ascertain the nature of any structural imperfections present. This is achieved from a plot of the total integral breadth (including size, faults and strains effects) $\beta_f(Å^{-1})$ versus Q.

The Williamson-Hall plot was introduced by Hall in 1953, and it is immediately apparent from this plot if there are both Q-independent and Q-dependent contributions to line breadths, since for the former, $\beta_f(A^{\circ-1})$ is the same for all orders of a reflection. It is also evident, from any scatter in $\beta_f(Å^{-1})$, which is greater than that expected from random errors, whether or not there is a direction or *hkl* dependence. This can be due to the shape of crystallites or domains, to the presence of faults or to anisotropy of elastic constants. Williamson-Hall plots can be interpreted as follow:

(a) Values of β_f lie on a horizontal line; so strain broadening is negligible and the crystallites are on average spherical.

(b) Values of β_f are the same for different orders of reflection, but vary systematically with lattice direction for different reflections; this means strain broadening is again negligible and the crystallite shape is not spherical. It is sometimes possible to deduce from the spread in β_f values whether the crystallites are prismatic or rod-like, are platelets or have some other form.

(c) The distribution β_f depends on *hkl,* but values, which may be zero for some reflections, do not vary systematically with Q or lattice direction; therefore broadening is due to "faults".

(d) Values of β_f lie on a straight line through the origin; so broadening is due to a distortion of the lattice, which is independent of direction.

(e) Values of β_f for different orders of reflection lie on a straight line through the origin, the slope of the lines varying systematically with lattice direction; hence there is a direction-dependent (anisotropic) strain broadening.

Samples, which only exhibit one of the above effects, are found to be very rare.

By using the Williamson-Hall plot, the type of structural imperfection present can usually be deduced and the strategy for further analysis of the data can be determined. In any study of microstructure, as many reflections are as available should be used.

It should be noted that in general the Williamson-Hall plot should only be used qualitatively, since the underlying assumption is that all the constituent profiles of *f(Q)* are Lorentzian , which will be valid rarely in practice [Langford; In *Defect and Microstructure* ...] .

Chapter VII

PHASE TRANSITION OF YBCO AT HIGH TEMPERATURE

(500°C to 600°C)

&

Twinning

Introduction :

The structural phase transition for YBCO at high temperatures shows entirely different characteristics to that at room or at slightly elevated temperatures (<400°C) which was studied in the chapter V.

Here, the oxygen dynamics are much faster. All the previous studies suggest a **second order** tetragonal (T) to orthorhombic (OI) phase transition, but the published *in-situ* neutron powder diffraction data, which cover that transition at this range of temperature, do not fully describe the **twinning** process which is an important aspect of this transition. It is well known that the properties influencing the current density, J_c, and the flux lattice density, Φ_B, in the cuprate high T_c superconductors are largely determined by the microstructure as observed on a length scale of some 100Å. Thus, for instance, the

twinning microstructure found in YBCO increases J_c by increasing the flux pinning effect, up to 10^5 A/cm^2 out to several Tesla [Civale et al; 1991] & [Kwok et al; 1991]. This length scale is clearly within the range of electron microscopy and of diffraction profile shape analysis, as measured using both x-ray and neutron diffraction methods [Shy D; 1996] & [David et al; 1989] and by electron microscopy, Fig.(7.1). Fig.(7.2) shows a schematic representation of the boundary between two adjacent twins.

Experimental measurements [Zhu et al; 1993] and theoretical studies [Salje et al; 1991] both show that, for most applications, the microstructure of the cuprate, is determined by the non-equilibrium treatment they have received during processing. This is not unwelcome, because it allows us to optimize the material through changes in the thermal history, in addition to any purely chemical changes. However, the whole process of optimizing this microstructure through control of the heat treatment can only be modeled through a detailed understanding of the processes involved. In this chapter, we report on efforts in this direction.

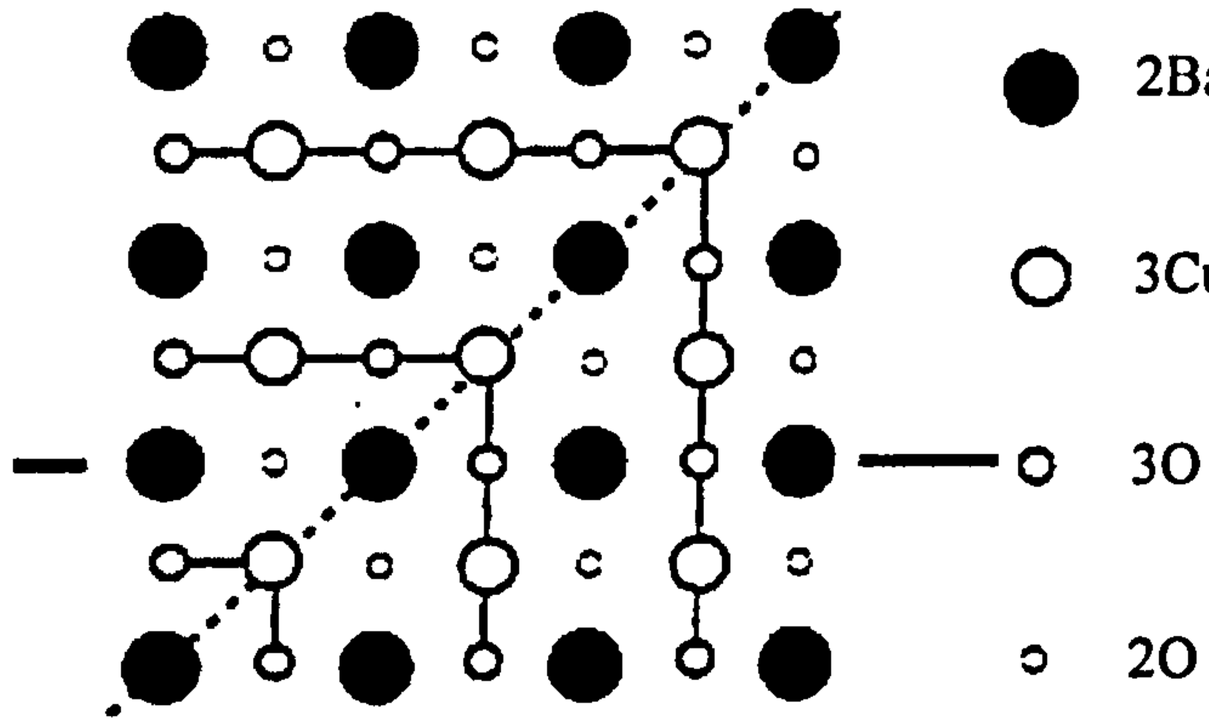

Fig.(7.2) A diagram of a twin boundary in $YBa_2Cu_3O_7$, each symbol represents a column of atoms perpendicular to the basal plane (from Beyers et al; 1989).

In general, one of the most significant features of crystalline microstructure that is controllable through appropriate annealing treatment is the domain size of a twin structure [Schmhal et al; 1989], produced as a result of a phase transition from a "para-elastic" phase (a high temperature phase with high symmetry) to a "ferro-elastic" phase (at lower temperatures with lower symmetry). The breaking of the symmetry generates elastic strains, which, in turn, drive the formation of a domain structure. Following the approach of Landau phase transition theory, we would expect to be able to define an "order parameter" in terms of the temperature, pressure and chemical composition of the sample that would quantitatively explain the transition process [Xu et al; 1989]. However, heat treatment in general produces microstructure that would not be in thermodynamic equilibrium under any conditions and to model such structure, in addition to describing the equilibrium structure, we need to be able to model the rate at which the structure would evolve towards equilibrium at any temperature.

In the case of $YBa_2Cu_3O_{6+x}$, $0<x<1$, the observed twinning results from the tetragonal (para-elastic) to orthorhombic (ferro-elastic) phase transition. Here, the order parameter is determined by the degree of oxygen ordering in the basal (Cu-O) plane. The values of the lattice parameters in this plane (*a* and *b*) depend on the fraction of Cu-Cu bonds that have

an oxygen on them - preferential occupation of one direction (conventionally the *b* direction) reduces the local strain energy. This process would determine the equilibrium structure for a free crystallite at low temperatures. In practice, however, the overall shape of the crystallite is constrained by its neighbors, so that the local strain is relieved by twinning along the (110) planes (both body diagonals of the *a b* rectangle have length $(a^2 + b^2)^{1/2}$). Equally, at higher temperatures, the introduction of twinning planes is a way of introducing disorder (entropy).

In this chapter, first (section VII.1) the very common features of the tetragonal to orthorhombic I phase transition are presented through three *in-situ* neutron powder diffraction isotherms at 500°C, 550°C and 600°C. Section VII.2, is dedicated to a quantitative analyses of the 600°C diffraction patterns as an example of the other isotherms measurements.

In Section VII.3, a simple model is presented for calculating the diffraction pattern, S(Q), from a twinned crystals by direct numerical Fourier Transformation. The objective of these calculations was to follow the development of the splitting in the peak as a function of the width of the twinned regions and the orthorhombicity, $S = 2(a-b)/(a+b)$). Section VII.4, then presents the results of the peak broadening analyses over the *in-situ* neutron and x-ray diffraction measurements performed during the evolution of the twin structure in YBCO.

Finally, in Section VII.5, the consistency between the model and experimental data and what this tells us about the evolution of the twinning structure, will be discussed.

i) Isotherms at 500°C- While keeping the temperature constant, the oxygen partial pressure (p.p.) was increased by the following steps: vacuum (~0.1 mbar), 1.5 mbar, 4.5 mbar, 5.5 mbar, 10 mbar, 18 mbar, 40 mbar and 150 mbar. The neutron diffraction data were collected at each pressure. To make sure of achieving thermodynamic equilibrium at each step, a long series of quick runs were performed, limited to a short d-spacing range to monitor the approach of the system to equilibrium. When there was a perfect match between the last three patterns, a full-range data set was collected. This procedure was employed after each pressure step as well. Because, to a very good extent, all measurements were performed at equilibrium conditions, the results were reversible, as some of them were repeated again at the end of each isotherm measuring stage.

Figure (7.4) shows the sequence of equilibrium diffraction patterns. The phase transition can be easily recognized by the broadening and splitting of some indicative reflections like the [*h00*] lines as they change from the original tetragonal pattern (under vacuum). Figs.(7.5_6) show the broadening and splitting of particular [200] and [100] peaks during the transition. Consistent with the data in chapter V, about the contraction along the *c* direction with increasing the oxygen content, Fig.(7.7) shows a lowering of d-spacing for the [004] peak as the sample absorbs oxygen and changes from tetragonal to the orthorhombic structures.

The most important feature of this transformation is the gradual peak broadening which arises because of the splitting effect but the resolution of the diffractometer (or sample broadening effects) makes it difficult to define the exact point of the splitting (second order T/O transition), but the fast reduction of the peak intensity after the transition, is a good indication (Fig.7.8).

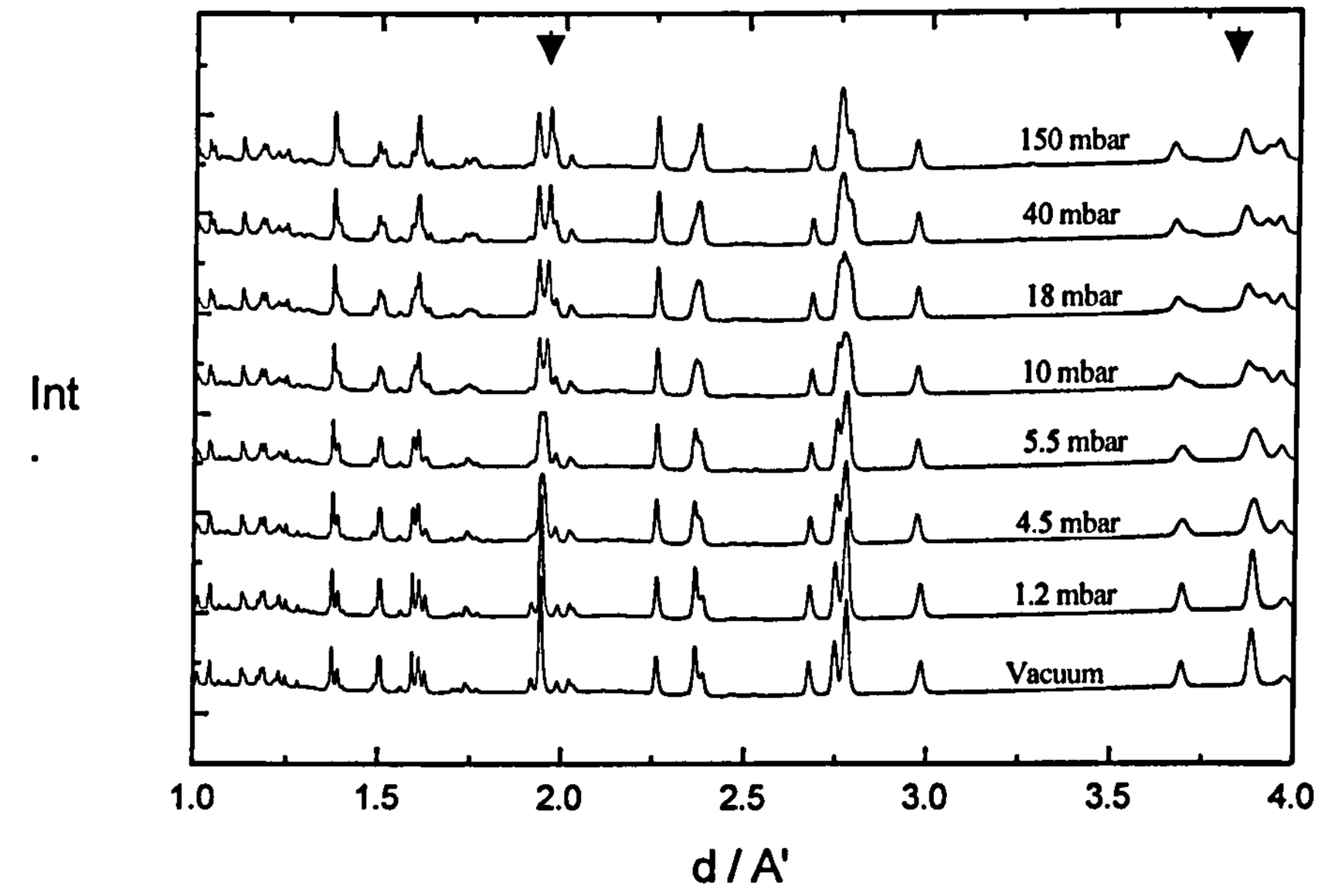

Fig.(7.4) A series of in-situ neutron diffraction patterns collected so as to show the phase transition at 500°C under different oxygen partial pressures. The arrows indicate two special [100] and [200] reflections (Figs.7.5_6)

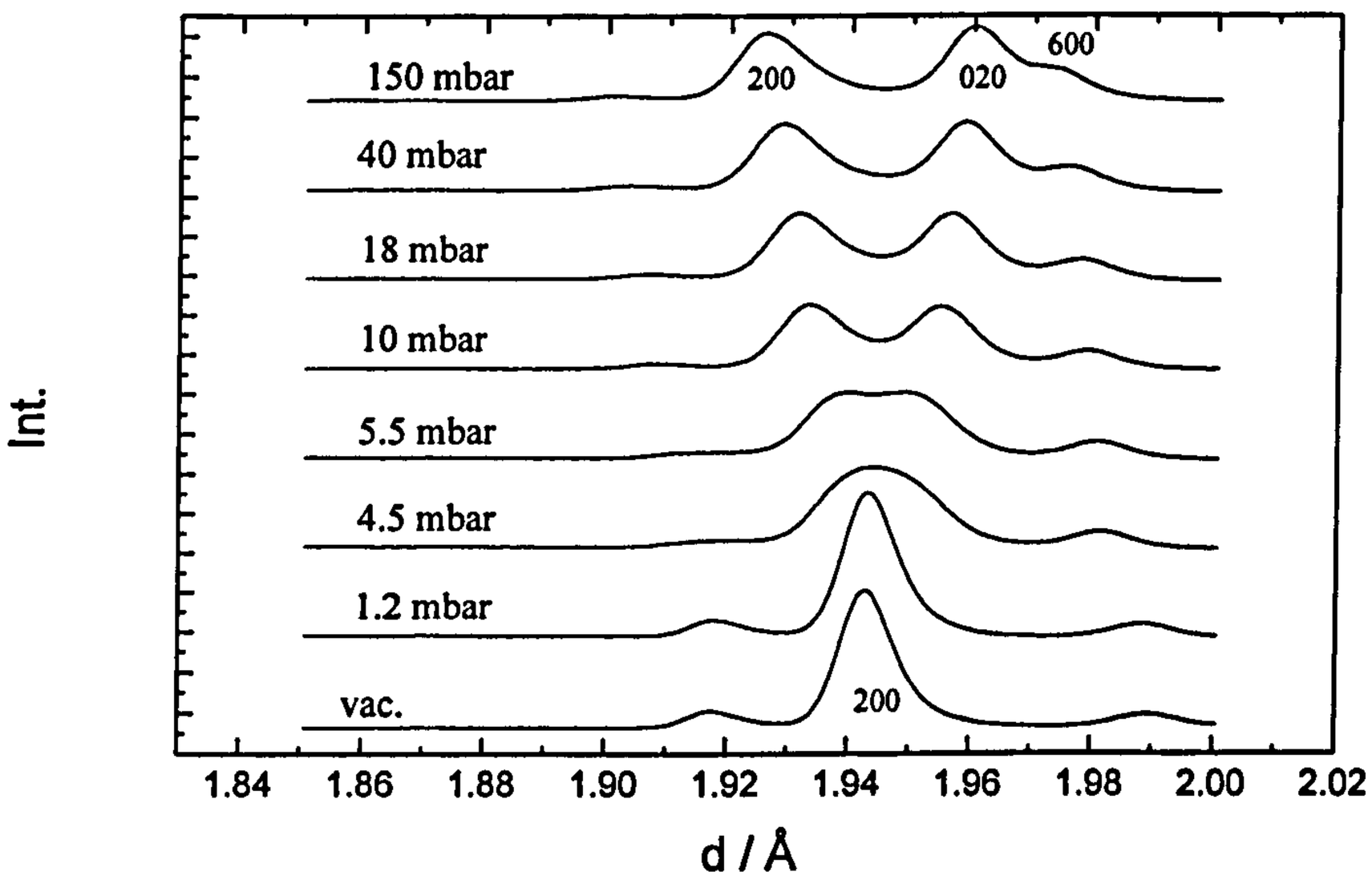

Fig.(7.5) Splitting of the [200] peak to [200] & [020] peaks after T/OI at 500°C

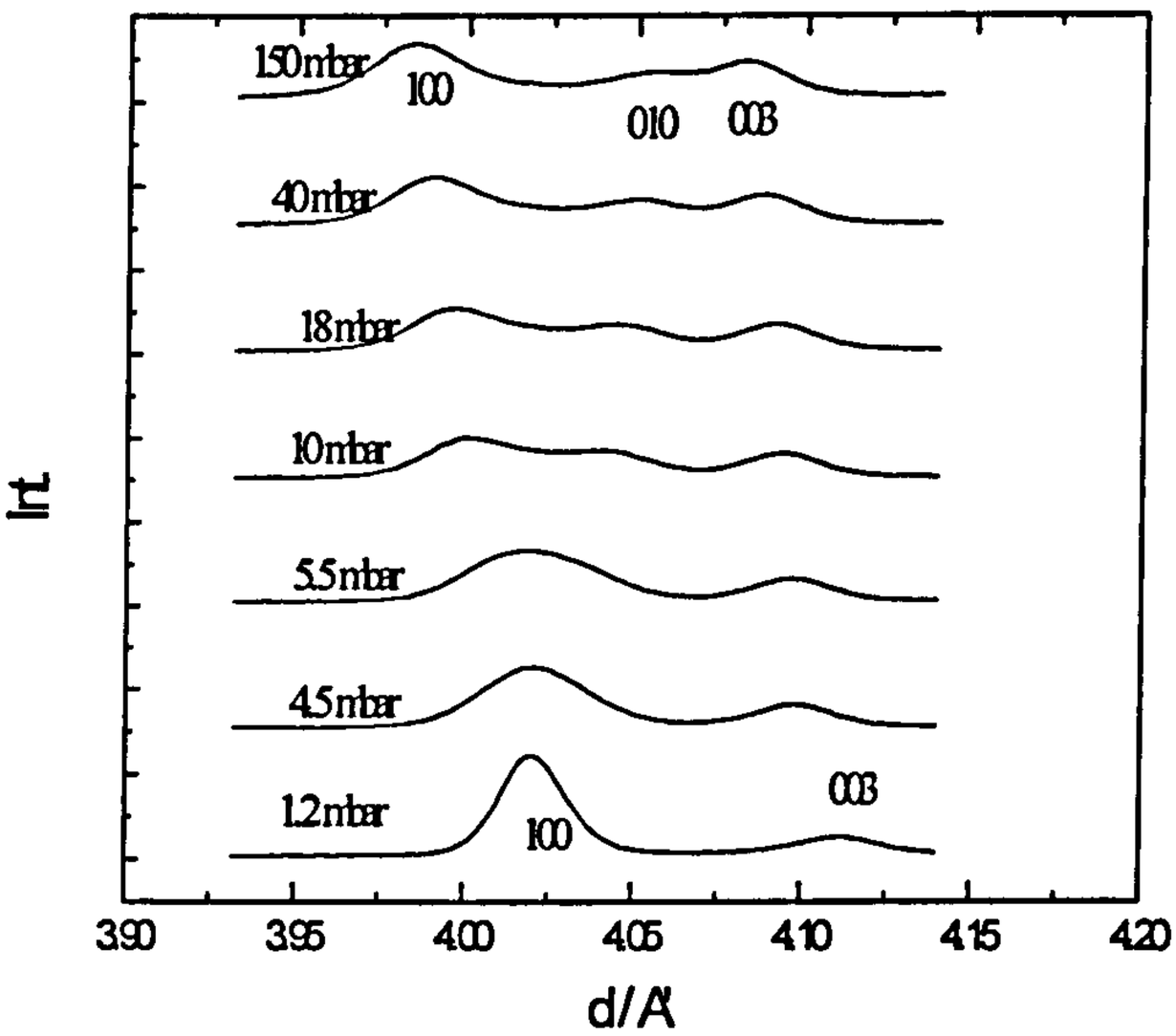

Fig.(7.6) Splitting of the [100] peak to [100] & [010] peaks after T/OI at 500°C

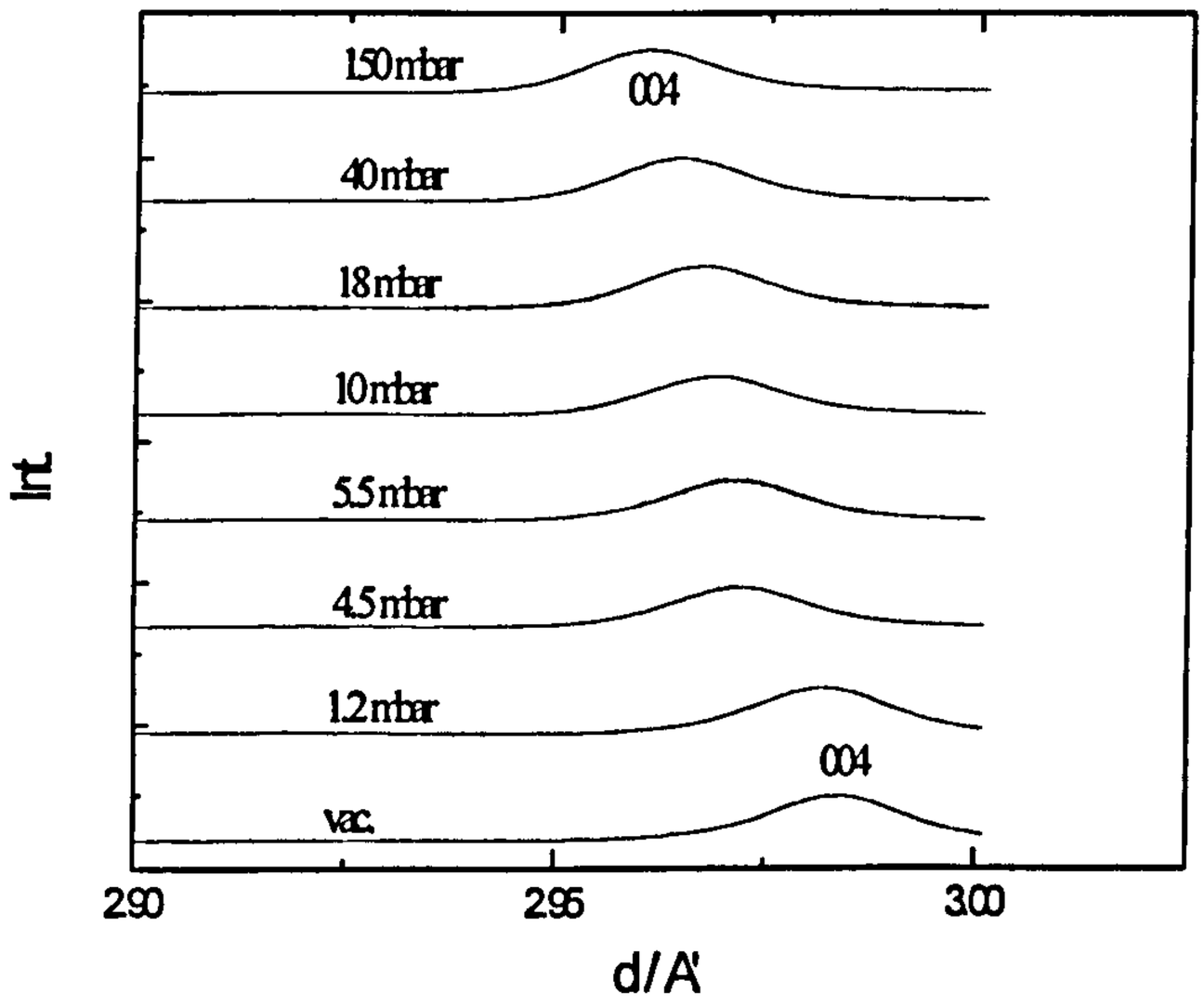

Fig.(7.7) The [004] peak's shift during T/OI, consistent with the contraction of *c* parameter

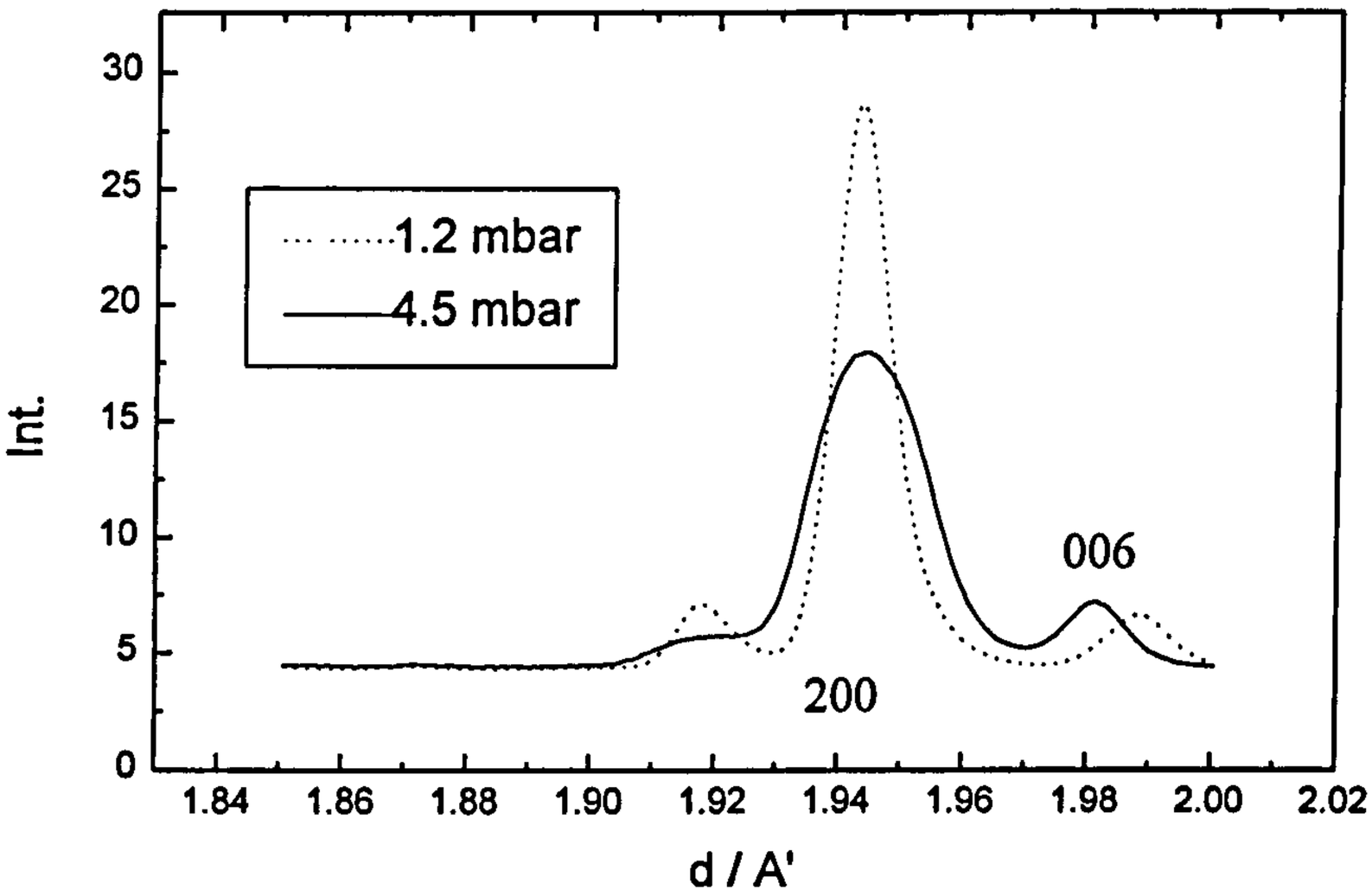

Fig.(7.8) Reduction of the intensity of the [200] peak after the phase transition at 500°C. The area of the peaks before and after the transition remains fairly constant. In fact, the broaden peak comes from two very close separate peaks [200 & 020].

This feature is exactly consistent to what we expect from a **second order** phase transition, in contrast to a first order transition (chapter V). During a 1st order transition the intensity of the initial phase peaks reduce whereas the intensity of a series of entirely new peaks goes up gradually as the sample passes through a mixed phase region.

As a significant feature of this *in-situ* data set, it should be noted in the 5.5 mbar pattern that, although the splitting for the [200]&[020] peaks is obvious, it is not apparent for the [100]&[010] reflections (Figs.7.9 & 7.6). This is consistent with the interpretation of reflections from twinning region in reciprocal space (described in section VII.3).

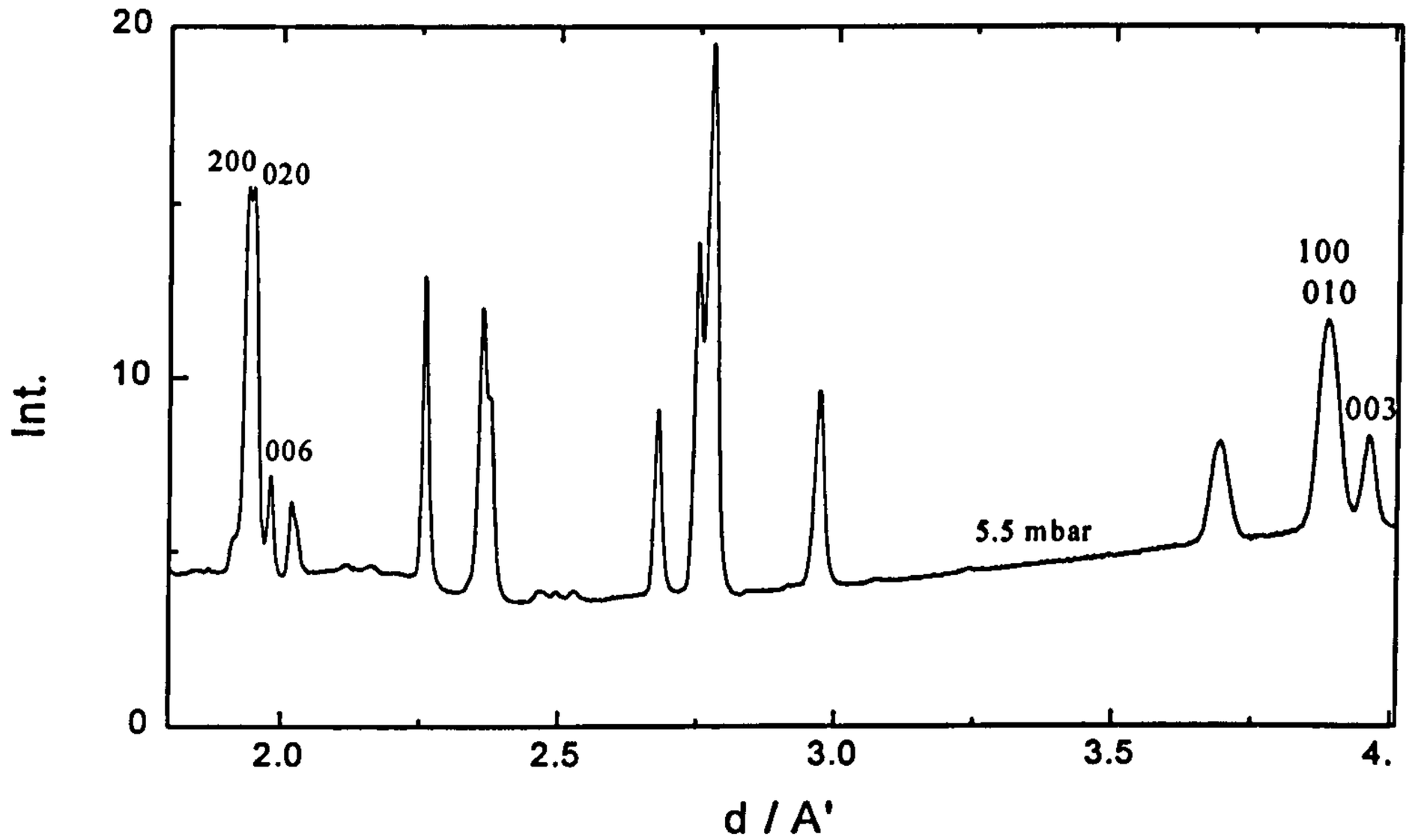

Fig.(7.9) **A** comparison of the splitting for [200] & [020] and [100] & [010] reflections at 500°C

With inspection of the [200] & [020] peaks in Fig.(7.6), it is clear that the T/OI transition at this temperature, must occurs between 1.5 to 3.0 mbar of oxygen p.p. whereas Mercer; 1997, suggests changes in the structure happen at about 4 mbar oxygen p.p. and Schleger et al; 1991, suggests at about 1.5 mbar oxygen p.p. for the T/OI transition at this temperature.

ii) Isotherms at 550°C – Similar data to the above results has been collected for points on the isotherms at 550°C (Fig. 7.10):

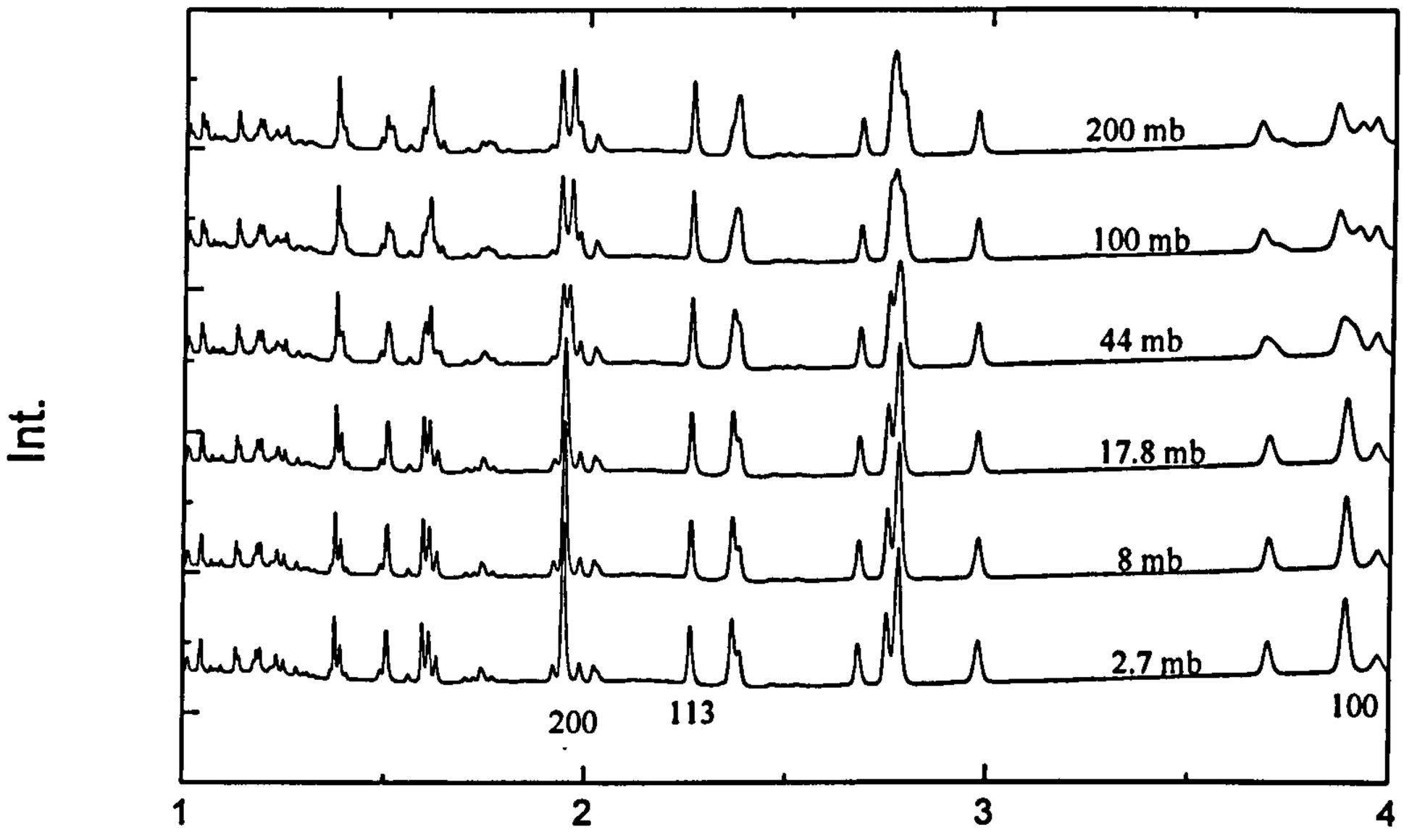

Fig.(7.10) Isotherm diffractions at 550°C

This series of patterns suggest that the T/OI transition for oxygen partial pressures takes place between 8 and 17.8 oxygen mbar (Mercer; 1997, suggests ~ 9.0 mbar and Schleger et al; 1991, suggests ~ 8.0 mbar of oxygen p.p).

By comparing the [*hhl*] peaks to the other peaks, we note for instance, that the intensity and the sharpness of the [113] peak remains intact during the T/OI transition, as a result of the twining in the basal plane, (this aspect is fully discussed in section VII.4).

iii) Isotherms at 600°C_ The measurements at different oxygen p.p. (vacuum, 40, 150, 200, 250, 300, 450, 750 mbar) at this temperature led to similar results as shown in Fig.(7.11) for some selected patterns.

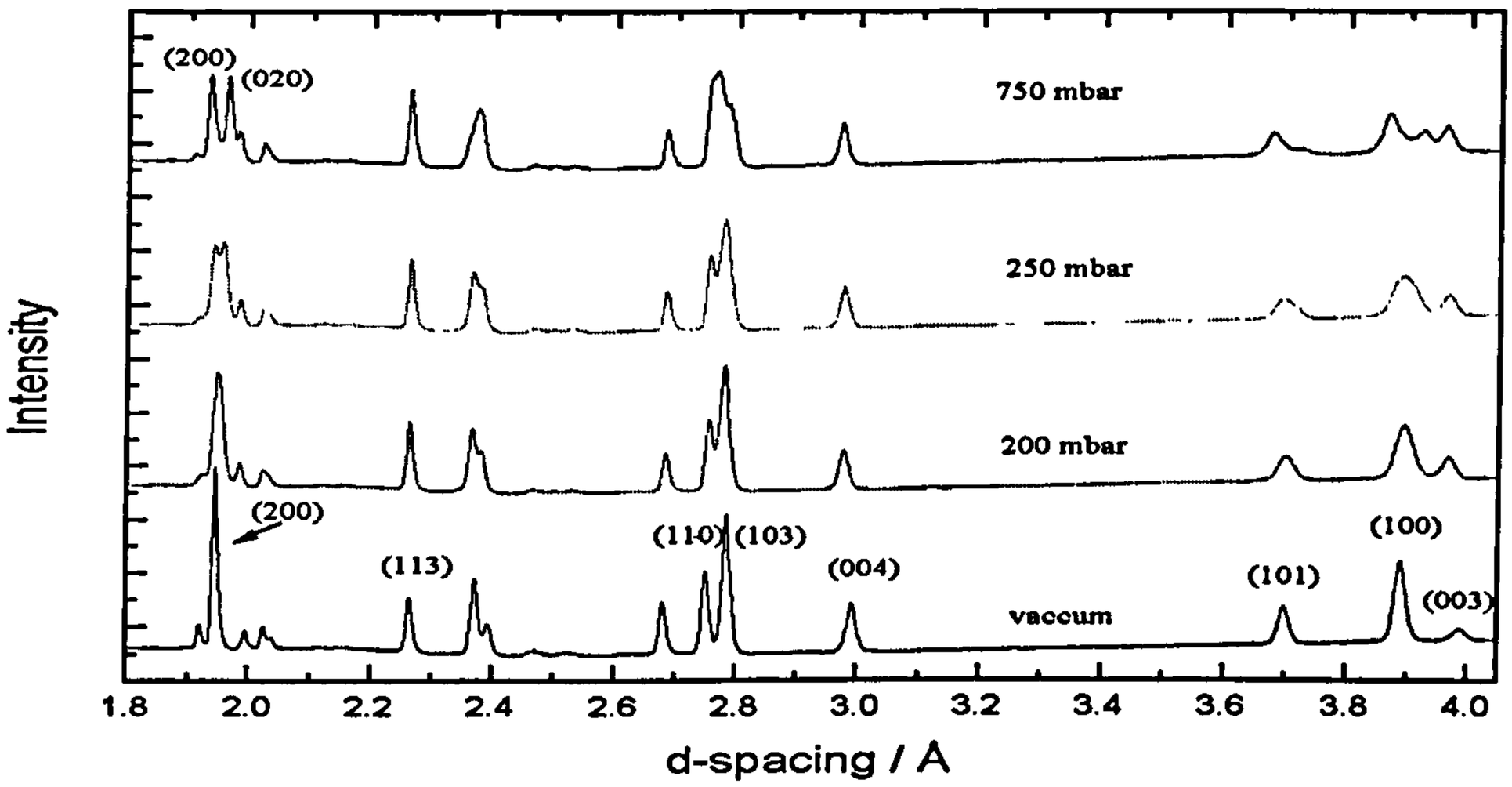

Fig.(7.11) Isotherm diffractions at 600°C

At this temperature, we made extra measurements on the very interesting high d-spacing region about 12 Å in particular to observe the [001] reflection (Fig.7.12).

Figure (7.12) shows a clear broadening of this line, consistent with the evolution of the [004] peak at 500°C (Fig.7.7). It is believed that the main factor in determining the peak width of the [00l] reflections along the *c* direction are the strain broadenings caused by stacking different oxygen deficient orthorhombic layers. Fig.(7.13) shows a side view of an oxygen deficient unit cell indicating that the occupancy probability of oxygen effects the *c* parameter.

VII.2) THE 600°C ISOTHERM ANALYSIS

Further analysis on the 600°C isotherm data, via the full pattern refinement (GSAS)[1] has been performed to study the structural (lattice parameter & site fraction occupancy) and microstructural aspects of the twins formation. The first pattern (Fig. 7.14) belongs to the pure tetragonal phase state of the sample at vacuum (~ 0.1 mbar) as a reference (equilibrated after 15 quick runs; each lasted 4min.). Table (7.1) shows the refined atomic positions in the tetragonal unit cell model:

The goodness of the refinement indicated by :

$\chi^2 = 47$ and $R_p = 0.019$

The lattice parameters are:

$a = 3.873 \pm 0.001$ Å ; $b = 3.873 \pm 0.001$ Å and $c = 11.918 \pm .003$ Å

The average oxygen site fraction in the basal plane:

$O_{15} = 0.082 \pm .0015$

Therefore the oxygen concentration is : $x \sim 0.16$

Atom	Occupancy	x	y	z	
Y	1	0.5	0.5	0.5	
Ba	2	0.5	0.5	0.1923	
Cu(1)	1	0	0	0	
Cu(2)	2	0	0	0.3605	
O(2)	4	0	0.5	0.3770	
O(4)	2	0	0	0.1550	
O(15)	0.08	0	0.5	0	

Table (7.1) A table showing the results of the Rietveld refinement performed on the sample at tetragonal phase (600°C & vacuum).

[1] Chapter V

When the oxygen partial pressure is raised to 150 mbar, the pattern from the equilibrated sample (after 53 quick runs; each 4min) starts to show peak broadening as a result of the T/OI transition, because the orthorhombic model (Table 7.2) refinement gives a better fit (Fig. 7.16) than the tetragonal model. The results of the refinement is:

$\chi^2 = 90.85$ and $R_p = 0.0262$ (whereas for the tetragonal model: $\chi^2 = 97.16$ and $R_p = 0.032$)

The lattice parameters are:

$a = 3.879 \pm 0.0009$ Å ; $b = 3.890 \pm 0.0009$ Å and $c = 11.873 \pm 0.0009$ Å

The average oxygen sites fraction in the basal plane:

O(1) = 0.4832±0.012 O(5) = 0.1664±0.004

Therefore the oxygen concentration is : x ~ 0.65

Atom	Occupancy	x	y	z	Thermal factor
Y	1	0.5	0.5	0.5	0.0084
Ba	2	0.5	0.5	0.1905	0.0116
Cu(1)	1	0	0	0	0.0180
Cu(2)	2	0	0	0.3594	0.0080
O(2)	2	0.5	0	0.3796	0.0010
O(3)	2	0	0.5	0.3759	0.0145
O(4)	2	0	0	0.1538	0.0353
O(1)	0.4832	0.5	0	0	0.0238
O(5)	0.1664	0.5	0	0	0.0925

Table (7.2) A table showing the results of the Rieveld refinement performed on the sample after transition to the orthorhombic phase (600°C & 150 mbar).

VII.3) TWINNING; THE MODEL

The model employed for the numerical simulations of diffraction from twins is based on the simple geometric arrangement of the atoms shown in Fig.(7.28), which is, nevertheless, sufficient to determine the salient features introduced by the twinned structure into the elastic scattering function, S(Q). In this simple model, the role of the oxygen atoms is to lengthen the *b* lattice parameter of the orthorhombic perovskite unit cell relative to the *a* parameter, to convert the structure from tetragonal to orthorhombic during the oxygen absorption process. The difference in *a* and *b*, in turn, produces a strain field which is represented by the orthorhombicity parameter, *S*, (*S*= 2(a-b)/a+b)). This elastic strain is best accommodated by forming twin boundaries perpendicular to the <110> direction. In a realistic model, the wall thickness between the twins would probably be some Å s. However, it is clear that the assumption here - that the twinning is completed in a single plane - will not significantly affect the calculated shape of the Bragg reflections, because the effect of a finite twin wall thickness would be merely to create additional broad diffuse scattering extending between the Bragg reflections [Locherer et al; 1996]. While the widths of the twinned regions are known to be fairly regular at ambient temperatures (transmission electron micrographs [Schmhal et al; 1989], [Xu et al; 1989]), we would expect them to show statistical fluctuations at higher temperatures. However, such fluctuations would just have the effect of smoothing the calculated shapes.

For simplicity in the 2D model (calculation), the twin's walls (in real space) are parallel to the $<\bar{1}10>$ direction and the distance between (110) planes is shown with "*l*". The twin's separation "T", is equal to the number of (110) planes, m, times by "*l*" (T = m×*l*, where m= 10, 20 30, 50, 70 in this study).

On the other hand, as is clear in the E.M. pictures (Fig.7.1), twinning makes the basal plane layers stripe-like pattern, which in this model the length of those stripes "L" (parallel to the $<\bar{1}10>$ direction) specified by another arbitrary integer times $R(=(a^2+b^2)^{1/2})$: L=n×R (in here n=100)

The elastic scattering function, S(Q), is first calculated in 2D for the **single crystal representation** (s.c.r), using the following expression:

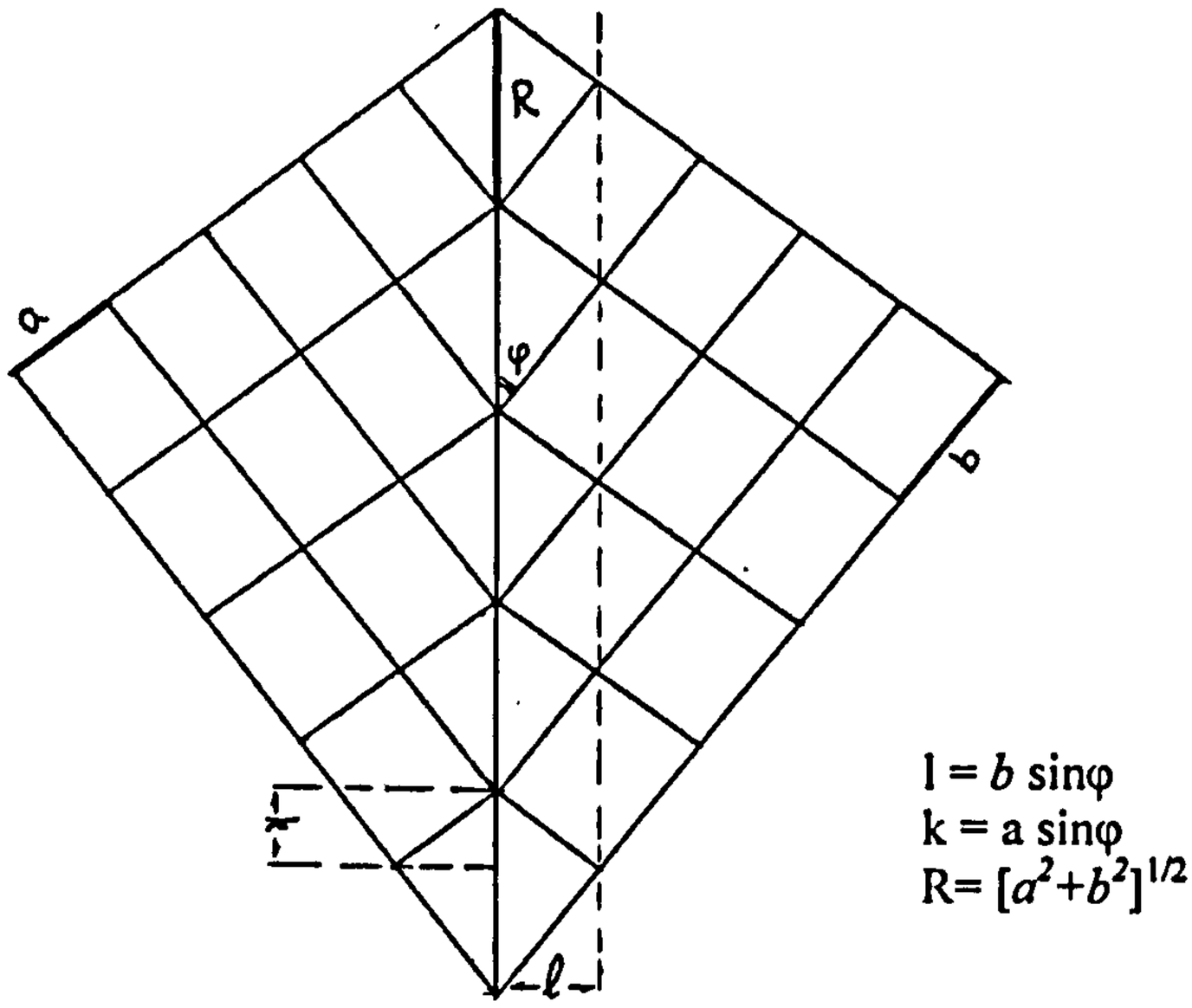

Fig.(7.28) The simple geometric model of two adjacent twins in the basal plane. In this model the sites of the Cu atoms are in the corners of the cells and the role of the oxygen atoms is just to lengthen the *b* parameter over *a*. Therefore the model can predict the main peculiarities of the diffraction pattern such as peak positions, the broadening and splitting of reflections, but not the relative intensities.

$$S(\vec{Q}) = \frac{1}{N}\sum_i \sum_j < \exp\{i\vec{Q} \bullet (\vec{r}_j - \vec{r}_i)\} > \qquad (7.1)$$

where $\vec{Q}$ is the scattering vector in the reciprocal space and $\vec{r}_j, \vec{r}_i$ are the scattering points

in the real space.

Here in the reciprocal space ,**Q** (=Q_x **i** + Q_y **j**) is the scattering vector parallel to the basal plane (Q_x is taken along the <110> direction), N is the total number of cells in the basal plane and the **r** vectors represent the position of the cell's corners (the Cu atoms). There is no need to model the actual atomic positions within the unit cell as we are not interested in predicting the structure factor, merely the general shape of peaks are under consideration[Turchin; 1965]. The corresponding S(Q) for a **powder pattern**

representation, p.p.r, can then be determined by integrating S(Q) over a circle of constant Q.

In this model, *S* is the orthorhombicity, (not be confused with the scattering function) and the total atomic sites in the model is N(=n x m). The general behaviour of the diffraction pattern can be inferred from the contour plots shown below for the [200], [020] reflections.

In the following plots, T is kept constant while *S* is varied. For T= 50 and L=100, Fig.(7.29_a) shows the [200] peak for the case of *S*=0 (or a=b, the tetragonal case) in the s.c.r. Here, the intensity pattern is in the form of a cross with a strong central peak. Consequently, the corresponding powder pattern also only shows a single peak with low intensity wings Fig.(7.29_b). The presence of diffuse scattering like feature in the wings is simply a matter of finite-size effects and it will be reduced for bigger size matrix calculations.

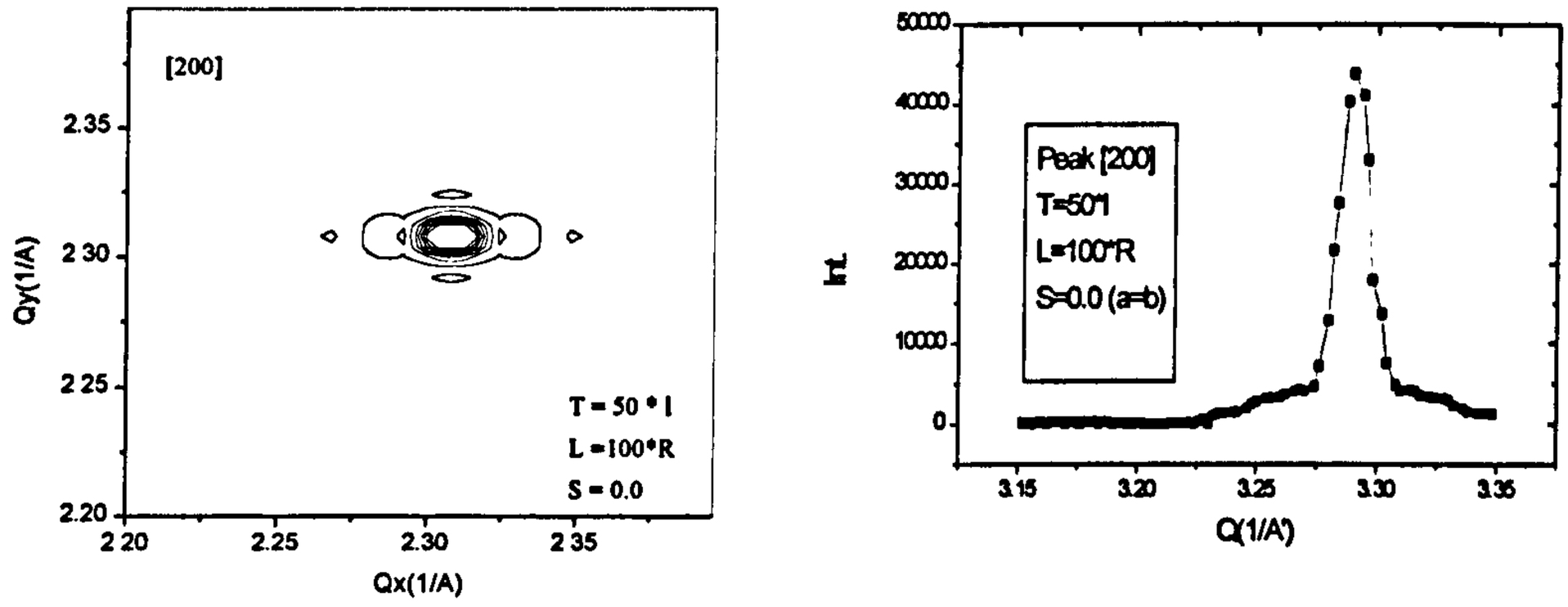

(a) **(b)**

Fig.(7.29) a_A single crystal presentation (s.c.r) for the [200] peak in the tetragonal phase. b_ the (p.p.r) for the same reflection.

As *S* increases by stages *S* = 0.003; 0.08; 0.013 (Figs. 7.30a_c), the [200] and [020] patterns gradually resolve themselves into two separate peaks and finally in Figs.(7.31) and (7.32) for *S*=0.018 and T=50**l* or T=70**l*, the splitting is quite clear. These patterns are just the superposition of the diffraction peak for each individual twin as in Fig. (7.33).

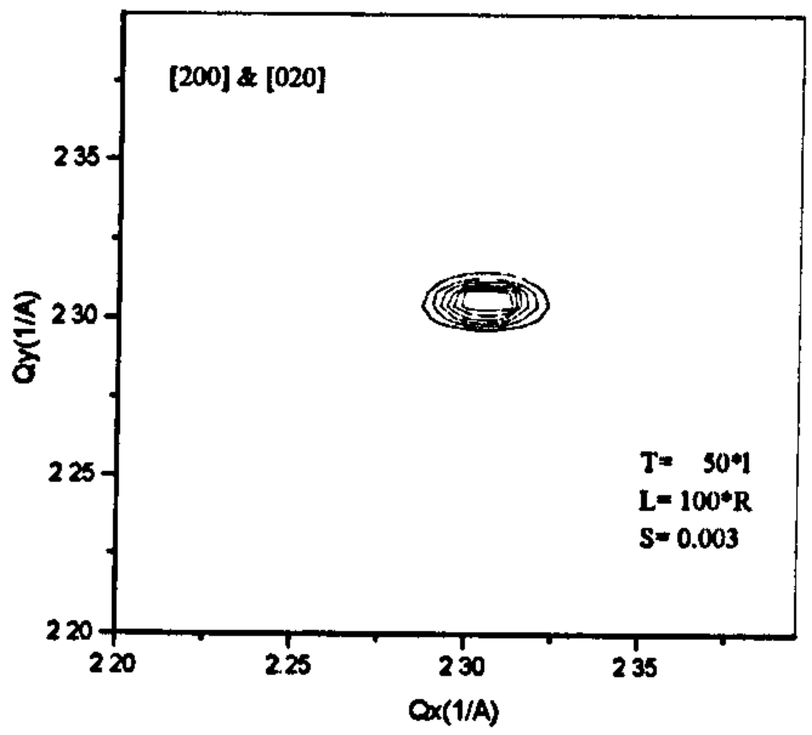

Fig.(7.30a) s.c.r for *S*=0.003 & T=50x*l*

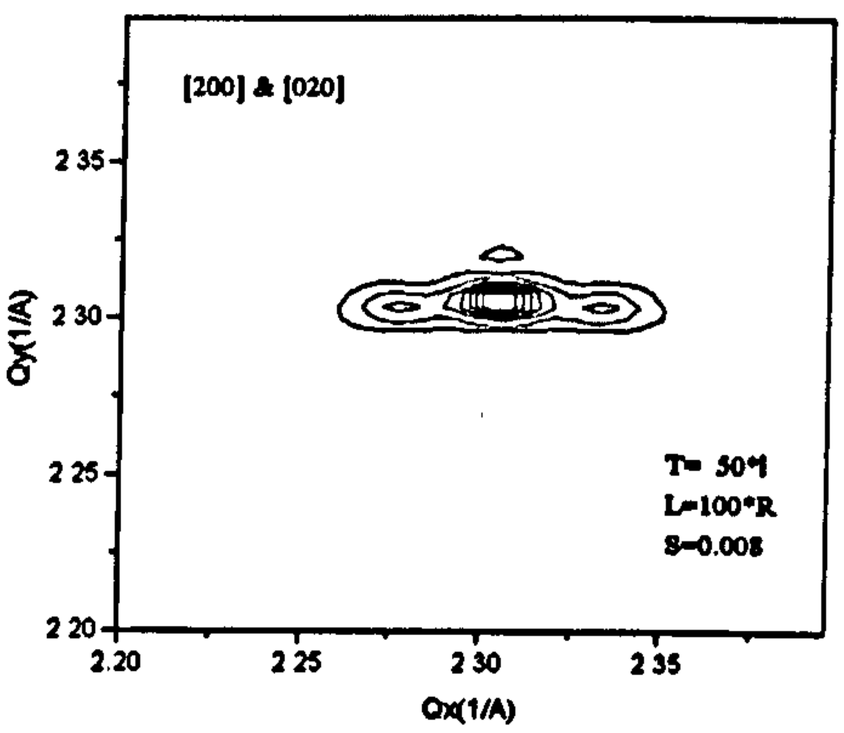

Fig.(7.30b) s.c.r for *S*=0.008 & T=50x*l*

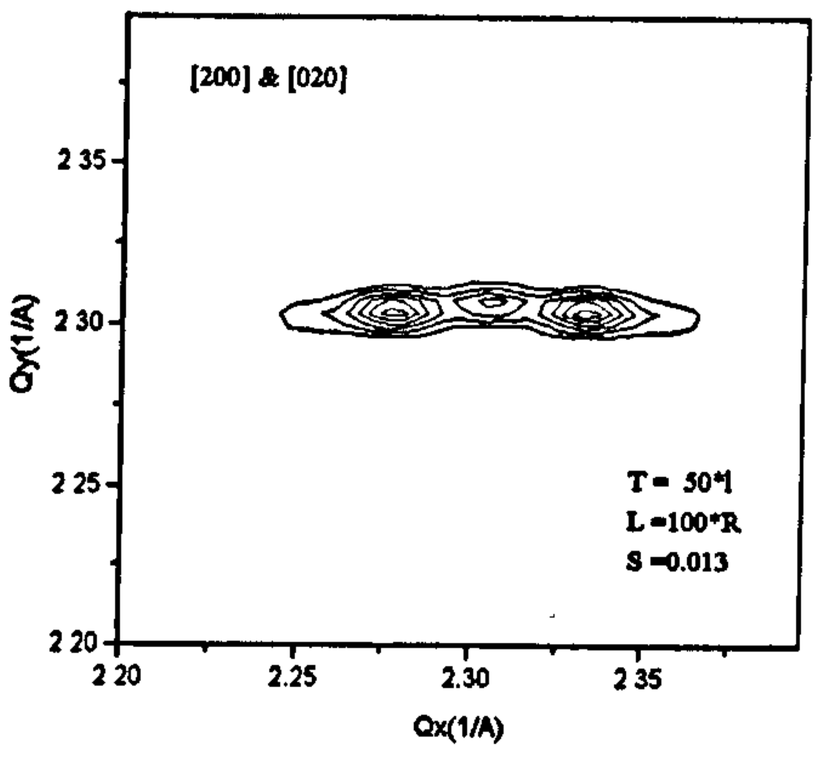

Fig.(7.30c) s.c.r for *S*=0.013 & T=50x*l*

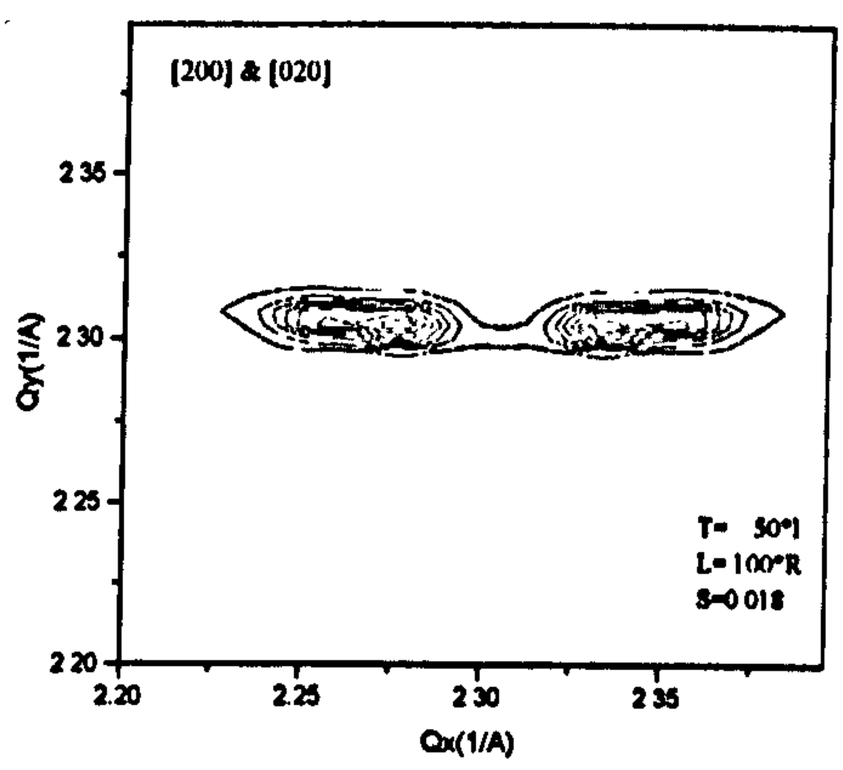

Fig.(7.31) s.c.r for *S*=0.018 & T=50x*l*

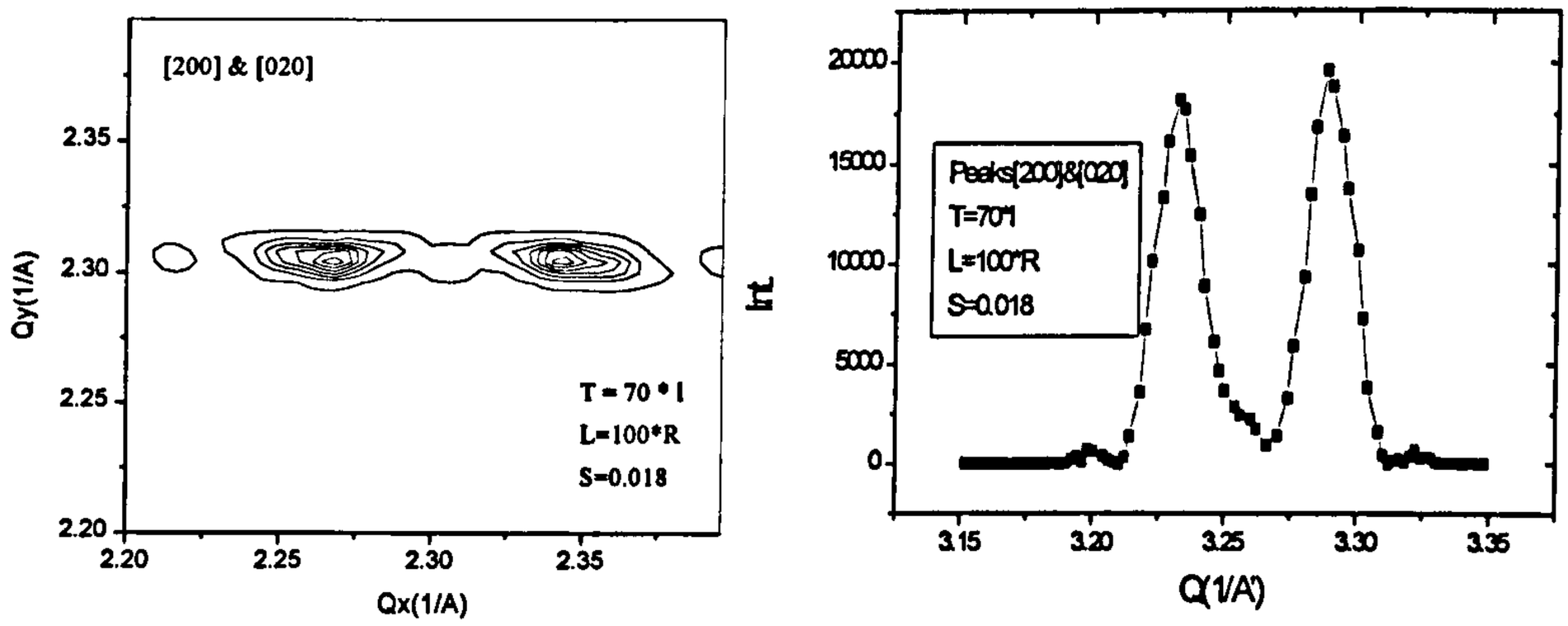

(a) **(b)**

Fig.(7.32) a_ s.c.r for S=0.003 & T=70xl, b_ p.p.r for S=0.003 & T=70xl , the two [200]&[020] peaks are entirly resolved

Based on the existing theory of twinning [McIntyer et al; 1989], [Zhu et al; 1993], as Fig. (7.33) shows, no splitting is observed for [$hh0$] reflections and the highest degree of splitting occurs for the [$h\bar{h}0$] reflections along the direction parallel to the twin plane ,<P>. On the other hand for each series of [hkl] spots, the separation would be stronger the greater the order of the Miller indices. Figures (7.34), (7.35) and (7.36) show the consistency of the results of the model's calculation with the predictions of the theory and the results of the TEM data [Xu et al; 1989] & [Saikaya et al; 1988]. The separation of the peaks is proportional to S, the width of the peak normal to the twinning plane (Q_x) is inversely proportional to T, while its width parallel to the plane, (Q_y) is inversely proportional to L, the length of the twin plane.

It is clear that the (p.p.r) version will also evolve from a single peak to split peaks. The additional modulation in the contours comes from the harmonics generated by the twins and would presumably be averaged out by statistical fluctuations in the twin separation.

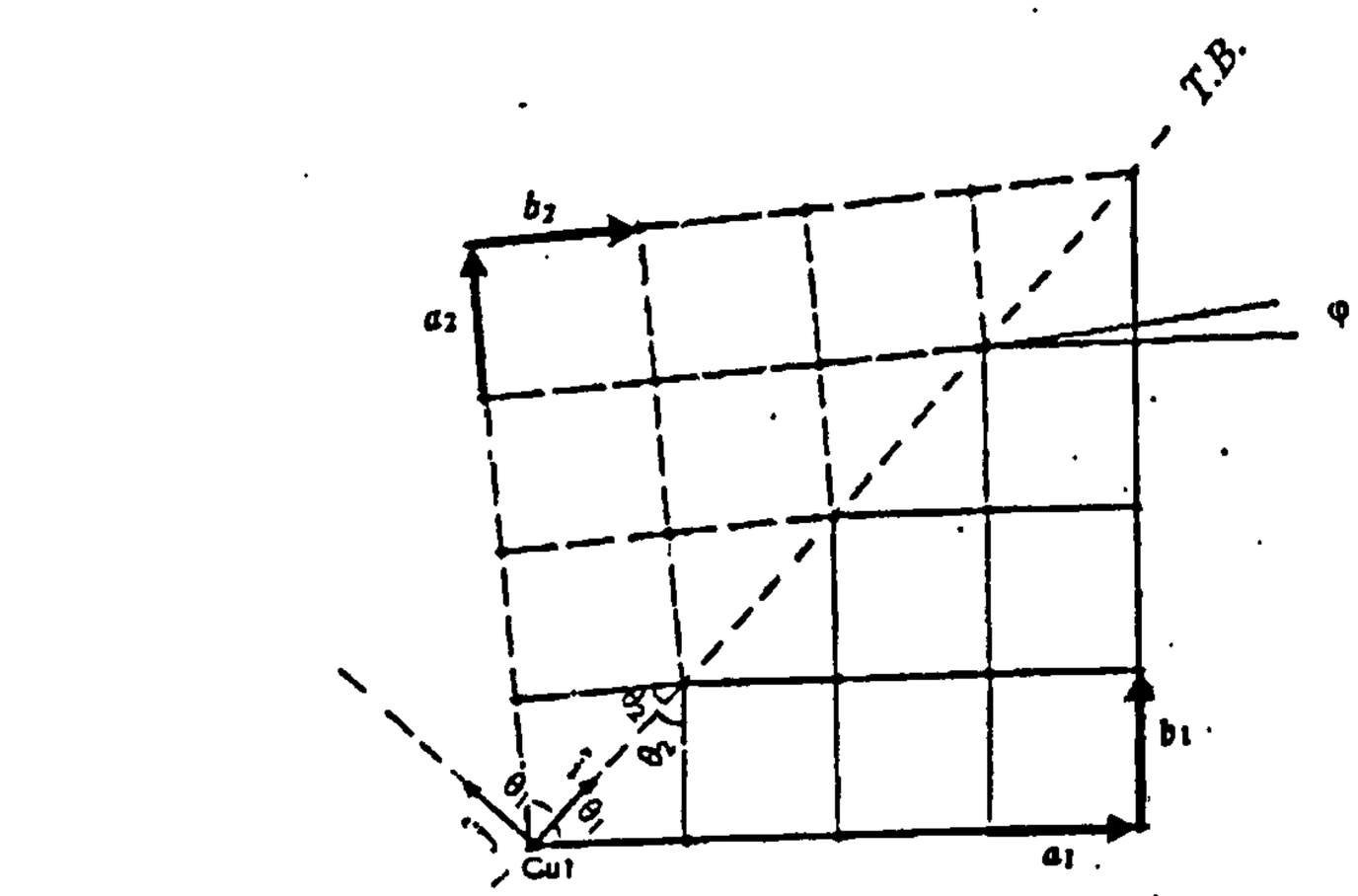

(a)

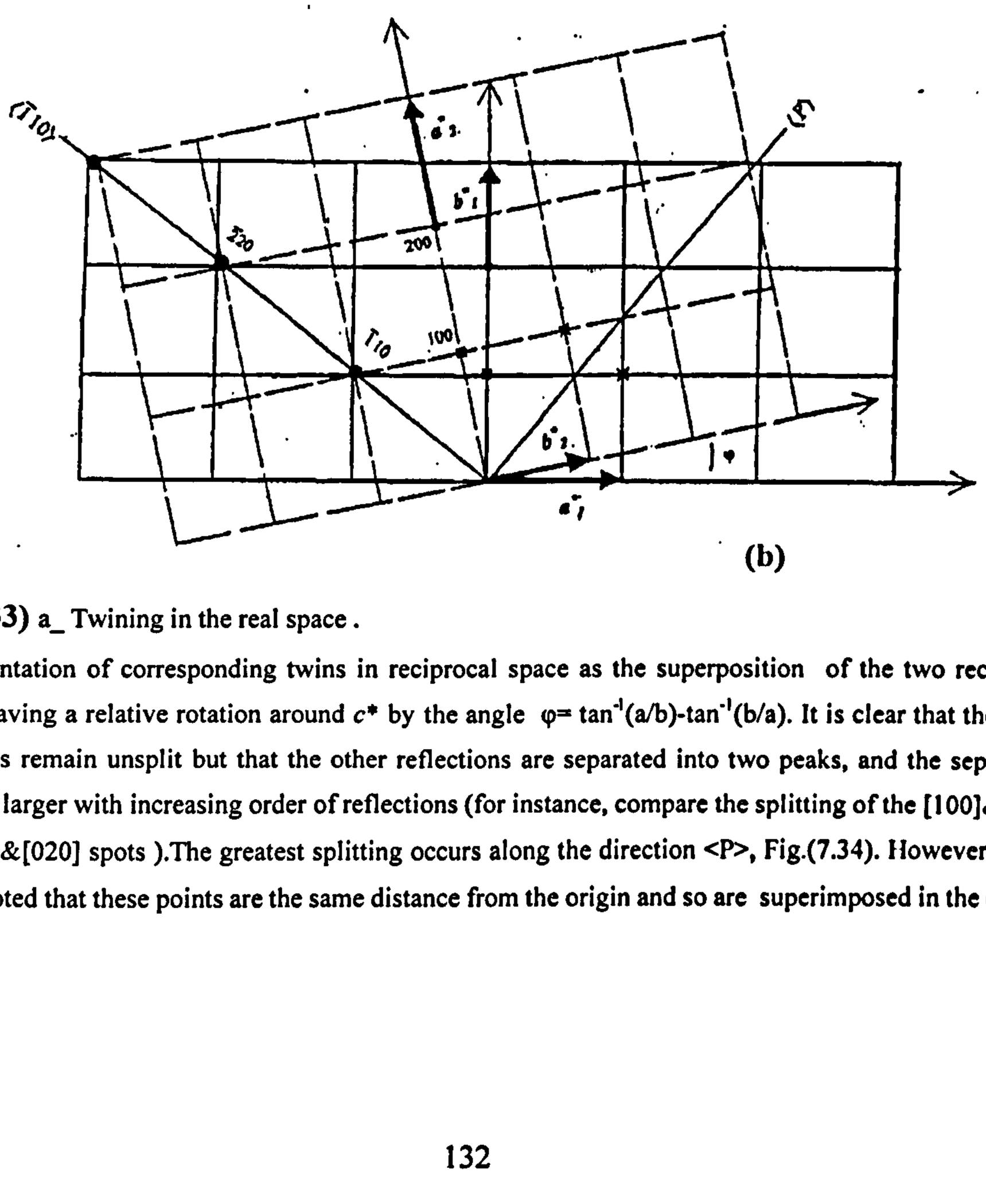

(b)

Fig (7.33) a_ Twining in the real space .

b_ Presentation of corresponding twins in reciprocal space as the superposition of the two reciprocal lattices having a relative rotation around c^* by the angle $\varphi = \tan^{-1}(a/b)-\tan^{-1}(b/a)$. It is clear that the [hh0] reflections remain unsplit but that the other reflections are separated into two peaks, and the separation would be larger with increasing order of reflections (for instance, compare the splitting of the [100]&[010] and [200]&[020] spots).The greatest splitting occurs along the direction <P>, Fig.(7.34). However it will also be noted that these points are the same distance from the origin and so are superimposed in the (p.p.r).

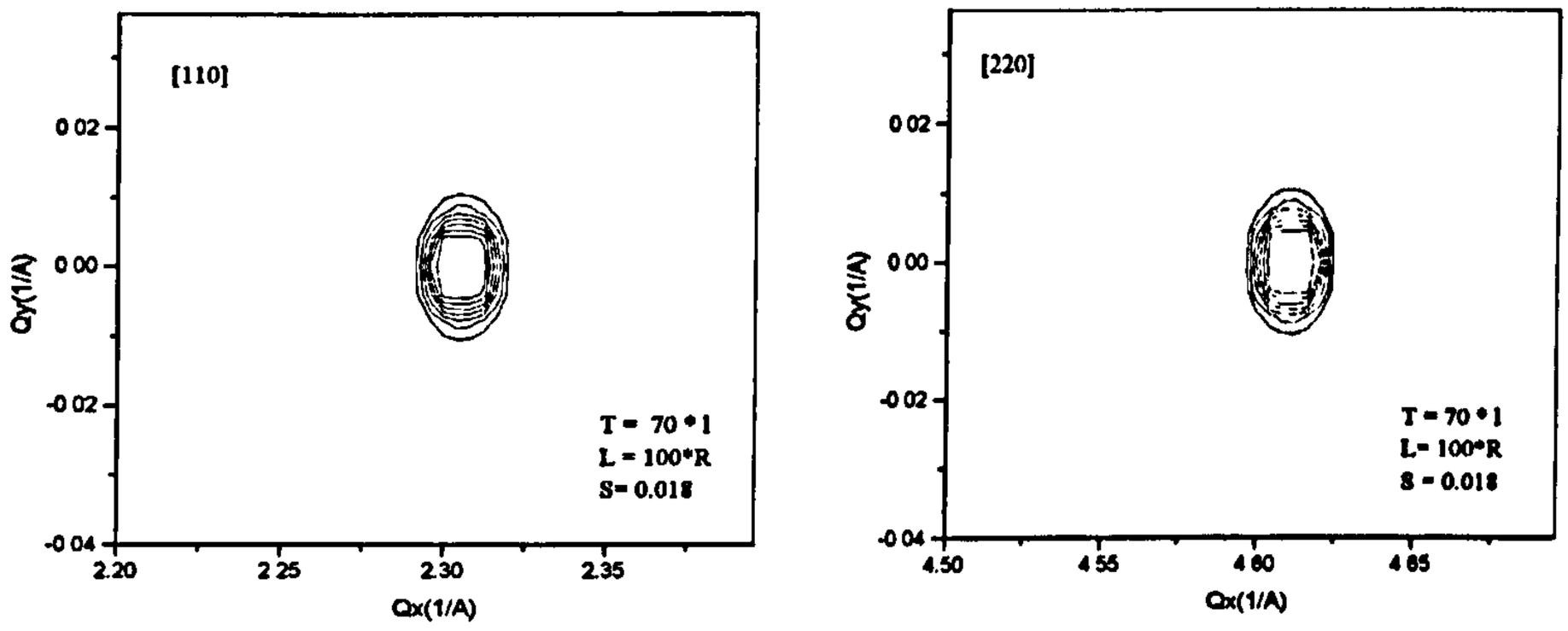

(a) **(b)**

Fig.(7.34) a_ Single [110] peak . b_ Single [220] peak. The broadening of the two peaks is the same because it is determined by the dimension of the twins.

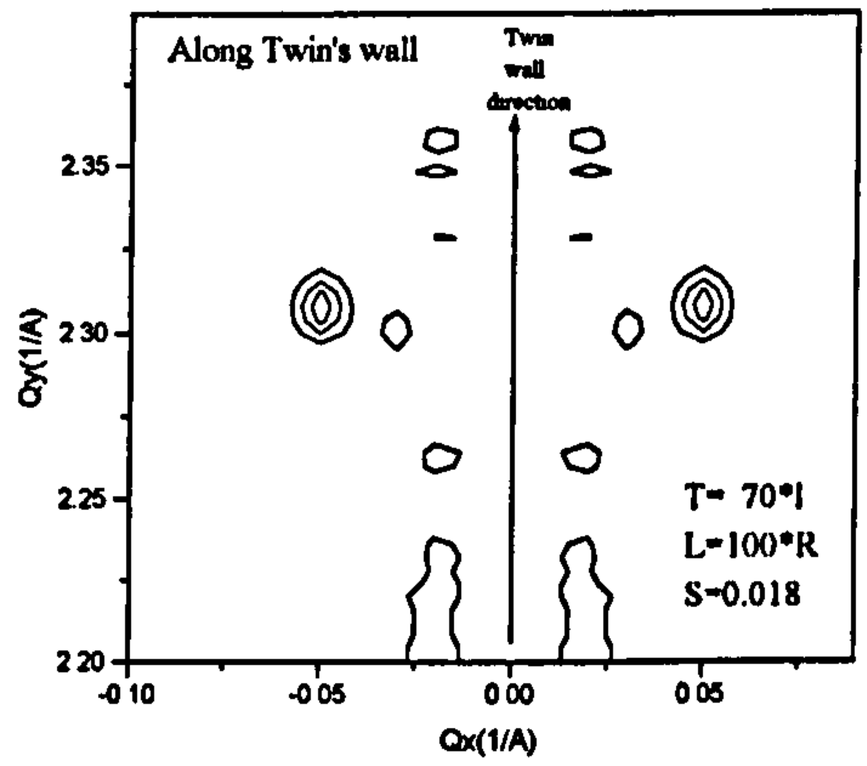

Fig.(7.35) The strong separation of the [1 1 0] peak along the twin's wall.

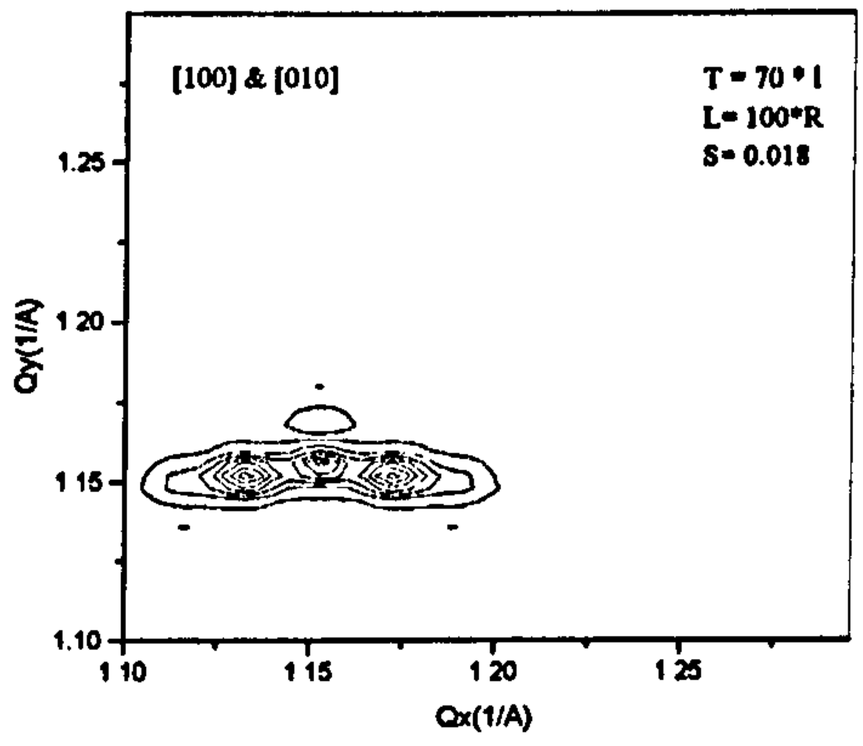

Fig.(7.36) With the same values of T, L and S as in the Fig.(7.32) this graph shows lower separation for the [100]&[010] peaks, while the interferences between the twins causes a weak middle peak as well, whereas for the same *S* and T, the [200]&[020] peaks are entirely split. The presence of this central peak can be traced in the experimental data (next section).

In the next series of (s.c.r) calculations for the [200]&[020] reflection, *S* is kept constant at 0.018 and T is varied (30 and 20 times *l*) Fig.(7.37).

Figures (7.37),(7.31) and (7.32) show the [200]&[020] reflections as calculated with a specified value of the orthorhombicity, *S*. Here, the interference effects again lead to a strong central peak for the small values of T, (small twin spacing). ***Therefore in powder diffraction data it is impossible to distinguish between a narrow twin microstructure (ordered orthorhombic phase) and the average tetragonal structure (disordered phase)*** (Fig. 7.37_c).

With the above considerations, the form of the pattern is determined by the product (*Sx*T). Indeed, the central peak and the split peaks appear with roughly equal intensity when: (*Sx*T) ~ (a constant in the order of 1.0), for instance compare Figs.(7.37_b) and (7.30_b). Indead, it can be proved that the phase difference between the diffraction from two adjacent twin area is (appendix D):

$$\Phi \approx 2\pi(h+k)\mathrm{T}\,S \qquad (7.2)$$

(in other word φ is the phase difference between the diffraction from the middle plane in the twinned region, in the presence and the absence of twinning)

If the phase difference is ~ π, the reflection at the mid position in either twin reflection will interfere destructively and at 2π constructive interference appears between the twin reflections. This path difference will occur at higher T as (*b*-*a*) gets smaller. Further, for a given (a-b), the condition is satisfied for progressively smaller T as (*h*+*k*) increases. For $\Phi >> \pi$, the scattering from one twin will be essentially incoherent at the position of the reflection from the other twin while for $\Phi << \pi$, the waves from each twin are essentially interfere coherently and one gets a single reflection between the twins with a width that depends on the total number of planes in the crystallite. .

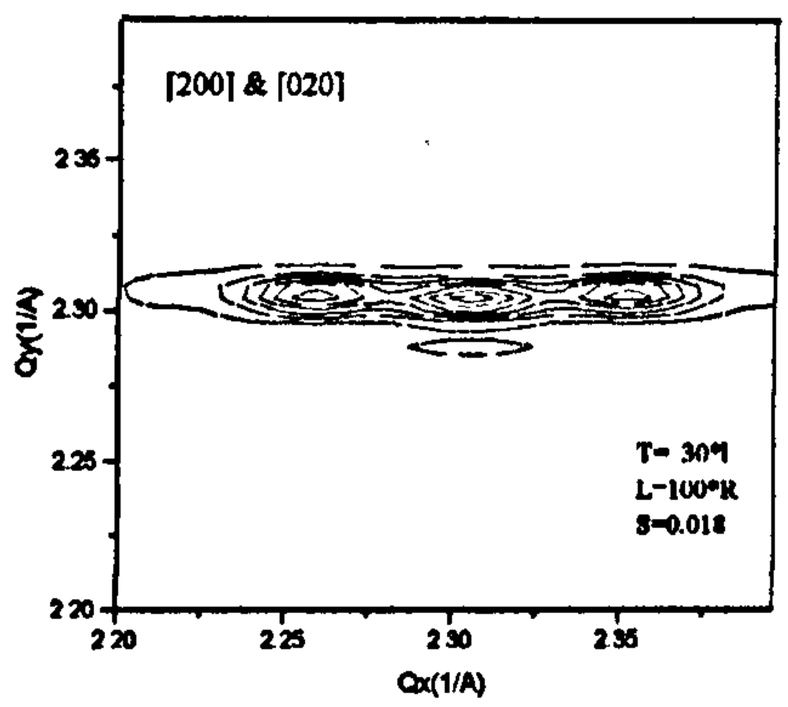

(a)

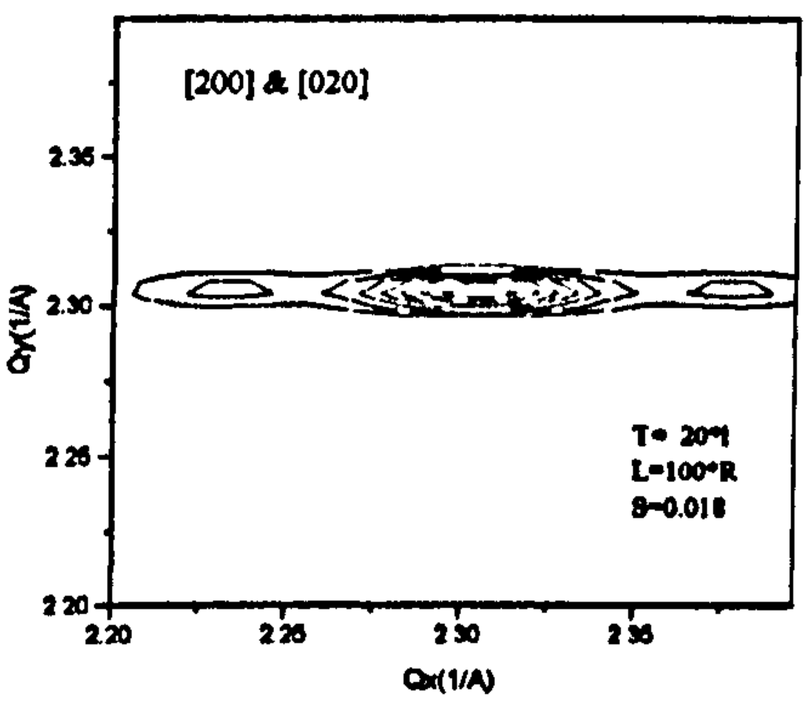

(b)

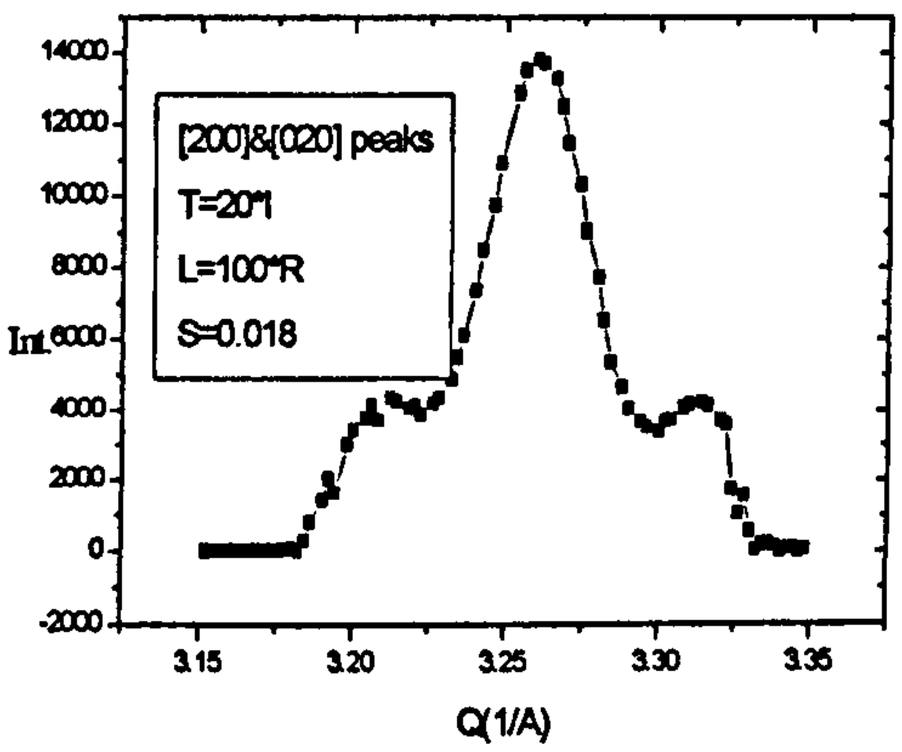

(c)

Fig.(7.37) The (s.c.r) for a_ T=30*l* ; b_ T=20*l* , c_ The (p.p.r) for the case (b)

One of the prominent predictions of these calculation is that the [*hh0*] peaks are always sharper than the [*h00*] peaks. This is because the geometry of the twin walls which are perpendicular to the direction <*hh0*>. In this direction, the plane spacing remains intact, so all the planes across the whole grain contribute to the corresponding [*hh0*] reflections, but this is not the case for [*h00*] reflections and the corresponding crystallographic plane's arrangement is disrupted with the next twin boundaries. This pure domain/grain size effect shows up in the model, (Fig. 7.38).

These calculations are for a pair of periodic structures twinned relative to each other and has been extended for two pairs of twinned regions (Fig.7.39). In this series of calculations S= 0.018 and T=10, 20, 50, 70. Here, when T becomes large i.e. is 50 or 70 (Figs.7.39_d-e), the peaks from each twin are clearly split into two. This is because the planes in the third region will have been shifted compared to where they would be in the absence of twinning. As this is half the plane spacing, the phase difference at the reciprocal lattice point will be π, i.e. the diffraction from the two regions exactly cancel each other out. However, as we move away from the perfect Bragg condition for this twin orientation, the phase difference changes from π. We thus see two peaks within the original envelope for a single twin.

For extended sets of twins of fixed spacing, clearly the intensity would resolve itself into a set of satellites at positions where the phase difference for each twinned region is $2n\pi$. However, in practice, the twin separation will fluctuate about some mean value and so these effects due to interference between pairs of twins will average out, leaving the above patterns as for a single pair of twins.

Calculations have also been performed for other twinned reciprocal lattice points and similar results are obtained except that the appearance of the central peak scales differently with S and T. How this happens is easily understood from the positions of the twinned reflections as shown in Fig.(7.33_b). As expected, for large (S x T), the reflections are as for superposition of the reflections from each twin, i.e. the width of each peak is inversely proportional to T and the reflections from each twin are separated

in proportion to *S*. Interference effects are only to be expected if these independent peaks begin to overlap. Thus, if we go out to the n^{th} order reflection, the separation of the twinned reflections will increase by a factor of n, and eventually, the peaks will become clearly separate.

Two important conclusions can be drawn from these figures. The first is that as *S* and T tend to zero, a central peak begins to grow and eventually replaces the side peaks. Thus, the simultaneous observation of the split peak and the central peak does not necessarily indicate the simultaneous existence of the OI and Tet. phases, i.e is not inconsistent with the transition being second order. For instance, the interesting points in this calculation is the appearance of a weak central peak between [100]&[010] or [200]&[020] (Figs.7.30 and 7.36). This provides an alternative explanation to the suggestion by Rand et al (1993) that this observation implies a mixture of OI and T phases.

The second point is that for a given S, close to the phase boundary, and one specified value of T, the central peak will only begin to disappear we go to higher order reflections.

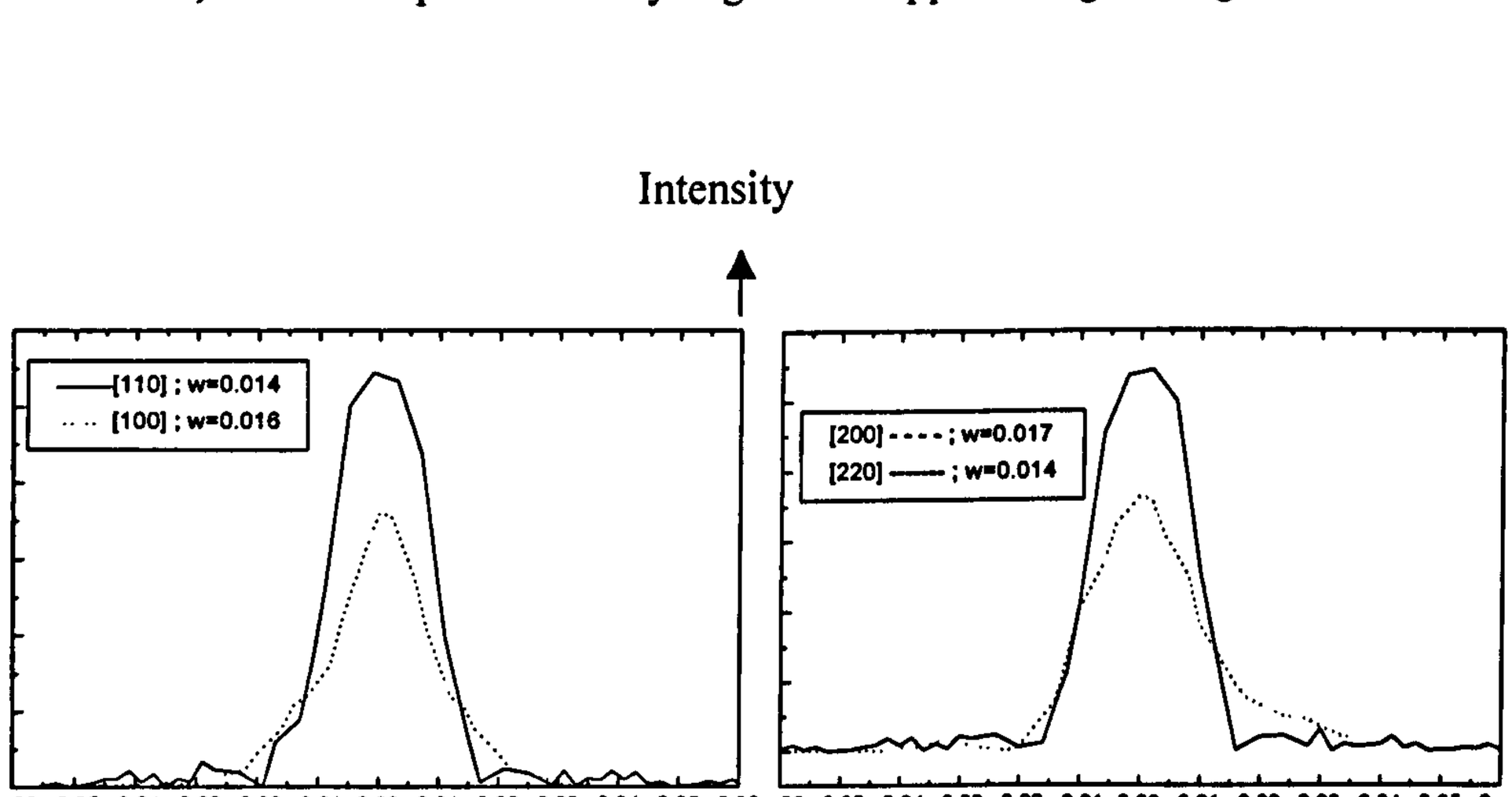

(a) **(b)**

Fig.(7.38) The comparison between the widths of the [*h00*] and [*hh0*] peaks , a_ [110] and [100] ; b_ [220] and [200] .

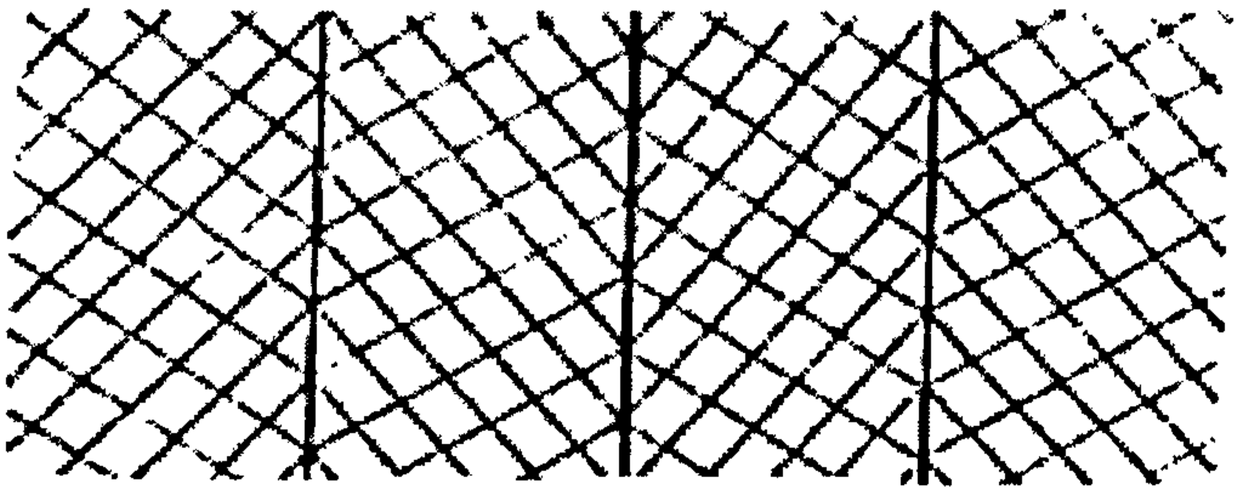

Fig.(7.39) a_4 twins model . **b** to **e** _ show the separation of [200]&[020] reflections with increasing the twin's width for constant values of S and L.

The interesting point is the re-splitting of each spot for T=50x*l*; 70x*l*

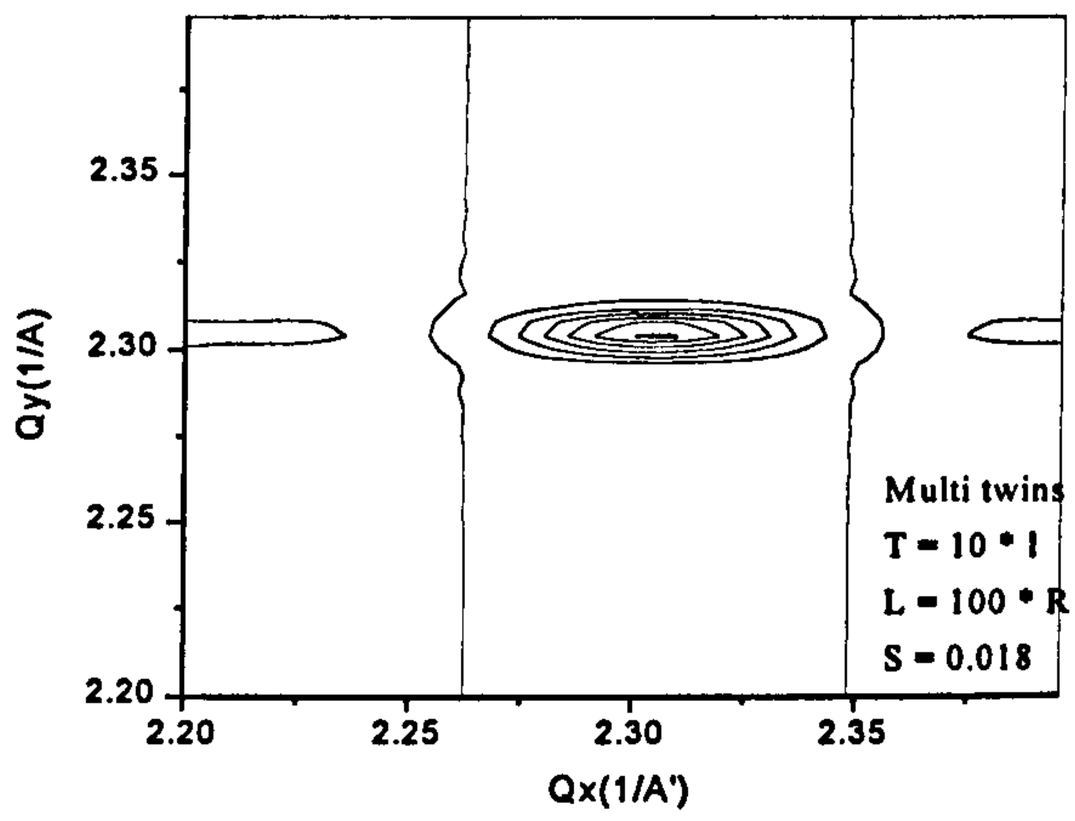

Fig.(7.39a) Multi Twins; T=10, S=0.014

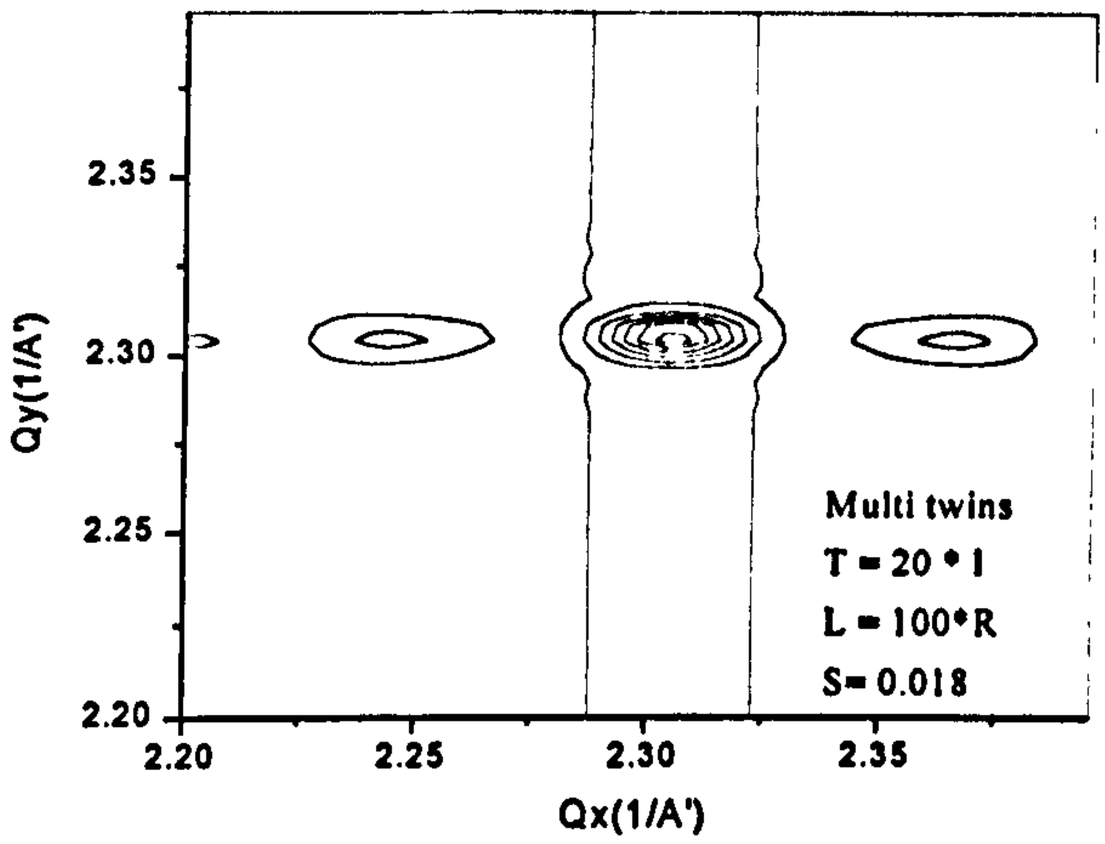

Fig.(7.39b) Multi Twins; T=20, S=0.014

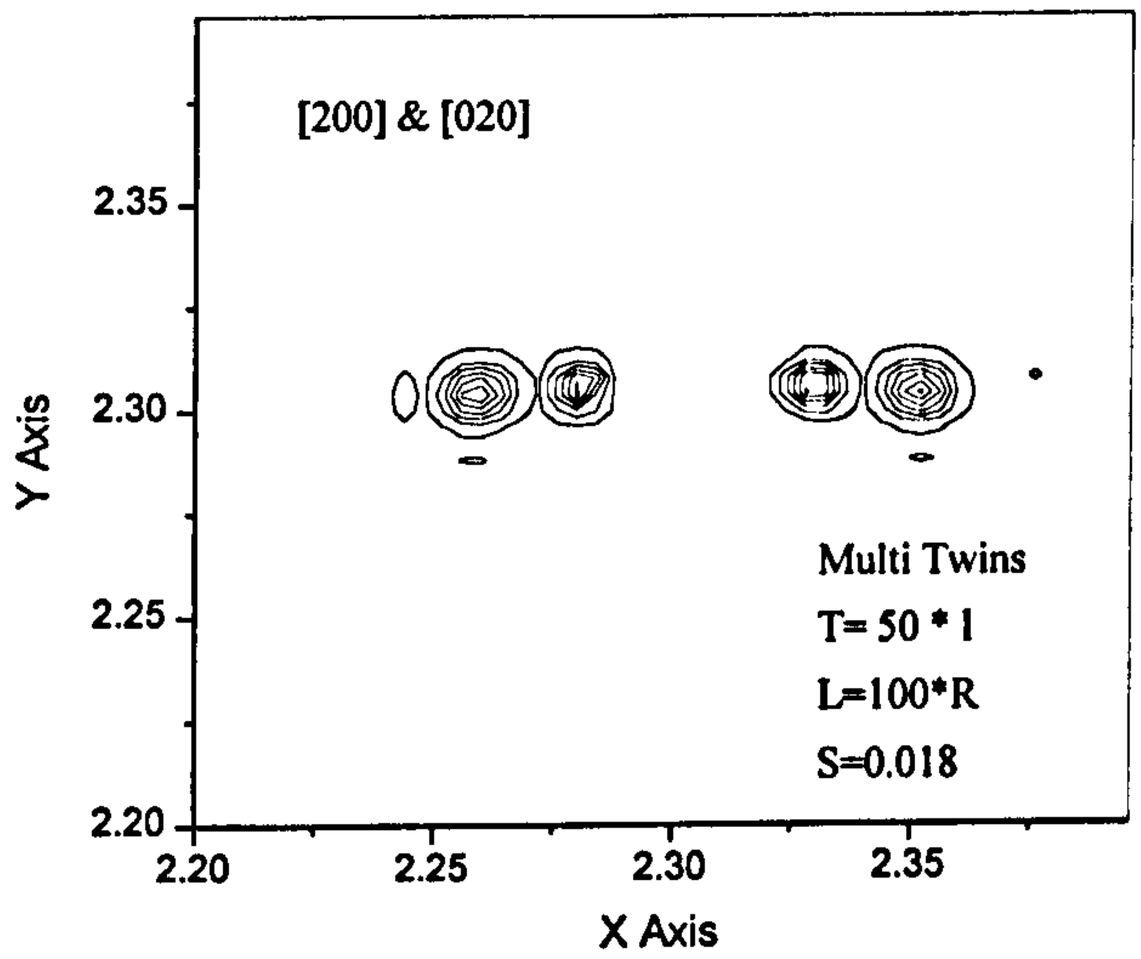

Fig.(7.39c) Multi Twins; T=50, S=0.014

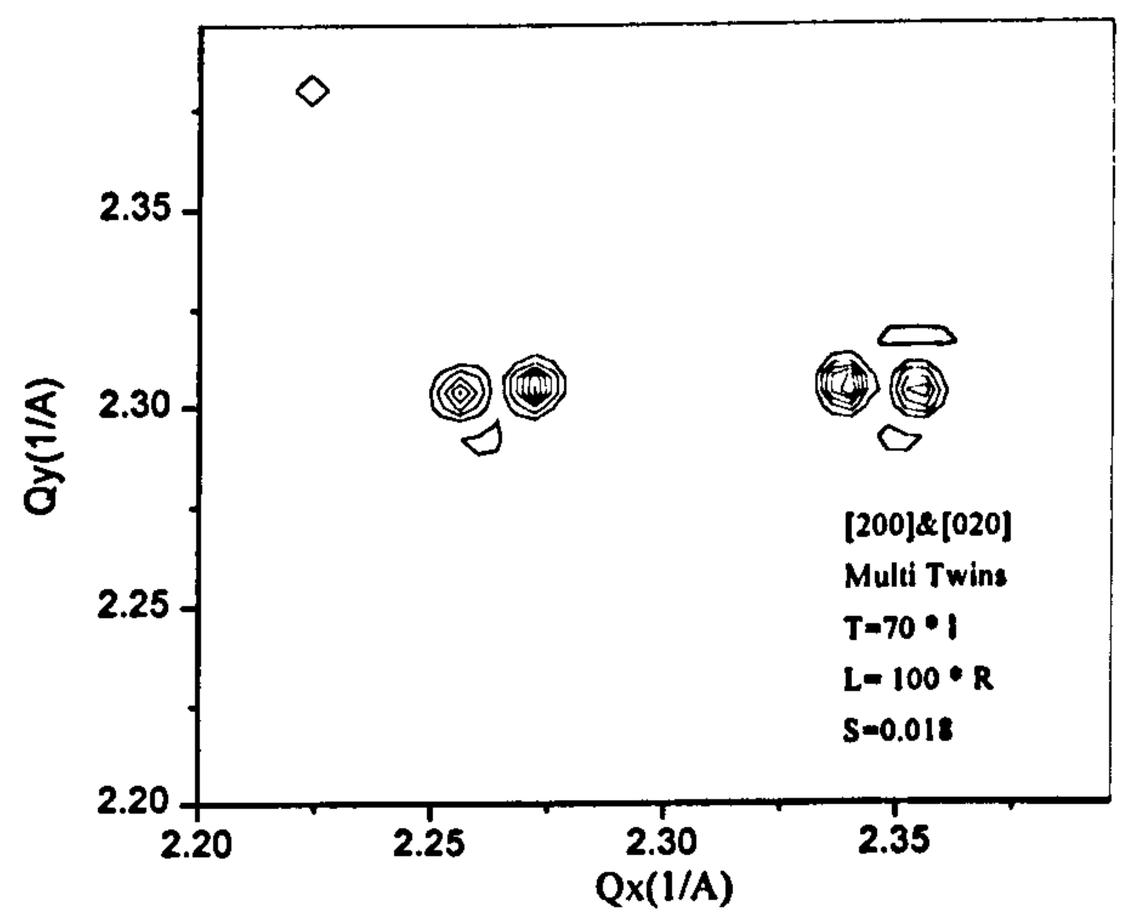

Fig.(7.39d) Multi Twins; T=50, S=0.014

VII.4) PEAK BROADENING ANALYSIS

The first step for any line broadening analysis is the deconvolution of the instrumental broadening effects from the collected data, and for this a satisfactory full profile refinement over a diffraction pattern from a standard sample is necessary. It is supposed that the "standard sample" is free of any crystal imperfections like strain & small crystallite size, so its pattern indicates the *g* profile (the instrumental resolution profile in chapter VI).

In GSAS (the software that was used for the profile refinement in here) the profile function for the TOF (Time Of Flight) collected pattern, *h* profile, supposedly is a convolution of a pulse shape function, E, and the aforementioned pseudo-Voigt function , P,(chapter VI).

$h(\Delta T)=\int P(\Delta T-t)E(t)dt$ (7.3)

where :

ΔT is the difference in TOF between the reflection position, T_0 ,and the profile point, T.

$E(t)=2Ne^{\alpha t}$ for $t<0$

$E(t)=2Ne^{-\beta t}$ for $t>0$ (7.4)

(α and β are the rise and decay coefficients for the exponentials , and N is the normalization factor , $N=\alpha\beta/2(\alpha+\beta)$)

$P(x)=\eta L(x)+(1-\eta)G(x)$ (x is a dummy variable) (7.5)

where :

$L(x)=(\gamma/2\pi)[(\gamma/2)^2+x^2]^{-1}$ (γ is the Lorentzian FWHM) (7.6)

$G(x)=(1/\sqrt{(2\pi\sigma^2)})\exp[-x^2/2\sigma^2]$ (7.7)

(σ^2 is the Gaussian variance and $\Gamma_g=\sqrt{(8\pi\sigma^2 ln\ 2)}$ is the Gaussian FWHM)

Therefore from [Thompson et al ; 1987] :

$\eta=1.36603\ (\gamma/\Gamma) - 0.47719(\gamma/\Gamma)^2 + 0.11116(\gamma/\Gamma)^3$ (7.8)

where Γ is the total FWHM of the pseudo-Voigt function given by [Von Dreele; 1982] :

$\Gamma=[\ \Gamma_g^5 + 2.69269\Gamma_g^4\gamma + 2.42843\Gamma_g^3\gamma^2 + 4.47163\Gamma_g{}^2\gamma 3 + 0.07842\Gamma_g\gamma^4 + \gamma^5]^{1/5}$ (7.9)

All of these quantities depend on the d-spacing of the plane in question as:

$\alpha = \alpha_1/d$

$$\beta = \beta_0+\beta_1/d^4$$

$$\sigma^2= \sigma_0^2+\sigma_1^2d^2+\sigma_2^2d^4 \quad (7.10)$$

$$\gamma = \gamma_0+\gamma_1d+\gamma_2d^2 \quad (7.11)$$

Therefore in the GSAS package, the refinable parameters for the introduced TOF profile are :

$\alpha_1, \beta_0, \beta_1, \sigma_0^2, \sigma_1^2, \sigma_2^2, \gamma_0, \gamma_1, \gamma_2$

Now after performing a full profile refinement for the formal standard sample pattern (a well prepared silicon powder) the values of the first three parameters are obviously related to the neutron pulse shape that emerges from the moderator and it would be rational if they are taken to be unchanged in the all the following full profile refinements. The remain parameters are used to calculate the instrumental broadening vs. d-spacing (the resolution function).

Figure (7.40) shows the standard sample (Si) refinement. The crystallographic data and the quality of the fit are:

The space group is : F d –3 m

The lattice parameter is : $a = 5.4309$ Å

$\chi^2 = 12.40$ and $R_p=0.0290$

As the Figs.(7.40_b-d) show, the widths of the calculated and observed peaks in the d-spacing range of interest (1.2 – 4 Å) are quite satisfactory for the subsequent de-convolution process.

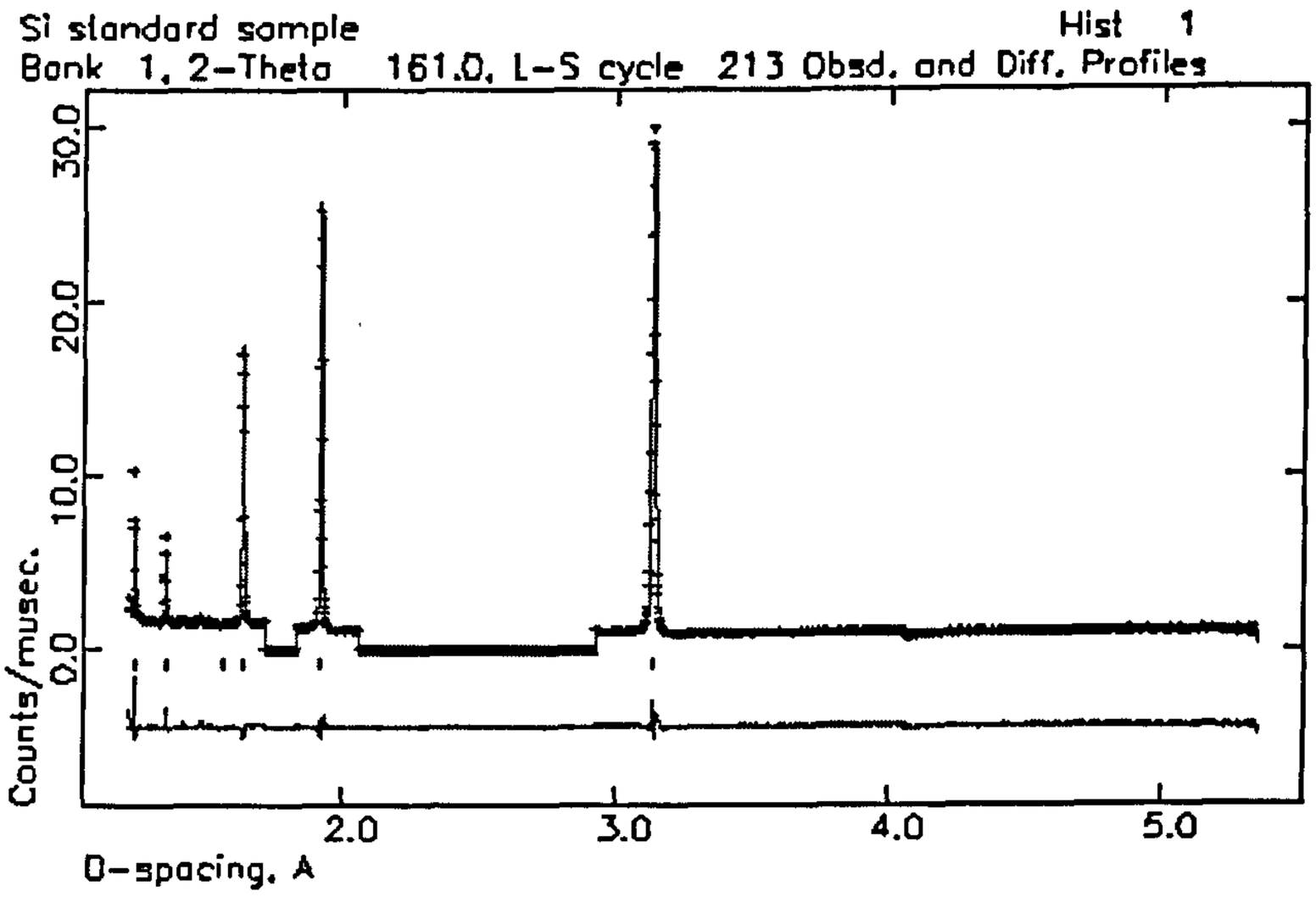

(a)

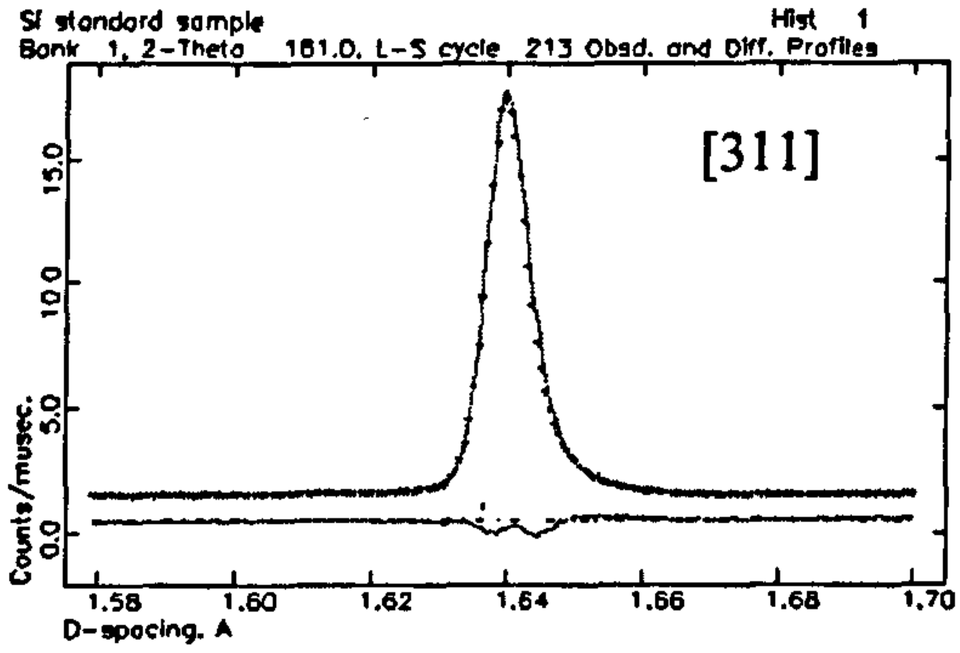

(b)

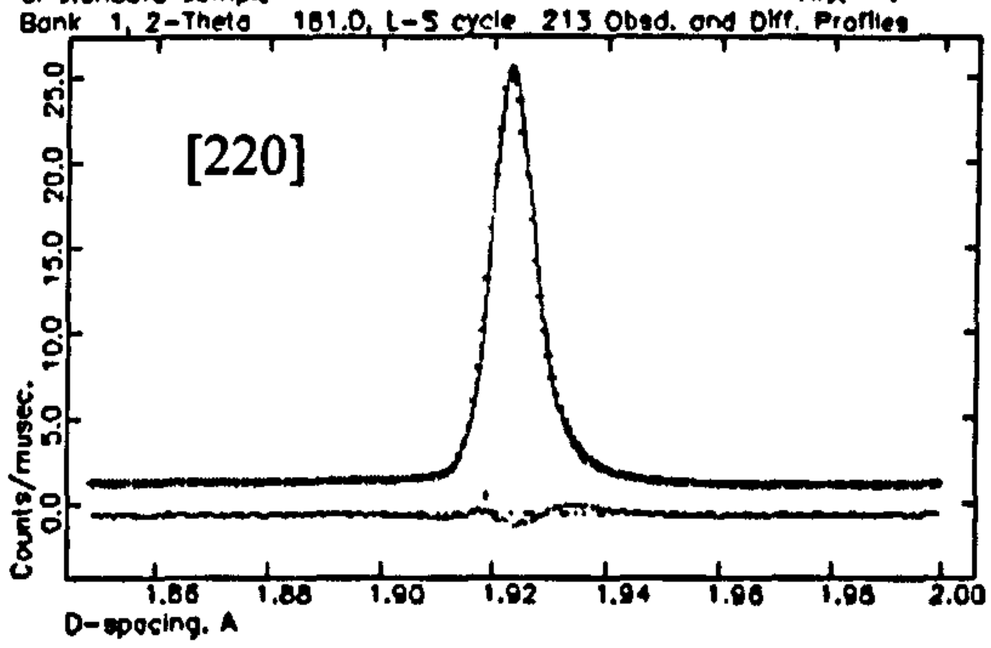

(c)

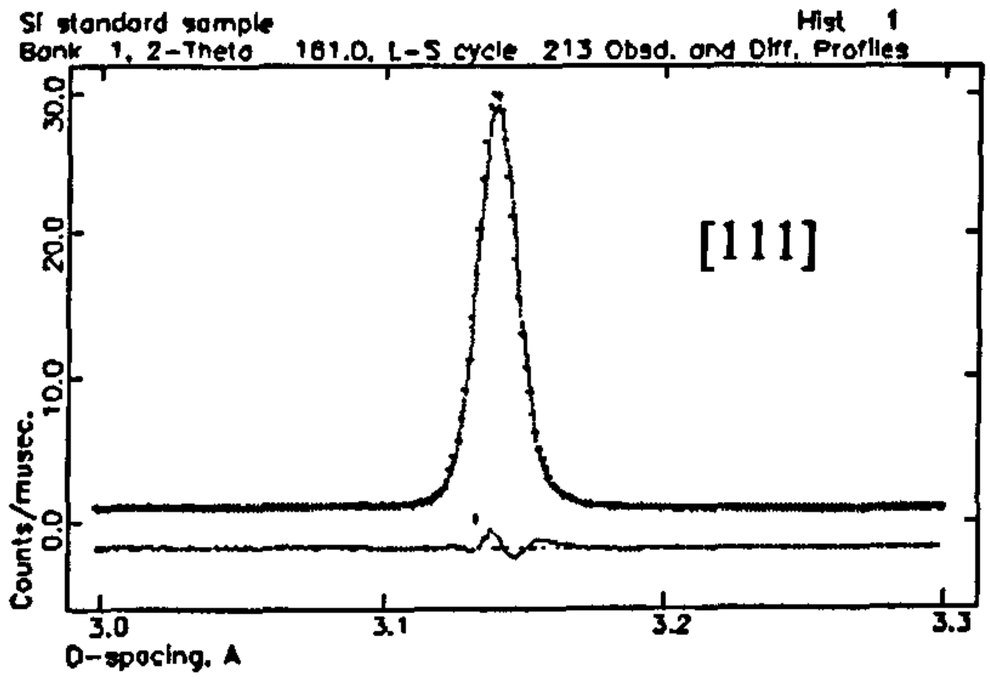

(d)

Fig.s (7.40) a_ the standard sample fit , the excluded regions show some diffuse scattering due to the fused quartz sample tube. b, c and d show different peaks in the range from 1.2 to 4.0 Å

Fig.(7.41) shows the profile parameters after the 600°C isotherms pattern's full profile refinement and table (7.3) presents the refined profile parameters for the standard sample and for the 600°C isotherms measurements (section VII.2).

Partial Pres. (mbar)	α	β_0	β_1	σ^2_0	σ^2_1	σ^2_2	γ_0	γ_1	γ_2
Standard	0.2611	0.0217	0.0239	0.0	203.3	48.7	0.0	25.90	0.0
Vacuum	//	//	//	0.0	533.94	34.16	0.0	14.05	0.89
40	//	//	//	//	789.5	35.1	//	18.54	0.20
150	//	//	//	//	552.8	17.7	//	21.94	0.0
200	//	//	//	//	620.4	49.2	//	31.91	0.0
250	//	//	//	//	595.6	47.9	//	25.46	0.0
450	//	//	//	//	817.0	69.5	//	27.35	0.83
750	//	//	//	//	440.5	92.0	//	42.77	0.52

Table(7.3) The profile parameters after the 600°C isotherms pattern's full profile refinement.

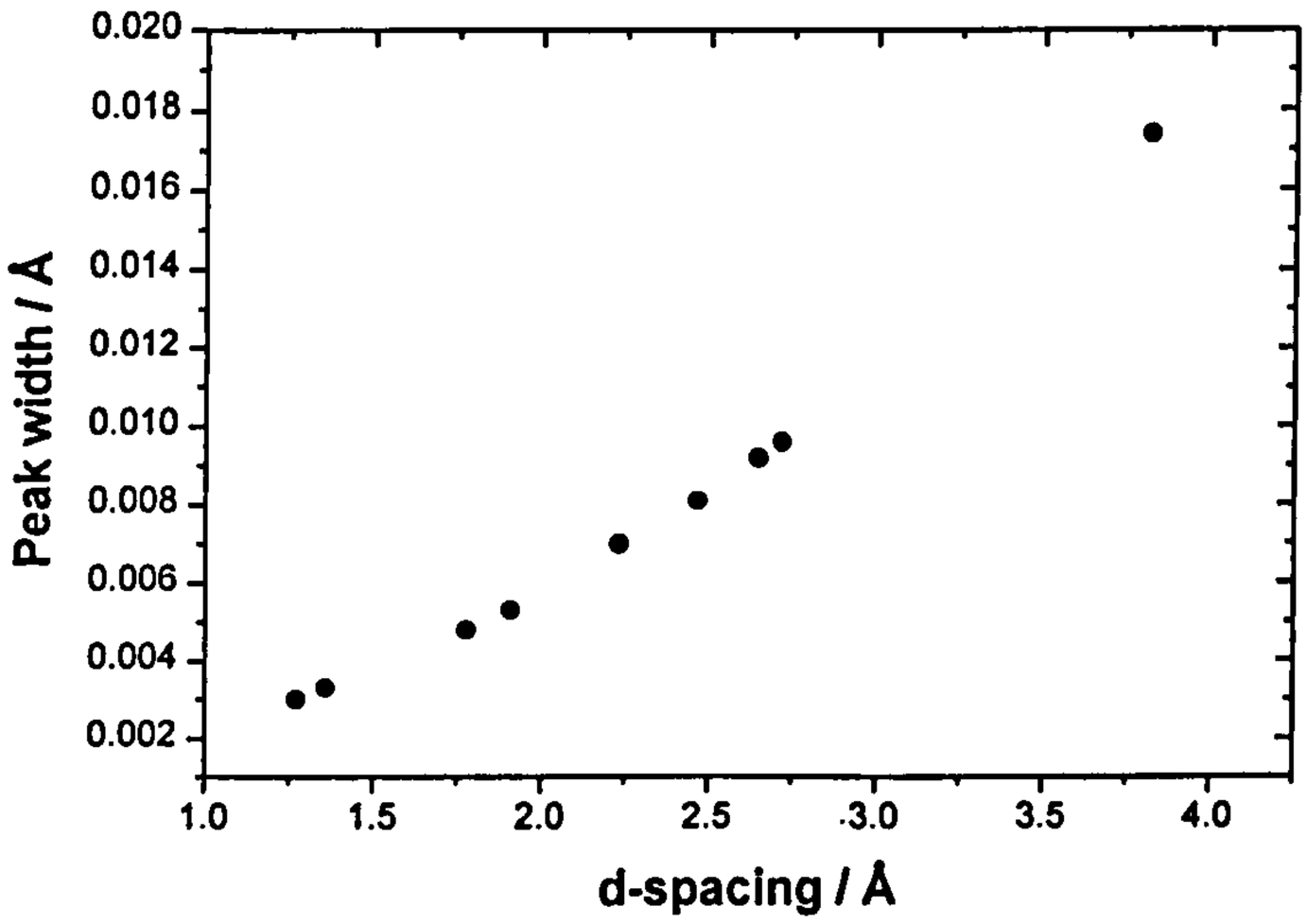

Fig.(7.41) The behavior of the peak widths vs d-spacing for standard sample (Si) in OSIRIS

The profile parameters from a TOF neutron powder pattern Rietveld refinement with GSAS can give information about the microstructure as below:

In the reciprocal space (i.e. Q scale*) associated with a sample, the isotropic strains cause a broadening for each point which is proportional to the distance of the point from the origin, i.e. $\Delta d^*/ d^* = \text{constant}$ (chapter VI).

In d-spacing then: $\Delta d / d = \text{constant}$ (for isotropic strain broadening).

On the other hand, in reciprocal space (Q), the crystallite size isotropic broadening makes all points the same size independent of the distance from the origin (chapter VI), thus: $\Delta d^* = \text{constant}$ (the reciprocal of this constant quantity is then proportional to the average particle size).

In real space (for TOF) the broadening is : $\Delta d / d^2 = \text{constant}$.

It is conventional in the literatures [Young;1993] & [GSAS manual (Von Dreele)] to attribute the strain broadening to the Gaussian part and the crystallite size broadening to the Lorentzian part of the pseudo-Voigt function, thus for the Gaussian part, if the peak width is given by σ: $\sigma^2 = \sigma^2_{strain} + \sigma^2_{cry.size}$ (7.12)

where: $\sigma^2_{strain} \propto (\Delta d / d)^2$ and $\sigma^2_{cry.size} \propto (\Delta d / d^2)^2$

Now if this equation compared to the Eq.(7.10), it may be written :

$\sigma^2_1 \propto (\Delta d / d)^2 \Rightarrow \sigma^2_1 d^2 \propto (\Delta d)^2$ (for strains) (7.13)

$\sigma^2_2 \propto (\Delta d / d^2)^2 \Rightarrow \sigma^2_1 d^4 \propto (\Delta d)^2$ (for cry.size) (7.14)

In the Eq.(7.10), σ^2_0 is a constant.

For the Lorentzian part, the behavior is similar: $\Gamma = \Gamma_{strain} + \Gamma_{cry.size}$

Where compared to (7.11) it is clear that:

$\gamma_1 \propto \Delta d / d \Rightarrow \gamma_1 d \propto (\Delta d)$ (for strain) (7.15)

$\gamma_2 \propto (\Delta d / d^2) \Rightarrow \gamma_2 d^2 \propto (\Delta d)$ (for cry.size) (7.16)

The γ_0 in Eq.(7.11) is another constant.

In GSAS , the quantity expressed as ' isotropic ***fractional strain*** ' is:

$D = (1 / C) [8 \ln 2 (\sigma^2_1 - \sigma^2_{1i})]^{1/2} \ 100\%$ (7.17)

Where C is the diffractometer constant (DIFC, is a refinable parameter in GSAS) that relates TOF to d-spacing and σ^2_{1i} is the instrumental contribution (come from the standard sample refinement).

On the other hand the quantity indicates the isotropic crystallite size is:

---

* $Q=d^*=2\pi/d$ therefore: $\Delta Q=\Delta d^*=2\pi \Delta d/d^2$ and $\Delta Q/Q = \Delta d/d$

$P = CK/\gamma_2$ (here K is the Scherrer constant of the order of unity) (7.18)

It is assumed that, for the standard sample, there is no the crystallite size effect. For this, the well prepared silicon sample's crystallite size must be greater than 10^{-5} m [Lipson & Steeple].

With more examination of the values in the table it is clear that for the analysis of peak broadening effect, a full pattern refinement package such as GSAS, which involves the isotropic model for interpretation of the line broadening effect, is not quite suitable . This is because of the strongly anisotropic peak broadening effects caused by the twinned microstructure on the YBCO samples in the orthorhombic phases [David; 1989].

Figure (7.42) shows the Williamson-Hall (W.H.) plots for two samples that are clearly inside the OI phase region (x =0.71, 0.83). The $(\beta)^*$ values are calculated from the parameters in Table (7.3), which have been obtained by full profile refinements, after de-convolution from the instrumental (standard sample) broadening.

It is clear that no anisotropic effects show up in this fit, because the β values are constrained to increase smoothly vs. Q and their extrapolation to the Q = 0 region yields an intercept on the β axis which is proportional to the inverse value of the average crystallite size [the spherical crystallite shape model, chapter VI]. In the recent version of GSAS there are some facilities to refine stacking faults and anisotropic microstrain effects based on the Stephen model (see chapter VI), but still there is no an adequate model to include the twinning effect which is the main concern of the author in this section.

Therefore to deal with the interesting anisotropic effects, it has been necessary to adopt the approach of analyzing each line independently in the relevant d-spacing range [Langford; 1999]. The major difficulty found for this method is how to resolve the highly overlapped peaks in the low d-space region (for instance the higher order reflections such as [115] and [300] are very difficult to resolve whereas, in the whole profile method it is possible to calculate each line width just analytically). For the many

---

* Integral breath

reflections examined by this method, an adequate fit is produced by assuming that the sample-dependent broadening effects (β), are predominantly Gaussian.

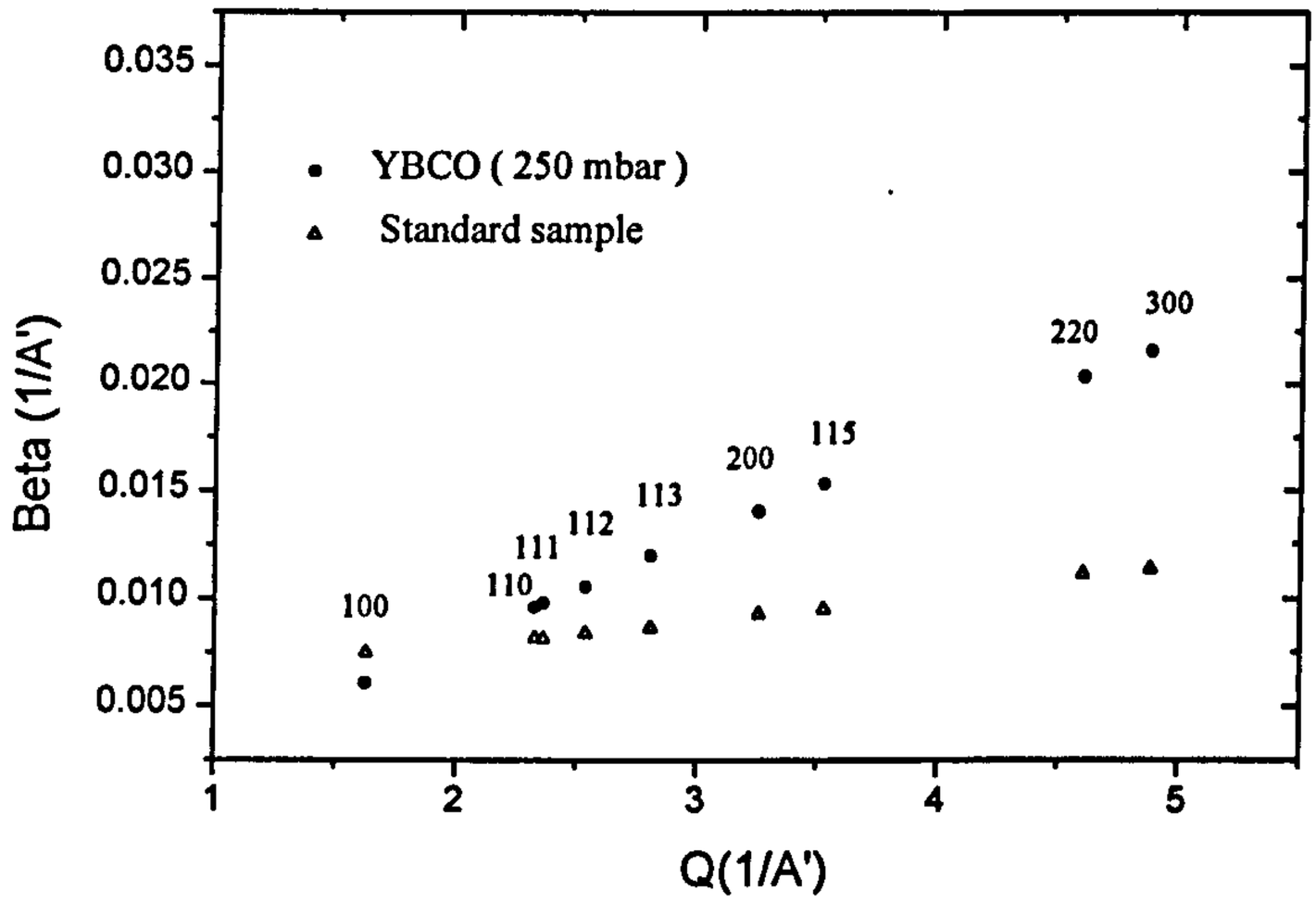

(a) At 600°C under 250 mbar oxygen p.p.

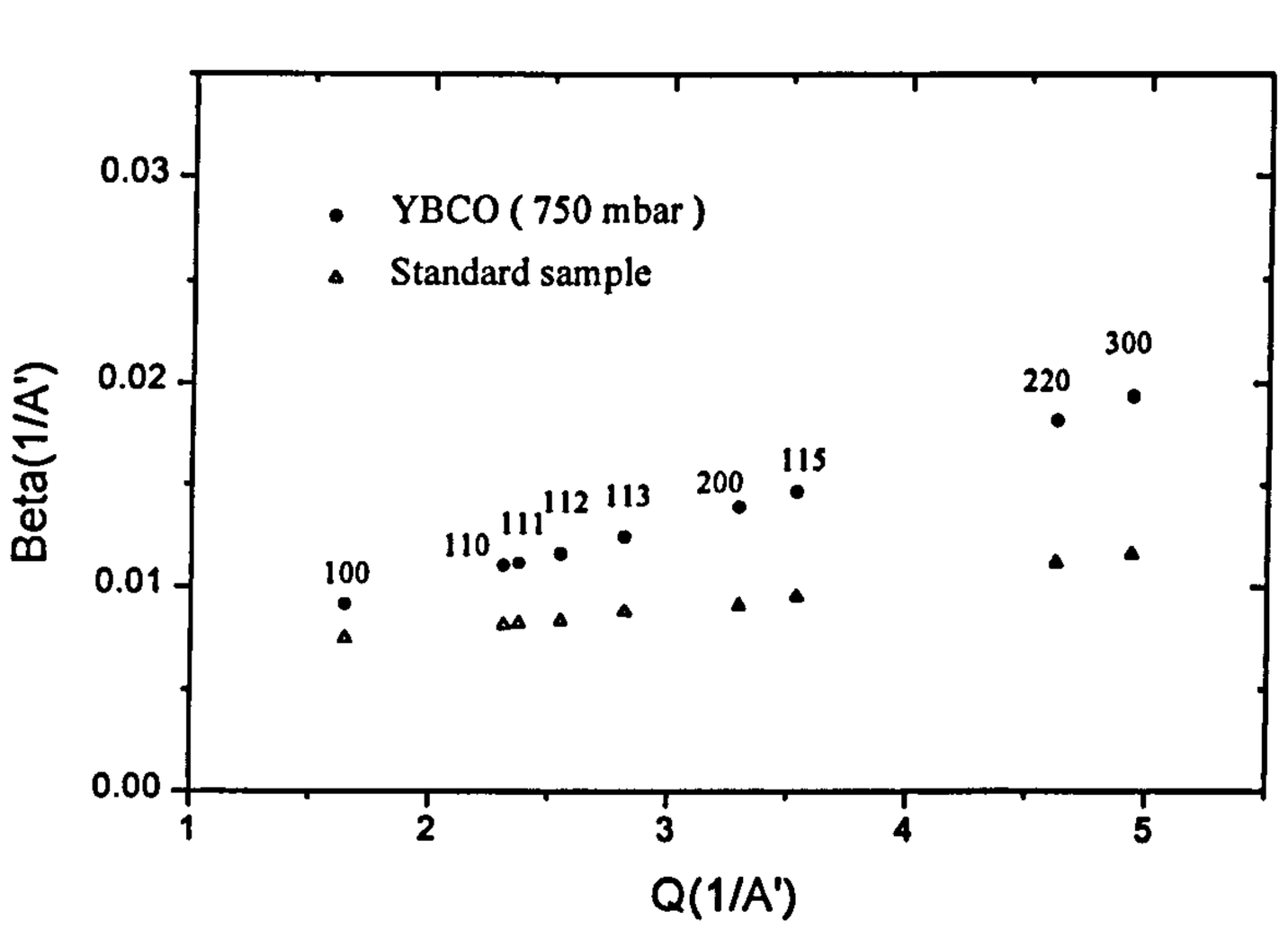

(b)

Fig.(7.42) Williamson-Hall plots of the isotropic peak widths as a function of Q_ for 600°c isotherms.

a)_ under 250 mbar oxygen partial pressure (p. p). b)_ under 750 mbar p.p.

It is clear that a full profile refinement results in a broadening that increases smoothly with Q.

Comparison with the standard sample, demonstrates the major effect due to strains.

Figs.(7.43_ a-e) show W.H. plot using the individual line profile fits for the same sequential peaks (Q-space) from the isotherm at 600°C. The Figs.(7.43a_b) relates to the tetragonal phase and they show again a smoothly increased behavior for the sequential peak widths vs. Q, indicating the strong residual strains, caused by the uniformly distributed tweed structure, after oxygen absorption in the lattice.

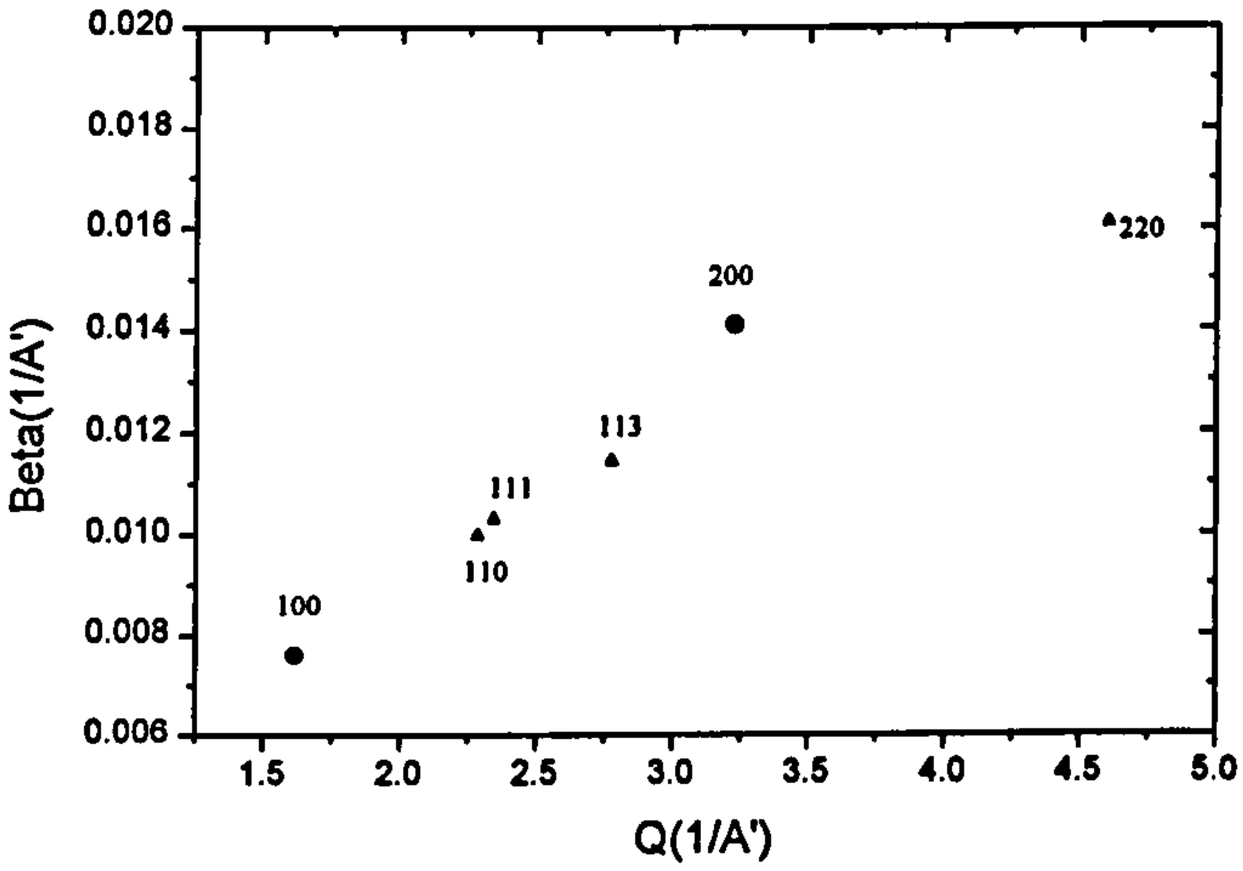

Fig.(7.43a) W.H. plot for sample under 0.5 mbar at 600°C (neutron diffraction – Tet. phase)

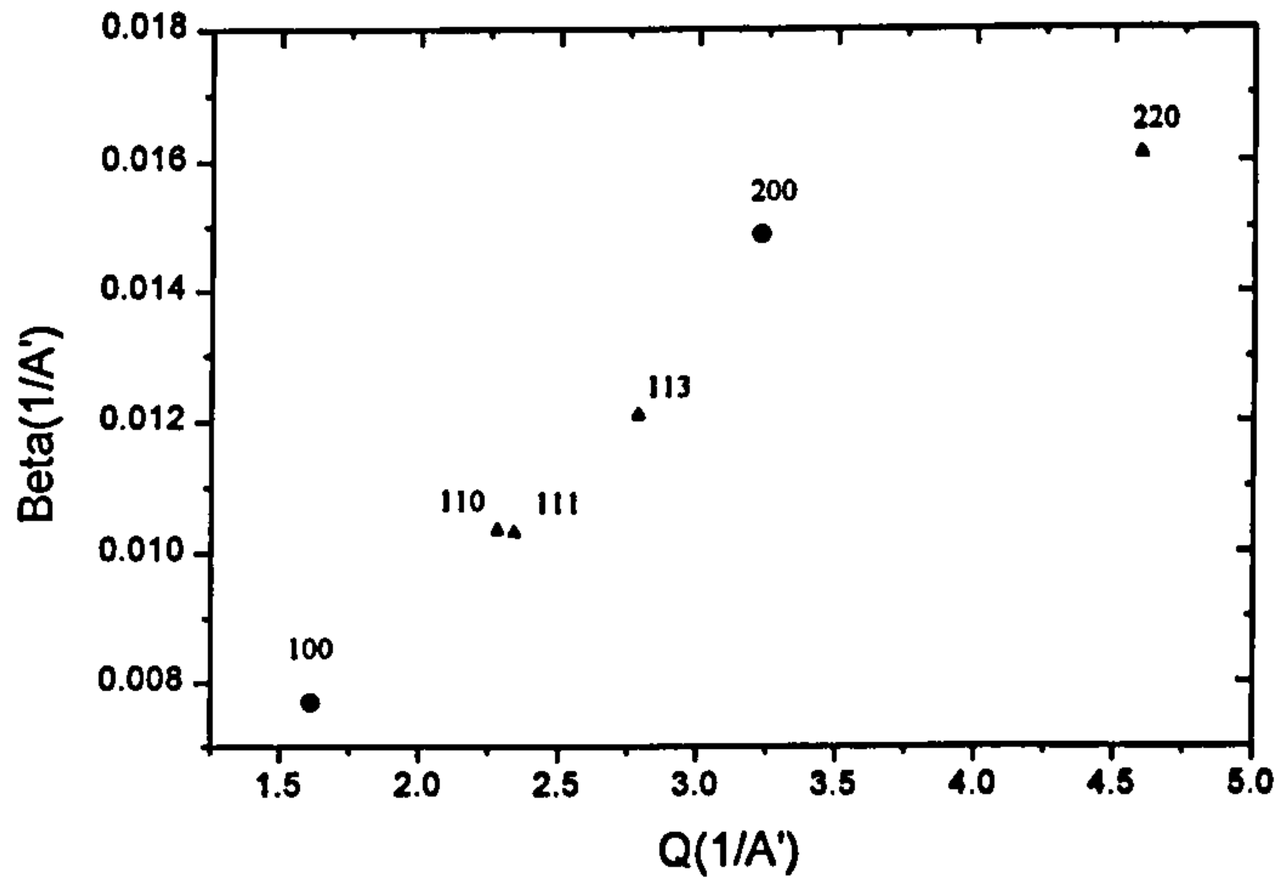

Fig.(7.43b) W.H. plot for sample under 40 mbar at 600°C (neutron diffraction – Tet. phase)

The rest of the figures (7.43c_e), show different behavior for the same sequential peak widths when the sample is brought into the Orthorhombic I phase. It is consistent with the anisotropic broadening effects which are generated, as expected by twining. The important points from this series of figures are that, on the one hand, the broadness of the [110]&[220] reflections drop down anomalously and, on the other hand, the widths of the peaks [100] & [200] are increased.

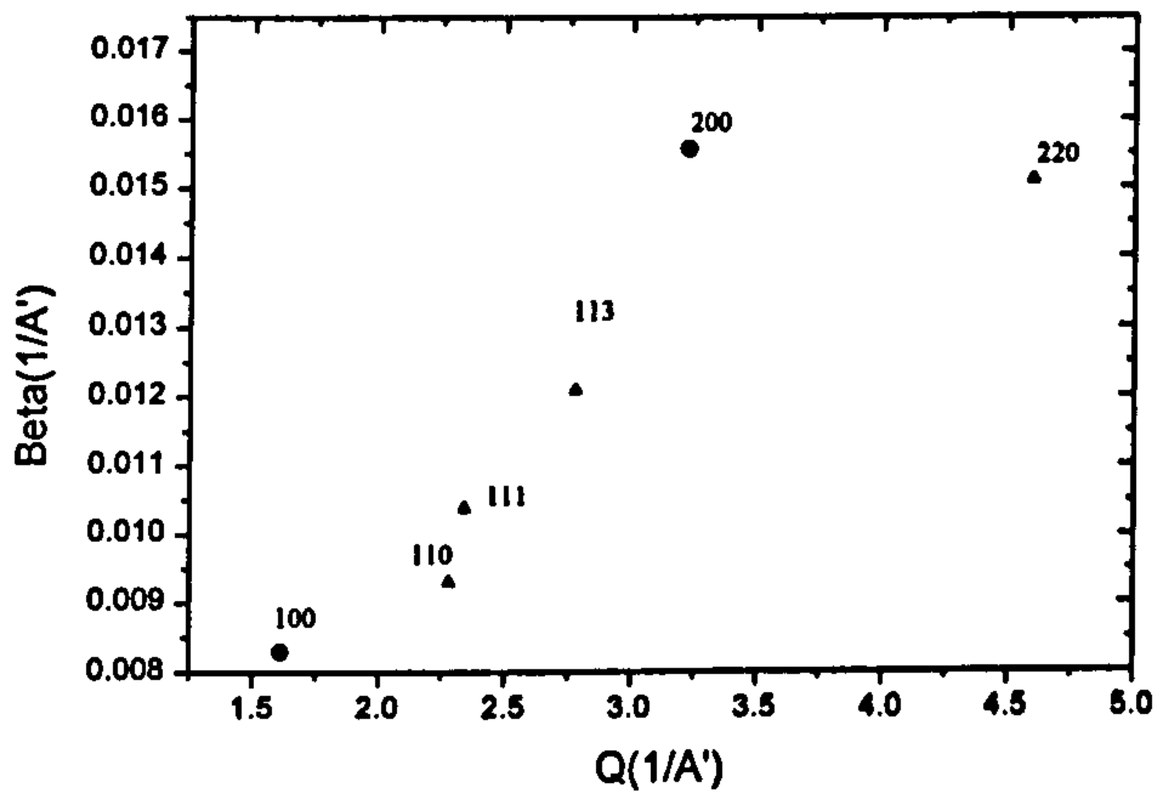

Fig.(7.43c) W.H. plot for sample under 150 mbar at 600°C (neutron diffraction)

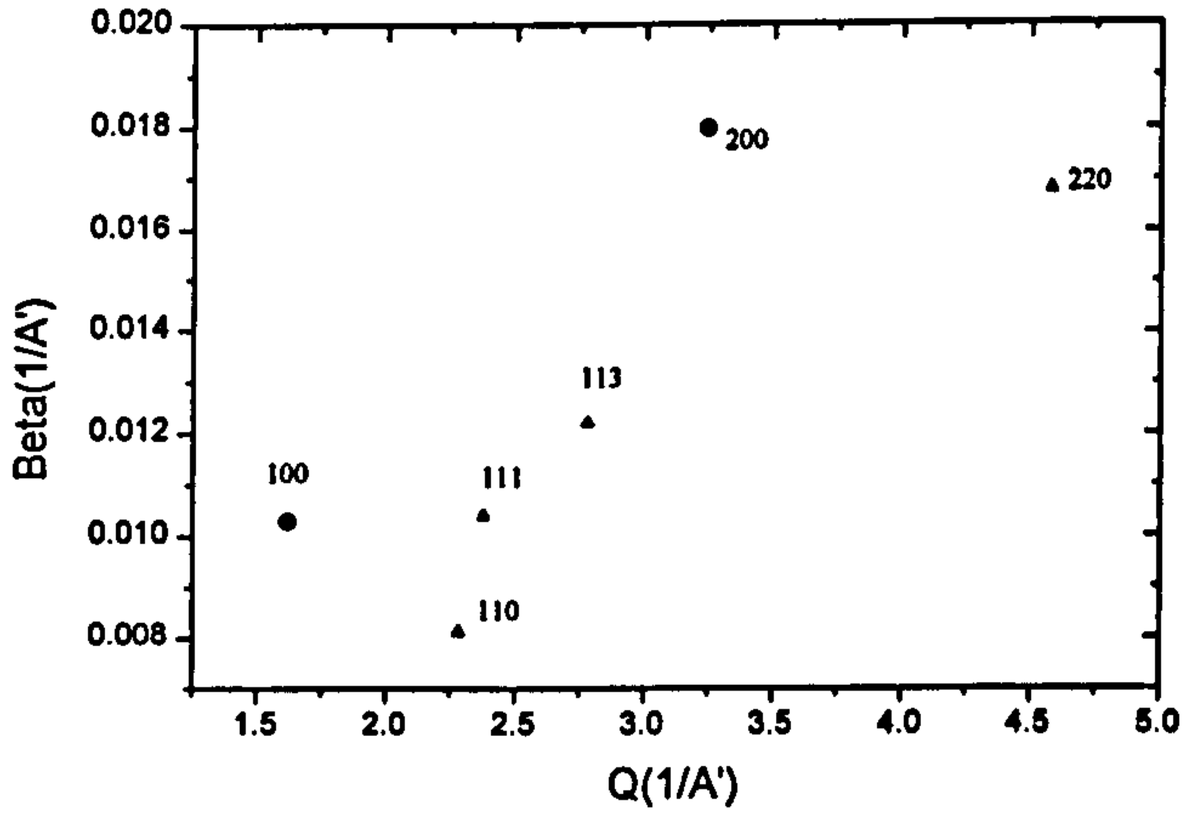

Fig.(7.43d) W.H. plot for sample under 300 mbar at 600°C (neutron diffraction)

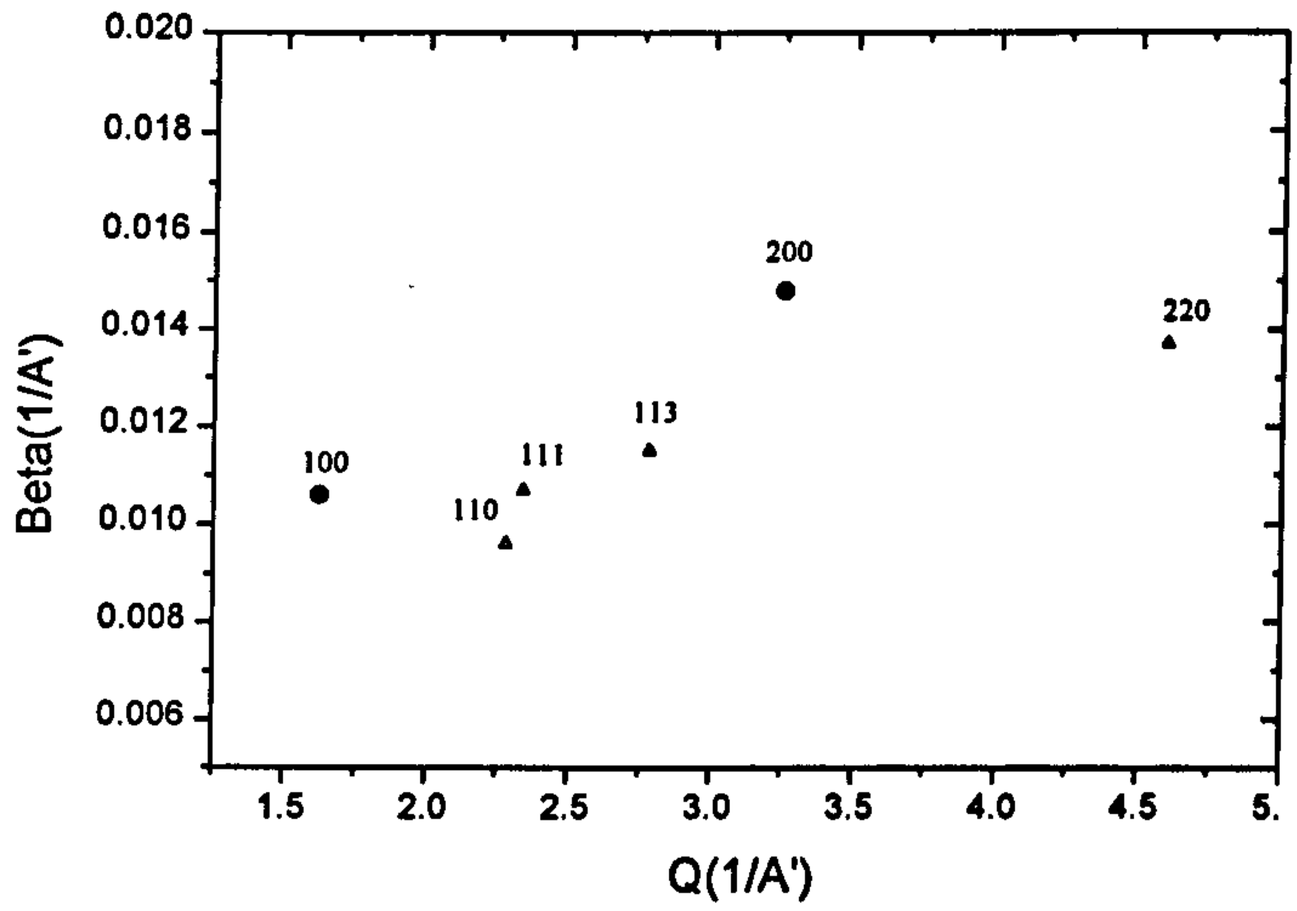

Fig.(7.43e) W.H. plot for sample under 750 mbar at 600°C (neutron diffraction)

Fig(7.44) shows a good comparison for the W.H. plots between isotropic (full profile refinement using GSAS) and the anisotropic (individual peak fitting) effects. Here the sample was under 750 mbar oxygen p.p. at 600°C (quite well into the Orthorhombic I phase region, x~0.78) and the data are deconvoluted from the instrumental broadening. The instrumental resolution curve was determined by measuring the diffraction pattern from a standard Si powder sample. It will be seen that the instrumental broadening is more or less independent of Q.

On a TOF (Time Of Flight) instrument, the time uncertainty due to the moderator is normally proportional to time i.e. $\Delta d/d$ is independent of d and hence ΔQ should increase with Q. However, on OSIRIS (the diffractometer that was used in this work; ISIS), there is a further contribution to the resolution due to the wavelength dependence of the critical angle in the incident neutron guide tube, i.e. $\Delta\theta \sim\sqrt{\lambda}$. This term will tend to reduce ΔQ as Q increases and hence, the overall broadening is more or less independent of Q.

It is clear that the [110] and [220] reflections show small sample dependent broadening, whereas the [*h00*] reflections are substantially broadened. This is clear evidence that (110) twinning is present. The extra broadening seen in [111] & [113] reflections is clearly due to limited crystallite size or mainly strain effects in the *c* direction.

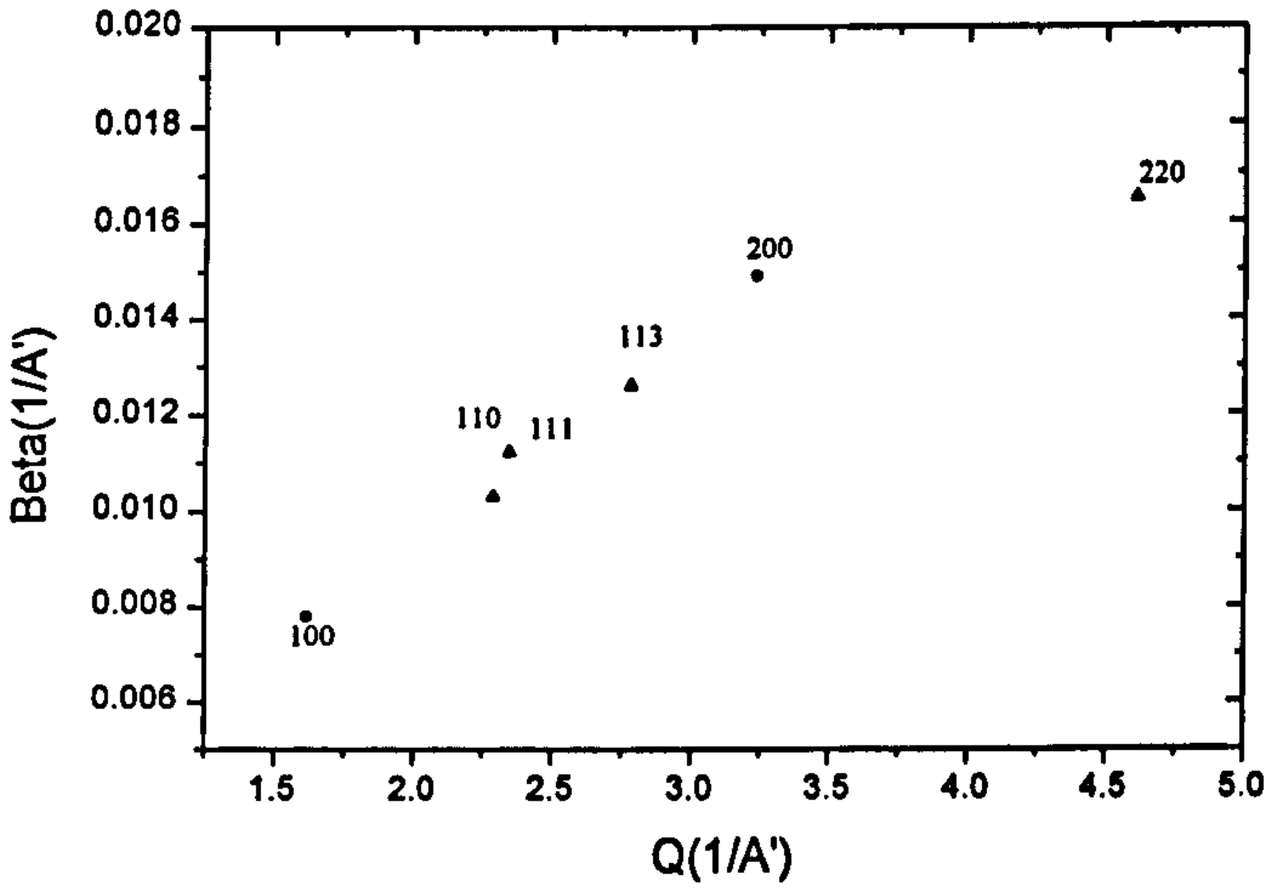

Fig.(7.46b) The sample under 0.5 mbar oxygen p.p. at 500°C (tetragonal phase)

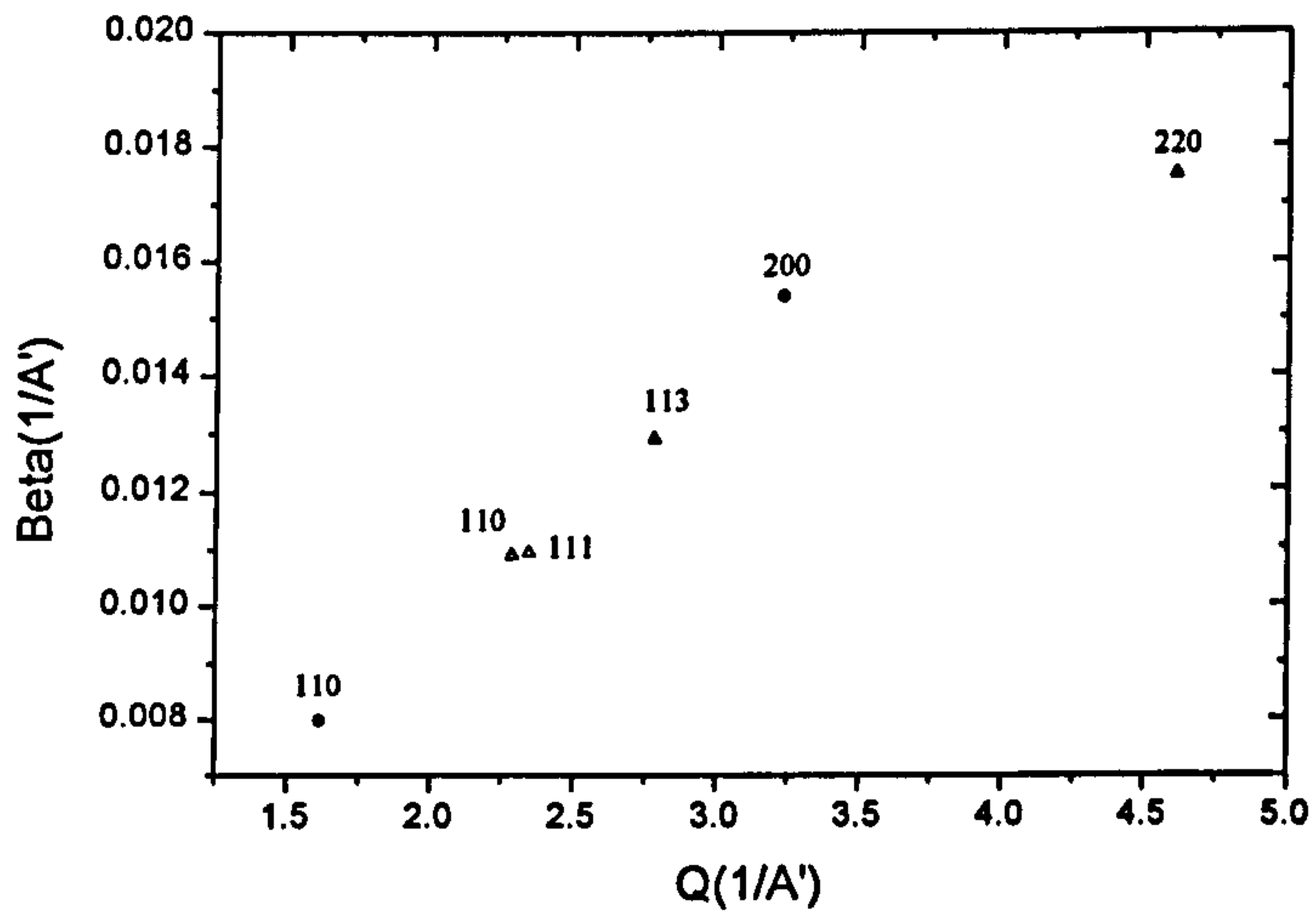

Fig.(7.46c) The sample under 1.5 mbar oxygen p.p. at 500°C (tetragonal phase)

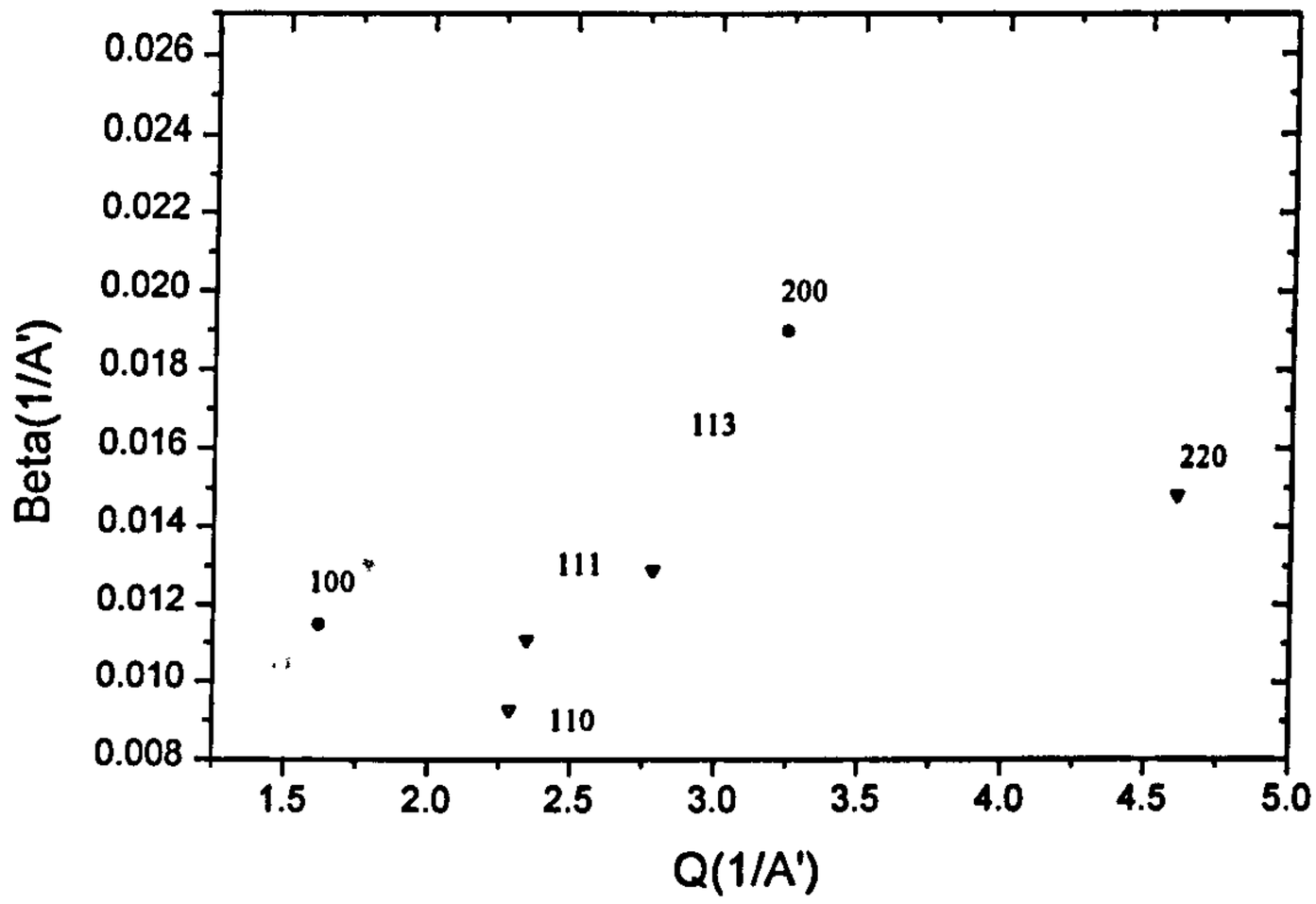

Fig.(7.46d) The sample under 4.5 mbar oxygen p.p. at 500°C (orthorhombic phase)

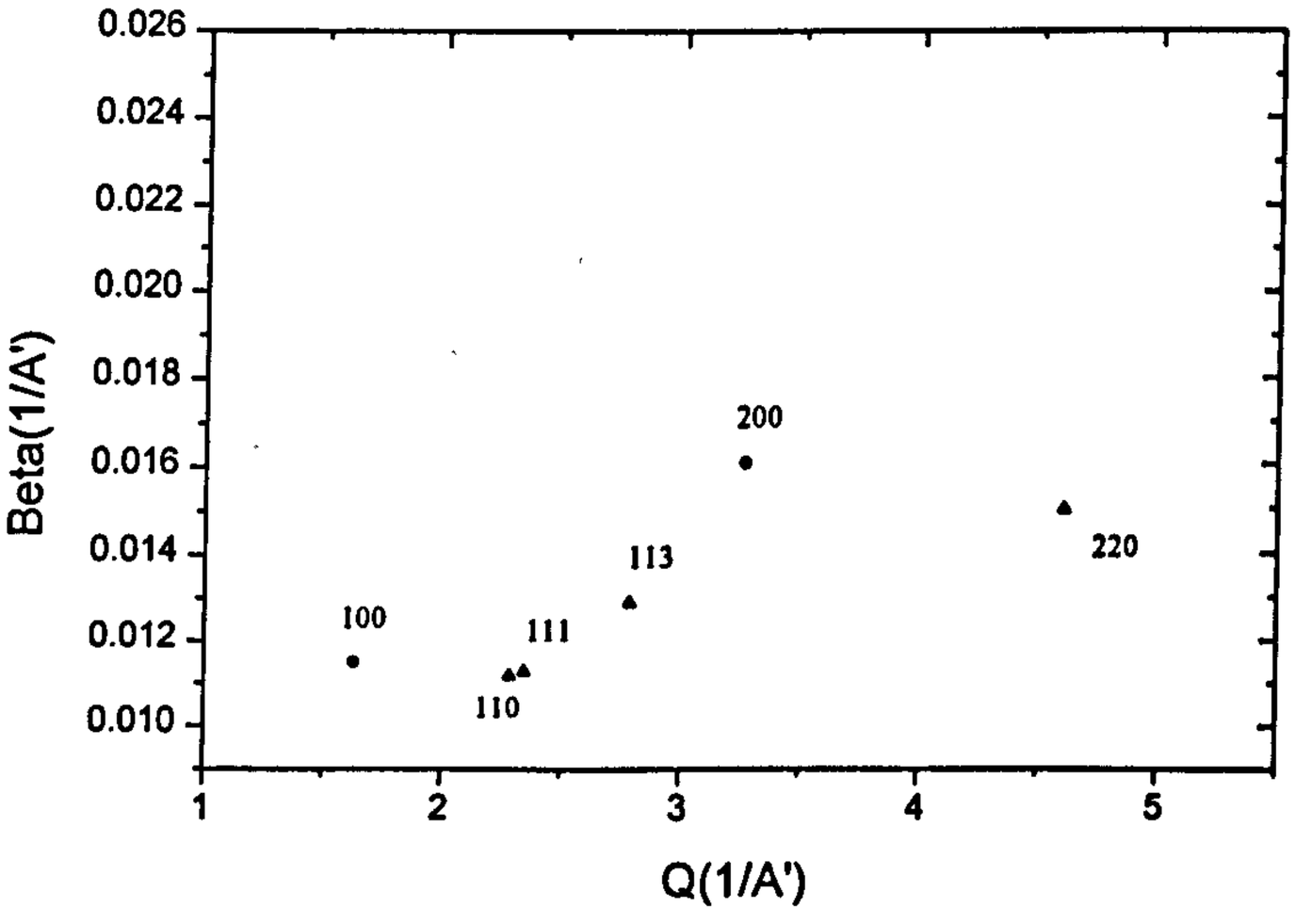

Fig.(7.46e) The sample under 150 mbar oxygen p.p. at 500°C (orthorhombic phase)

Fig (7.47) shows a similar results for the *in-situ* powder neutron diffraction isotherms at 550°C.

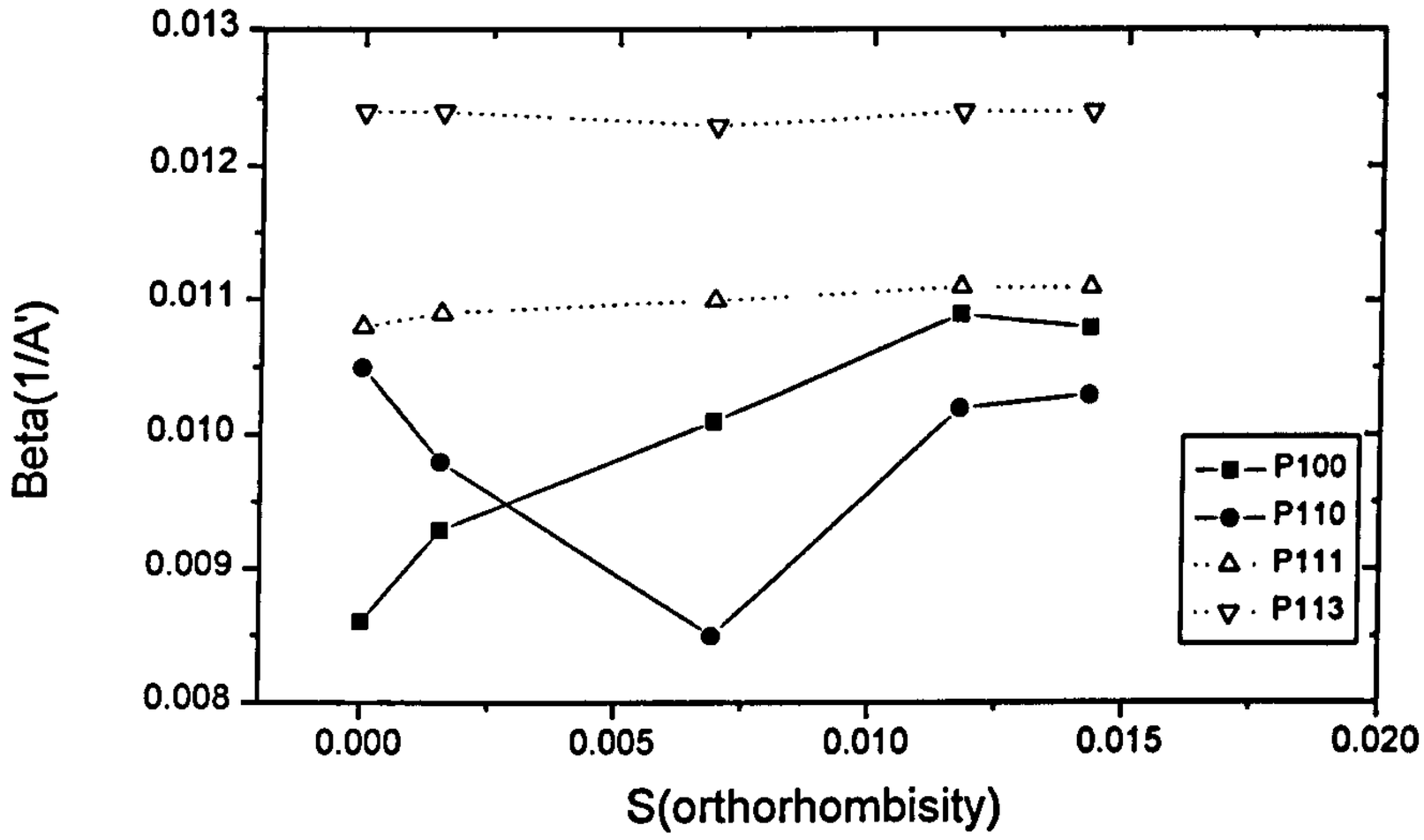

Fig.(7.47) Variation of the peak widths in reciprocal space with Orthorhombicity (∝ the oxygen p.p.) at 550°C.

Figure (7.48) illustrates the broadening values for the two separate powder x-ray diffraction experiments on the same sample in the tetragonal ($x \approx 0.15$) and orthorhombic ($x \approx 0.95$) phases at 300°C. The peak widths from these data are also plotted against Q spacing. The 300°C has been chosen because it was the highest temperature available for the furnace on the XRD instrument.

Again the same behavior for the breadths of the sequential peaks in the tetragonal and orthorhombic phases can be seen. The broadening in the Tet. phase is large and varies smoothly with Q.

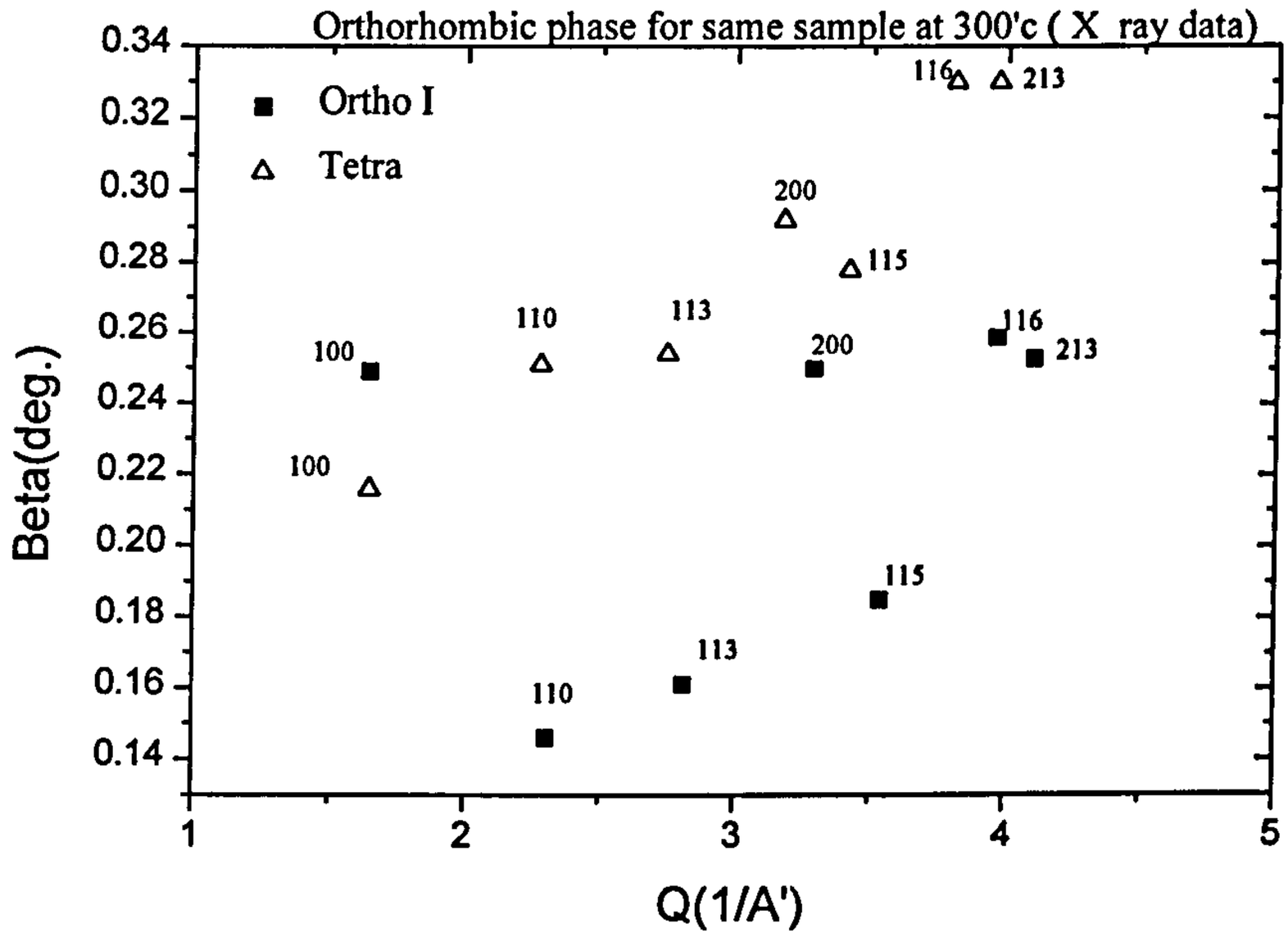

Fig.(7.48) Broadening data in Q space for x~0.95 (OI phase) and x~0.15 (Tet. phase). The x-ray results show the same trend as in Figs.(7.44_45) , for the sequences of the peak widths for both OI & Tet phases.

This section ends with a comparison between [*0h0*] and [*h00*] line widths at 500°C and 600°C. From Figs.(7.49a_b) it is clear that, the [*0h0*] reflections are substantially broader than [*h00*] lines just after Tet/OI phase transition (*S*~0.) but with increasing *S*, the widths of the two series of reflections come closer together. It is because the occupancy of the (0,1/2,0) *b*-chain sites take place faster than the decrease of occupancy of the (1/2,0,0) sites [Goncharov et al; 1993]. Since the oxygen ordering process in the orthorhombic phase contains forming clusters of short parallel b-chains in the basal plane, the partial relaxation of internal stresses between them is likely to occur during chain growth.

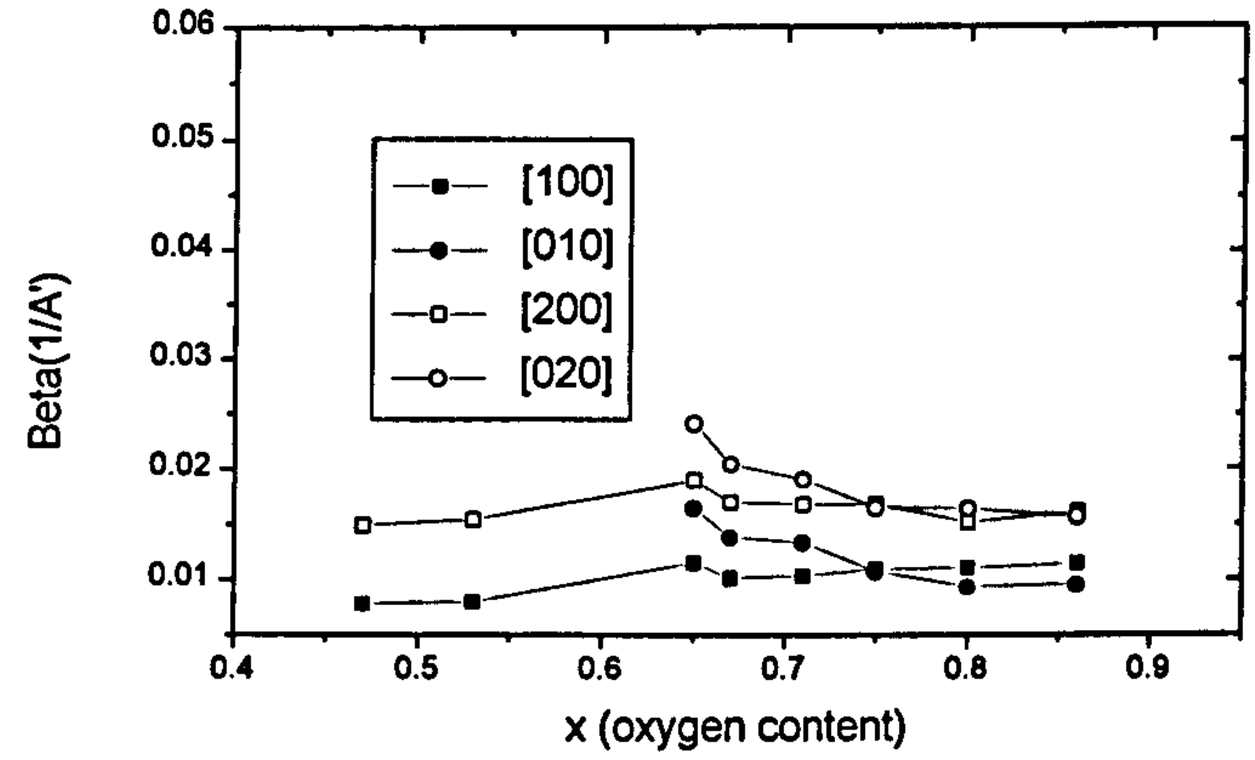

(a) At 500°C

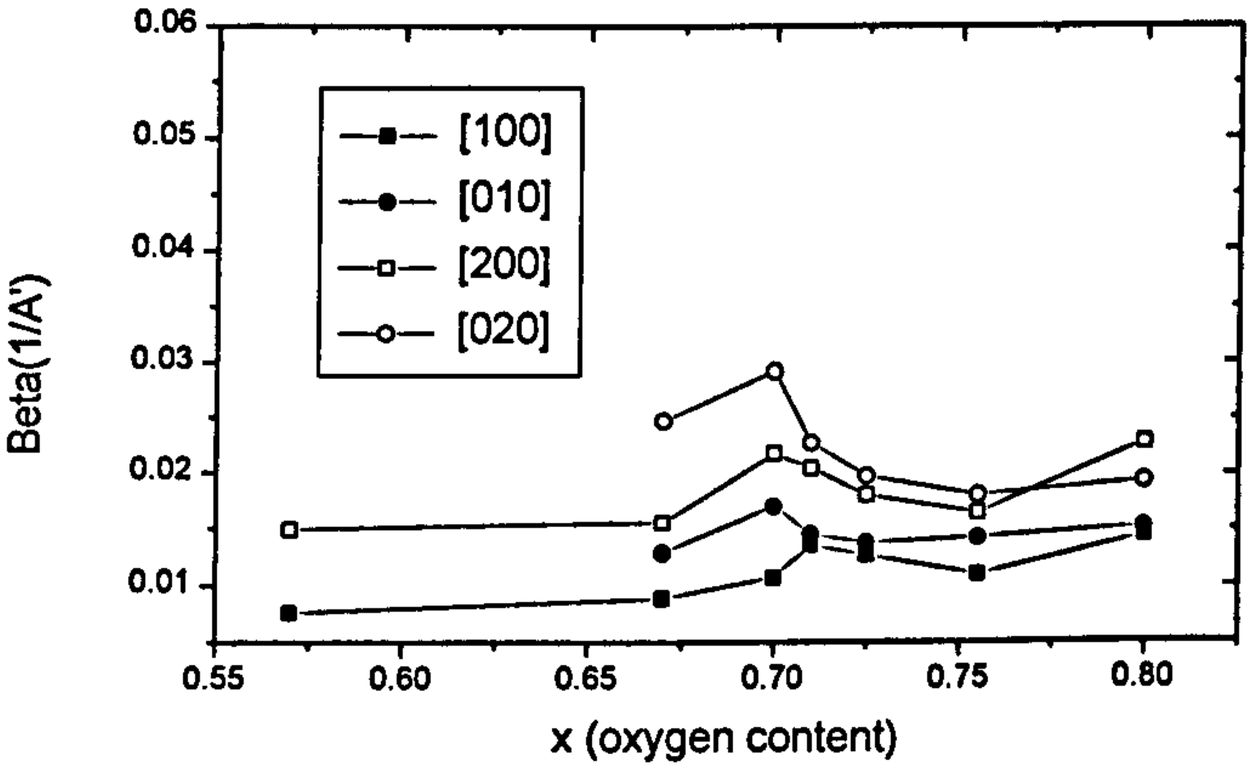

(b) At 600°C

Fig.(7.49) A comparison between [*h00*] and [*0h0*] line widths a_ at 500°C, b_at 600°C

VII.5) COMPARISON OF MODEL WITH DATA

Based on the simple model presented in section VII.3, it is possible to simulate the powder diffraction peaks and compare them with their corresponding measured profiles. Figs.(7.50_51_52) show reasonable consistency between the model and the measured diffraction patterns for the [200]&[020] and [100]&[010] reflections. Although the model is very simple and just includes the Cu atoms in the basal plane (at the corner of the rectangular in the Fig. (7.28)) and the presence of oxygen atoms counted as changing the *S* (orthorhombicity) values, but there is good agreement between the main features of the calculated pattern and the diffraction profile such as their widths and the relative intensities between them. In Fig.(7.52), the model predicts a broad single peak made of two superposed [100]&[010] peaks and the data conforms that. The discrepancy between their widths is due to the value of T (the number of (110) planes in each twin lamella).

One of the prominent points of that model is the prediction of a central peak corresponding to a range of *S*x T values before a complete separation between [*h00*] and [*0h0*] reflections, during the tetragonal to orthorhombicl phase transition. For the reasonable match between the model and diffraction pattern in Fig.(7.50), it is possible to estimate the twin's width in terms of the value of T roughly (because the *S* value for the diffraction profile and the model calculation is very close). Fig.s(50a_b) suggest an estimate average value of T~50 for the sample at 500°C under 10 mbar oxygen p.p.

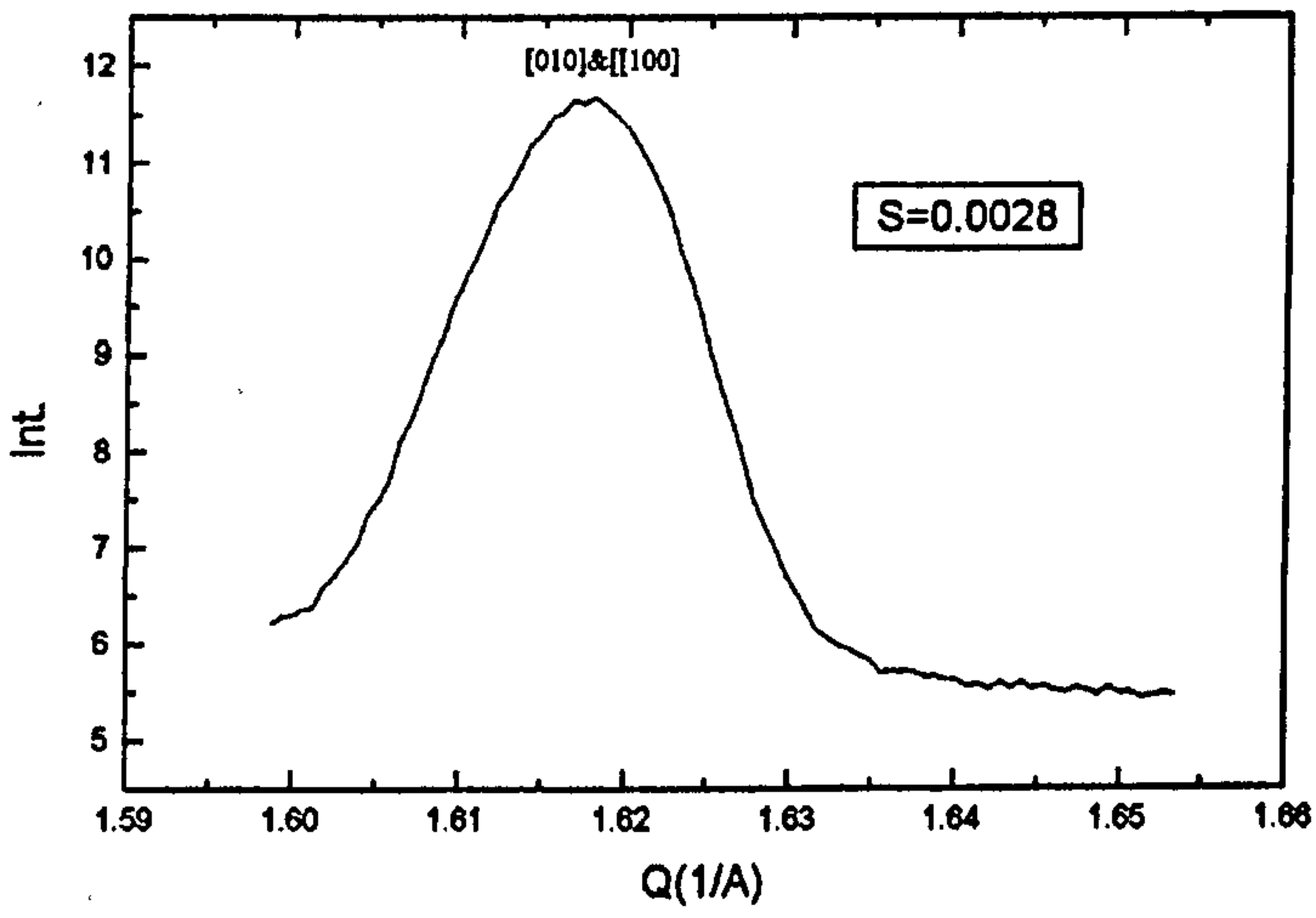

(a)

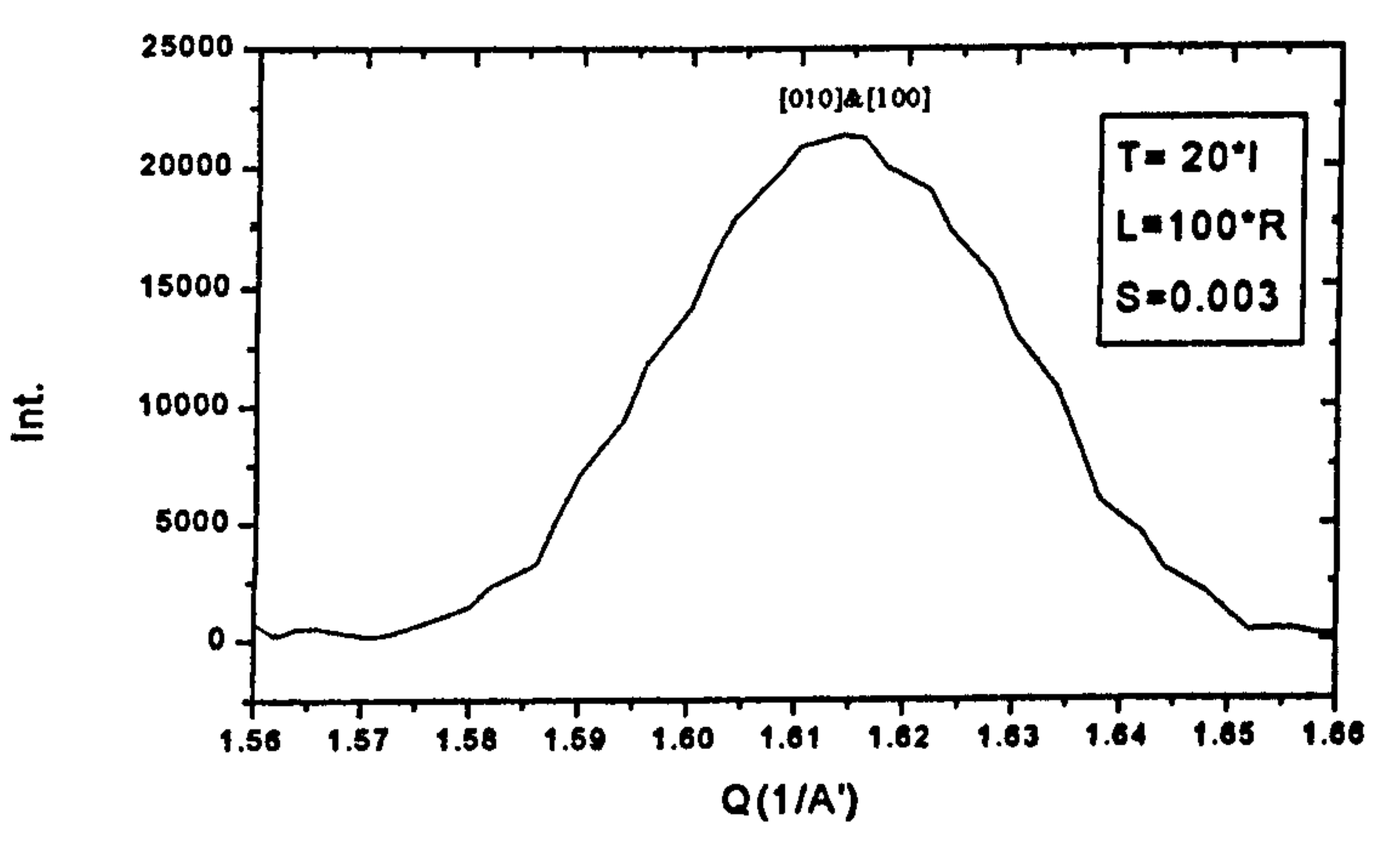

(b)

Fig.(7.52) a_ The diffraction pattern under 4.5 mbar oxygen p.p. at 500°C, b_ The calculated profile. Obviously the calculated model is broader than the data and this is due to insufficient value for T in the calculation and the comparison would be better for a higher values.

The effect of the presence of the central peak on some reflections at higher d-spacing region has probably misled some authors to conclude the co-existence of the tetragonal and orthorhombic I phases [Fig.7.53 ; Rand et al(1993)], from which it can be concluded that the Tet/OI phase transition is first order!. In contrast to many other reports, this work, using the mixed model for full profile refinements, leads to a worse result in all cases.

Figs.(7.54_57) show the effect of the central peak on the [100]&[010] profiles shape at 500°C. The pattern in Fig.(7.57) shows two different fits with and without central peaks to clarify the effect of presence of the central peak.

In general, according to Eq.(7.2) the higher intensity of the central peak (c.p) indicates a lower width for the twin's stripe and vice versa. As is clear, the intensity of the central peak gradually decreased with increasing the oxygen p.p., but the unexpected fairly high intensity for the 150mbar oxygen p.p. pattern indicates that, for high values of S (~0.018 in this case), as the Mean Field Theory predicts [Sarikaya et al; 1988], T can be independent of S. Therefore this is attributed to the fulfilling the coherence condition by limited values of T (section VII.3).

Figs.(7.58_60) show the same trait for [100]&[010] reflections at 600°C

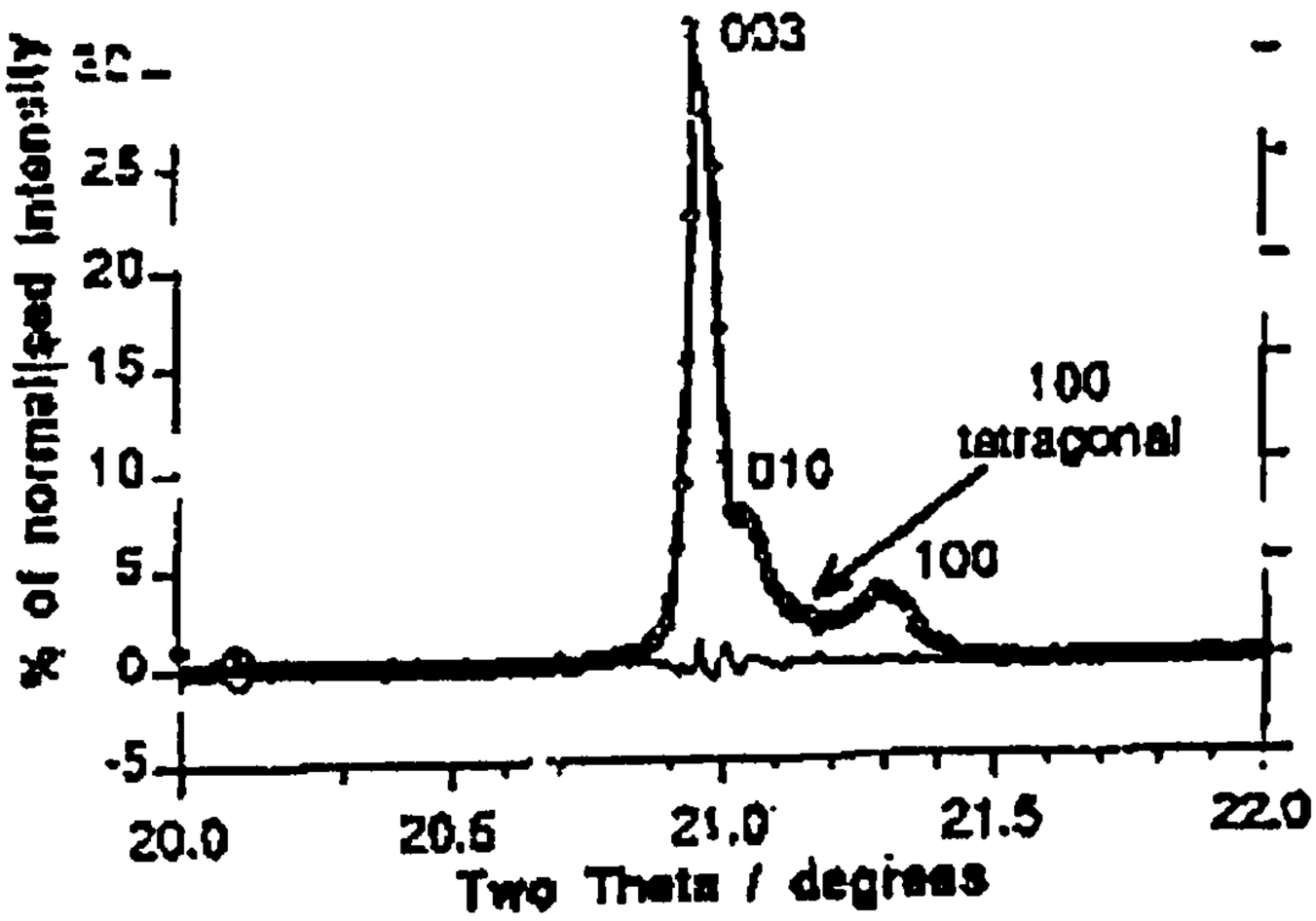

Fig.(7.53) The[003-010-100] peak group is successfully modelled by including a tetragonal component[from Rand et al; 1993]

IV.6) CONCLUSION

In this chapter firstly, it has been investigated whether the T/OI phase transition is a second order transition. There is good agreement between the results and those of other studies.

Secondly, the effect of twining on the diffraction pattern has also been investigated.

The simulated pattern shows line broadening, as expected from a twinned system as the number of planes in each twin and the orthorhombicity both approach zero. Then the observed diffraction peak shapes for YBCO were measured in equilibrium as a function of oxygen partial pressure has been analyzed and have shown that the observed broadening was consistent with the model that the lattice is twinned in the <110> direction in the orthorhombic phase and that the number of lattice planes in each twin increases from zero at the T/O phase boundary in a similar way to the increase in the orthorhombicity. The prominent aspects of the results from the model are:

a) Diffraction from a sequence of thin twinned regions can show a diffraction pattern that looks like a mixture of orthorhombic and tetragonal phases so that care must be exercised in concluding that there is a two-phase region in the phase diagram.

(b) The [*hh0*] reflections always remain much narrower than the others, consistent with (110) twinning.

(c) The x-dependence of the [*h00*] reflections is consistent with a model in which the width of twins increases with increasing orthorhombicity

(d) The variation in the (00l) reflections suggests that the appearance of the OI phase introduces anti-phase boundary faults in the c-direction

(e) By comparison of the calculated and real data, it is possible to estimate the twin's widths in their early stage of formation.

Chapter VIII

CONCLUSIONS AND RECOMENDATIONS

VIII.1) CONCLUSIONS

A high purity $YBa_2Cu_3O_{6+x}$ powder sample was studied using oxygen partial pressure controlled *in-situ* high resolution x-ray and neutron diffraction. Oxygen composition and structural changes, were measured in the temperature range 200°C - 300°C and 500°C-600°C, with oxygen pressure range vacuum to 1bar. The results obtained join the ranks of the plethora of previous and often contradictory studies.. These contradictions often occur due to experimental errors. It was found that the utmost care is required in experimental procedure, to gain information on this system, due to the low equilibrium oxygen pressures and the slow kinetics encountered. Results obtained form a reference for sample preparation and processing, and act as a comparison to predictions from theoretical models of the system. They also provide important information regarding the microstructure which can be used to understand technical implications of these materials related to the weak link behaviour and other physical properties. The results were found to be close to the most reliable of the earlier measurements.

The main conclusions of this thesis are:

a) The character of the YBCO's OII superlattice region of the structural phase diagram at elevated temperature (200°C-300°C) has been studied by powder x-ray *in-situ* and by complementary neutron powder diffraction, whereas the majority of the previous experimental data comes from high resolution electron microscopy (HREM), or single crystal neutron diffraction. In this work, it was presented some strong experimental evidence to support the **first order** characteristic transition between tetragonal and OII phase in agreement with Khachaturyan (1988) and the de Fontaine model [Wille & de Fontaine; 1988].

b) We have also seen some evidence of a first order transition feature for the other part of the low and elevated temperature zone of the phase diagram between the OII and OI phases, but this still needs more studies.

c) The other interesting point in this work was the observation of the OII diffraction features at 300°C in contrast to the other reports that limited it to less than 150°C [Poulsen et al; 1996] & [Schwartz et al;1993], so it seems the boundary of the OII phase region in the YBCO's structural phase diagram must be corrected at least up to 300°C.

d) The tetragonal to OrthoI phase transition was found to occur over a small range in concentration ($O_{6.52}$-$O_{6.6}$) at high temperatures (500°C-600°C). These observations were made using the neutron diffraction study; and were in agreement with several previous studies (Jorgensen 1987, Schleger 1992).

e) An *hkl* dependency of the peak width was found to occur after the tetragonal to OrthoI phase transition. This dependency was due to different domain dimensions in different directions, as a result of twins forming. The [*hhl*] peaks were found to be sharp, as their direction extends along the diagonals of the lattice cell and therefore these planes remain coherent at the twin domain boundary. The [*hhl*] peak width is thus a measure of the dimension of the grain in which the twins lie. The[*h00*] peaks were found to be broad and are determined by the dimensions of the twins, as the coherence in these planes is lost at the twin domain boundary. This observation is in agreement with David (1989), Poulsen (1991) and Rand (1993), but was much more pronounced in the present study.

f) The microstructure was found to change immediately before and after the tetragonal to OrthoI phase transition. These changes were concluded to be due to the variation of the tweed-twin structure. Indications of this were observed in the Williamson-Hall analysis of the neutron diffraction patterns.

g) The twin domain size was found to be proportional to orthorhombicity, just after the T/OI phase transition at a constant temperature. For higher values of orthorhombicity (≥ 0.09) the twin domain size seems to be independent of orthorhombicity in agreement

with theory (Khachaturyan 1983, Sarikaya 1988, Xu 1989). This was determined from the peak widths of diffraction patterns.

h) A picture was found to emerge of the structural changes as follows: in the tetragonal phase the oxygen atoms are always ordered in the form of short chains in small clusters, with an equal amount ordered in the a and b direction. As the tetragonal to OrthoI phase transition is approached the clusters grow, resulting in a tweed-like pattern. This ordering of the oxygen atoms results in strains or mismatches along the c-direction which produces a lack of coherence and broad [*00l*] peaks. At the transition the oxygen orders along a preferred direction resulting in a macroscopically orthorhombic structure, but the strains produced by the orthorhombicity cause twins to form. As oxygen is added at a fixed temperature the orthorhombicity increases and thus increases the strain and the twin's interfacial energy which results in a fluctuation in the size of the twin separation.

VIII.2) RECOMMENDATIONS

Recommendations will be separated into two groups; the first contains proposed improvements and extensions of the phase boundary study for OII and OIII phases, and the second involves proposed development in the modeling of the neutron diffraction studies from a twinned sample.

i) In this study, one interesting issue is the existence of a mixed (T+OII) phase region at elevated temperature range (200°C-300°C) which indicates strongly that the T/OII phase transition is a first order transition, but the extension of the mixed region has been estimated by linear extrapolation, whereas it seems more accurate data are necessary to define the extension of the fairly complicated superstructure areas in the orthorhombic phase region.

Using an Intelligent Gravimetric Analysis (IGA) equipped with an ultra high vacuum system would enable us to make samples with the exact expected stoichiometry for OII ($0.4<x<0.7$) and OIII ($0.7<x<0.85$). The use of a low thermal mass furnace would allow more accurate control of the sample temperature and a temperature-controlled room would allow measurements to be performed over longer time periods. This would allow the full characterisation of points in the phase diagram where slow time dependencies were encountered.

The inspection of the character of these phase transitions character (whether they are first or second order transition) and the existence of any super structural effects along the *c* direction could be the most prominent aspects of this study.

ii) Diffraction studies from the twinned system could be improved by modifying the model to include the random fluctuations of the twin's boundary separation and by taking into account the presence of oxygen atoms in the basal plane (O(1)& O(5) sites) an appropriate corresponding probability (Metropolis algorithm in Monte-Carlo method; 1953).

This is important especially because in Eq.s(3.3-7.19) the twin spacing is proportional to the square root of the twin's interface energy, γ, and this quantity rationally has a functional relation to the oxygen content and therefore to the orthorhombicity, *S*. The

investigation for the shape of this functionality will define the appearance of twins just after the T/OI second order phase transition.

This model which has been improved properly in the present work, can be used to analyze more neutron diffraction measurement data when they are collected around the phase boundary. As Fig.(7.43) shows, the de-convoluted width of the most important [110] reflection is almost comparable with the resolution of the OSIRIS (at ISIS; U.K), thus in order to get more accurate data, it is suggested using a high resolution neutron diffractometer.

One of the interesting finds of the present study was the evolution of the *hkl*-dependent peak widths, which provides information about the extent of domains in different directions. Unfortunately, neutron time is heavily in demand and is difficult to obtain but this type of study could be performed successfully, using a good laboratory x-ray diffraction kit. The x-rays will be sensitive to the coherence of the domains in the same way as neutrons. Development of a pressure controlled chamber and temperature stage for the *in-situ* measurements is required and efforts are presently being made to this end. Unfortunately, for the present XRD system the available temperature stage is restricted to temperatures below 300°C, but interesting work remains to be done in this range.

A Rietveld refinement model containing *hkl*-dependent peak width parameters should be developed to allow more accurate determination of the lattice parameters and oxygen contents. The model could also be designed to refine the domain dimensions, in each *hkl* direction, from the whole pattern rather than from an individual peaks as done at present.

APPENDIX A

THEORETICAL MODELS OF OXYGEN DIFFUSION AND PHASE TRANSITION IN YBCO (0<x<1)

Introduction[1]

A very significant amount of experimental data exists on the x-T structural phase diagram of $YBa_2Cu_3O_{6+x}$ and all these need a theoretical framework to be fit in. In principle, a satisfactory theoretical model should address both structural and thermodynamic aspects of the problem:

1) All the observed YBCO phases, including the ordered phases (OII, OIII, etc.)
2) The nature of the phase transition boundaries and (the possible) the miscibility gaps between them
3) The exact position of the phase boundaries
4) The O(1) and O(5) oxygen occupancies as a function of x and T
5) The oxygen chemical potential as a function of x and T, for comparison with the measured values of oxygen p.p.

The general approach goes under the name of *lattice gas model.* Here the equilibrium states are calculated exactly in a mean-field approximation, based on an isotropic long-range interaction between oxygen atoms in the basal plane. [Khachaturyan et al; 1988]. It has been proved that the superconducting properties of YBCO are strongly dependent on the oxygen ordering in the Cu-O basal plane. The most prominent feature of

[1] A very useful summery of the theoretical models, has been presented by Radaelli (1998)

Khachaturyan's phase diagram is the presence of a miscibility gap between the Tet. and OI phases at finite temperatures.

Another approach was adopted by de Fontaine et al (1987) in which they considers two sublattices of oxygen atoms α and β (equivalent to the O(1) and O(5) sublattices), and includes in the calculation only short-range interactions: a nearest-neighbor (NN) inter sublattice interaction potential V1, and two next-nearest-neighbor (NNN) inter-sublattice interactions: V2 ("intra-chain", through the Cu atoms) and V3 ("intra-chain", through the "empty" site (1/2,1/2,0)) This is equivalent to an Ising model with asymmetric NNN interactions, and is often called ***ASYNNNI*** model (following section).

Many of the computational models used to study the behaviour of oxygen in $YBa_2Cu_3O_{6+x}$ as a function of chemical potential (oxygen partial pressure) and temperature have been performed using a 2-D lattice. As a first approximation this is valid, due to the fact that only the O(1) and O(5) sites are available for occupancy and, as mentioned before, diffusion in the *c* direction is much smaller than in the *a*-*b* plane. Initially, only short-range Columbic interactions between oxygen atoms were considered and quite good agreement was found between these 2-D models and the tetragonal to OrthoI phase transition at high temperatures, but details of the microstructure could not be accurately modeled. The three interaction parameters considered in this type of model are shown in Fig. (A.1).

At least three distinct phases have been observed experimentally. A tetragonal phase in which the Oxygen sites are randomly occupied and somehow evenly short O-Cu-O chains in *a* and *b* directions, when $x < 0.4$. At high Oxygen concentrations ($x = 1$) there is a stable orthorhombic phase, orthorhombicI (OI), corresponding to the 92°K superconducting critical temperature, T_c. In this phase there are ordered long. O-Cu-O... chains along the *b* direction. In the intermediate concentrations ($x = 0.5$) there is another stable orthorhombic phase, orthorhombic II (OII), which has the 60°K T_c.
This phase is composed of long ...O-Cu-O... chains also along the *b* direction too but in every other columns.

The experimental investigation for the structural phase boundaries (T-x, phase diagram) on YBCO is very controversial due to the fact that the final structure of the system is severely affected by the using different processing methods for making samples from the raw materials.

Later models introduced strain parameters, charge degrees of freedom (the energetic contributions, due to the doping effects of the oxygen in other regions of the structure) and longer-range Coulombic interactions. Such models had a greater success in accurately modeling this system (Schleger 1994, Parlinski 1993, Salje 1991, Semenovskaya 1993). One such model, concerns the evolution of the microstructure, when passing through the tetragonal to orthorhombic phase boundary (Salje 1991, Parlinski 1993).

A.1) The Model

The model that has been used to investigate the process of Oxygen diffusion in the basal plane of YBCO is called "*ASYNNNI* " (ASYmmetric Next Nearest Neighbours Ising). This model was first described by de Fontaine et al. in 1987. In this model the basal plane in YBCO has been simplified by two interlocking square lattices, For one, the Oxygen sites placed up to each Cu site (0.5, 0), and for another, the Oxygen sites are on the right hand site of each copper atom (0 ,0.5).

Three types of interaction are assumed in this model, they are Fig.(A.1a):
V1 : Repulsions between nearest neighbor Oxygen atoms, 6.9 mRy.
V2 : Attraction between two O atoms by intervening a Cu atom which it is responsible for forming the O-Cu-O chains,-2.4 mRy.
V3 : Repulsion due to next nearest neighbor Oxygen atoms without intervening a Cu atom, 1.1mRy. It is believed that this interaction causes the formation of the OII superlattice structure.

The basal plane is represented in the program by an N x N lattice. Here N is twice of the number of Cu atoms minus one.

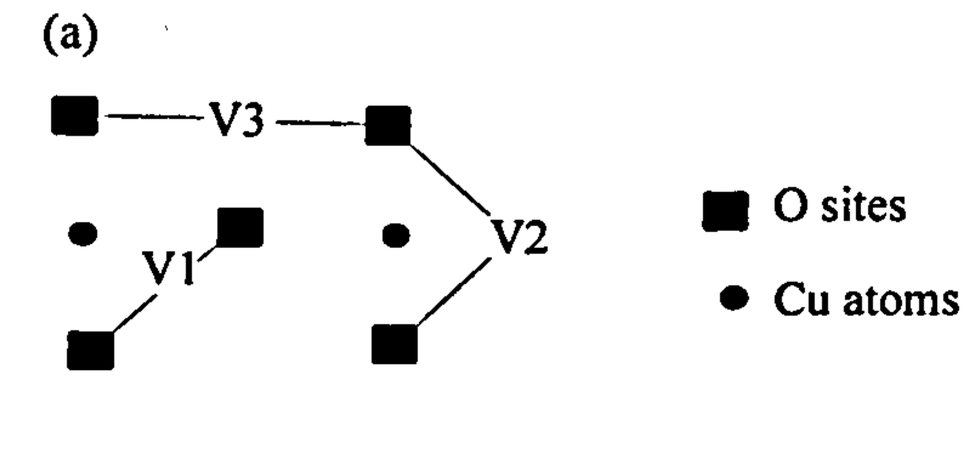

Fig.(A.1) a_ The interactions b_ Available O sites on the basal plane shown by squares

The system's total energy, Hamiltonian, H, for these interactions, according to the popular Ising model, is written as in Equ. (A-1) below, where C_j is the site occupancy variable for each Oxygen site j, e.g. $C_j = 1$ if the site is occupied, and 0 if it is not.

$$H = \sum_{i,j}^{nn} V_1 C_i C_j + \sum_{i,j}^{nnn(nonCu)} V_2 C_i C_j + \sum_{i,j}^{nnn(Cu)} V_3 C_i C_j \qquad \text{(A-1)}$$

The first summation accounts for the number of filled nearest neighbor oxygen sites. The second and third summations take into account the next nearest neighbor sites separated by and not separated by a copper atom respectively. The Hamiltonian is minimized when the system in favor of the V2, with forming more O-Cu-O chains.

At low and intermediate values of temperatures and concentration (T & x) this tendency produces the OII phase and at higher T & x (T>300°K & x > 0.6), the OI phase would be favored. The Oxygen ordering processes in YBCO take place in the Cu-O basal plane and this is the only part of the system which is modeled in the program. There are also experimental facts that the oxygen diffusion take place within the individual basal planes and not from one plane to the other.

Alternative models-

Beyond the 3-potential *ASYNNNI* model, at zero temperature, only completely ordered phases are expected to be stable. However, only OI, Tet, and OII phases, which are partially disordered for all oxygen contents expect for x=0.,0.5 and1.0 respectively, are present in the x-T phase diagram calculated with the above model. Higher-order phases can only be stabilized by a longer-range interaction potential, presumably a long-range extension of the inter-chain V3 potential. In fact, Monte Carlo simulations including an additional next-nearest chain(NNC) repulsive term yield a series of full-chain-ordered superstructures at zero temperatures [de Fontaine et al; (1990) and Ceder et al; (1991)].

In the *ASYNNNI* model, internal degrees of freedom, such as a mobile charge and unpaired spin, which can be created on the O-Cu-O chains because of oxygen doping to the basal plane, are being ignored in the Hamiltonian (Equ. A-1). It has been proposed that the introduction of these factors into ASYNNNI model leads to a better agreement between the model and the experimental T/OI phase transition [Schleger et al; 1994].

Haugered , 1997, used another model called ***Extended ASYNNNI*** to describe the free energy of short O-Cu-O chain fragments, whilst preserving the standard ASYNNNI model for long chains. This means using a modified temperature dependent V_2 interactions energy for Oxygen jumps that evolve short chains

A.2) MONTE CARLO METHOD

The Monte Carlo method in statistical physics is a numerical technique for studying how systems approach a thermodynamical equilibrium state. Its name indicates the vital role of random characteristics of the method and it is executed by using a random number generator. The method really came into its own with the development of high speed digital computers. The first successful application of this method was carried out in 1953, when Metropolis et al. simulated a fluid by a rigid sphere model.

The main advantage of the Monte Carlo method is that it gives numerical information in which the only assumptions made are the effective interactions between different particles in the system and also that "only one particle can occupy each site position". The method is exact in principle because the results are accurate except for statistical errors, which can be made as small as required by taking enough averages i.e. as long as one is prepared to invest in enough computer time.

Canonical Monte Carlo model or NVT (Number & Volume & Temperature constants) ensemble is used in the work presented here. The thermodynamic average of various observable quantities <G>, such as the internal energy, is given by:

$$< G >= \frac{\sum_{x} G^{x} \exp(-H_{x} / k_{B}T)}{\sum_{x} \exp(-H_{x} / k_{B}T)} \qquad \text{(A-2)}$$

where G^{x} & H_{x} are in turns the value of an observable and the Hamiltonian of the system at the configuration x.

In its simplest form a Monte Carlo integration would proceed by repeatedly choosing a configuration at random, calculating the observable quantity G^{x} for this configuration and the weighting the result by a probability as: $\exp(-H_{x} / K_{B}T)$. After a large number of configurations which they are sampled, the average value of G, <G>, can be found. The above simple random sampling method is, however, a very inefficient way of

calculating <G>. This is because of the term $\exp(-H_x / K_B T)$ varies over many orders of magnitude at most of the interesting temperatures. Also only a relatively few configurations contribute significantly to the average. This means that too much time is spend sampling unimportant regions of low probability and hence of low weighting factor, which in turn would produce a very inaccurate estimate of <G>.

A more efficient approach is "***importance sampling***" techniques to generate configurations according to some probability and then weight them evenly, i.e. to take a average over a canonical distribution for all available configurations. This achieved using a technique originally outlined by Metropolis.

If the sampling of the configuration is not carried out randomly, but according to some probability P_X, the thermodynamic average becomes:

$$<G> = \overline{G} = \frac{\sum_{x=1}^{Nc} G^x P_x^{-1} \exp(-H_x / k_B T)}{\sum_{x=1}^{Nc} P_x^{-1} \exp(-H_x / k_B T)} \qquad \text{(A-3)}$$

where Nc is the total number of configurations used. An obvious choice for the sampling probability is the Boltzmann distribution itself, i.e.

$$P_x \propto \exp(-H / k_B T)$$

and so we can write : $$\overline{G} = \frac{1}{Nc} \sum_{x=1}^{Nc} G^x \qquad \text{(A-4)}$$

Configurations cannot be rejected from this average simply because they are the same as previous configurations, neither can this be rejected on energy grounds. However any set of configurations selected randomly, or sequentially, will have a Boltzman distribution and so will yield a valid average.

It is possible to generate a sequential series of configurations such that each configuration can be obtained from the previous one by applying a transition probability $P_{x-->x'}$. In other words, it is possible to generate a random walk of points, such that the transition

from one point x, to the next x', is governed by the transition probability $P_{x-->x'}$. In the limit where Nc becomes infinite it can be shown that [Gould & Tobochnik; 1988] :

$$P_x P_{x-->x'} = P_{x'} P_{x'-->x}$$

so the ratio of transition probabilities is given by :

$$\frac{P_{x-->x'}}{P_{x'-->x}} = \exp(-\delta H / k_B T)$$

where (A-5)

$$\delta H = H_{x'} - H_x$$

normally the transition probability is chosen to be:

$$P_{x-->x'} = \exp(-\delta H / k_B T) \quad \text{if} \quad \delta H.>0 \qquad \text{(A-6)}$$

$$= 1 \quad \text{if} \quad \delta H \leq 0$$

this allows you to decide whether a given jump will occur by comparing the transition probability to a random number, r, in the range $0 \leq r \leq 1$.

The above procedure generally called ***Metropolis algorithm*** .

A.3) LIMITATIONS

Size of the system- One of the biggest problems associated with the Monte Carlo method is the necessity of performing calculations on a lattice which contains a fairly small number of particles (relatively small size of 2D basal plane) whereas the real system probably contains around 10^{26} particles.

Obviously the results gained from such a small system have to be examined to see if they are relevant to the macroscopic system, so it is important to use different lattice sizes to investigate these finite size effects, thus in the present work, the dimension of the basal plane is varied arbitrarily.

Even if a relatively large lattice is used, care must still be taken to ensure that the boundary conditions used are compatible with the expected ordered structure at any temperature or concentrations. This is not a problem for the orthorhombicI structure as any lattice size is compatible. If this is not done, it can seriously affect the results.

Boundary Conditions -To keep the requirement of a reasonable computing time, the number of particles in the system cannot be too large. This means that suitable boundary conditions have to be chosen in order to minimize the resultant surface effects. This is easily achieved by using the so called periodic boundary conditions, as originally used by Metropolis et al. Under these conditions the system is supposed as a central box which it is surrounded by an infinite array of identical boxes i.e. we are deal with an quasi-infinite system. This is done by allowing a diffusing atom to leave the central box and enter the next one, since this box is identical copy of the central box, we can just let it re-enter the central box on the other side. Of course boundary conditions have to be used when calculating the energy of the old and new positions whenever a jump takes place near the edges.

Random Numbers – Since the Monte Carlo method is based on the creation of a random chain of configurations, it is important to determine whether or not the random number sequences that is used in the calculation, are truly random. These random numbers are generated by using some deterministic algorithms and so cannot be considered truly random. However, if for these number's sequences, it can be shown to somehow satisfy the statistical properties of a real random number sequence (i.e. have a uniform distribution in an specific range, and be free from any correlations), it is said to be pseudo-random and can be used in place of the real sequence. The uniformity of the distribution can be checked by generating a large number of random numbers, RN, then by dividing the total range into N equal intervals, the number of RNs that fall into the i_{th} interval, n_i, must be very close to n, which it defines as:

$$n = \frac{1}{N}\sum_{i=1}^{N} n_i$$

This means its Mean Square Deviation (msd), σ_n, must be small :

$$\sigma_n = [\frac{\sum_{i=1}^{N}(n_i - n)^2}{N}]^{\frac{1}{2}}$$

In this work the random number generator of the ***Turbo C***, TC, compiler has been employed and for checking this requirement, after generating of 25000 RNs in the range of [0,99] the results are acceptable, Fig.(A.2).

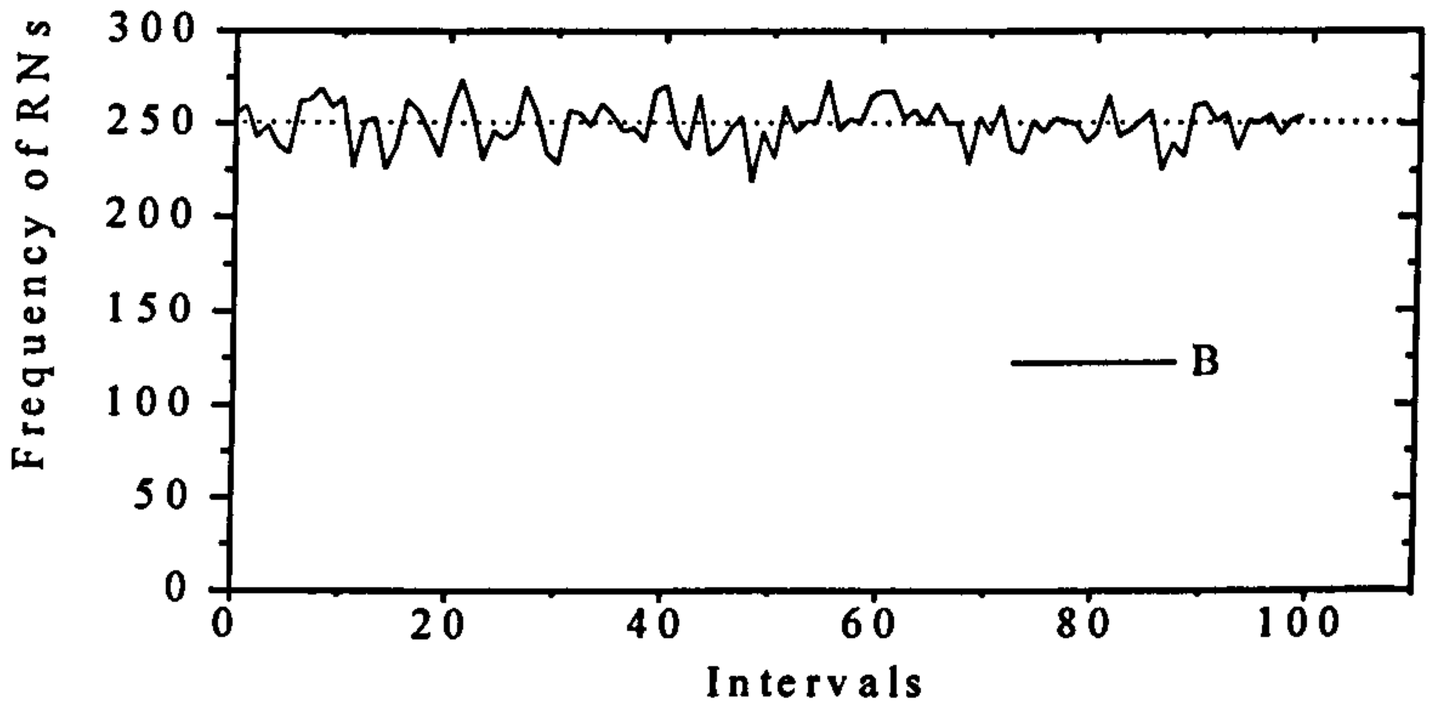

Fig.(A.2) Frequency distribution for turbo C random number generator, after generating 25000 numbers in the range of [0;99]

As is obvious, the number of RNs fluctuates around the expected value, 250 (the doted line). The σ_n is also small, 0.78, as expected. Fig.(A.3) shows the distribution of deviation of the numbers that fallen in each interval from the mean value , 250, can be fitted by Gaussian function.

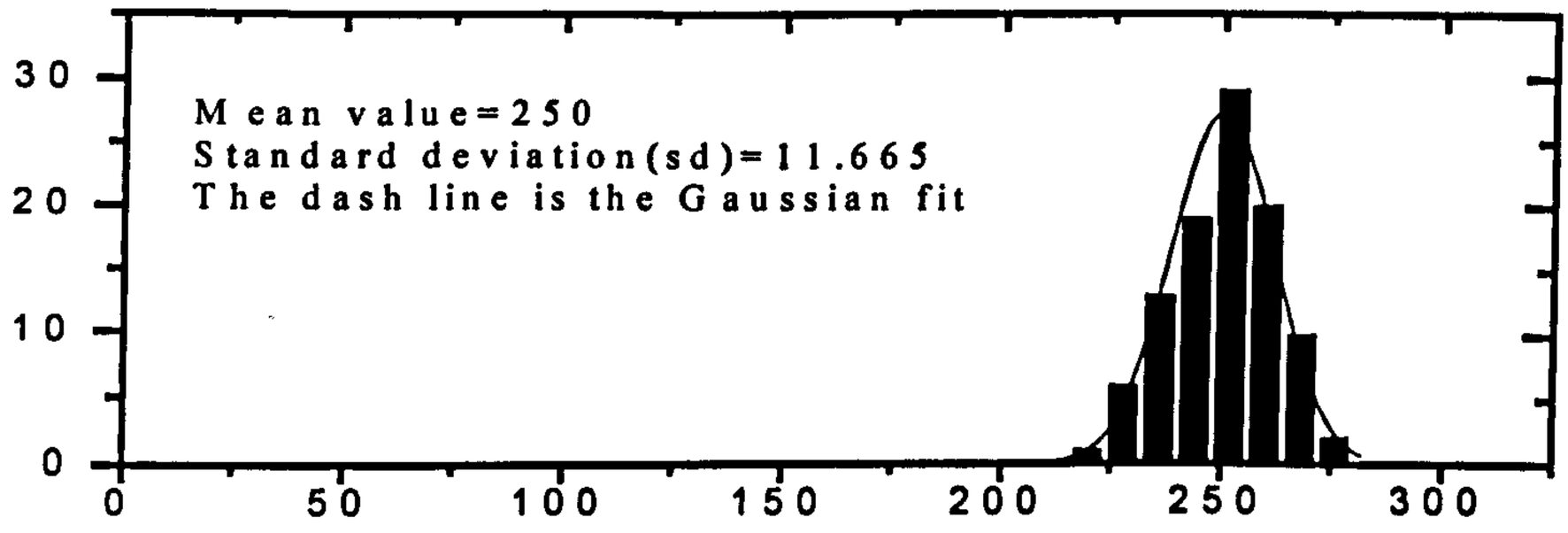

Fig.(A.3) Distribution of deviations against distance from the mean value

Some practical details of the Monte Carlo method

The first step in a Monte Carlo simulation for this system is to specify an initial state in which the available sites are populated with vacancies and oxygen atoms to the required concentrations. So, after producing a frame lattice consisted of the Cu atom sites, each allowed oxygen site first examined by a RN, if the RN is equal or less than the expected concentration, then that site will be loaded by an oxygen atom, otherwise it will be left as a Vacancy. In practice, the choice of the initial state has no effect on the calculation, but in some circumstances an initially ordered state can significantly reduce the amount of computation required. The energy of this configuration is then calculated according to the aforementioned Oxygen – Vacancy interactions (V1,V2 and V3).

For the next step, the change in the total energy because of jumping of the Oxygen atoms to their nearest neighbor sites is calculated and from the $\Delta E = E_f E_i$ after this exchange, the transition probability is calculated, $p_{x\text{-->}x'}$. Now a RN is selected in the range of $0 \leq r \leq 1$, and compared with the value of $p_{x\text{-->}x'}$. If $r \geq p_{x\text{-->}x'}$ the exchange is rejected and the original configuration becomes the next one in the sequence, otherwise it is accepted so a new configuration is generated. This procedure can be repeated many times to form a Markov chain of N_c configurations which tend toward the equilibrium value as N_c become large.

Since the configurations in the chain differ by only a small amount, the following configuration will be highly correlated. This means that it is important to let sufficient time elapse when taking averages to ensure that the different configurations which are used in the averaging process are independent, to all intents and purposes.

An estimation of the error in the method was obtained by performing a series of runs, with the same system parameters (i.e. temperature, oxygen concentration) but using different random number sequence. The error could then be obtained by comparing the main parameters obtained in the different runs.

Figures (A.4_7) show the result of the Monte-Carlo simulation for the basal plane, with different dimension, L, and different oxygen content, x. For all calculations the temperature is 300°K. The green site shows the place of an already chosen oxygen atom

this thesis, therefore a calculated phase diagram from one of the other authors, is presented here to compare with the experimental data which have been presented in this thesis (Fig. A.8).

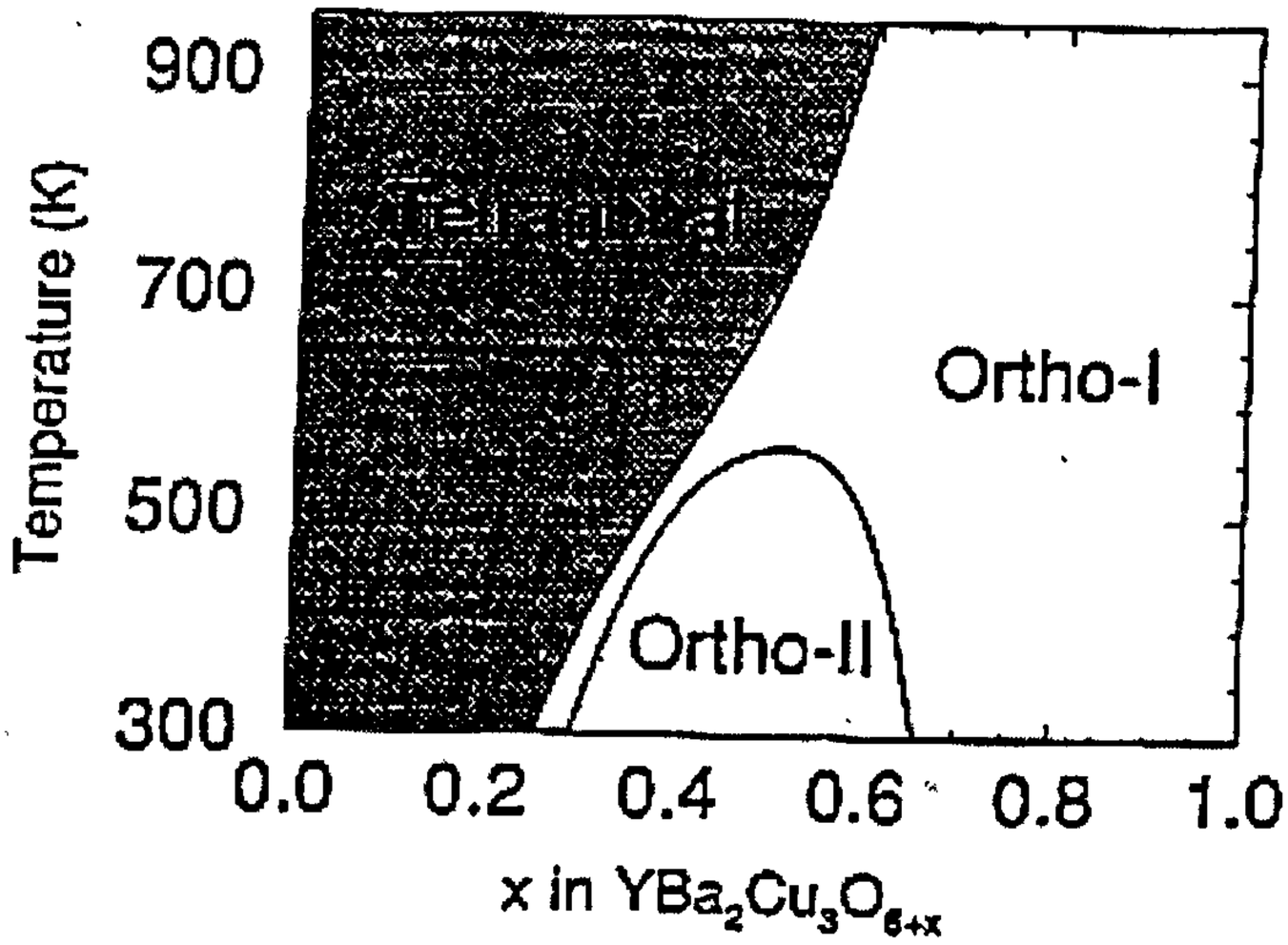

Fig.(A.8) A display of the temperature, oxygen content, phase diagram of the YBCO system, taken from the study of Schleger et al (1992).

APPENDIX B

VOLUMETRIC METHOD TO STUDY OXYGEN DIFFUSION IN YBCO

The familiar ideal gas law:

$$PV = nRT = Nk_BT$$

where P is pressure, V volume, and T absolute temperature, N is the number of molecules of gas, and n is the number of moles, R is the gas constant (8.31451 $Jmol^{-1}K^{-1}$) and k_B is the Boltzmann constant (1.38062×10^{-23} JK^{-1}), arises from a combination of Boyle's law with the proportionality of pressure and temperature for constant volume.

All gases approach ideality as their density is reduced and they become more dilute. Experiments have been performed to determine how close many gases come to being ideal. Monoatomic gases, such as helium, are found to satisfy Boyle's law over a large range, but diatomic gases, such as oxygen, are found to deviate quite rapidly from ideality as their pressure is increased. In fact, oxygen is one of the least ideal of the common gases, deviating by about 2% from ideality over a pressure range up to 10 bar. Since these experiments are not conducted at any pressure above 1 bar, it is reasonable to consider the oxygen used to be ideal.

In a volumetric process it is possible that the temperature and volume of the oxygen gas can be controlled manually. Hence by measuring the changes in the partial pressure caused by absorption (desorption) into (from) the sample, the diffusion process in the solid can be studied.

Diffusion is the process by which atoms are transported through a lattice in such a way as to minimize the Gibbs Free Energy. There are two standpoints from which diffusion of atoms about a material may be viewed: a microscopic view, looking at the ' random walk' of a single atom through available sites, and a macroscopic view, considering the flux of all atoms down a concentration gradient. These description are termed ***tracer*** diffusion and ***chemical*** diffusion respectively. In either case, in a solid, atoms must diffuse by moving between lattice or interstitial sites. To do this, they must have sufficient thermal energy to overcome the potential barrier between the sites, and so, in

general, diffusion rates increase with temperature. Since this experiment will be examining macroscopic properties of the material, it is the chemical diffusion that can be observed directly.

The Fickian diffusion equation (that define the chemical diffusion coefficient D_c):

$$\mathbf{J} = -D_c \nabla c$$

where **J** is the current of the diffusing material and c is the local concentration, have been solved for the simplified case of an instantaneous change in chemical potential at the surface of a sphere [Crank J; "The Mathematics of Diffusion" 2nd Ed., Clarendon press, Oxford, 1975]. The solution consists of a sum of diminishing exponentials. Taking just the first of these, the time constant can be identified as:

$$\tau = a^2 / (\pi^2 D_c)$$

where a is the particle size.

The chemical diffusion coefficient for each step of the absorption (desorption) at each temperature has been calculated from the time constant of the fitted exponential. It should be noted that the fitted time constant is far less precise in value than the equilibrium pressure, a typical error being 10%.

Experimental Apparatus : The design of the rig is shown schematically in Fig.(B.1).Basically, it consists of two buffer volumes, a number of pressure measuring devices, a gas inlet and outlet, connected to a vacuum pump, and a sample chamber. The parts were connected using ½" bore steel tubes in the low pressure (10 mbar) sections and ¼" tubes in the higher pressure (2 bar) sections, with a 1" tube leading to the vacuum pump. VCR connections were used to join together the parts of the rig. The vacuum pump required KF fittings, while the sample chamber was connected using a CF fitting. The gas cylinder was attached to the gas inlet using a Swagelock connection.

The two buffer volumes were standard volume steel vessels. A Penning gage was used to measure the vacuum within the system, and two Baratron pressure transducers, manufactured by MKS Instruments Inc., were used to measure the pressure within the rig across two different ranges (0-10 mbar and 0-2 bar). The gas inlet simply allowed the connection of various gas cylinders to the rig.

APPENDIX C

TGA (ThermoGravimetry Analyses)

In this technique for the study of YBCO, the oxygen content was determined by following the weight of the sample as a function of temperature from room temp. to 1000°C with heating gradient of 20°C/min in a constant rate gas flow of [Ar+H_2 (5%)]. Until ~ 400°C, there was no any weigh change and after that different reactions carried out. The XRD analyses at the final stage, indicated that only Cu, BaO, and Y_2O_3 were present. Calculations are based on the overall reaction in Eqn.(C.1):

$$2YBa_2Cu_3O_x + (2x-7)H_2 \rightarrow 4BaO + Y_2O_3 + 6Cu + (2x\text{-}7)H_2O \qquad (C.1)$$

WT % : (The mass of the final products, M_f) / (Initial mass of the sample, M_i)

but : $M_i = 2\,(\,554.223 + 15.999x\,) = 1108.446 + 31.998x$

and : $M_f = 225.807 + 4\,(\,153.339\,) + 6\,(63.546)$ (without the water vapor mass because it escapes from the system) so : WT % = (1220.439) / (1108.446 + 31.998x)

after finding the value of (WT %) from the graph in below, we can find the value of x.

now : WT % = 91.675

Therefore: x = 6.96

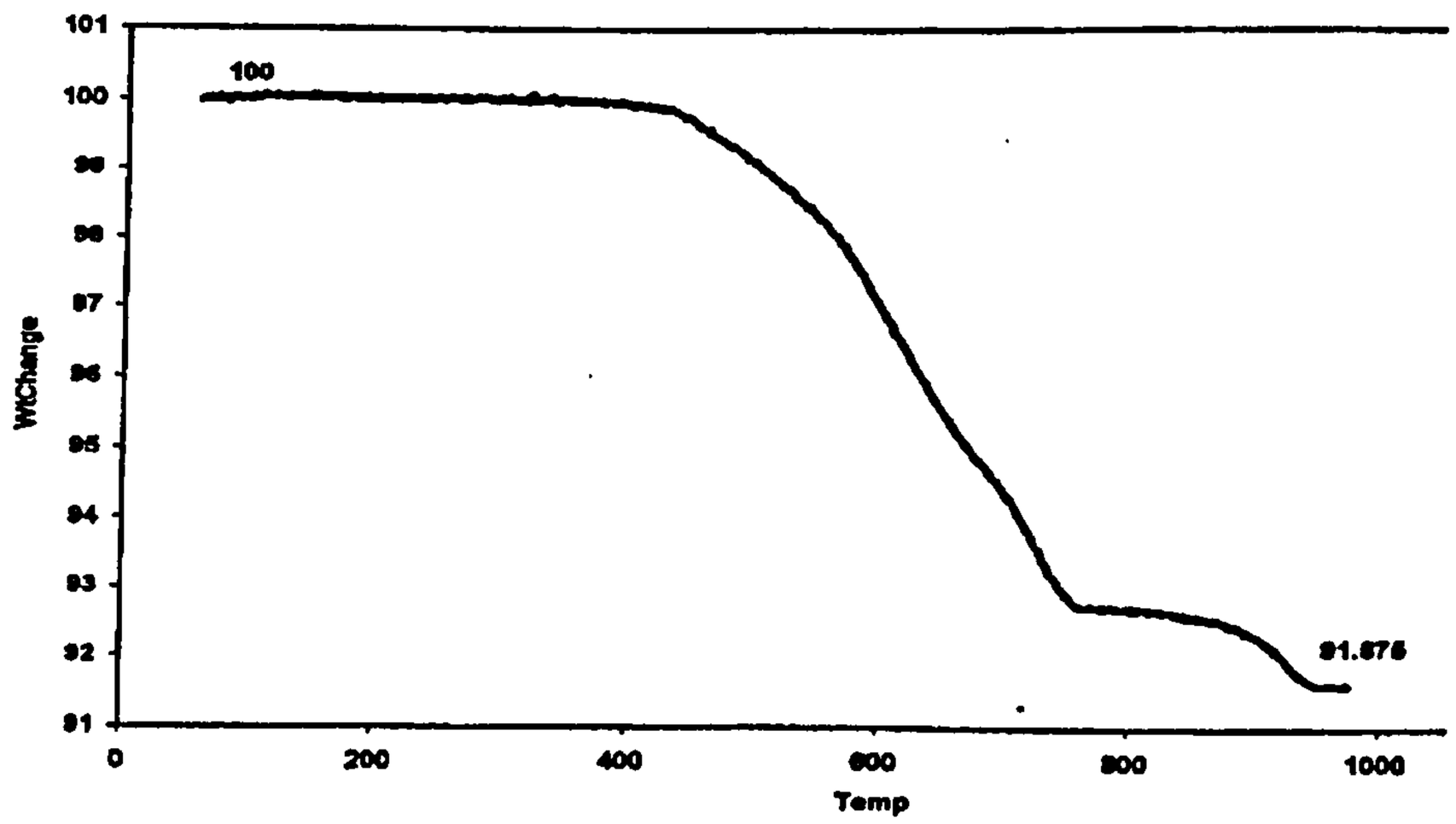

The TGA measurement on YBCO to find out the Oxygen content.

Appendix D

PHASE DIFFERENCE BETWEEN TWO ADJACENT TWINS

Figure shows two adjacent twins in real space:

(Twin Boundary)

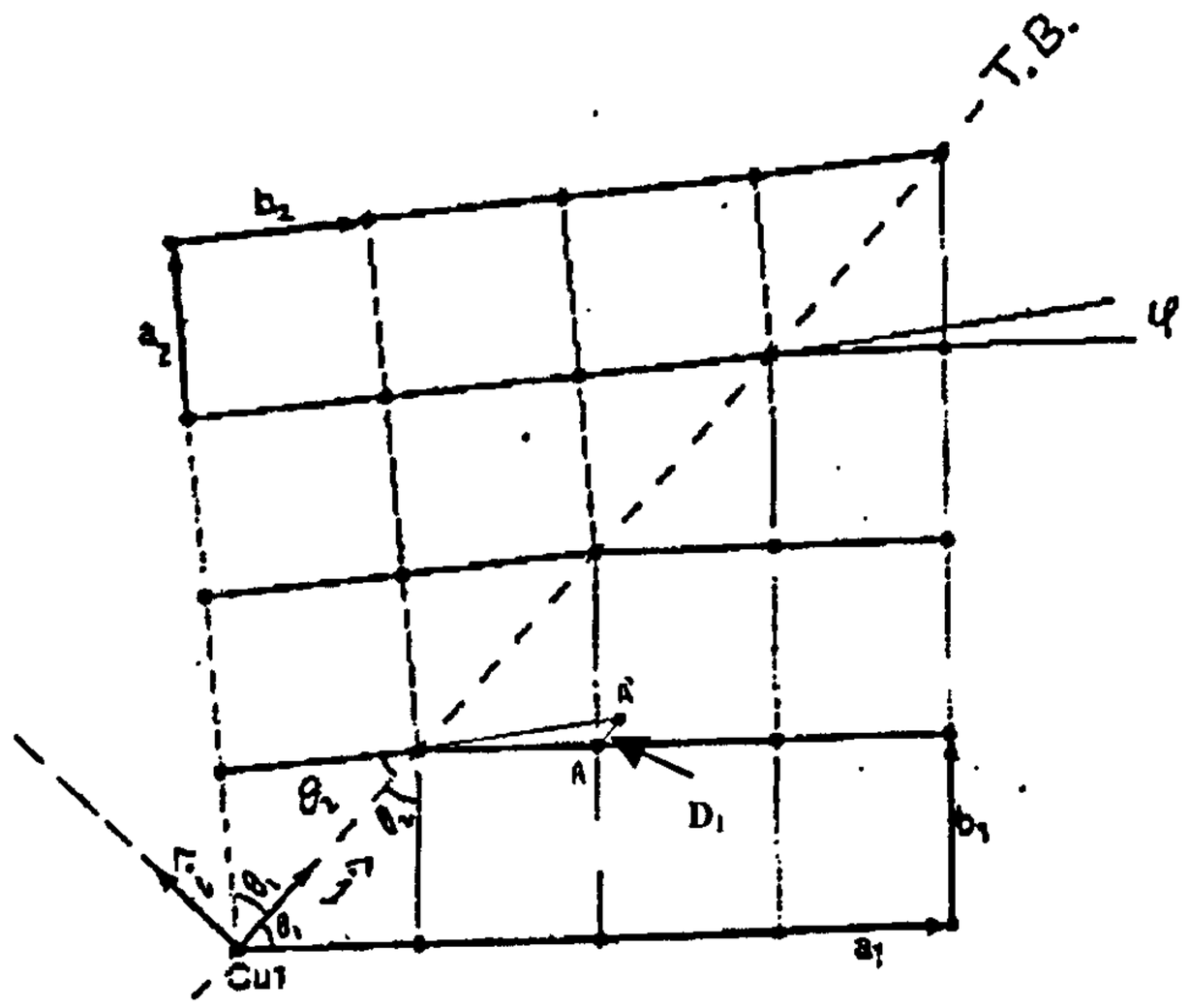

Using the Cartesian co-ordinate system in real space as:

i ⊥ the twin boundary (T.B.) & **j** ∥ (T.B.)

If : $|\mathbf{a}_1|=|\mathbf{a}_2|=a$ & $|\mathbf{b}_1|=|\mathbf{b}_2|=b$

So: $\sin\theta_1 = \cos\theta_2 = b/\sqrt{(a^2+b^2)} = b/R$ (where: $R=\sqrt{(a^2+b^2)}$)

$\sin\theta_2 = \cos\theta_1 = a/R$

and $\mathbf{a}_1 = -a\cos\theta_2\,\mathbf{i} + a\sin\theta_2\,\mathbf{j}$ and $\mathbf{b}_1 = b\cos\theta_1\,\mathbf{i} + b\sin\theta_1\,\mathbf{j}$

$\mathbf{a}_2 = a\cos\theta_2\,\mathbf{i} + a\sin\theta_2\,\mathbf{j}$ and $\mathbf{b}_2 = -b\cos\theta_1\,\mathbf{i} + b\sin\theta_1\,\mathbf{j}$

The separation between two scatterer in one twin, A, and it's ghost counterpart, A',

from the other twin ; in the first plane from the T.B. is in the **j** direction : $\mathbf{D_1}=\mathbf{b_2}-\mathbf{a_1}$

Now : $\mathbf{D_1}=(-b\cos\theta_1 + a\cos\theta_2)\,\mathbf{i} + (b\sin\theta_1 - a\sin\theta_2)\,\mathbf{j}$

Hence: $\mathbf{D_1}=(-ab/R + ab/R)\,\mathbf{i} + (b^2/R - a^2/R)\,\mathbf{j}$

So the separation is parallel to the T.B. and this separation in the t^{th} layer after T.B. is:

$$\boxed{\mathbf{D_t} = [\,T\,(b^2-a^2)/\sqrt{(a^2+b^2)}\,]\,\mathbf{j}}$$

In reciprocal space

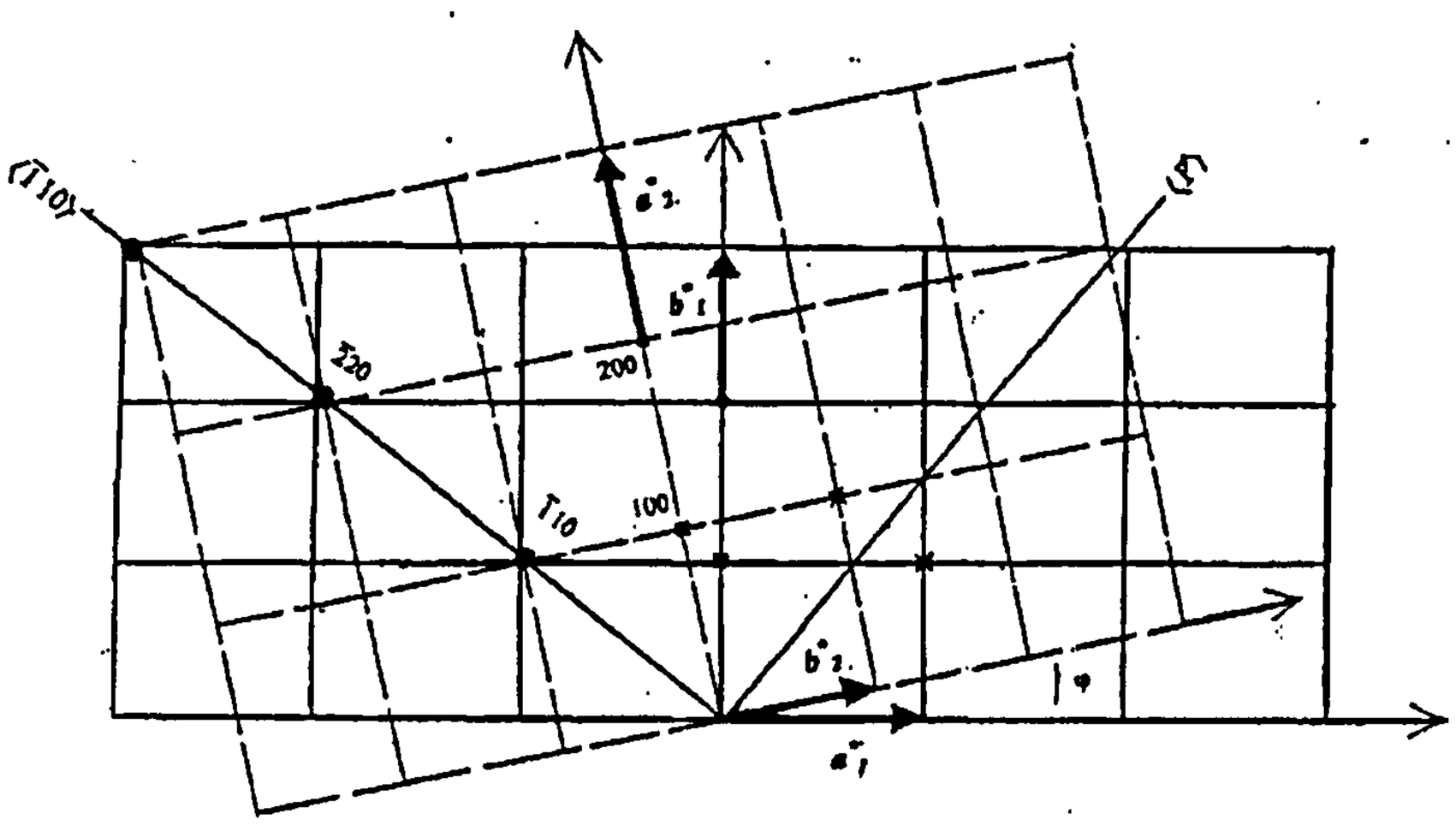

Using the Cartesian co-ordinate system in reciprocal space also is possible as :

$\mathbf{i} \parallel \langle 1\ \bar{1}\ 0 \rangle$ & $\mathbf{j} \parallel \langle p \rangle$

and : $|\mathbf{a^*_1}| = |\mathbf{a^*_2}| = a^*$ & $|\mathbf{b^*_1}| = |\mathbf{b^*_2}| = b^*$

$\sin\theta^*_1 = \cos\theta^*_2 = a^*/\sqrt{(a^{*2}+b^{*2})}$ (if: $\sqrt{(a^{*2}+b^{*2})} = R^*$)

so : $\sin\theta^*_2 = \cos\theta^*_1 = b^*/R^*$

Therefore: $\mathbf{a^*_1} = -a^*\cos\theta^*_2\,\mathbf{i} + a^*\sin\theta^*_2\,\mathbf{j}$ & $\mathbf{b^*_1} = b^*\cos\theta^*_1\,\mathbf{i} + b^*\sin\theta^*_1\,\mathbf{j}$

$$\mathbf{a}^*_2 = \; a^* \cos\theta^*_2\, \mathbf{i} + a^* \sin\theta^*_2\, \mathbf{j} \qquad \& \qquad \mathbf{b}^*_2 = -\, b^* \cos\theta^*_1\, \mathbf{i} + b^* \sin\theta^*_1\, \mathbf{j}$$

For each pair of splitted points in effect of twining in the basal plane , such as :

$\mathbf{Q_{hk}} = h\,\mathbf{a}^*_1 + k\,\mathbf{b}^*_1$ and $\mathbf{Q_{kh}} = k\,\mathbf{a}^*_2 + h\,\mathbf{b}^*_2$

The separation of these points is:

$$\mathbf{D}_{q\,hk} = \; \mathbf{Q_{hk}} - \mathbf{Q_{kh}} = h(\mathbf{a}^*_1 - \mathbf{b}^*_2) + (\mathbf{b}^*_1 - \mathbf{a}^*_2)$$

Now: $\mathbf{a}^*_1 - \mathbf{b}^*_2 = (-a^* \cos\theta^*_2 + b^* \cos\theta^*_1)\,\mathbf{i} + (a^* \sin\theta^*_2 - b^* \sin\theta^*_1)\,\mathbf{j}$

$$= (-a^{*2}/R^* + b^{*2}/R^*)\,\mathbf{i} + (a^*b^*/R^* - b^*a^*/R^*)\,\mathbf{j}$$

$$\mathbf{a}^*_1 - \mathbf{b}^*_2 = [(b^{*2} - a^{*2})/R^*]\,\mathbf{i}$$

and: $\mathbf{b}^*_1 - \mathbf{a}^*_2 = (b^* \cos\theta^*_1 - a^* \cos\theta^*_2)\,\mathbf{i} + (b^* \sin\theta^*_1 - a^* \sin\theta^*_2)\,\mathbf{j}$

$$= (b^{*2}/R^* - a^{*2}/R^*)\,\mathbf{i} + (b^*a^*/R^* - a^*b^*/R^*)\,\mathbf{j}$$

$$\mathbf{b}^*_1 - \mathbf{a}^*_2 = [(b^{*2} - a^{*2})/R^*]\,\mathbf{i}$$

Hence: $\mathbf{D}_{q\,hk} = (h+k)\,[(b^{*2} - a^{*2}) \,/\, \sqrt{(a^{*2} + b^{*2})}]\,\mathbf{i}$

This means that the reciprocal space separation between the [hk0] and [kh0] points depends **on the order of reflection (h & k) .**

Now the phase differences caused by the separation in the real space from any vector in reciprocal space ,**Q** , is : $\Phi = \mathbf{Q}.\mathbf{D}_t \rightarrow \pi$ these two points are anti phase and the resultant diffracted intensity, I(Q), is zero ($I \alpha e^{-\Phi}$) .

As the costume:

$a^* = 2\pi / a$, $b^* = 2\pi / b$ and $\mathbf{Q_{hk}} = h\,\mathbf{a}^*_1 + k\,\mathbf{b}^*_1$ (in the basal plane)

Therefore the phase differences from the separated points in the t^{th} layer after T.B. is:

$$\Phi_{hk}(t) = \mathbf{Q_{hk}} \,.\, \mathbf{D}_t =$$
$$[h\,(-a^* \cos\theta^*_2\, \mathbf{i} + a^* \sin\theta^*_2\, \mathbf{j}) + k\,(b^* \cos\theta^*_1\, \mathbf{i} + b^* \sin\theta^*_1\, \mathbf{j})] \cdot$$
$$[t\,(b^2 - a^2) / \sqrt{(a^2 + b^2)}]\,\mathbf{j}$$

$$= (h\, a^{*} \sin\theta^{*}_{2} + k\, b^{*} \sin\theta^{*}_{1}) \left[t\,(b^2 - a^2) / \sqrt{(a^2 + b^2)} \right]$$

$$= (h + k)\, t \left\{ (a^{*}\, b^{*} / R^{*}) \left[(b^2 - a^2) / R \right] \right\} = (h + k) \left[2\pi\, t\,(b^2 - a^2) / (b^2 + a^2) \right]$$

if $a \approx b$ so : $(a + b) \approx 2 \langle a \rangle$ & $a^2 \approx b^2 \approx \langle a \rangle^2$

therefore : $\Phi_{hk}(t) \approx 2\pi\, t\,(h + k) \left[(b - a)\ 2 \langle a \rangle / 2 \langle a \rangle^2 \right]$

Hence : $\boxed{\Phi_{hk}(t) \approx 2\pi\, t\,(h + k)\, S}$ (where : $S = (b - a) / \langle a \rangle$)

This is a useful result, because it indicates with .increasing the separation of the two

counterpart scatterers from the T.B. the phase differences increases as well, until it reaches to

the unti-phase condition and therefore in reciprocal space, two twin's area produces

two separate spots.

References

*Algia A A, Anda E V, Moran-Lopez J L; *Phys. Rev.*B **42** (1990) 4288

*Arlt G; Sasko P; *J. Appl. Phys.* **51**, No 9 (1980) 4955

*Barsch G R, Horvitz B, Krumhansl J A; *Phys. Rev. Lett.* **59** (1987) 1251

*Bourdillon A, Tan Bourdillon N X; "High Temperature Superconductors: Processing and Science" (1994), Academic Press Inc.

*Browning D, Pennycook S J; "Characterization of High Tc Materials...", *Cambridge Univ.press* (2000)

*Blagoev K B, Wille L T; *Phys.Rev.*B **48** (1993) 6588

*Burns G; "High-Temperature Superconductivity", Academic Press, INC(1992).

* Beyers R L, Shaw T M; *Solid State Phys.* **42** (1989) 135

*Bacon G E; "Neutron Diffraction" (3rd Edition), Clarendon Press, Oxford (1975)

*Ceder G, Asta M, Carter W C, Sluiter M, Mann M E, Kraitchman M, de Fontaine D; *Phys.Rev.*B **41** (1990) 8698

*Civale L, Marwich A D, Worthington T K, Kirk M A, Thompson J R, Sun Y, Clem J R, Kursin-Elbaum L, Holtzberg F; *Phys.Rev.Lett.***67** (1991) 648

*Ceder G, Asta M, de Fontaine D; Physica C **177** (1991) 106

*Chrosch J, Salje E K H; *Physica C* **235** (1994) 1265

*de Fontaine D, Ceder G, Asta M; *Nature* **343** (1990) 544

*de Fontaine D, Wille L T, Moss S C, *Phys.Rev.*B **36** (1987) 5709

*Delhez R, de Keijser Th H and Mittemeijer E J; *Fresenius Z Anal Chem* (1982)312

*Delhez R, de Keijser Th H, Langford J I, Louer D, Mittemeijer E J, Sonneveld E J; chapter 8 "The Rietveld Method" edited by **Young R A**, Oxford Science Publications (1993)

*David W I F, Moze O, Licci F, Bolzoni F, Cywinski R, Kilconye S, *Physica* B **156** (1989) 880

*Fleming R M, Schneemeyer L F, Gallagher P K, Batlogg B, Rupp L W, Waszczak J V; *Phys.Rev.*B **37** (1989) 7920

*Dou S X, Zhou J P, Savvides N, Bourdillon A J, Sorrell C C, Tan N X, Eastering K E; *Philosophical Magazine Letters* **57** (1988) No.2, 149

*Fan Z G, Zhuang Y X, Yang G, Shao R, Zhang G F; *Journal of Alloys and Compounds* **200** (1993) 33

*Fang M M, Kogan V G, Finnemre D K, Clem J R, Chumbley L S, Farrell D E; *Phys. Rev.*B **37** (1988) 2334

*Gerdanian P, Picard C, Physica C **204** (1993) 419

*Gallagher P K, O'Bryan H M, Sunshine S A, Murphy D W; *Mat. Res. Bull* **22** (1987) 995

*Goncharov V A, Suvorov E V; chap. 2 from "The Real Structure of High-Tc Superconductors" Ed. By: Shekhtman V S (1993), Springer Series in Materials Science **23**

*Houska & Kuzel R; "In *Defect and Microstructure Analysis by Diffraction"* Edited by Snyder R L; Jaroslav F; Bunge H J, IUCr , *Oxford Science Publications* (1999)

*Hirst P J, Drake A, Rand M, Abell J S; *Physica C* **235** (1994) 371

*Haugard H, Uimin G, Selke W; *Physica* C **275** (1997) 93

*Jorge G A, Rodriguez E; *Phys. Rev.*B **61** (2000) 103

*Jorgensen J D, Veal B W, Paulikas A P, Nowiki L J, Crabtree G W, Claus H, Kwok W K, *Phys. Rev.* B **41** (1990) 1863

*Jorgensen J D, Shaked H, Hinks D G, Dabrowski B, Veal B W, Paulikas A P, Nowicki L J, Crabtree G W, Kwok W K, Nunez L H; *Physica C* **153** (1988) 578

*Jorgensen J D, Veal B W, Kwok W K, Crabtree G W, Umezawa A, Nowicki L J, Paulikas A P; *Phys. Rev.*B **36** (1987) 5731

*Jorgensen J D, Beno M A, Hinks D G, Soderholm L, Volin K J, Hitterman R L, Grace J D, Schuller I K, Segre C U, Zhang K, Kleefisch M S; *Phys. Rev.*B **36** (1987) 3608

*Khachaturyan A G, Morris J W; *Phys.Rev.Lett.* **61** (1988) 215

*Khachaturyan A G; "Theory of structural Transformation in Solids" (1983) Chap.11, Wiley (New York)

*Kwok K W, Welp U, Vinokur V M, Fleshler S, Downey J, Crabtree G W 1991 *Phys.Rev.Lett.***67** 390

*Khlyustikov I N, Buzdin A I; *Advances in Physics* **36**, No 3 (1987) 271

*Kersin Z V & Wolf S A; "Fundamentals of Superconductivity", Plenum Press, New York (1990)

*Liang R, Bonn D A, Hardy W N; *Physica* C **236** (2000) 57

*Le Bail A; Sixth International School and Workshop of Crystallography, Jan. 2000 Ismailia Egypt.

*Langford J I; *J Appl Cryst* **11** (1978) 10-14

*Langford J I; In *Defect and Microstructure Analysis by Diffraction* Edited by Snyder R L; Jaroslav F; Bunge H J, IUCr , Oxford Science Publications (1999)

*Lipson H & Steeple H; "Interpretation of X-ray powder Diffraction Patterns" *Macmillan.London* (1970)

*Locherer K R, Hayward S A, Hirst P J, Ghrosch J, Yeadon M, Abell J S, Salje E K H, *Phil. Trans. R. Soc. Lond.* A **354** (1996) 2815

*Latage et. al; 1990

*Marshal A F et al; *Phys.Rev.*B **37** (1988) 9353

*Mercer M, Ph.D thesis, "A study of oxygen in the YBCO, H-T_c superconducting material" Univ. of Salford, (1996)

*McCormark R, de Fontaine D, Ceder G; *Phys.Rev.*B **45** (1992) 12976

*McIntyre G J, Renault A, Collin G; *Phys. Rev.*B **37** (1987) 5148

*McIntyre G J, Renault A; *Physica B* **156** (1989) 880

*Meuffels R, Naeven R, Wenzel H; *Physica C* **161** (1989) 539

*Moodie A F, Whitfield H J; *Ultramicroscopy* **24** (1988) 329

*Poulsen H F, von Zimmermann M, Schneider J R, Andersen N H, Schleger P, Madsen J, Hadfield R, Casalta H, Liang R, Dosanjh P, Hardy W; *Phys. Rev.B* **53** (1996) 15335

*Poulsen H F, Andersen N H, Andersen J V, Bohr H, Mouritsen G O; *Phys.Rev.Lett.* **66** (1991) 465

*Poulsen H F, Andersen N H, Lebech B; Physica C **173** (1991) 387

*Pandey D, Tiwari V S, Singh A K, Wadhawan V K, Somayazulu M S; *Phase Transition* **27** (1990) 165

*Parlinski K, Heine V, Salje E K H; J. Phys.Cond. Matt. 5(1993) 497

*Radaelli P G; "Structural Anomalies, Oxygen Ordering and Superconducting in $YBCO_{6+x}$", from "Neutron Scattering in Layered Copper-Oxide Superconductors" Ed. by: Furrer A (1998), Kluwer Academic Publishers (London)

*Radaelli P G, Segre C U, Hinks D G, Jorgensen J D; *Phys. Rev.* B **45** (1992) 4923

*Rand M, Langford J I, Abell J S; *Philosophical Maggazine B* **68** (1993), No.1, 17

*Rao C N R, Nagarajan R, Vijayaraghavan R; *Supercond. Sci. Technol.* **6** (1993) 1-22

*Reyes_Gasga J, Krekles T, Van Tendeloo G, Van Landuyt J, Bruggink W H M; *Solid State Communications* **70**, No 4 (1989) 269

*Roy T, Mitchell T E; *Philosophical Magazine* A **63** (1991) No.2, 225

*Salomons E, de Fontaine D; *Phys.Rev.*B **16** (1990) 10152

*Schleger P, Hardy W N, Yang B X; *Physica C* **176** (1991) 261

*Schleger P; PhD Thesis, Thermodynamics of oxygen ordering in YBCO, University of British Columbia, Canada (1992)

*Schleger P, Hardy W.N, Casalta H; *Phys. Rev.*B **49** (1994) 514

*Schleger P, Hadfield R A, Casalta H, Andersen N H, Poulsen H F, von Zimmermann M, Schneider J R, Ruixing Liang, Dosanjh P, Hardy W N; *Phys.Rev. Lett.* **74** (1995) 1446

*Schwartz W, Blaschko O, Collin G, Marucco F; *Phys. Rev.*B **48** (1993) 6513

*Selke W, Uimin G V; *Physica C* **214** (1993) 37

*Semenoskaya S, Khachaturyan A G; *Phys. Rev.* B **46** (1992) 6511

*Shi D; "High T_c Materials" World Scientific Publisher (1996)

*Stephens P W; *J. Appl. Cryst.* **32** (1999) 281

*Sterne P A, Wille L T; *Physica C* **162** (1989) 223

*Stokes A R; *Proc Phys Soc London* **61** (1984) 382

*Squires G L; "Introduction to the theory of thermal neutron scattering", Cambridge Univ. Press (1978)

*Salje E, Parlinski K, *Supercond.Sci. Tech.* **4** (1991) 93

*Schmhal W W, Putnis A, Salje E, Freeman P, Graeme-Barber A, Jones R, Singh K K, Blunt J, Edwards P P, Loram J, Mirza K; *Phil.Mag.Lett.* **60** (1989) 241

*Semenovskaya S, Khachaturyan A G, *Phys.Rev. Lett.* **61** (1989) 2223

*Sarikaya M, Stern E A; *Phys.Rev.*B **37** (1988) 9373.

*Semenovskaya S & Khachaturyan A G; *Physica D* **66** (1993) 205.

*Shekhtman V S, "The Real Structure of High-Tc Superconductors" (1993), Springer series in Materials science **23**

*Thompson P, Cox D E, Hastings J B; *J.Appl.Cryst* **20** (1987) 79

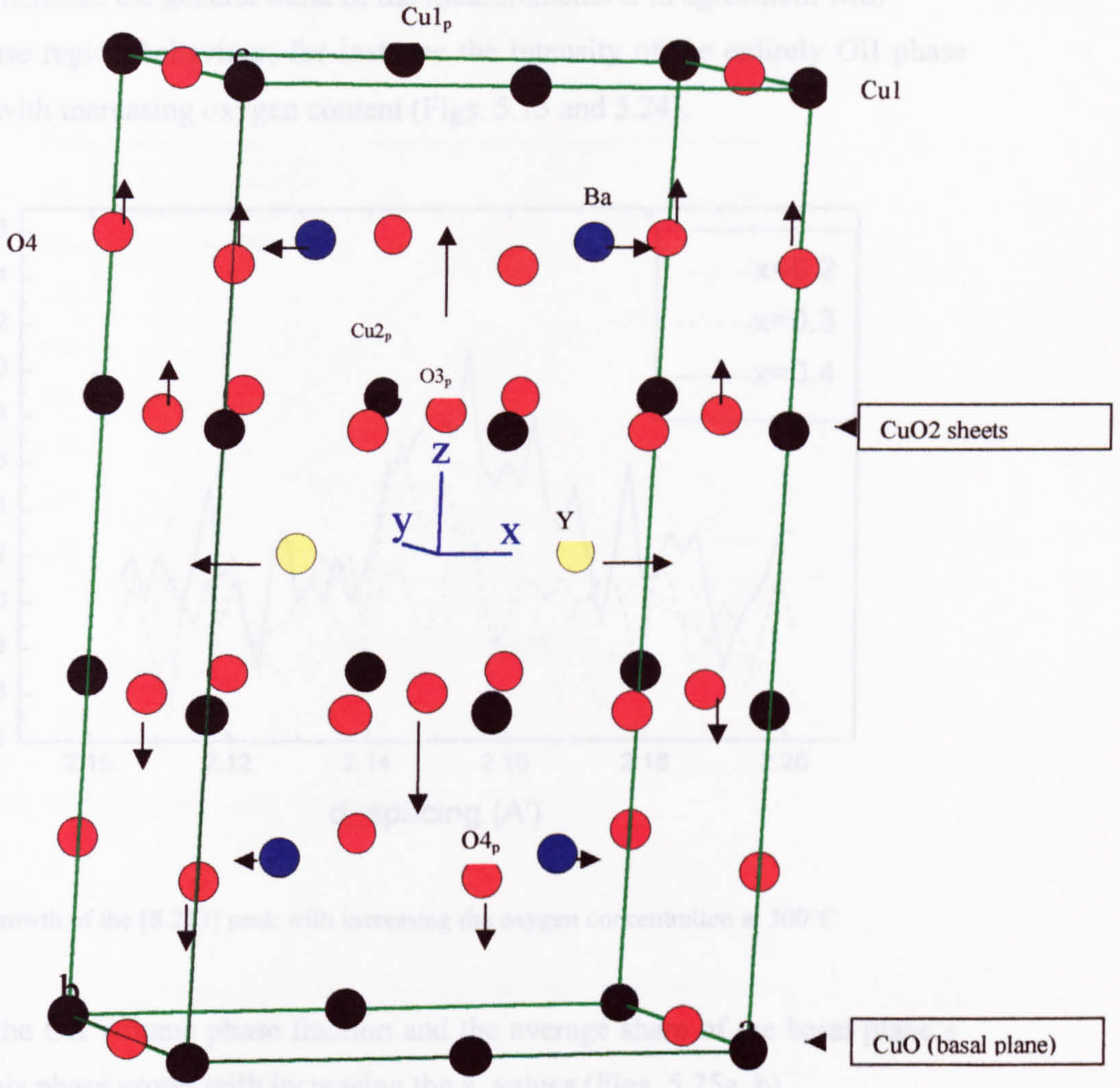

Fig.(5.23) The GSAS structural refinement suggests the relative atomic displacements (the arrow's length) schematically .

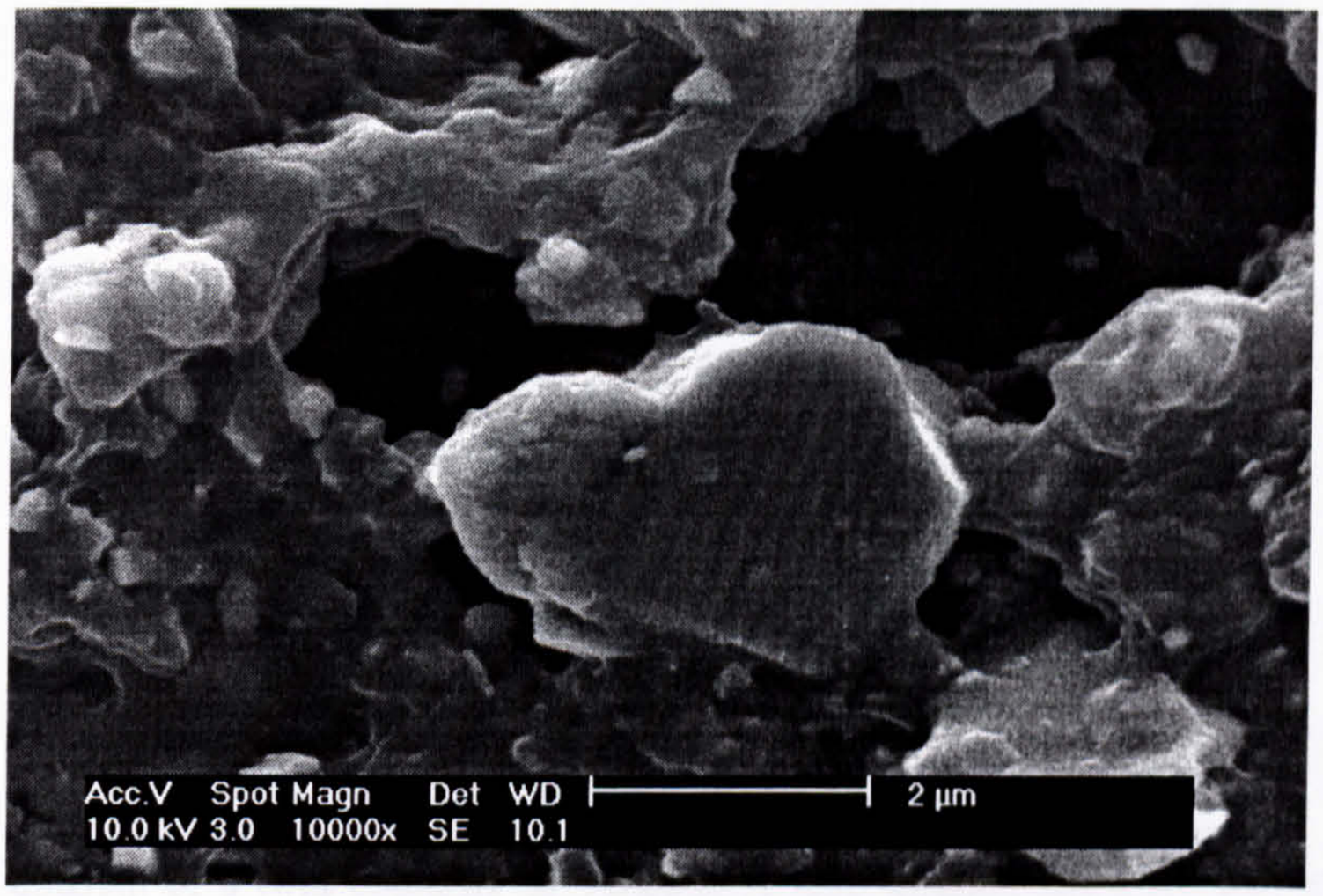

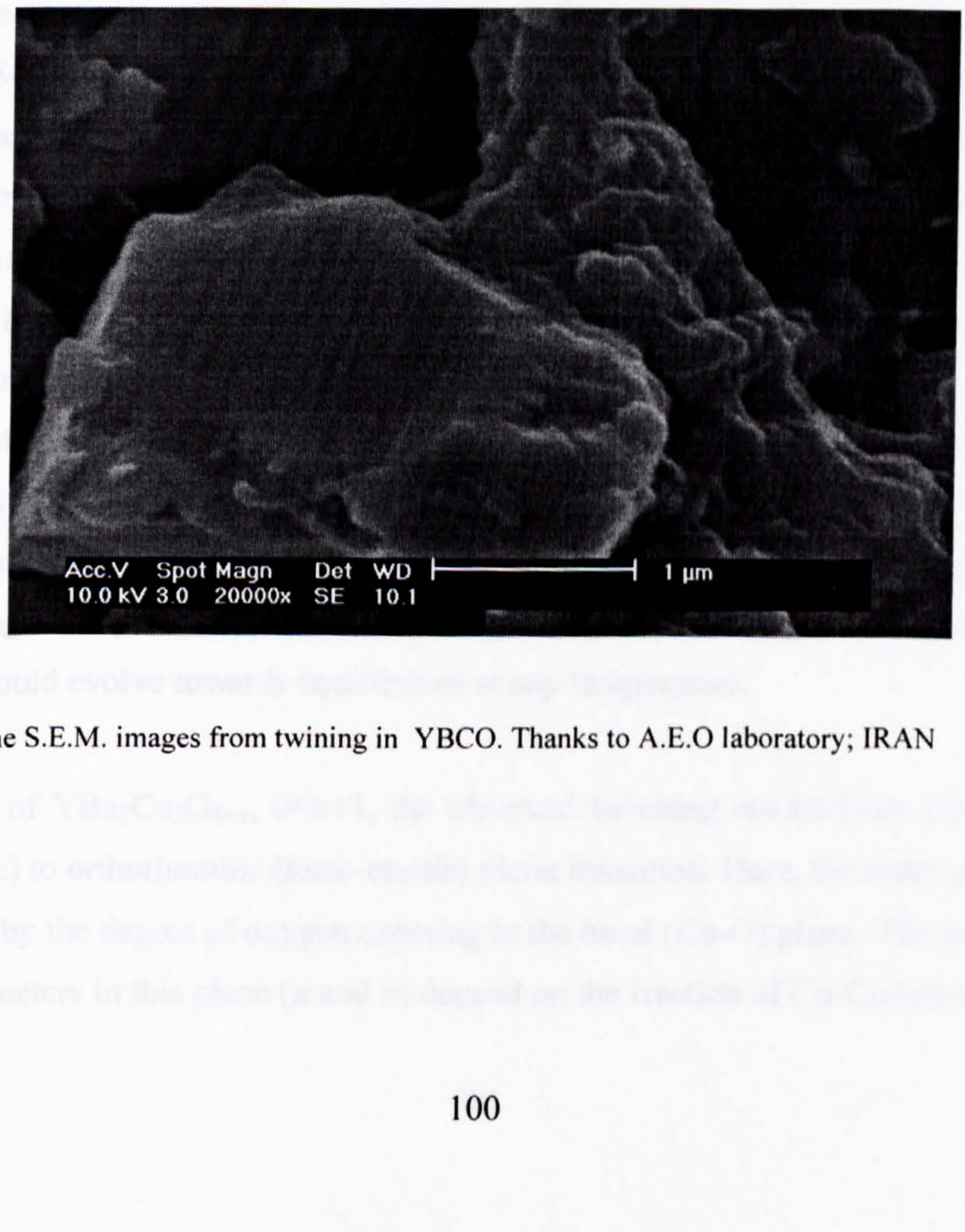

Fig.(7.1) The S.E.M. images from twining in YBCO. Thanks to A.E.O laboratory; IRAN

VII.1) T/OI PHASE TRANSITION

According to a number of previous studies, at high temperature (>400°C) the T/OI phase transition in YBCO is **second order** and it has been shown by a sharp boundary between the tetragonal and orthorhombic I phases (Figure 5.1, chapter V). This is probably because of the fast diffusion of oxygen atoms within the basal planes and the relatively high value of the oxygen content in the sample, $x > 0.5$.

The set-up for the present *in-situ* diffraction experiments, (Fig. 7.3) consisted of a quartz sample tube, which was fed by a small bore tube from a gas rig. Several baffles were clamped to it to prevent heat transfer up from the furnace volume. The gas rig was fitted with two 1 litre standard volumes, acting as a buffer volume and a 10 mbar Baratron to read low pressure; a 1 bar Baratron to read the higher pressures a vacuum port and an oxygen inlet port.

The sample was studied using the OSIRIS diffractometer of ISIS described in chapter IV. Diffraction patterns were obtained over 1.0 – 12.0 Å range of d-spaceing. Similar to the measurements below 400°C, using the Sievert's method to measure the amount of oxygen removed, the sample was first taken into the tetragonal phase, $x \sim 0.15$.

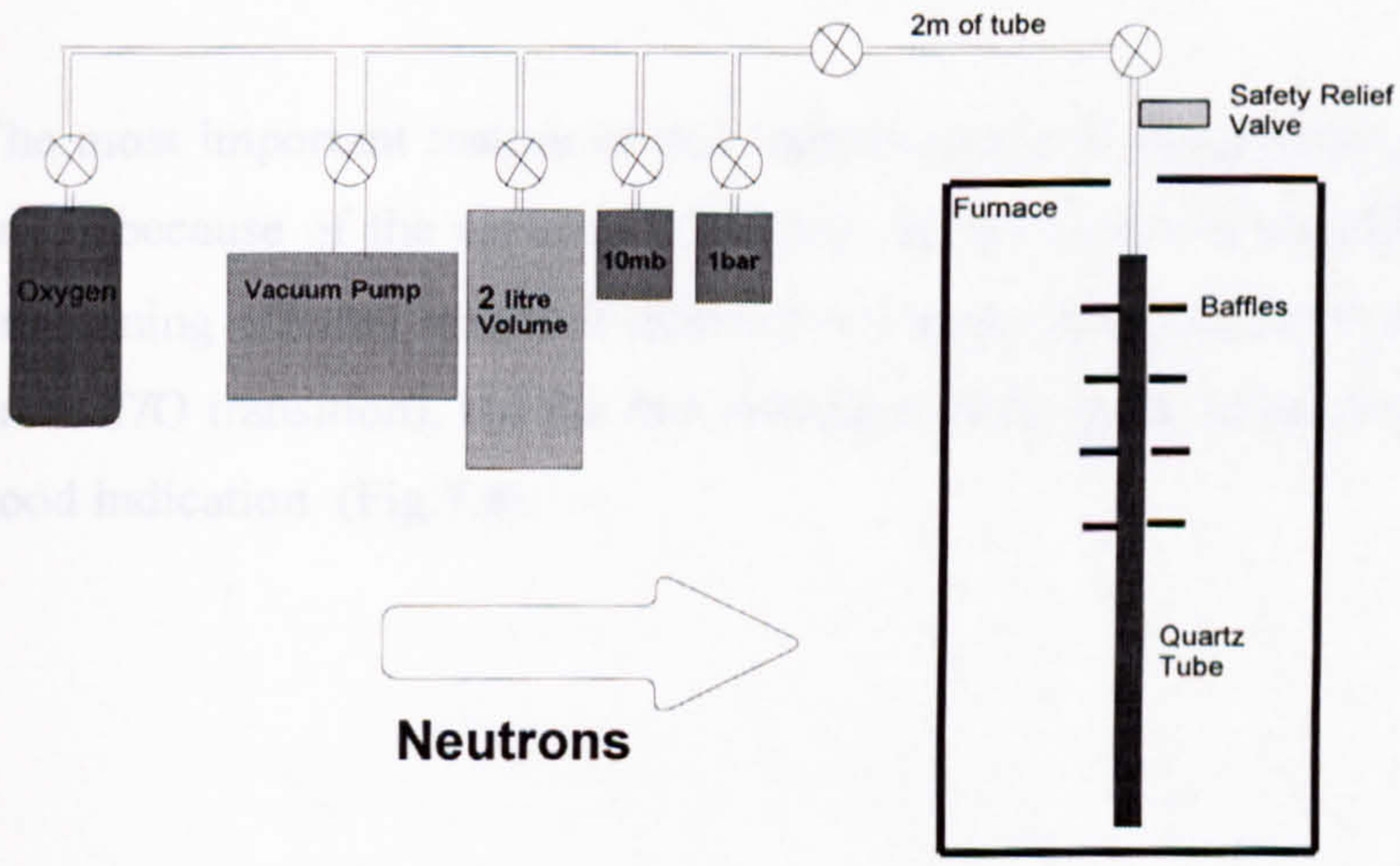

Fig.(7.3) A schematic representation of the experimental set-up used during the neutron diffraction studies .

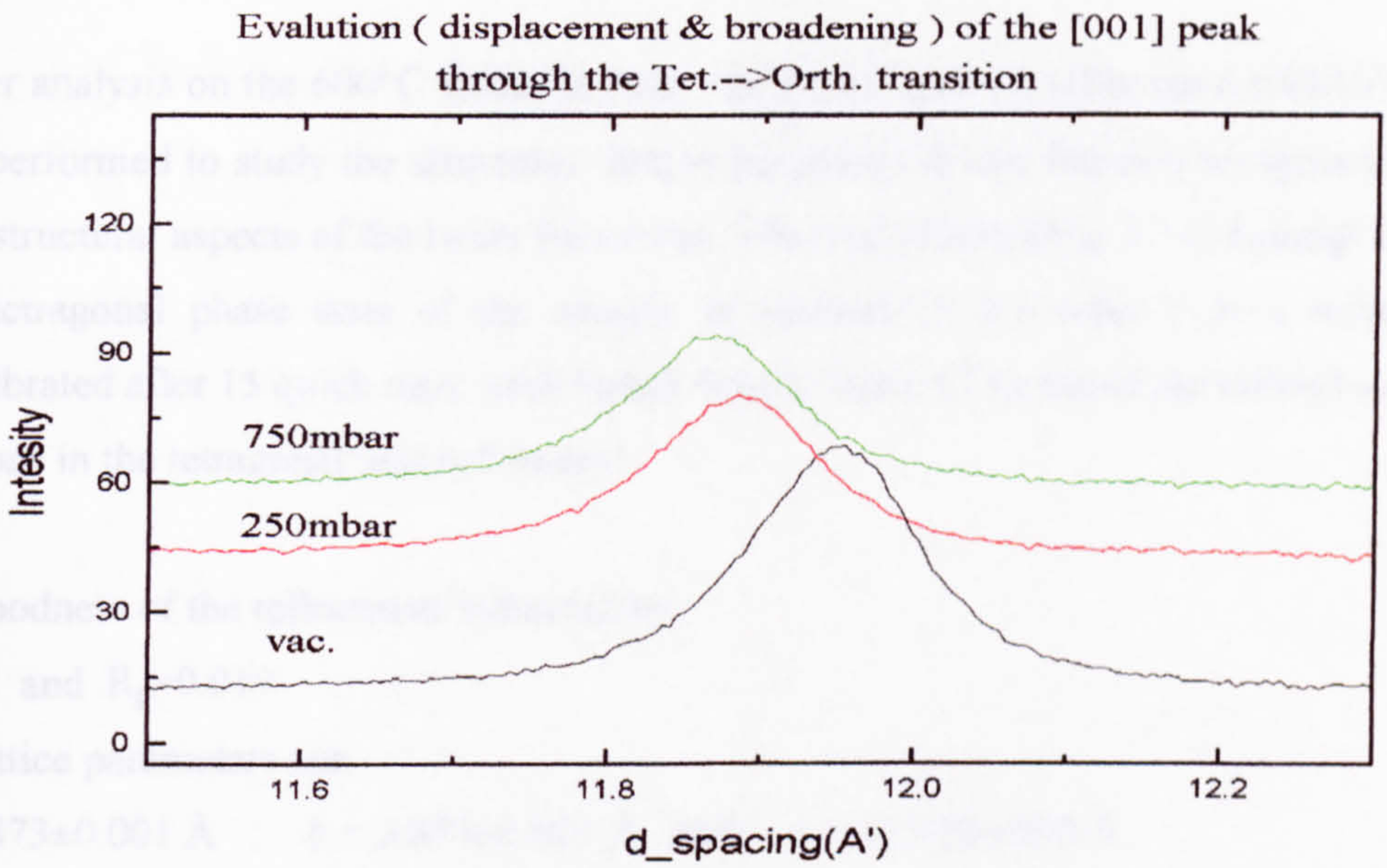

Fig.(7.12) Isotherm measurements for [001] peak at 600°C

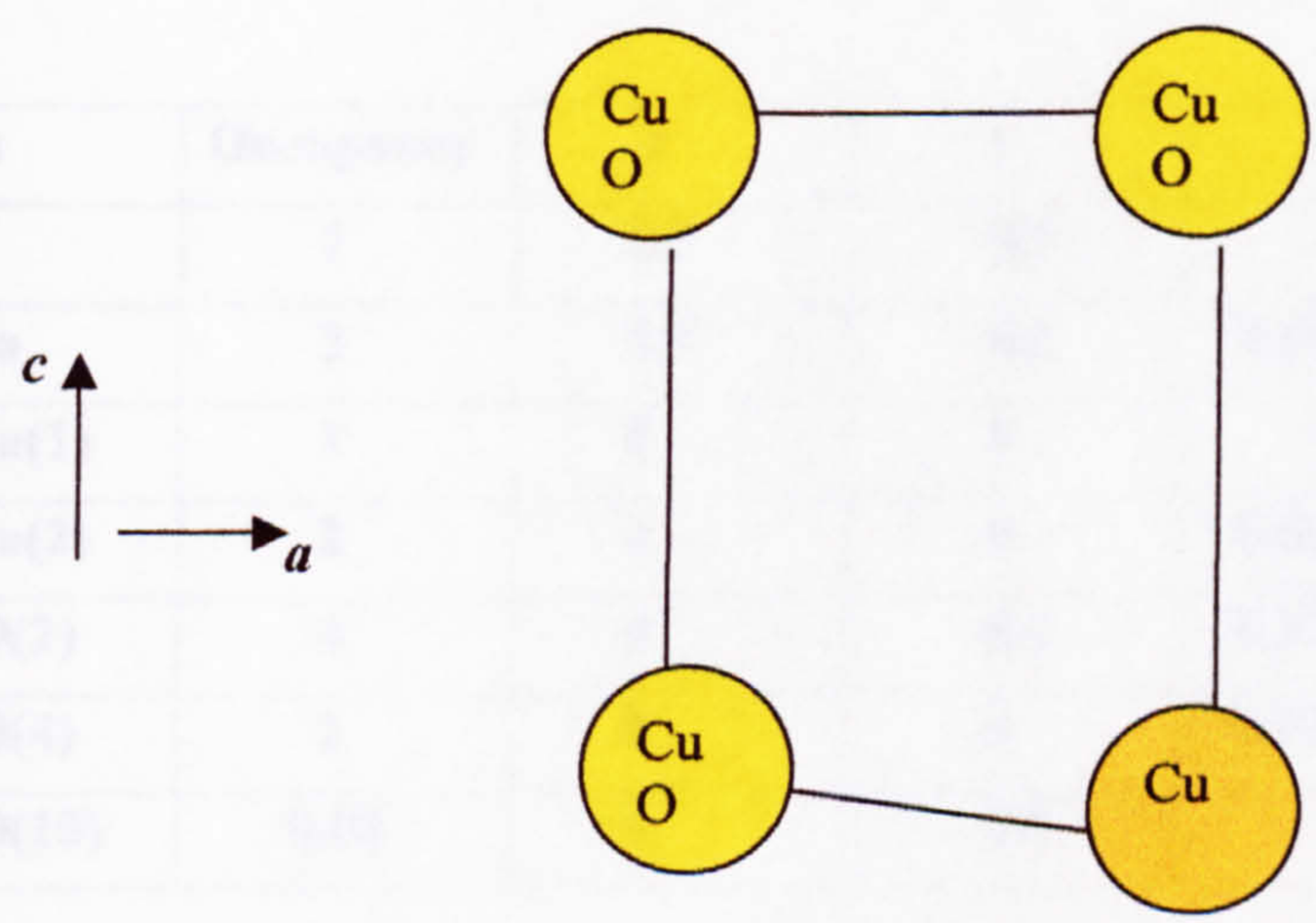

Fig.(7.13) A side view of a deformed unit cell, corresponds to an oxygen vacancy in the *b* direction, behind one of the Cu atoms at the corner which makes a large strain effect.

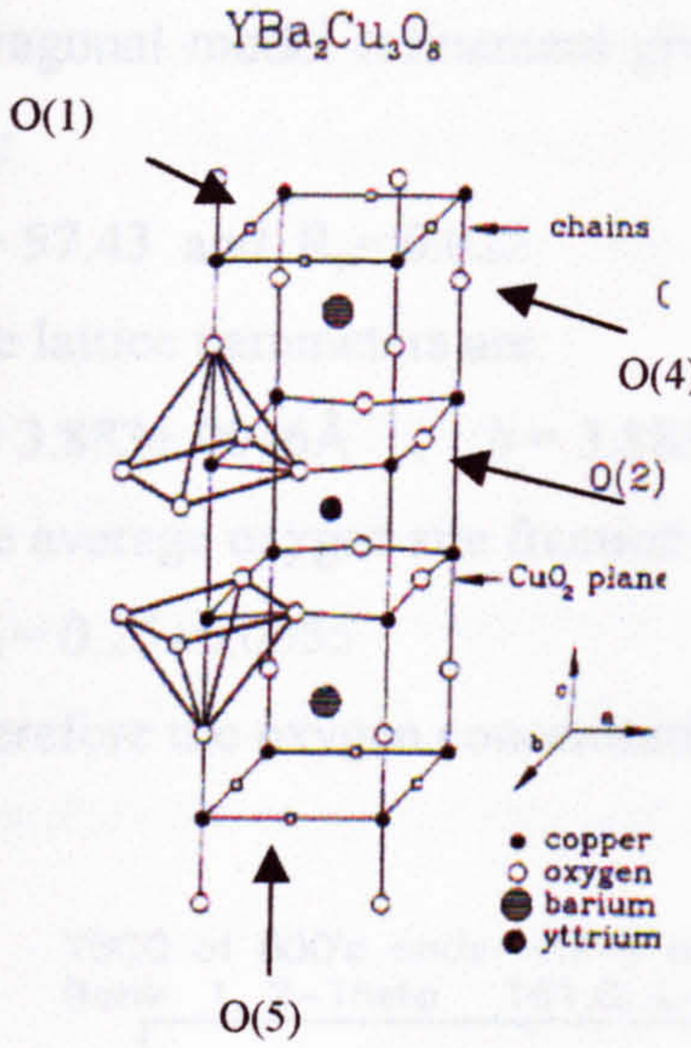

(a)

The O(15) site occupancy in table (7.1) indicates the average oxygen site occupancies in the basal plane where O(1) is the site for making the Cu-O-Cu chains along the *b* direction and O(5) is the oxygen site along the *a* direction. If the oxygen content is not exactly 6 (or x=0), this means that the extra oxygen atoms occupy O(1) or O(5) sites randomly (or locally in chains with equal probability in *a* or *b* directions).

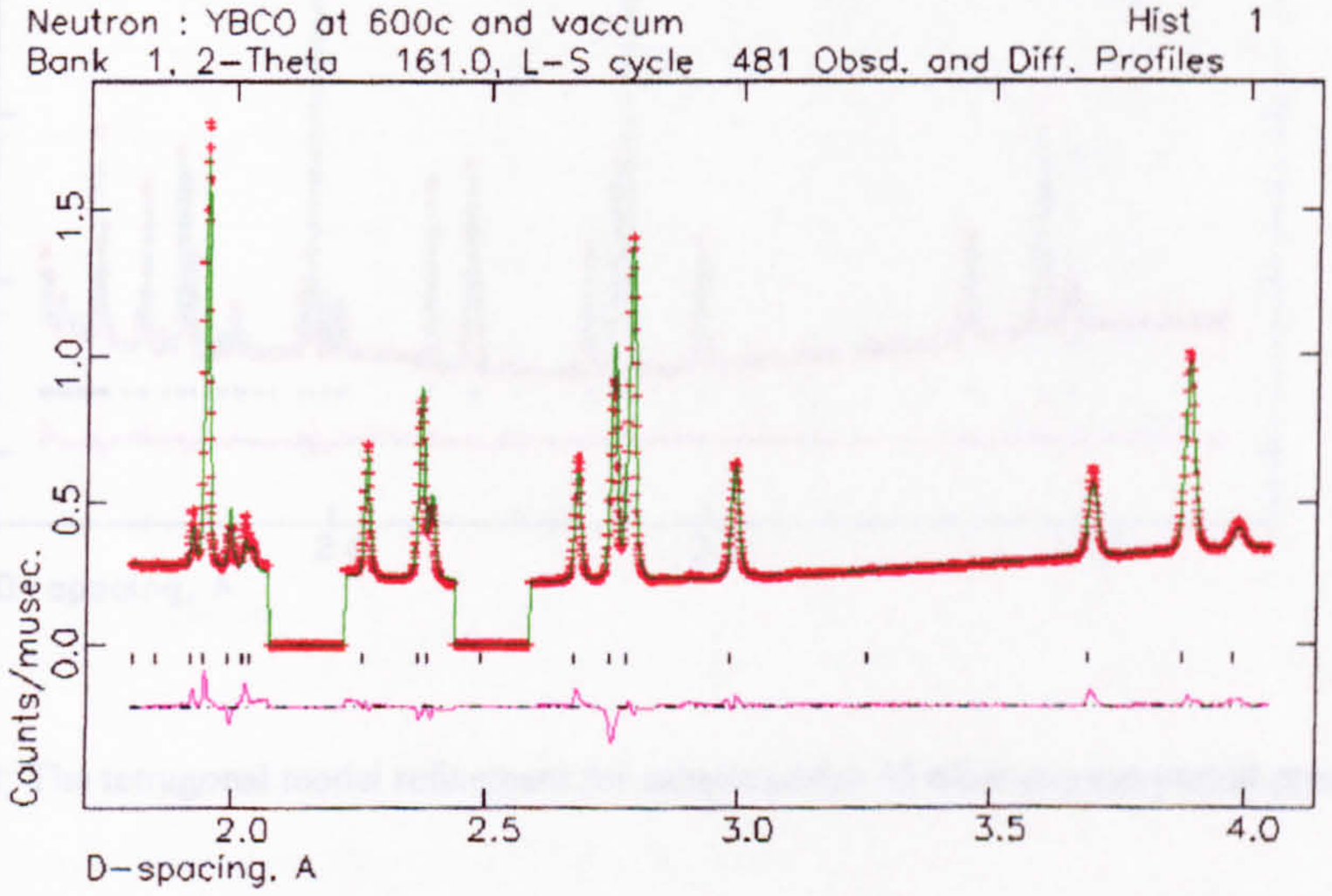

(b)

Fig.(7.14) a_ The tetragonal model; b_ the refinement for sample under vacuum , some parts have been cut because of the background from the sample tube (fused quartz).

When the sample is equilibrated at an oxygen p.p.of 40 mbar (after 15 quick runs; each 4min.), the sample still remains in the tetragonal phase (including tweeding), because the tetragonal model refinement gives the best fit (Fig.7.15). The results of the refinement are:

$\chi^2 = 57.43$ and $R_p = 0.022$

The lattice parameters are:

$a = 3.883 \pm .0016$Å ; $b = 3.883 \pm 0.0016$ Å and $c = 11.899 \pm 0.0045$ Å

The average oxygen site fraction in the basal plane:

$O_{15} = 0.25 \pm 0.0055$

Therefore the oxygen concentration is : $x \sim 0.5$

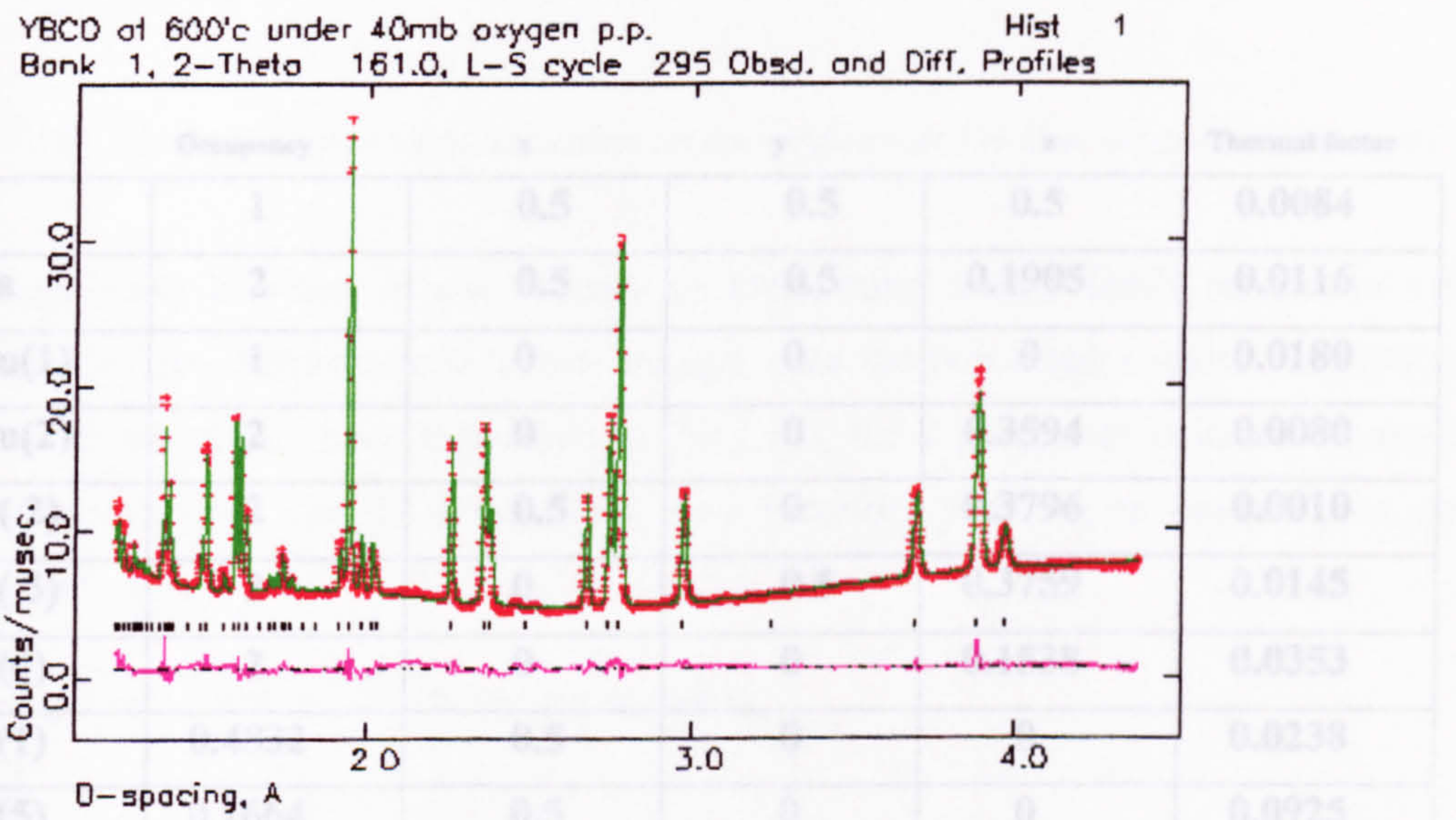

Fig.(7.15) The tetragonal model refinement for sample under 40 mbar oxygen partial pressure.

From the results it is clear that the lattice parameter *a*, is expanded and there is contraction in the *c* parameter, because of the higher oxygen site occupancy in the basal plane.

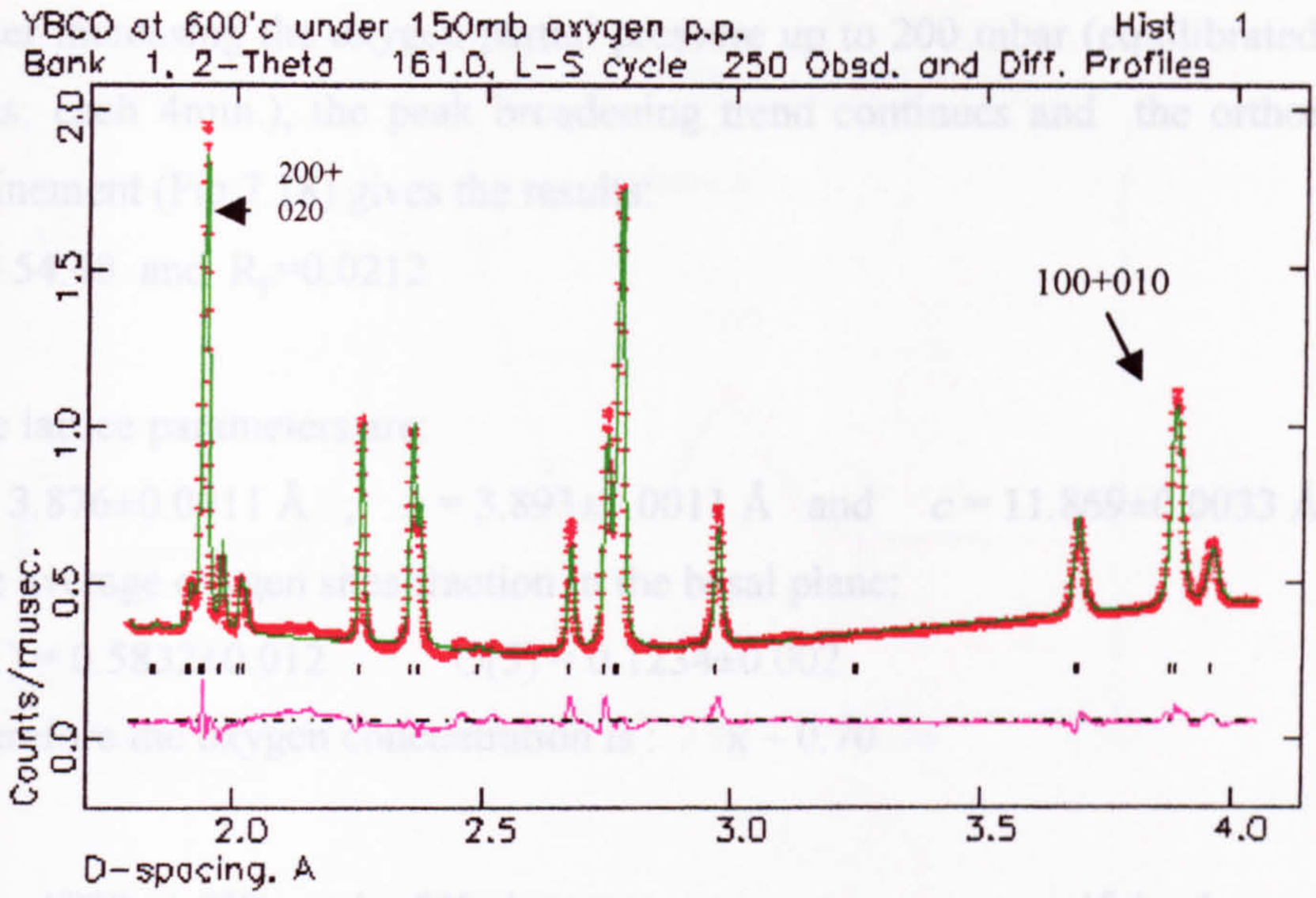

Fig.(7.16) The orthorhombic model refinement for the sample under 150 mbar oxygen partial pressure.

The separation between *a* and *b* leads to broadening in the [*h00*] reflections (the resolution of the diffractometer is not enough, note the two toggles under the [100] & [010] peak which has been magnified in Fig.7.17), the *c* parameter is in the course of further contraction. The T/OI transition must therefore occur at an oxygen pressures around 100 mbar.

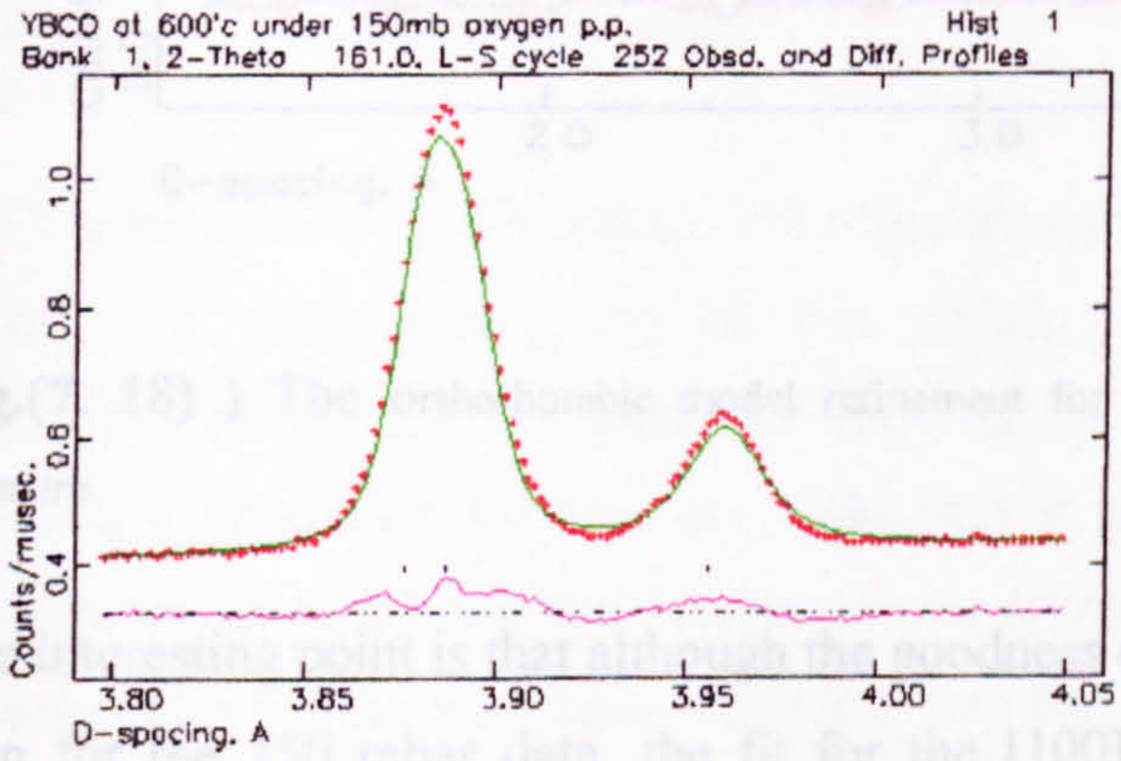

Fig.(7.17) The broadening of the [100]&[003] cluster peaks under 150 mbar oxygen partial pressure at 600°C

After increasing the oxygen partial pressure up to 200 mbar (equilibrated after 27 quick runs; each 4min.), the peak broadening trend continues and the orthorhombic model refinement (Fig.7.18) gives the results:

$\chi^2 = 54.40$ and $R_p = 0.0212$

The lattice parameters are:

$a = 3.876 \pm 0.0011$ Å ; $b = 3.893 \pm 0.0011$ Å and $c = 11.869 \pm 0.0033$ Å

The average oxygen sites fraction in the basal plane:

O(1) = 0.5832±0.012 O(5) = 0.1234±0.002

Therefore the oxygen concentration is : x ~ 0.70

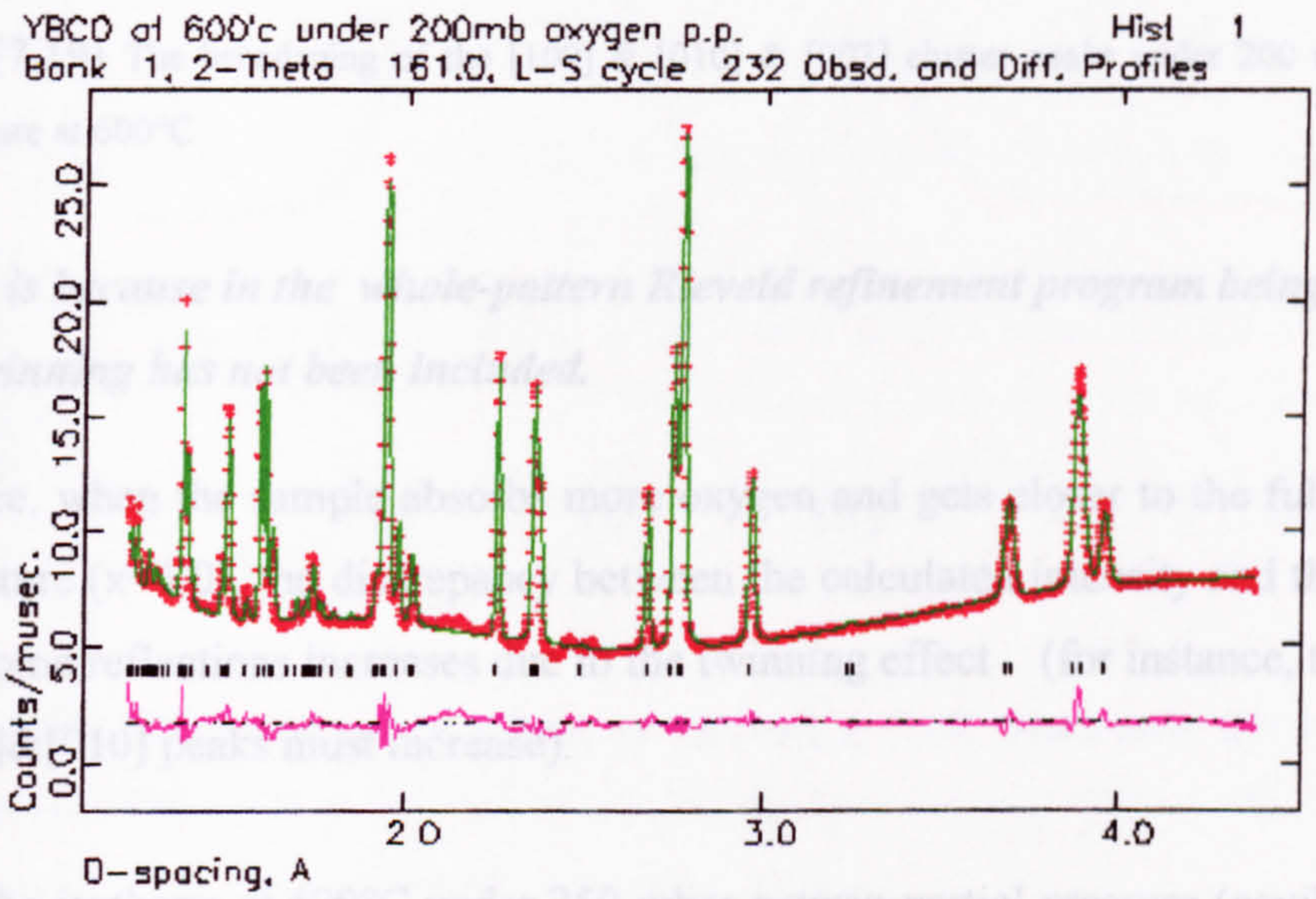

Fig.(7. 18)) The orthorhombic model refinement for the sample under 200 mbar oxygen partial pressure.

The interesting point is that although the goodness of the fit for the entire pattern is better than for the 150 mbar data, the fit for the [100] & [010] reflection gets worse. The separation of toggles increases a bit, but the intensity and the width of the experimental data, are greater than in the calculated profile.

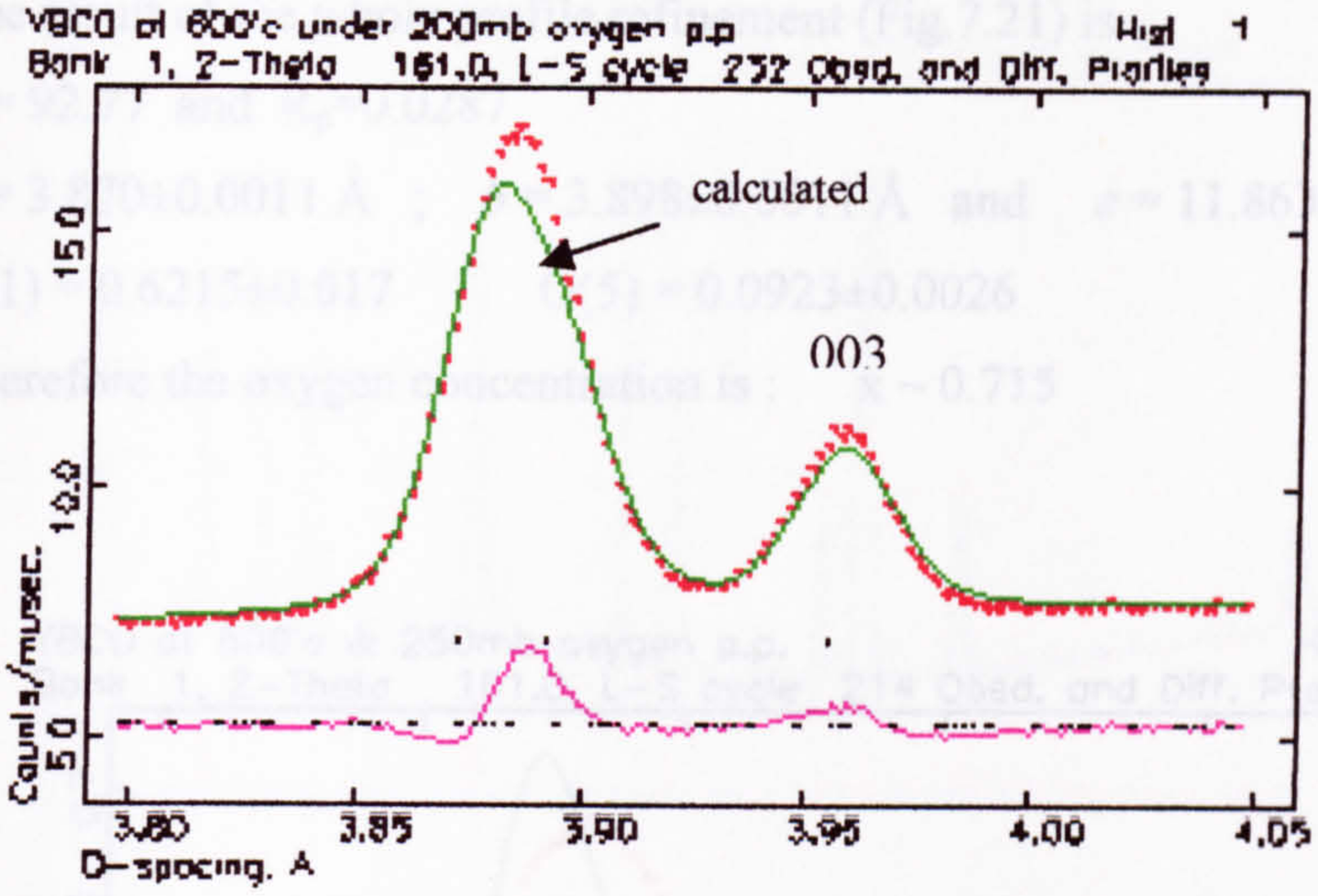

Fig.(7.19) The broadening of the [100] & [010] & [003] cluster peaks under 200 mbar oxygen partial pressure at 600°C

This is because in the whole-pattern Rieveld refinement program being used, the effect of twinning has not been included.

Hence, when the sample absorbs more oxygen and gets closer to the fully orthorhombic structure (x=1.0), the discrepancy between the calculated intensity and the observed data for some reflections increases due to the twinning effect (for instance, the widths of the [100]&[010] peaks must increase).

For the isotherm at 600°C under 250 mbar oxygen partial pressure (equilibrated after 30 quick runs; each 4min.), the fit, Fig. (7.20), shows more differences between the calculated results and the experimental data for the [100] & [010] lines. The model predicts a separation for the two peaks that is greater than for the real data! This is because in the model, the main reason for the splitting is the difference between the *a* and *b* parameters but the coherence effect between thin twinned regions, can stop the splitting trend between the two reflections (section VI.3).

The result of the whole profile refinement (Fig.7.21) is :

$\chi^2 = 92.77$ and $R_p = 0.0287$

$a = 3.870 \pm 0.0011$ Å ; $b = 3.898 \pm 0.0011$ Å and $c = 11.863 \pm 0.0033$ Å

O(1) = 0.6215±0.017 O(5) = 0.0923±0.0026

Therefore the oxygen concentration is : x ~ 0.715

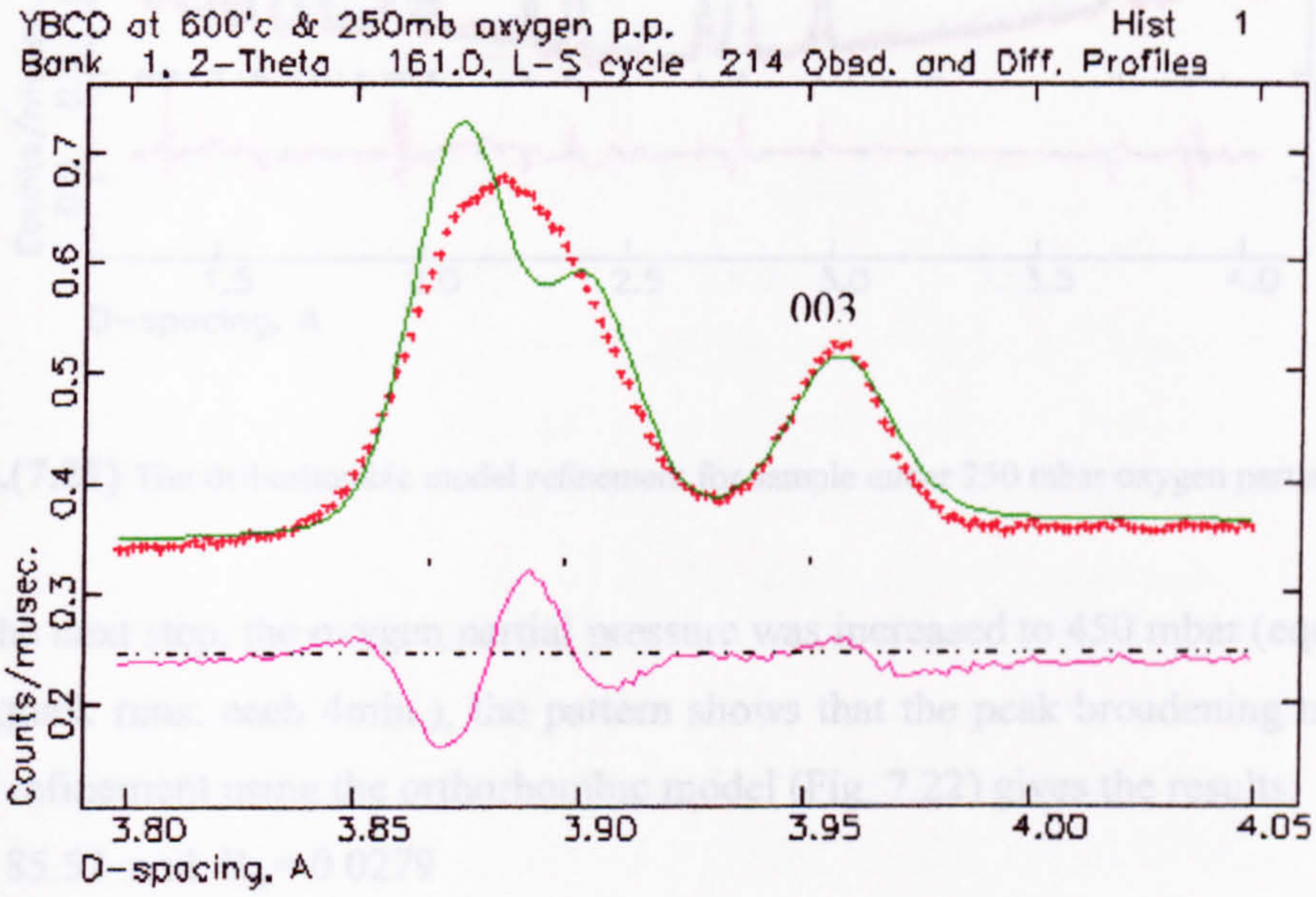

Fig.(7.20) The broadening and splitting of the [100] & [010] peaks under 250 mbar oxygen partial pressure at 600°C

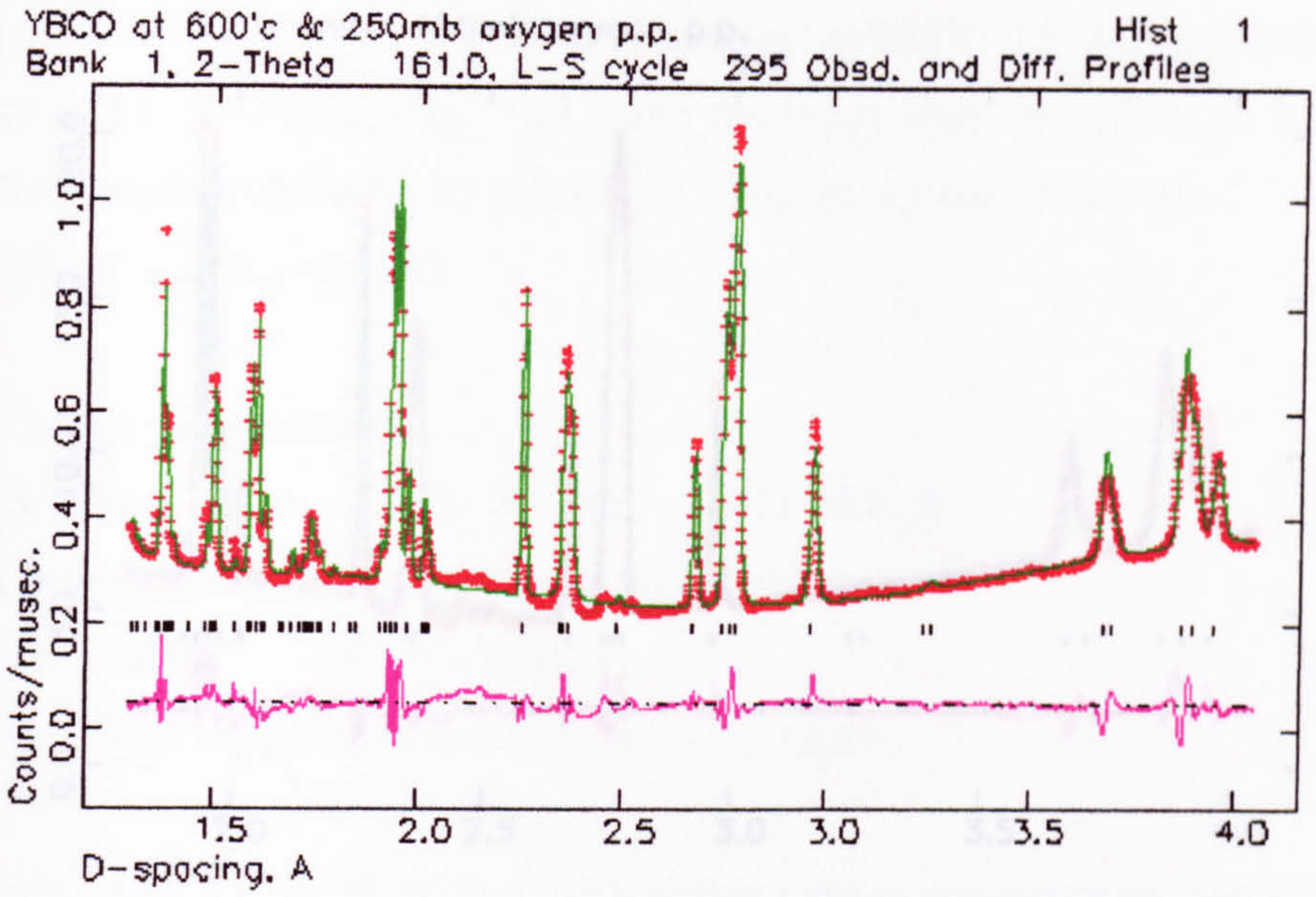

Fig.(7.21) The orthorhombic model refinement for sample under 250 mbar oxygen partial pressure

In the next step, the oxygen partial pressure was increased to 450 mbar (equilibrated after 24 quick runs; each 4min.), the pattern shows that the peak broadening trend continues and refinement using the orthorhombic model (Fig. 7.22) gives the results:

$\chi^2 = 85.52$ and $R_p = 0.0279$

The lattice parameters are:

$a = 3.862 \pm 0.0017$ Å ; $b = 3.907 \pm 0.0017$ Å and $c = 11.859 \pm 0.005$ Å

The average oxygen sites fraction in the basal plane:

O(1) = 0.6832±0.019 O(5) = 0.0769±0.002

Therefore the oxygen concentration is: $x \sim 0.76$

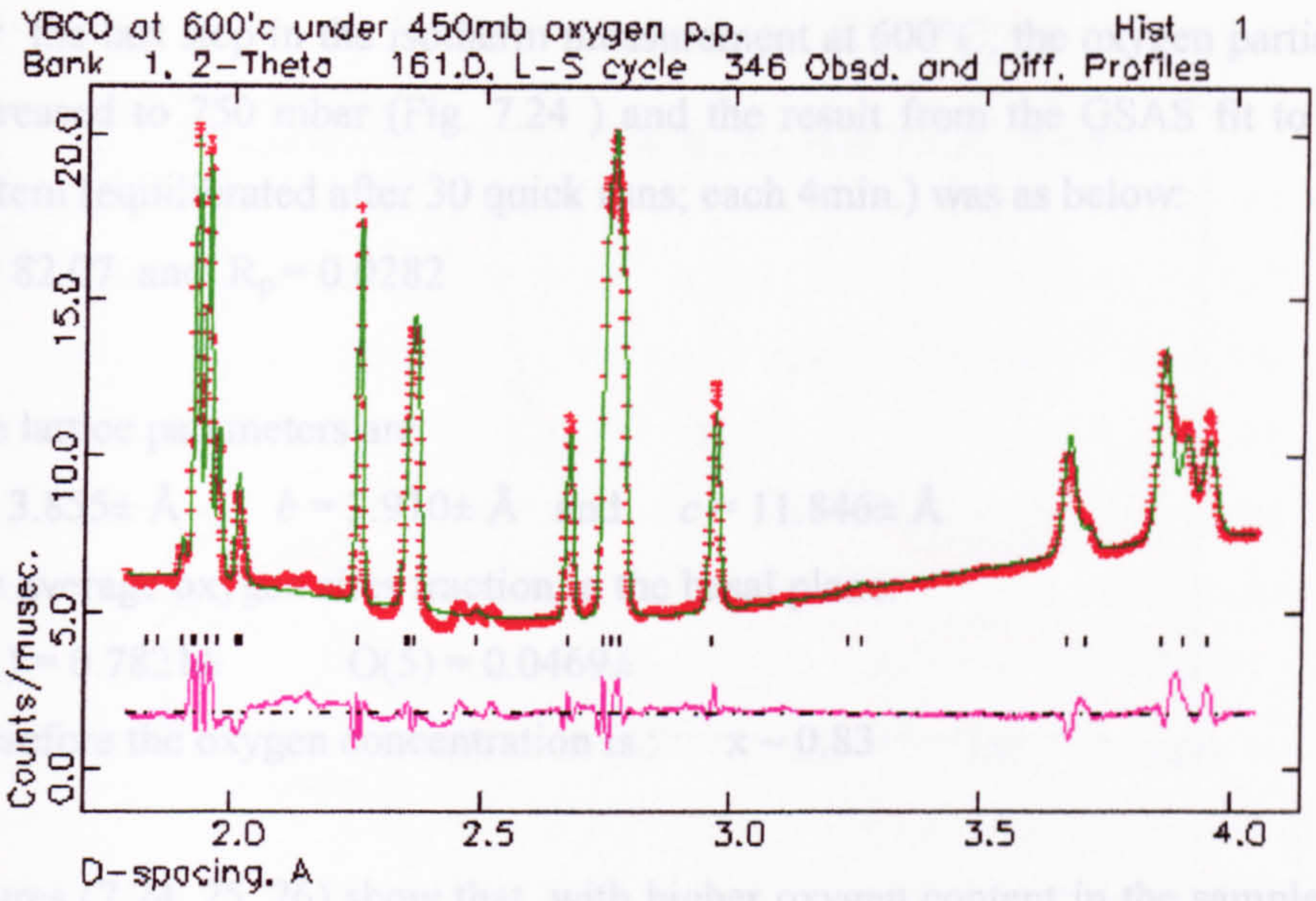

Fig.(7. 22) The orthorhombic model refinement for the sample under 450 mbar oxygen partial pressure

Again there is a big discrepancy between the model and data for the clearly separated [100] & [010] peaks (Fig.7.23). The model again predicts more separation than is indicated by the experimental data (same for [200]&[020] lines).

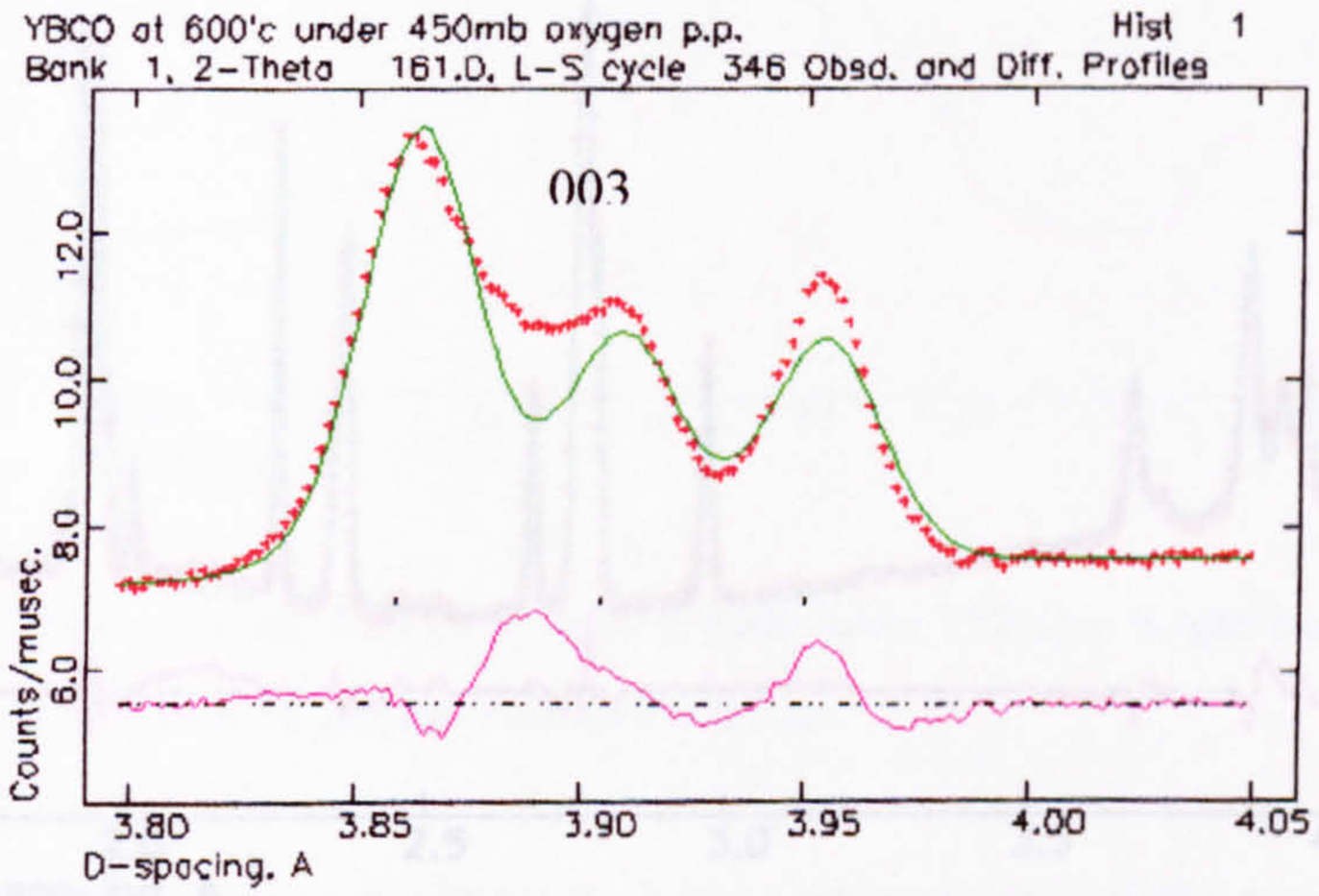

Fig.(7.23) The broadening and splitting for the [100&010] peaks under 250 mbar oxygen partial pressure at 600°C

For the last step in the isotherm measurement at 600°C, the oxygen partial pressure was increased to 750 mbar (Fig. 7.24) and the result from the GSAS fit to the diffraction pattern (equilibrated after 30 quick runs; each 4min.) was as below:

$\chi^2 = 82.07$ and $R_p = 0.0282$

The lattice parameters are:

$a = 3.855\pm$ Å ; $b = 3.910\pm$ Å and $c = 11.846\pm$ Å

The average oxygen sites fraction in the basal plane:

O(1) = 0.7821± O(5) = 0.0469±

Therefore the oxygen concentration is : $x \sim 0.83$

Figures (7.24_25_26) show that, with higher oxygen content in the sample and therefore further separation of the [*h00*] &[*0h0*] peaks, the difference between the model and the data is reduced, and this could be due to an increase in the twin's spacing and hence a decrease in the interference effects between adjacent twins (next section).

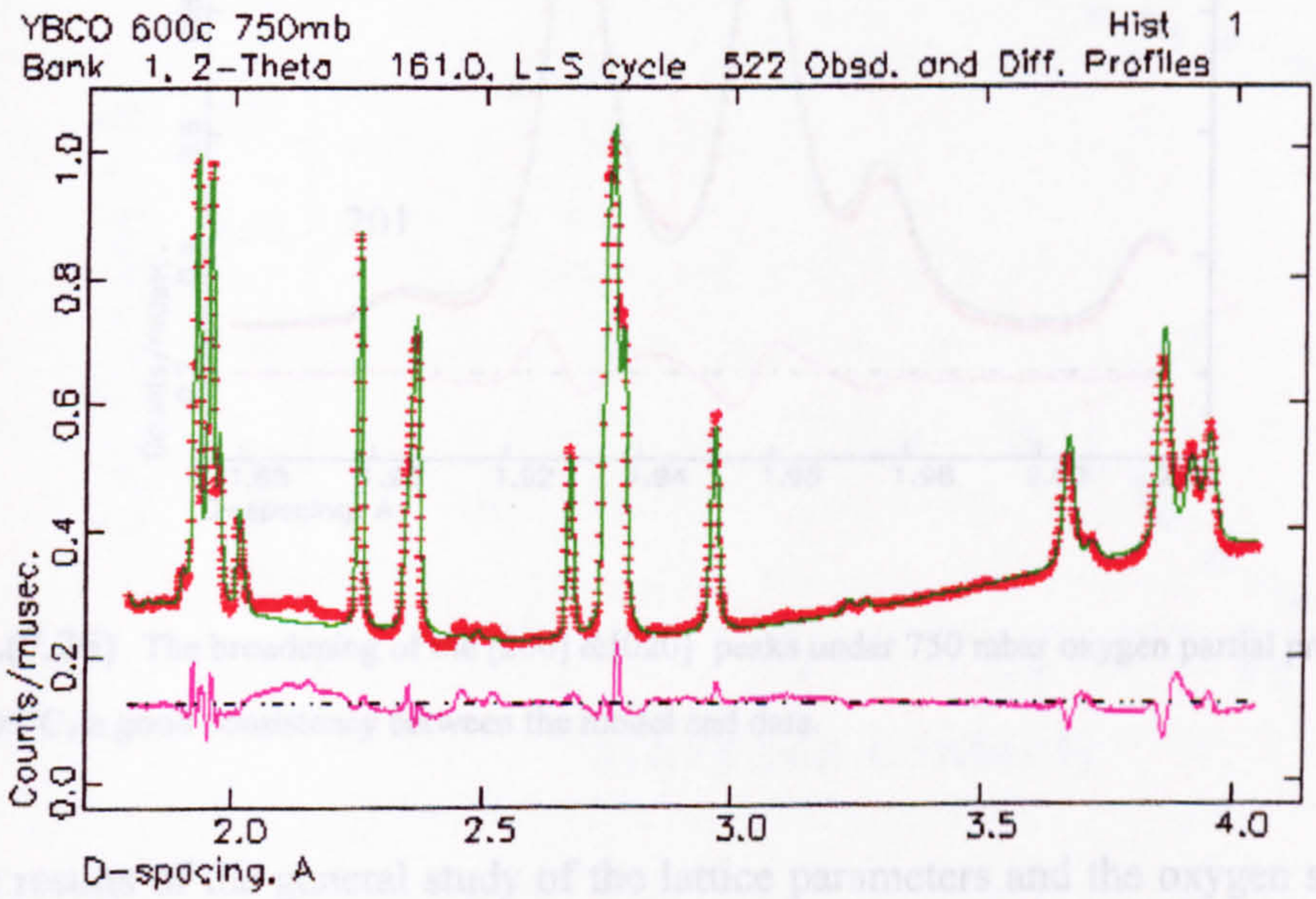

Fig.(7.24)) The orthorhombic model refinement for sample under 750 mbar oxygen partial pressure

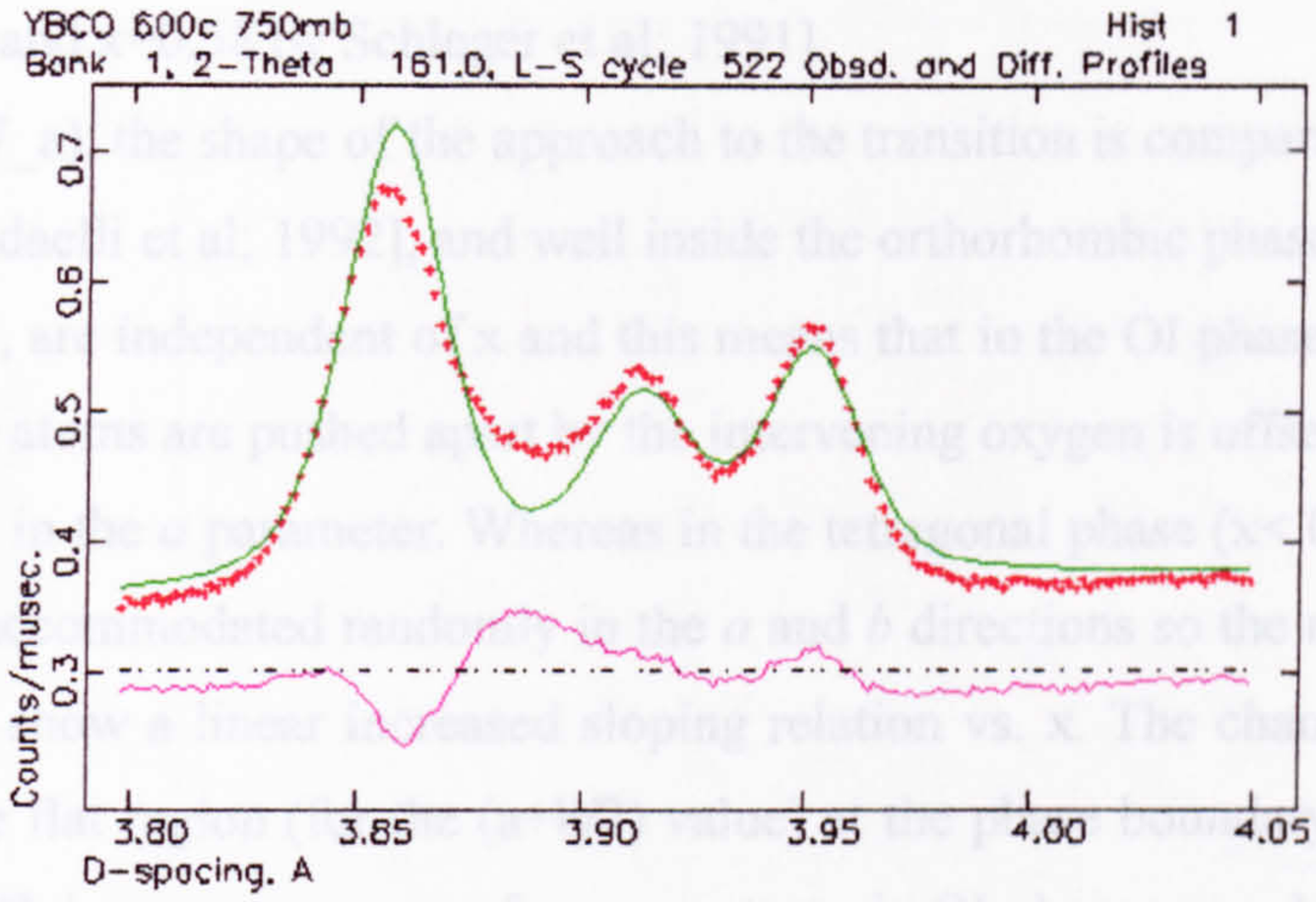

Fig.(7.25) The broadening and splitting for the [100] &[010] peaks under 750 mbar oxygen partial pressure at 600°C .

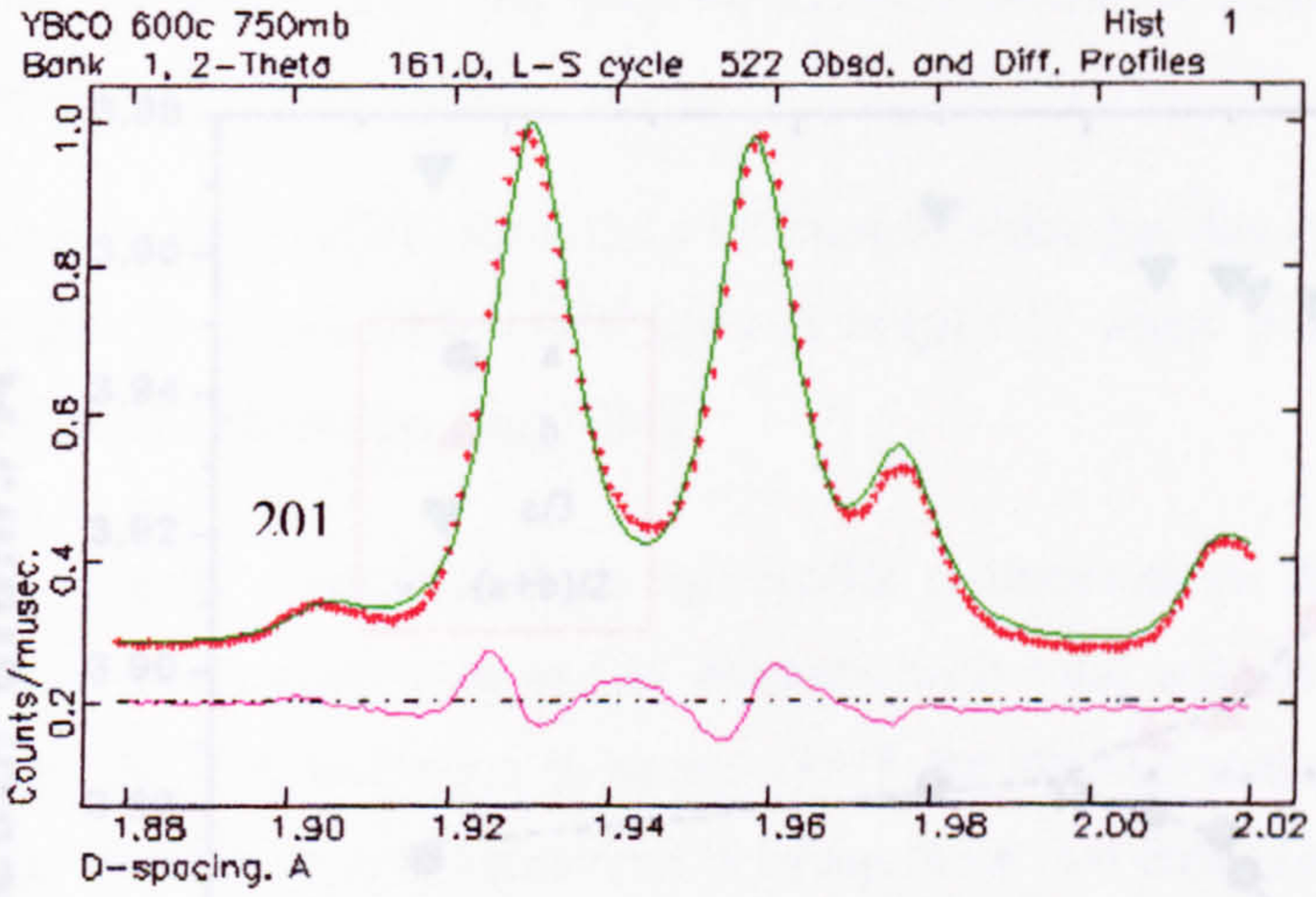

Fig.(7.26) The broadening of the [200] &[020] peaks under 750 mbar oxygen partial pressure at 600°C, a good consistency between the model and data.

The results of the general study of the lattice parameters and the oxygen site occupancy fraction in the basal plane are presented in Figs.(7.27_a,b). In both graphs, the exact bifurcation points (the T/OI phase boundary) have been deduced by extrapolation. It is

estimated to be just about x = 0.59 consistent with the other studies [x=0.57 by Meuffels et al; 1989 and x=0.58 by Schleger et al; 1991].

In Fig.(7.27_a), the shape of the approach to the transition is comparable with some other studies [Radaelli et al; 1992], and well inside the orthorhombic phase, the mean values of the *a* and *b*, are independent of x and this means that in the OI phase the extension in the *b* as the Cu atoms are pushed apart by the intervening oxygen is offset by a corresponding contraction in the *a* parameter. Whereas in the tetragonal phase (x< 0.5), because oxygen atoms are accommodated randomly in the *a* and *b* directions so the mean values of these parameters show a linear increased sloping relation vs. x. The change from the upward slope to the flat region (for the (a+b/2) value) at the phase boundary would suggest that the more efficient arrangement of oxygen atoms in OI phase are achieved by pulling out oxygen from the O(5) sites and reordering them on the O(1) sites, in addition to the absorption of new oxygen atoms and their accommodation them along the *b* direction (Fig.7.27_b).

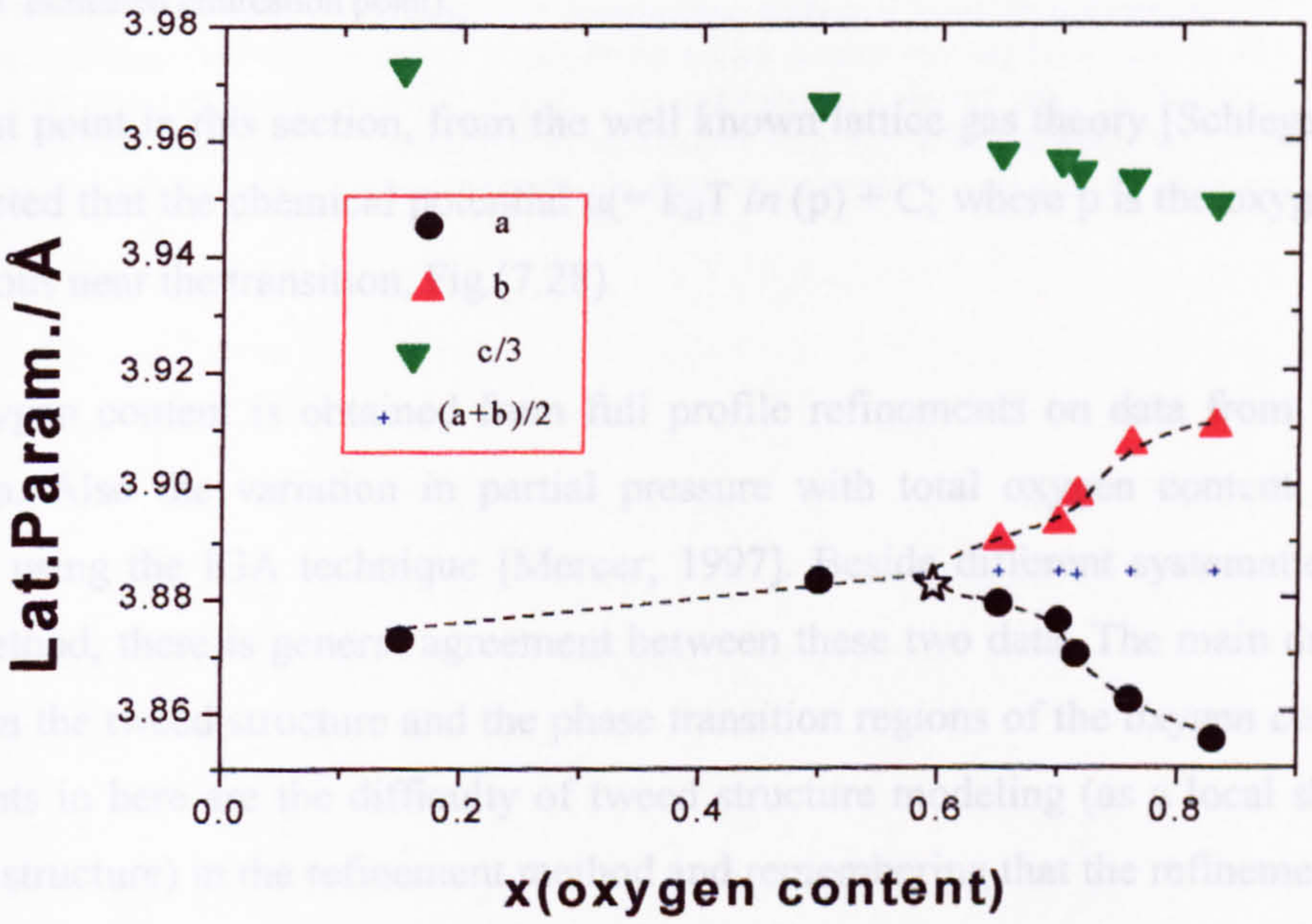

Fig.(7.27_a) The variation of the lattice parameters vs. oxygen content at 600°C.The star shows the estimated bifurcation point. Error bars are equal or smaller than the size of the symbols.

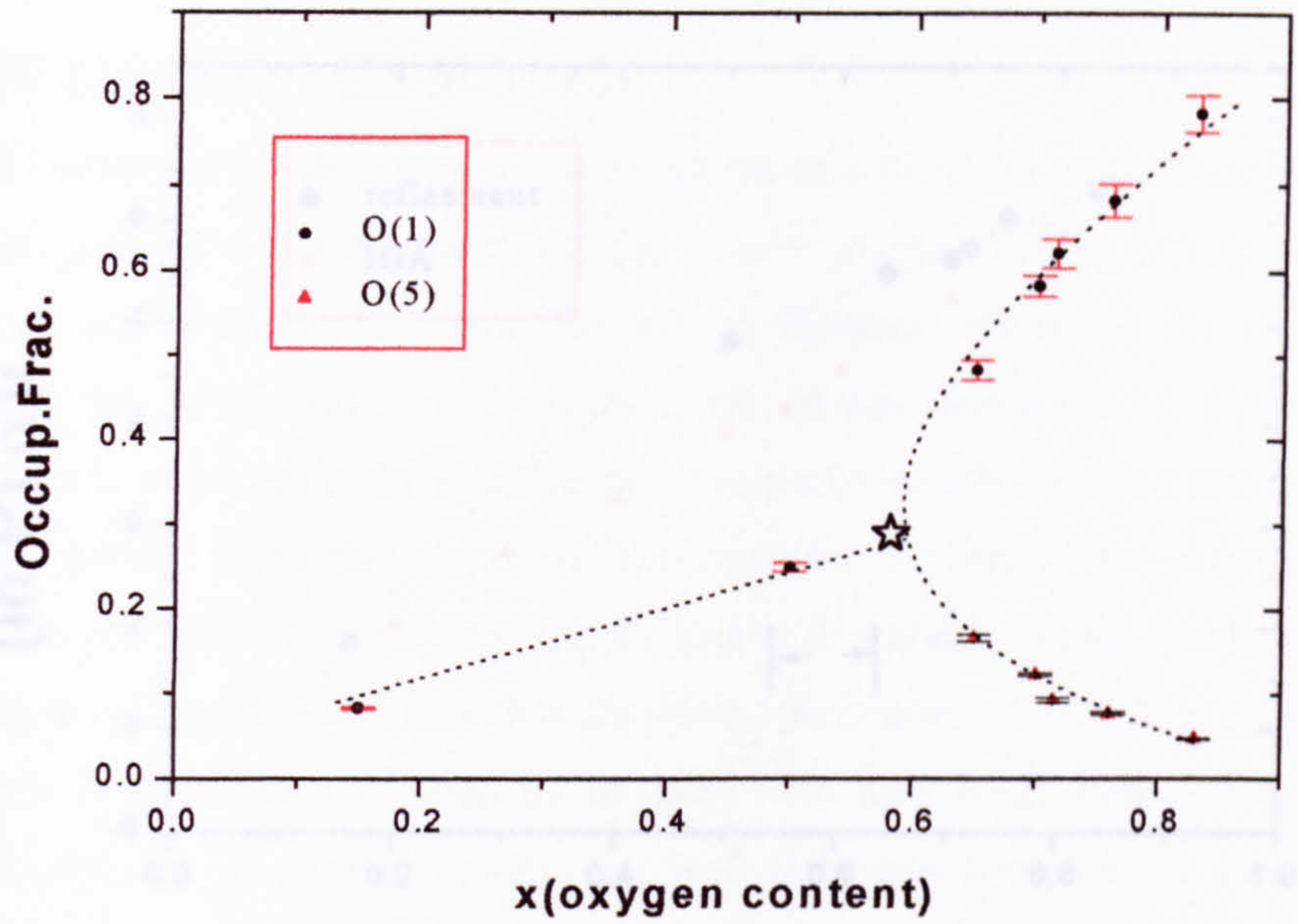

Fig.(7.27_b) The variation of the basal plane site occupancy fraction vs. oxygen content at 600°C (the star is the estimated bifurcation point).

As a last point in this section, from the well known lattice gas theory [Schleger; 1991] it is expected that the chemical potential $\mu(= k_B T \, ln \, (p) + C$; where p is the oxygen p.p.) is continuous near the transition, Fig.(7.28).

The oxygen content is obtained from full profile refinements on data from the 600°C isotherm. Also the variation in partial pressure with total oxygen content, measured directly using the IGA technique [Mercer; 1997]. Beside different systematic errors in each method, there is general agreement between these two data. The main discrepancy occurs in the tweed structure and the phase transition regions of the oxygen content. The comments in here are the difficulty of tweed structure modeling (as a local short range ordered structure) in the refinement method and remembering that the refinement method will lose any disordered oxygen atoms. Both techniques show the pressure variation to be continuous, with a smooth tangent across the T/OI phase transition, consistent with the theory of a second order transition in a lattice-gas systems [Mercer: 1997] and [Schleger; 1991].

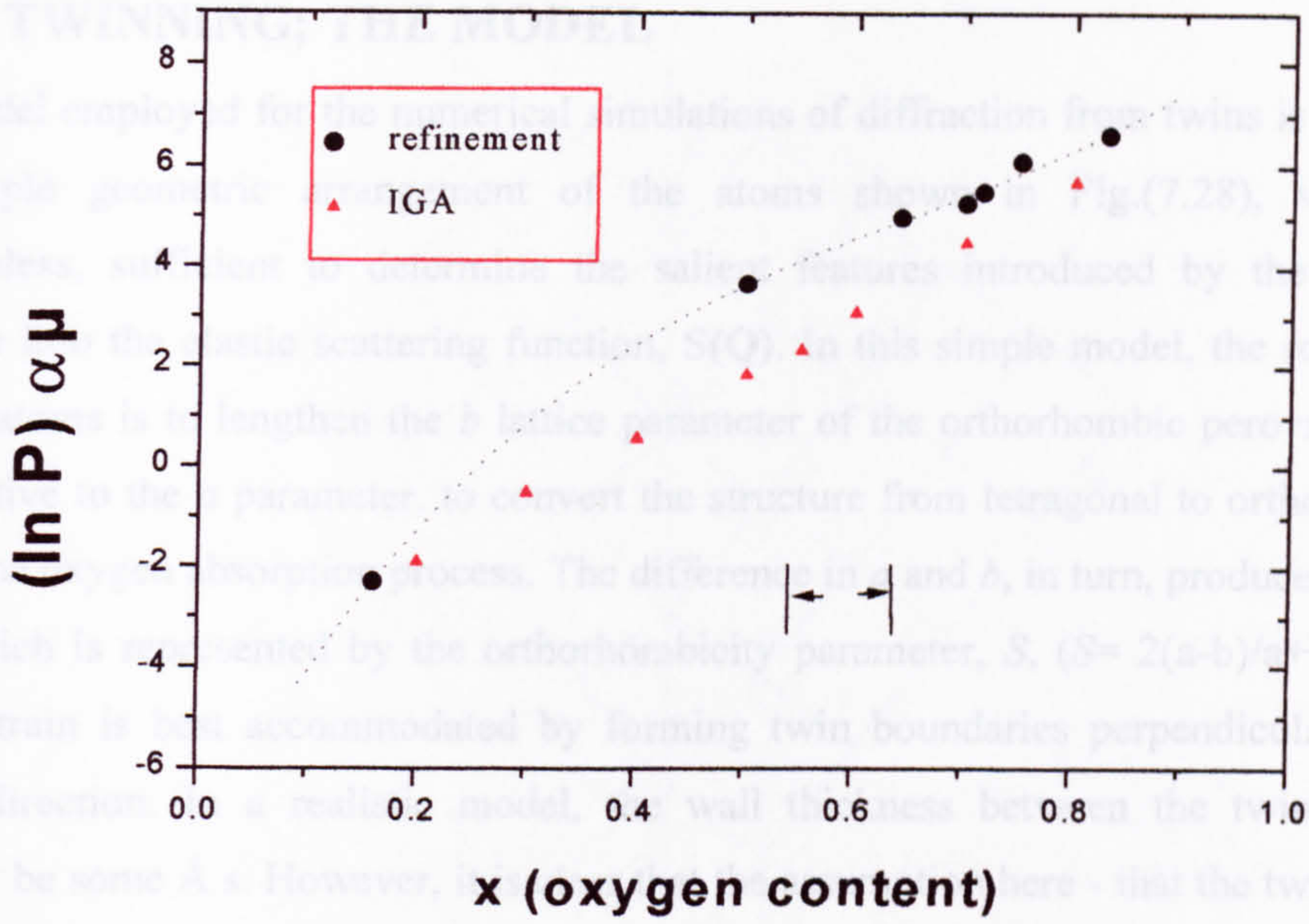

Fig.(7.28) Oxygen pressure versus oxygen composition extracted from the isotherm at 600°C. In the interesting stoichiometric range (0<x<1), oxygen atoms are mobile moving from O(5) to O(1) sites and making a long range order structure (OI phase). The graph shows a plateau which indicates the chemical potential is smooth around the T/OI transition (comparable with Fig. 5.12 in chapter V). The isotherm measurements at 600°C using gravimetric method (IGA), were prepared by Michelle Mercer (Ph.D thesis)

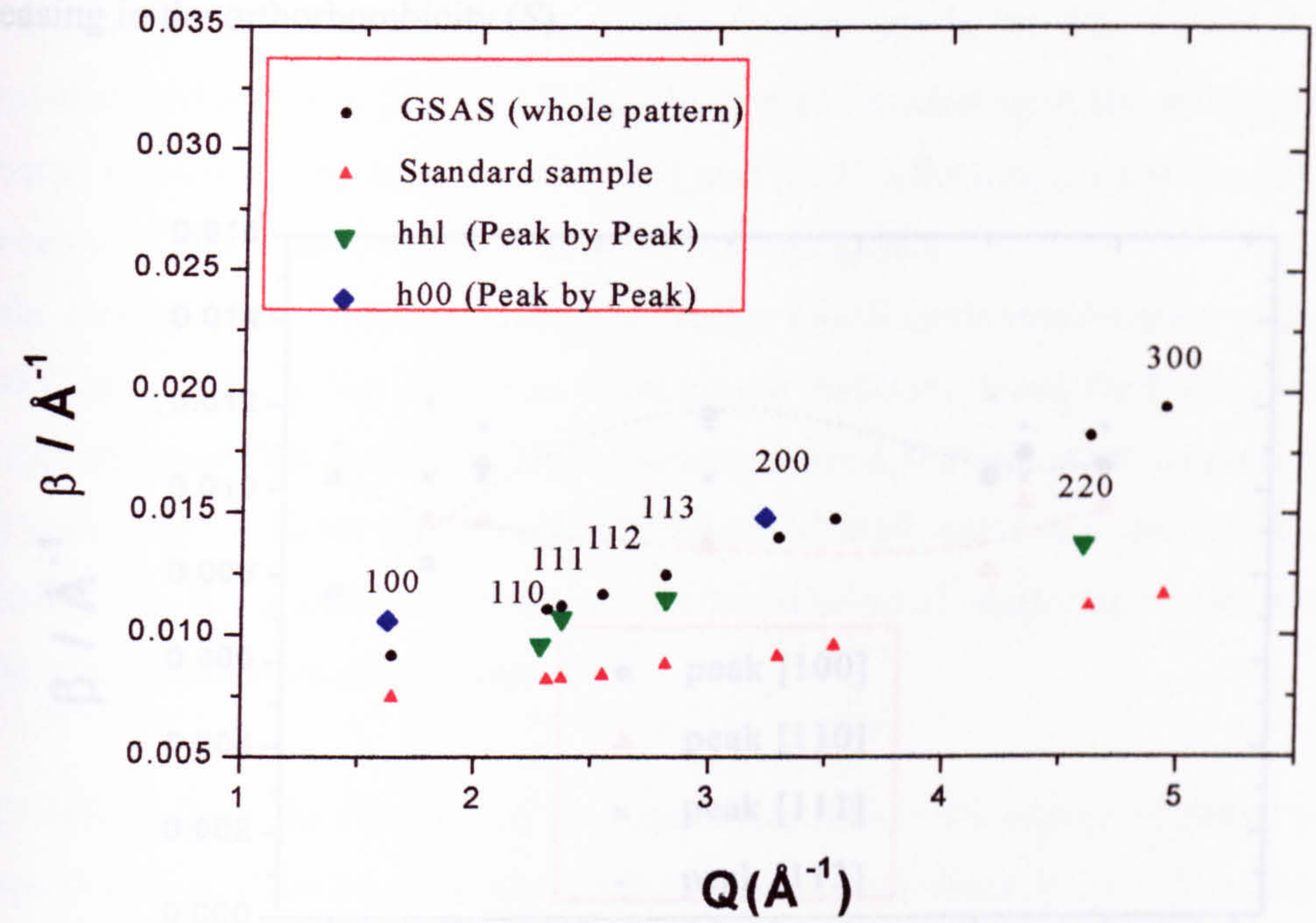

Fig.(7.44) A Williamson-Hall plot of the widths in Q space for the data at 600°C and 750 mbar oxygen partial pressure.

Figure (7.45) presents the evolution of the individual peak widths (measured after the sample was equilibrated at successive oxygen pressures steps) while the sample crosses the tetragonal/orthorhombic phase boundary and going further into the OI phase. When the sample is in the tetragonal phase (<150 mbar; S=0), the breadth of the peaks generally increases with the order of reflection. However, after crossing the phase boundary, $S\neq0$, as the sample absorbs more oxygen atoms, the [*hh0*] peaks become narrower while the [*h00*] peaks become broader. The implication of the above argument is that the form of the [*h00*] peaks is determined by the term $(h+k).(S\mathrm{x}T)$, so.for $(h+k)$ $(S\mathrm{x}T)\ll1$, we get a single peak and for $(h+k).(S\mathrm{x}T)\gg1$, we get two separated peaks, whereas for $(h+k).(S\mathrm{x}T)\approx1$, the coherent effects are important (section VII.3). The broadening of [100] reflection just after transition can be attributed to the coherence effects between very narrow twins which makes the resolution of [100]&[010] peaks becomes very

difficult and to some extent inaccurate, whereas the narrowing in the [110] reflection indicates the spreading of the twinning structure throughout the whole crystallite, with increasing in the orthorhombicity (S).

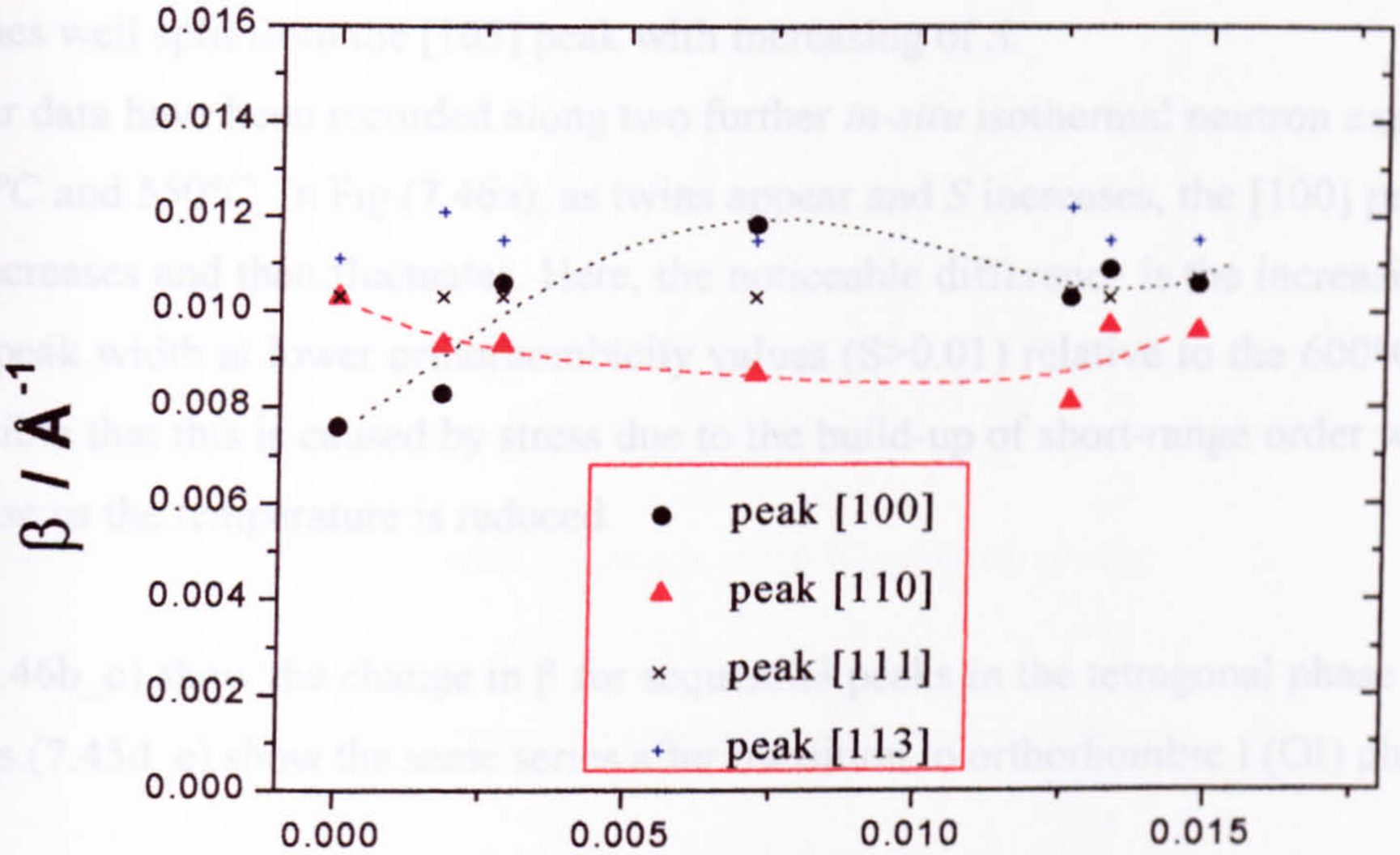

Fig.(7.45) Variations of the peak widths in reciprocal space as a function of the orthorhombicity measured at 600°C. The doted and dashed lines are a guide to the eye for the [100] and [110] peaks respectively.

More discussion comes from the following formula which has been introduced in chapterIII:

$$T = [G\gamma / ES^2] \qquad (7.19)$$

where T is the twin separation, G is average grain size and E is the shear modulus. Now, according to a mean field prediction if $\gamma \propto S^2$ [Saikaya et al; 1988], this suggests that T becomes independent of S, but due to the intensive repulsion between O atoms as a result of the reduction in the O-O sites distance, across the twin boundary (T.B.) and the formation of an oxygen depleted layer in the vicinity of a T.B. [Moodie et al (1988) and Bourdillon et al (1994)], it seems that the mean field suggestion is not appropriate at least for highly oxygen deficient samples just after Tet/OI transition ($S \geq 0$). Nevertheless, if we still accept a kind of functional relation for higher powers of S like, $\gamma(S^3)$, at least around

the phase boundary where S tends to 0 ($S \rightarrow 0$), the twin spacing, T, will increase from zero as S increases. For intermediate ranges of S, according to the mean field assumption, the value of T remains constant, besides the fluctuations in the line widths. At higher values of orthorhombicity ($S \geq 0.012$) the unexpected broadening of this reflection can be attributed to overlapping between the [110] and [013] reflections, while the [013] peak becomes well split from the [103] peak with increasing of S.

Similar data have been recorded along two further *in-situ* isothermal neutron experiments at 500°C and 550°C. In Fig.(7.46a), as twins appear and S increases, the [100] peak width first increases and then fluctuates. Here, the noticeable difference is the increasing of the [110] peak width at lower orthorhombicity values (S>0.01) relative to the 600°C data. It is possible that this is caused by stress due to the build-up of short-range order within the OI phase as the temperature is reduced.

Figs.(7.46b_c) show the change in β for sequential peaks in the tetragonal phase whereas the Figs.(7.45d_e) show the same series after transition to orthorhombic I (OI) phase.

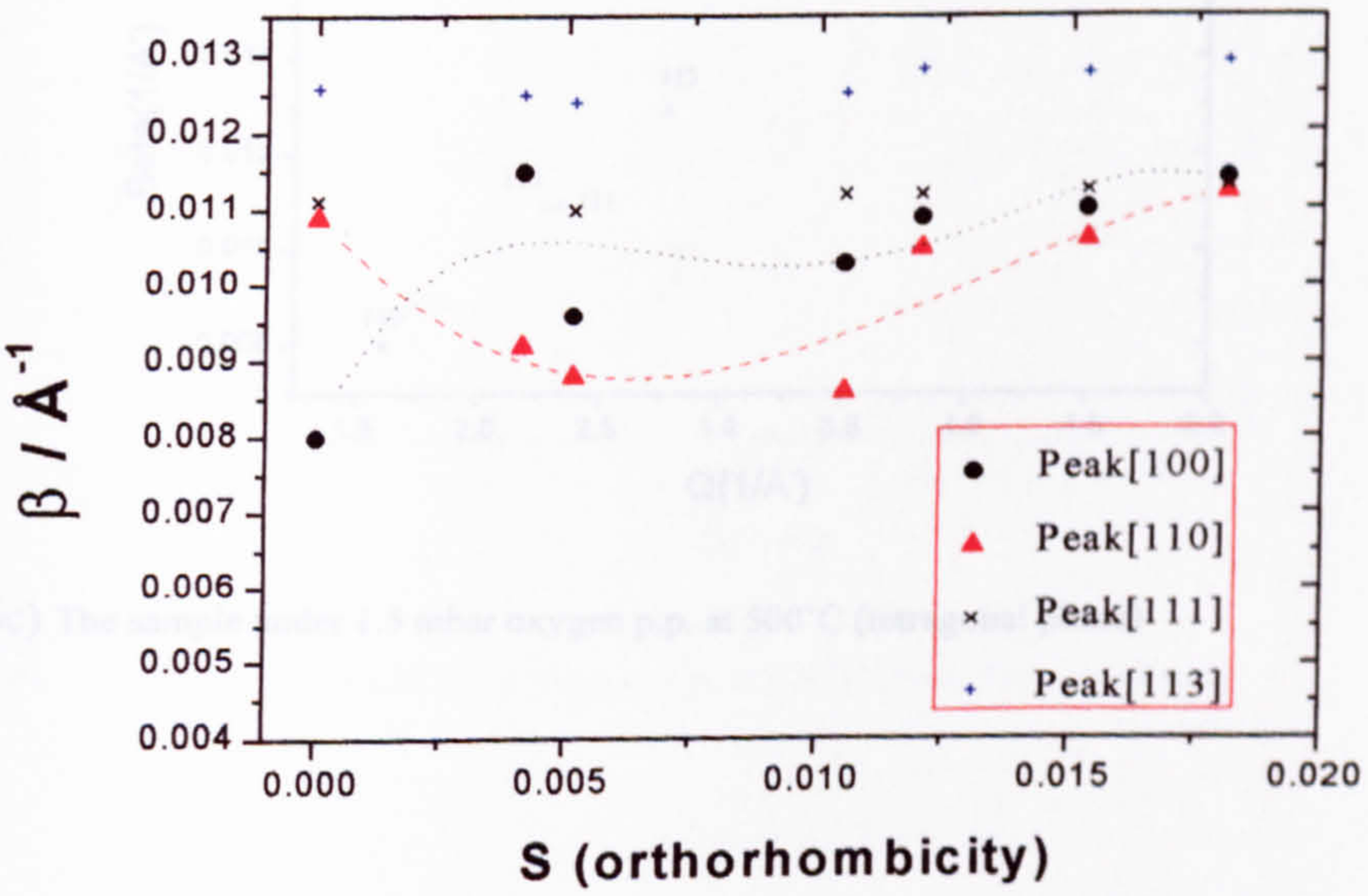

Fig.(7.46a) Plots of individual peak widths for a series of diffraction patterns recorded for increasing orthorhombicity at 500°C. The dotted and dashed lines are a guide to the eye for the [100] and [110] peaks respectively.

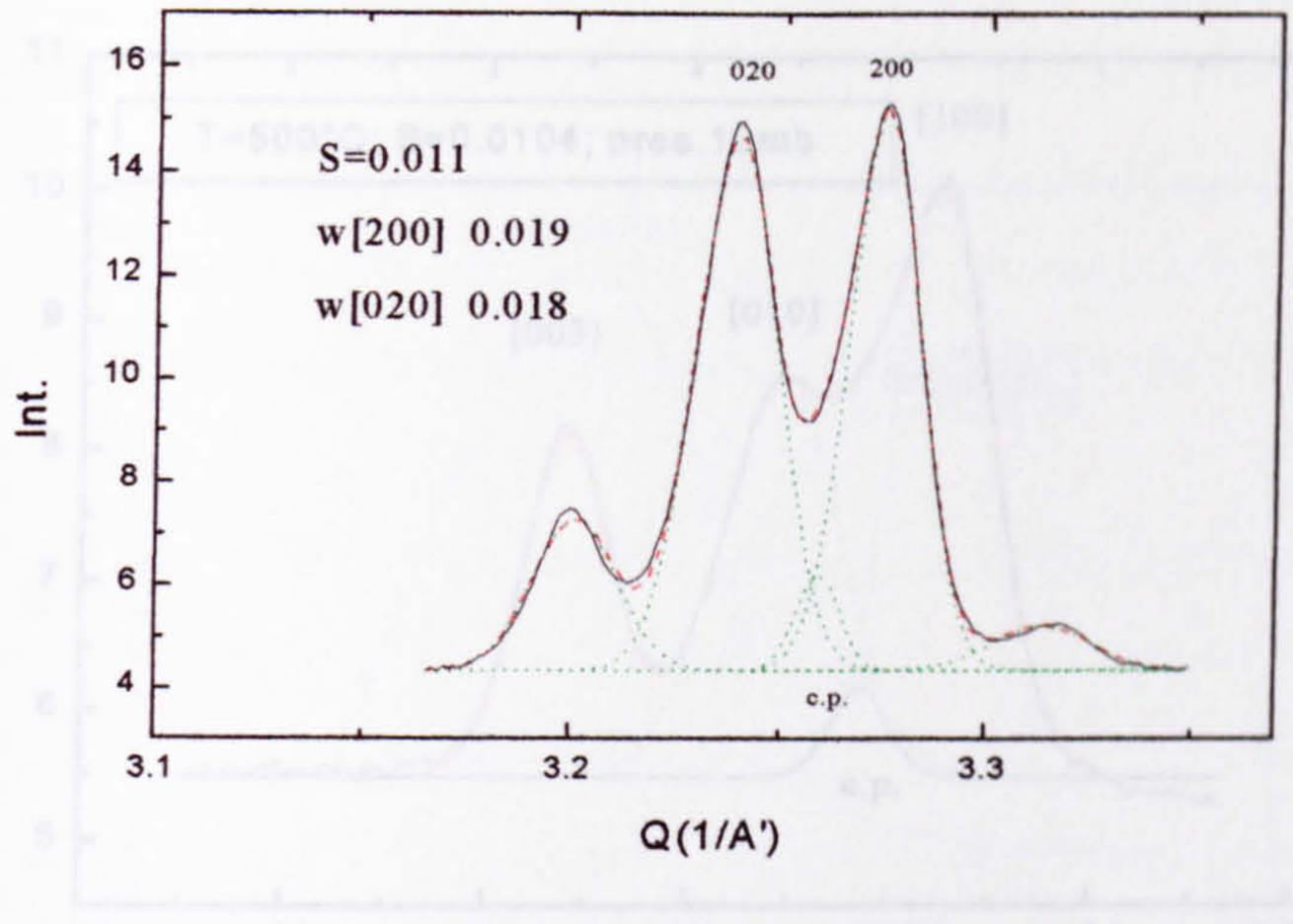

(a)

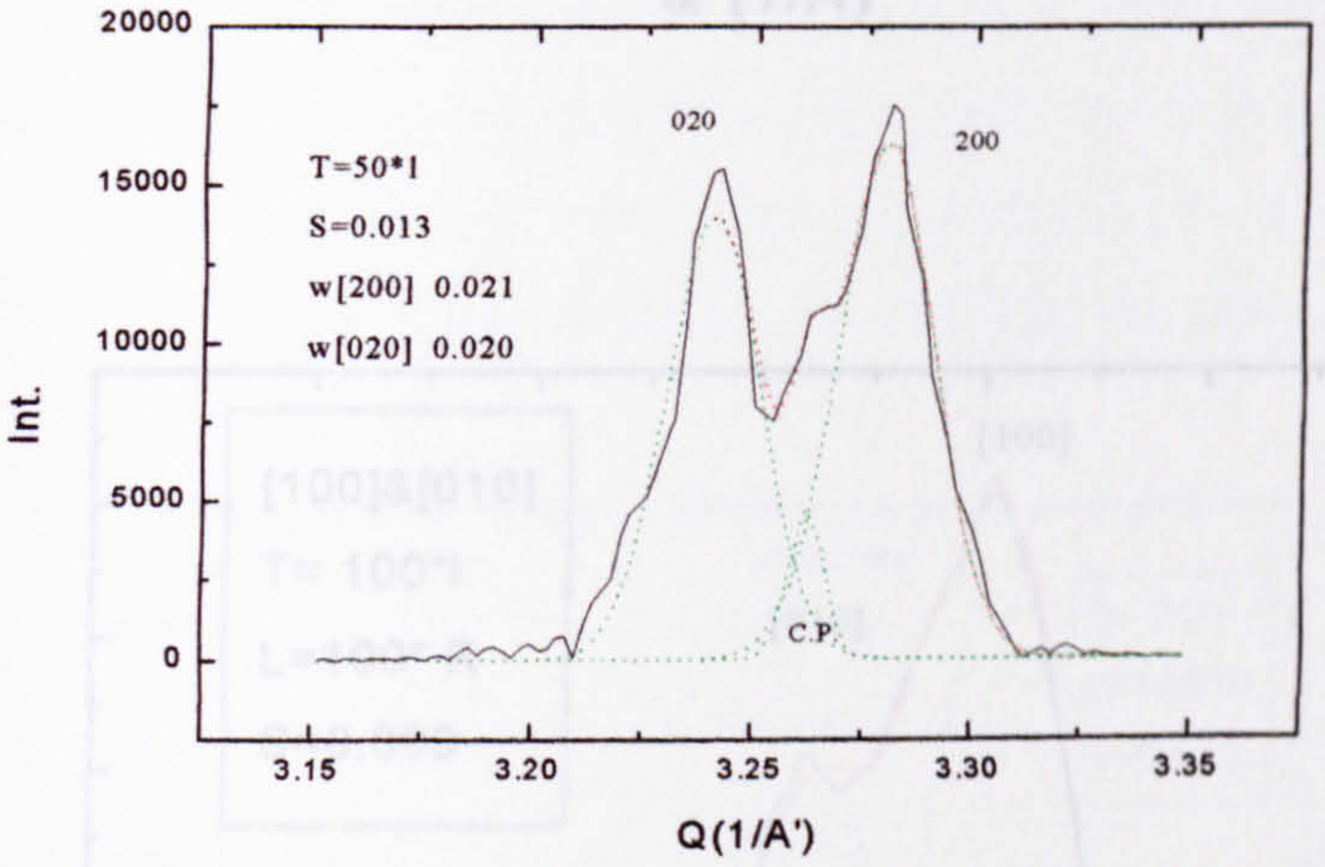

(b)

Fig.(7 50)

(a) Diffraction pattern for [200]&[020] reflections fitted by Gaussian profile shape function. The fit indicates a small central peak for S=0.011 (sample under 10 mbar oxygen p.p.at 500°C.

(b) The calculated pattern for S=0.013 and T=50 in Q space, again fitted by Gaussian functions.

The pattern shows a small central peak , comparable with the diffracted data in the part (a).

The peak widths of the diffracted [200]and [020] in Q scale are 0.016 and 0.019 $Å^{-1}$

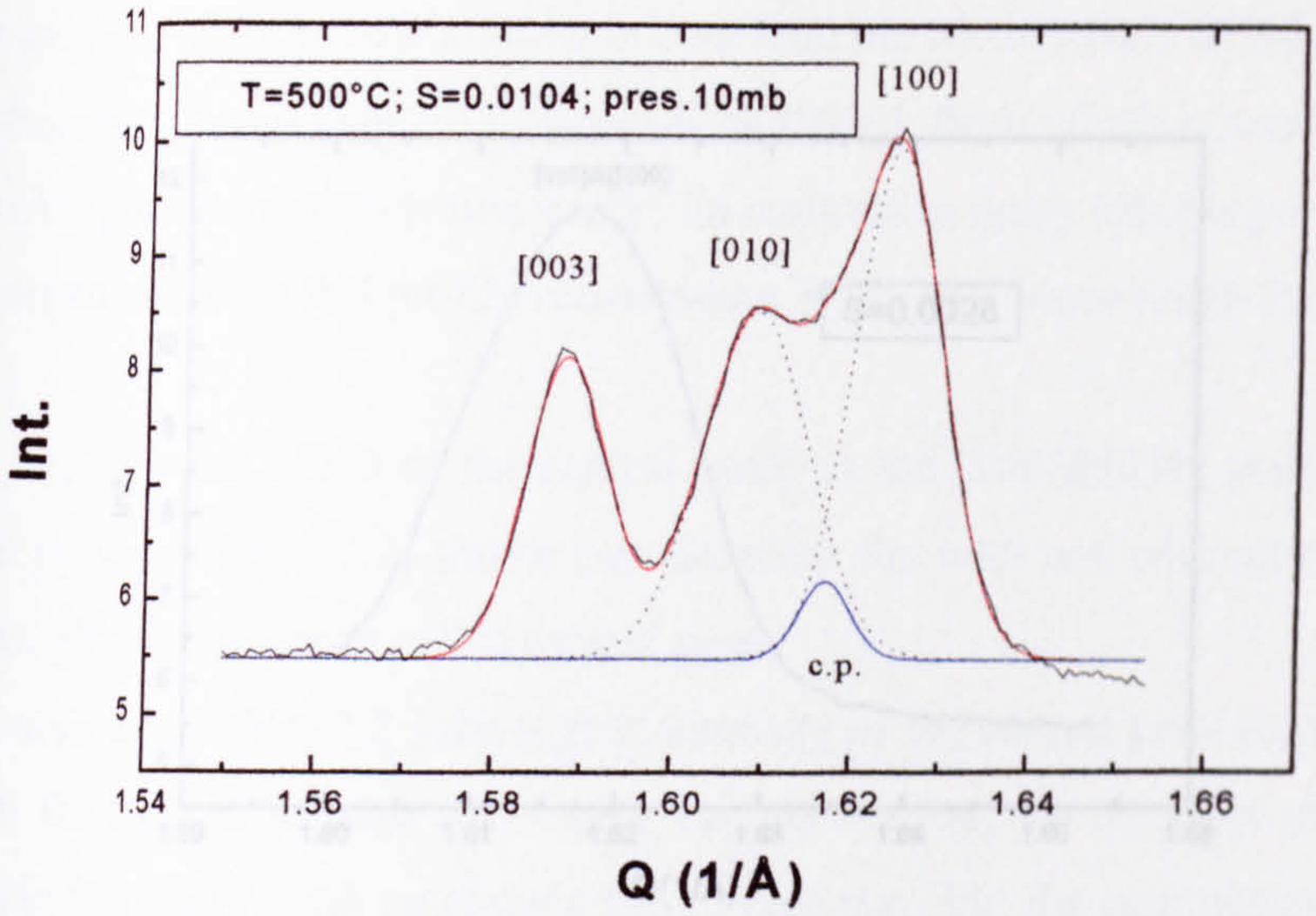

(a)

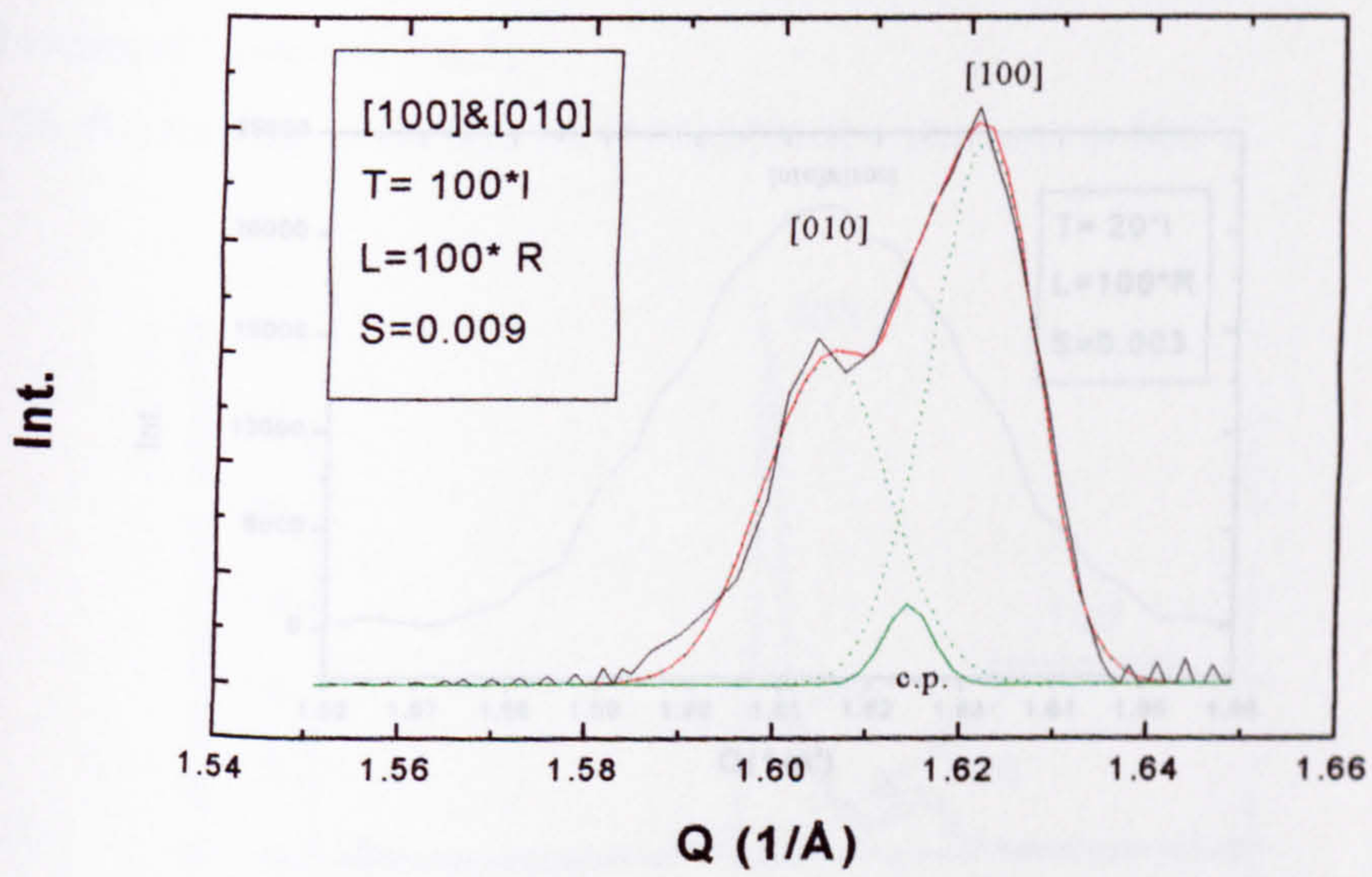

(b)

Fig.(7.51) a_ The sample under 300mbar oxygen p.p. at 600°C, b_the calculated profile with same orthorhombosity

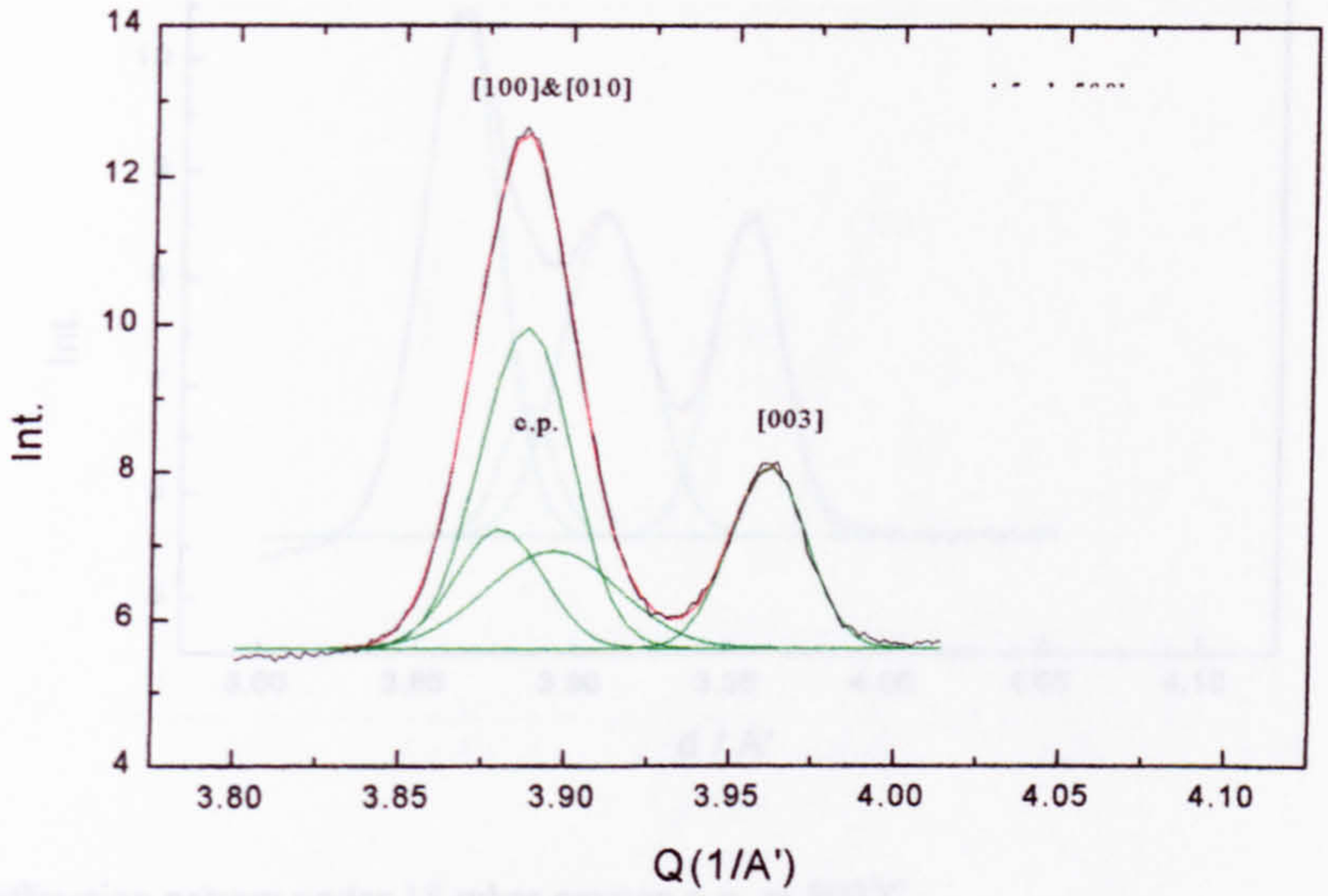

Fig.(7.54) Diffraction pattern under 4.5 mbar oxygen p.p. at 500°C

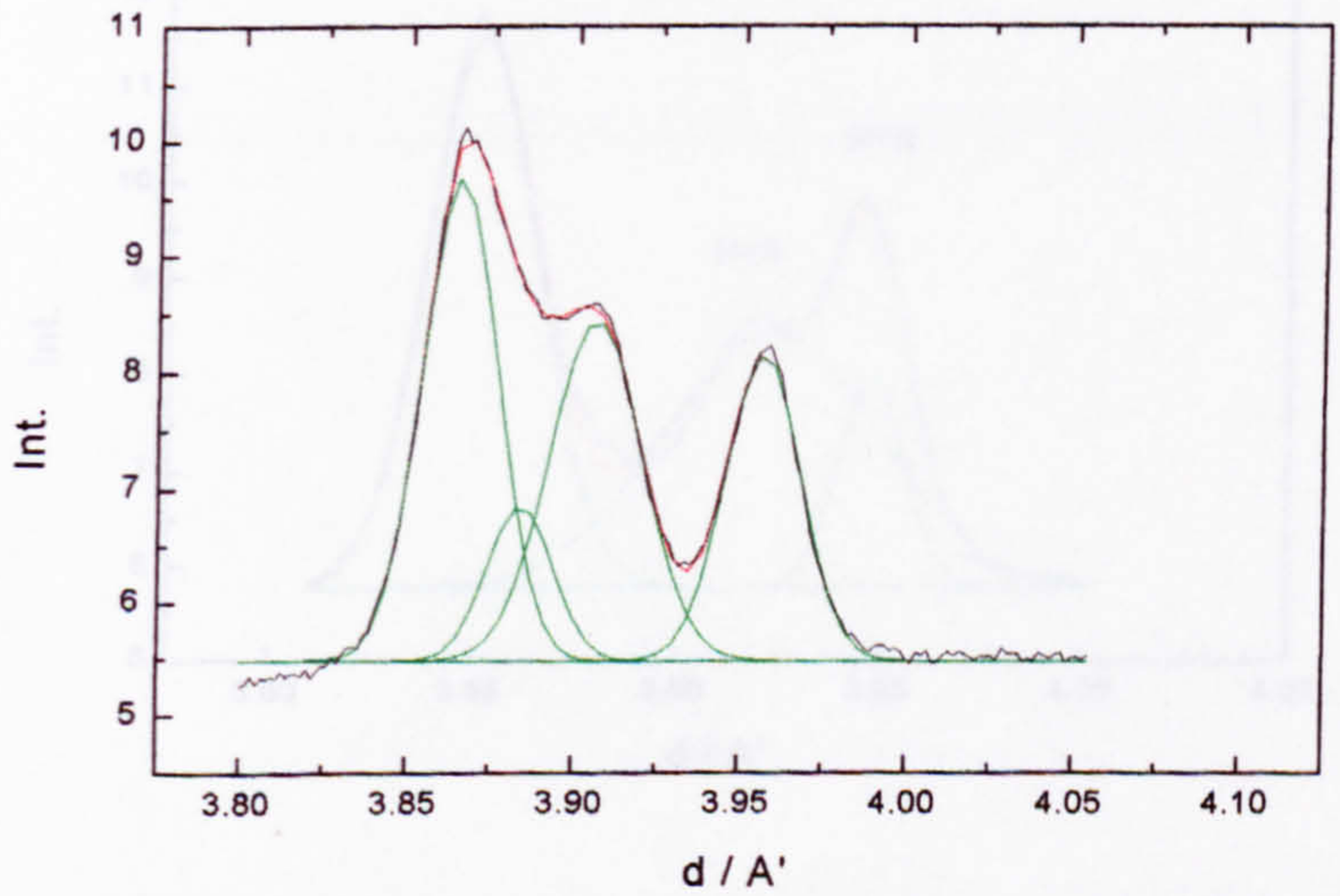

Fig.(7.55) Diffraction pattern under 10 mbar oxygen p.p. at 500°C

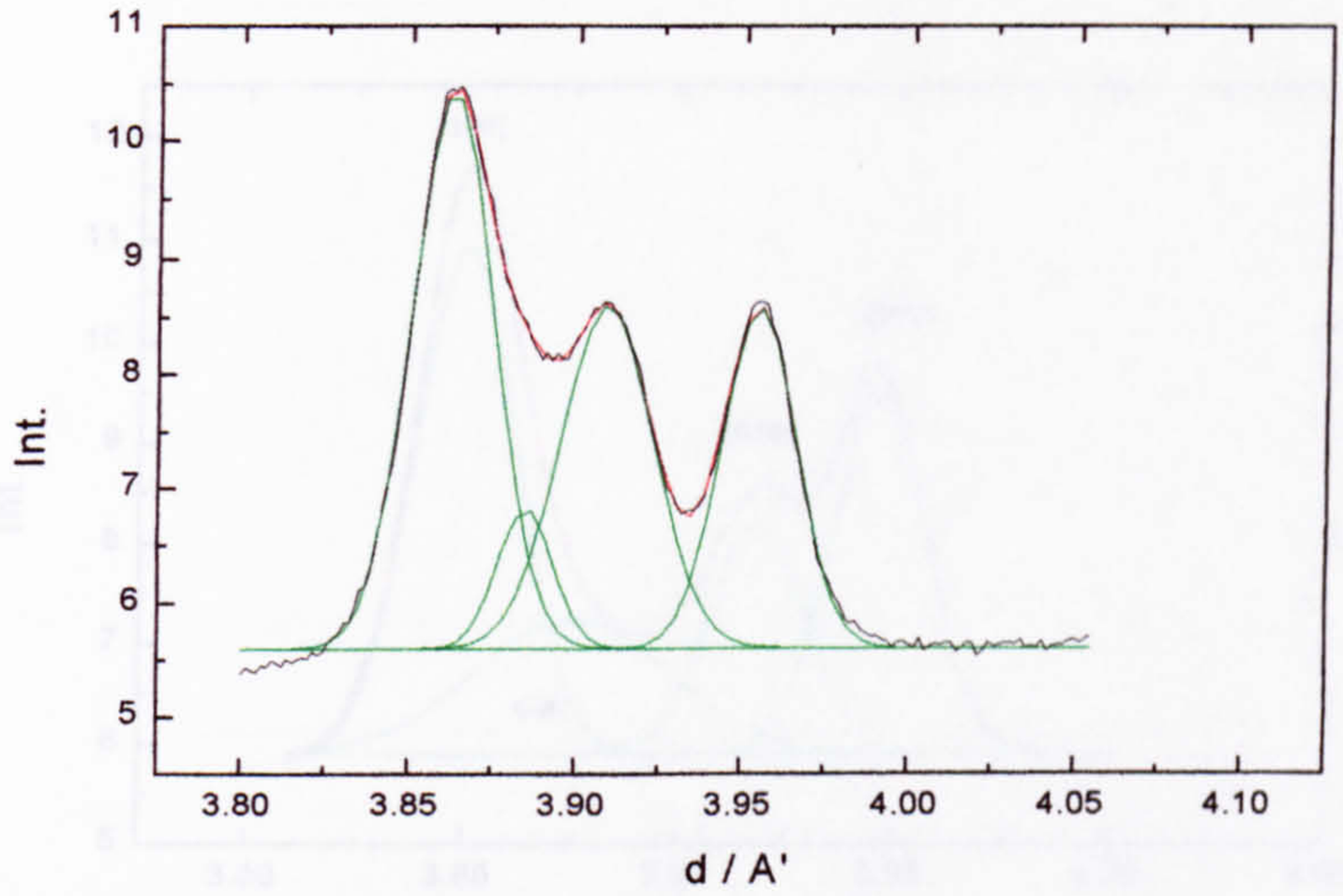

Fig.(7.56) Diffraction pattern under 18 mbar oxygen p.p. at 500°C

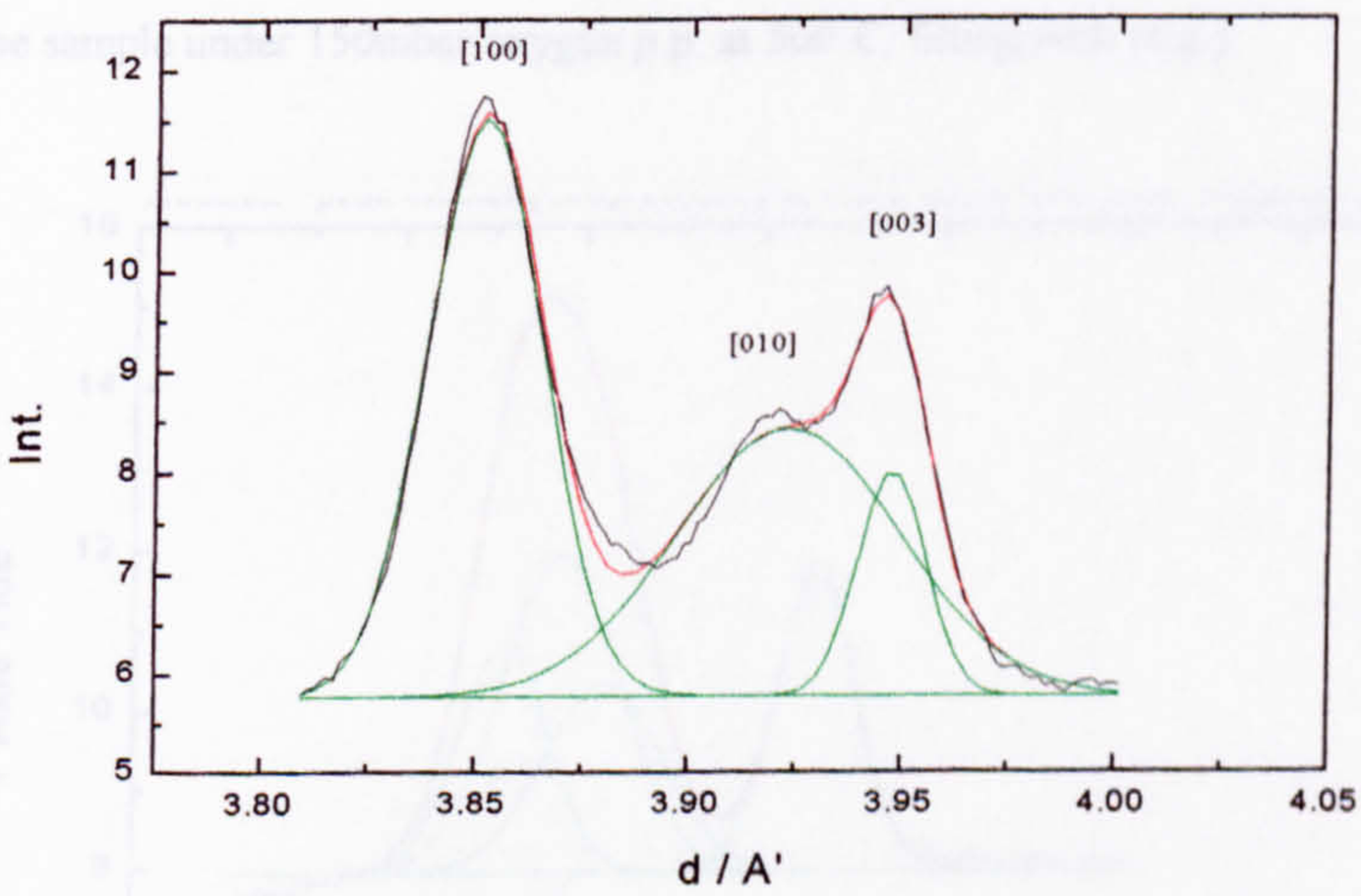

(a)

Fig.(7.57a) The sample under 150mbar oxygen p.p. at 500°C, fitting without central peak(c.p.).

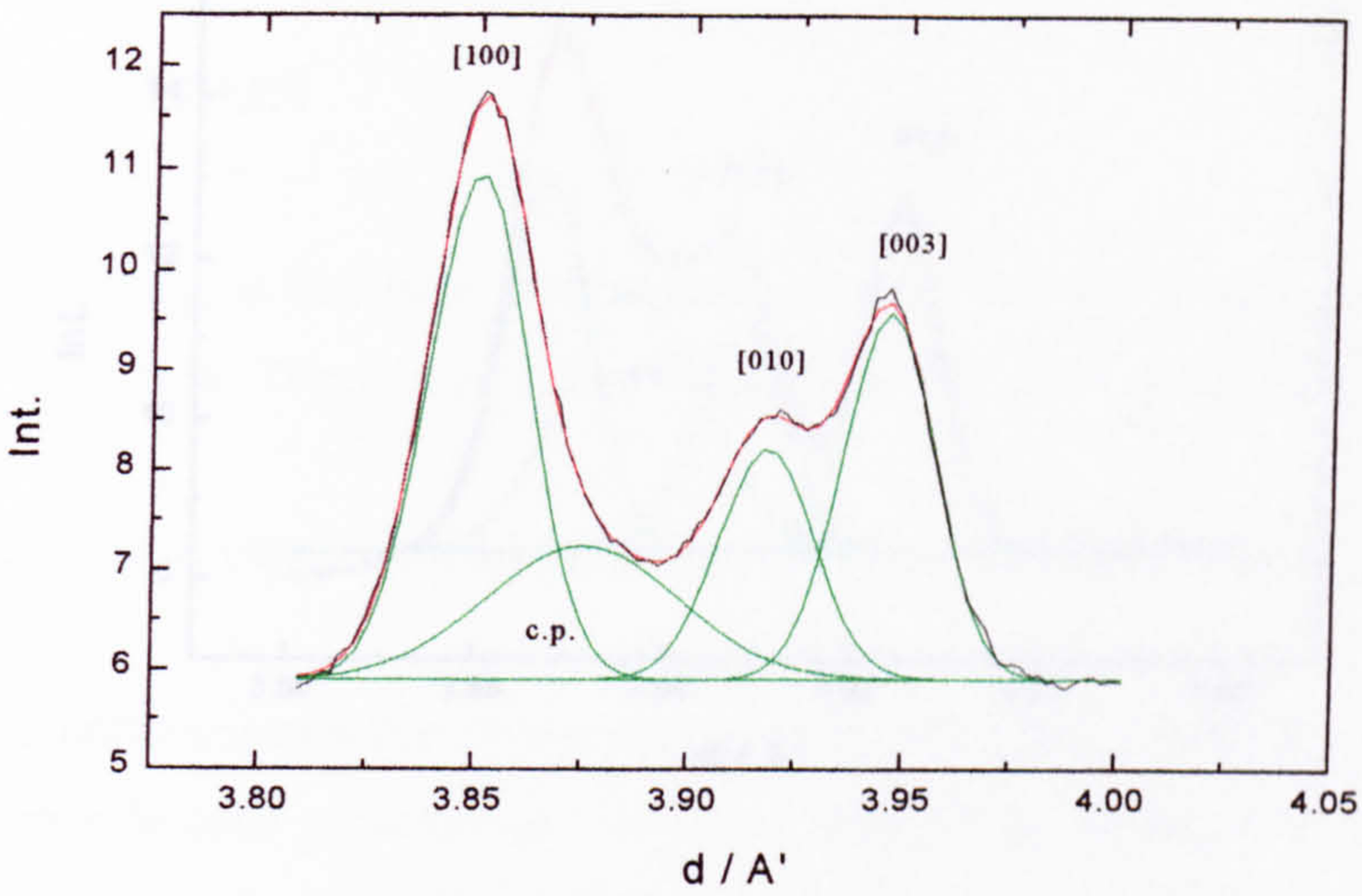

(b)

Fig.(7.57b) The sample under 150mbar oxygen p.p. at 500°C, fitting with (c.p.)

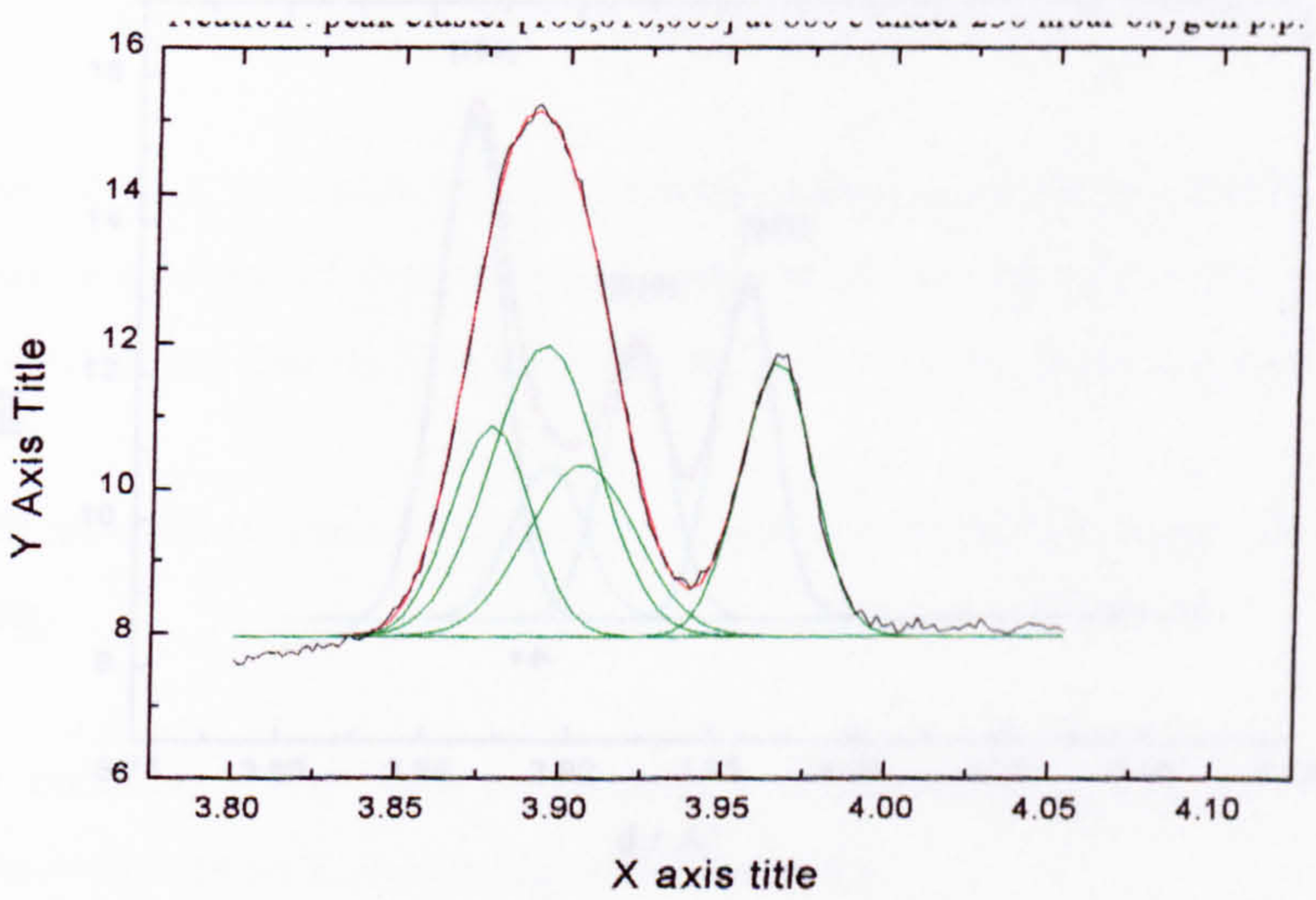

Fig.(7.58) Diffraction pattern under 200 mbar oxygen p.p. at 600°C

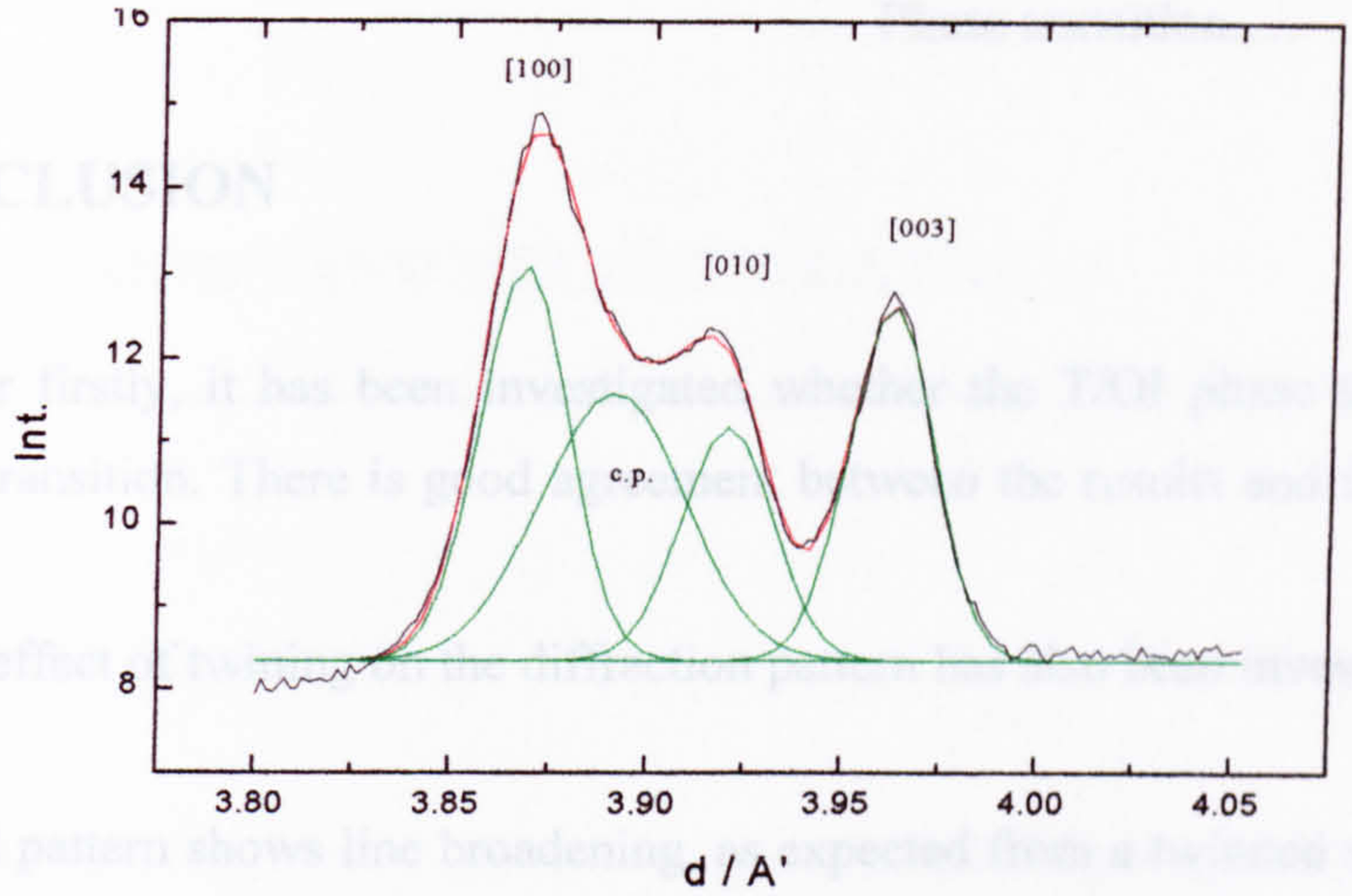

Fig.(7.59) Diffraction pattern under 450 mbar oxygen p.p. at 600°C

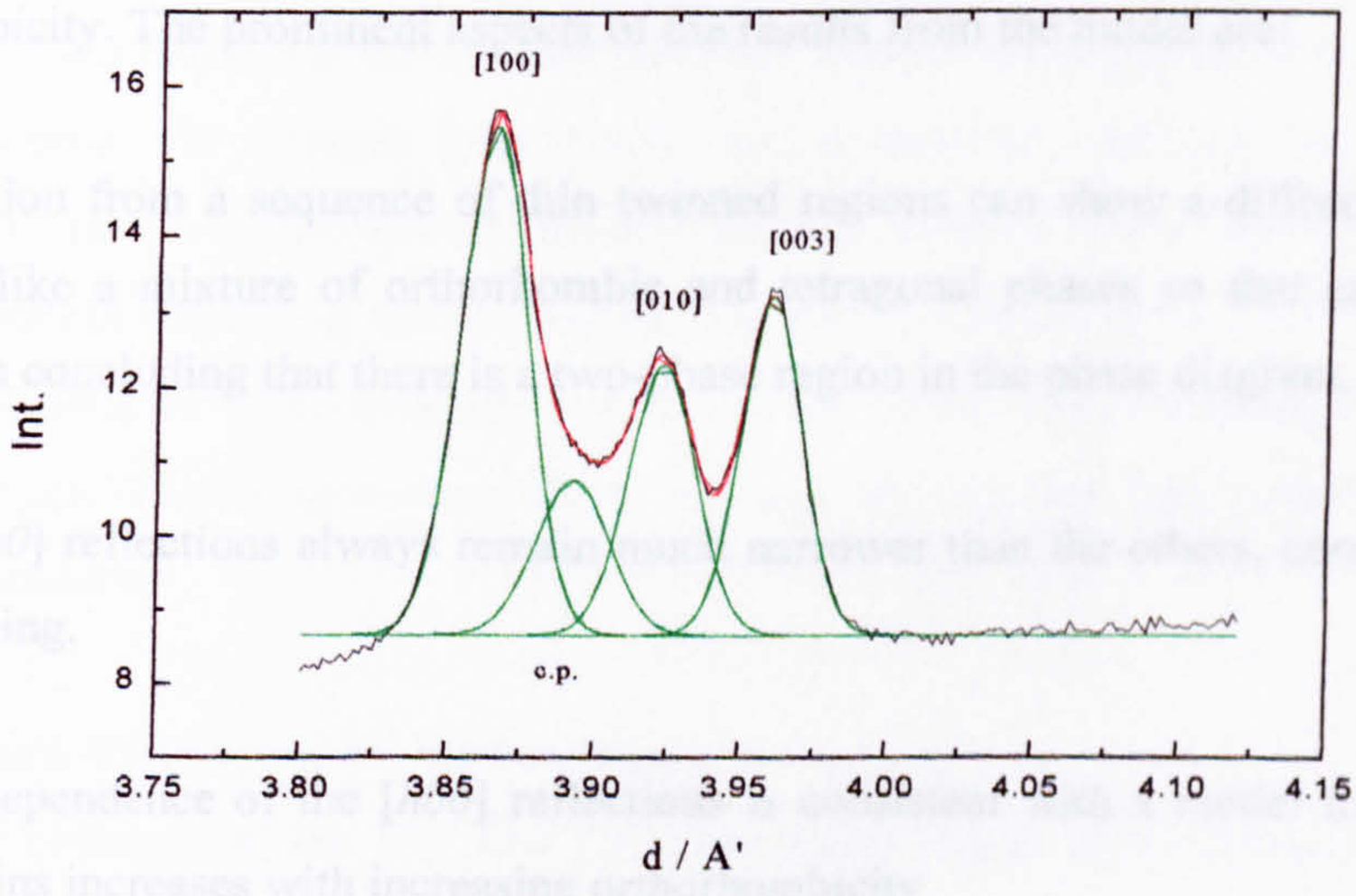

Fig.(7.60) Diffraction pattern under 750 mbar oxygen p.p. at 600°C, (S≈0.0148)

as a tracer. The simulation shows better agreement with experiment at higher oxygen concentrations (OI phase).

A.4) RESULTS

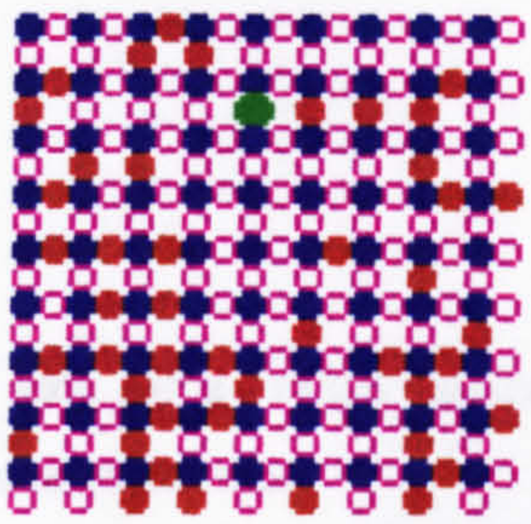

Fig.(A.4a) The initial state for a (18x18) lattice including 46 oxygen atoms (x = 0.6) which are distributed randomly between empty sites.

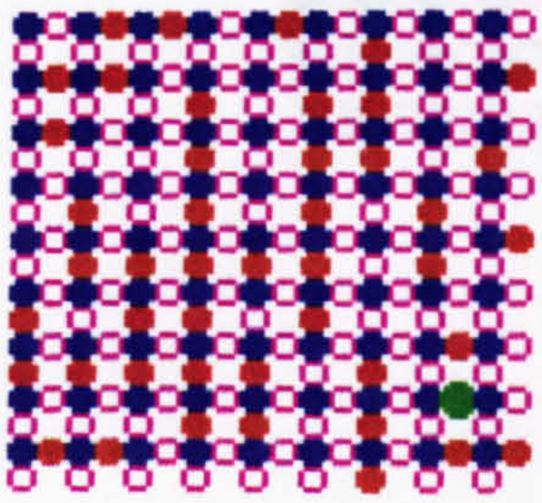

Fig.(A.4b) The final state for that lattice after 1500 cycles of Monte-Carlo calculations. The oxygen atoms now show a long-range ordered configuration with fairly long chains parallel to the *b* direction.

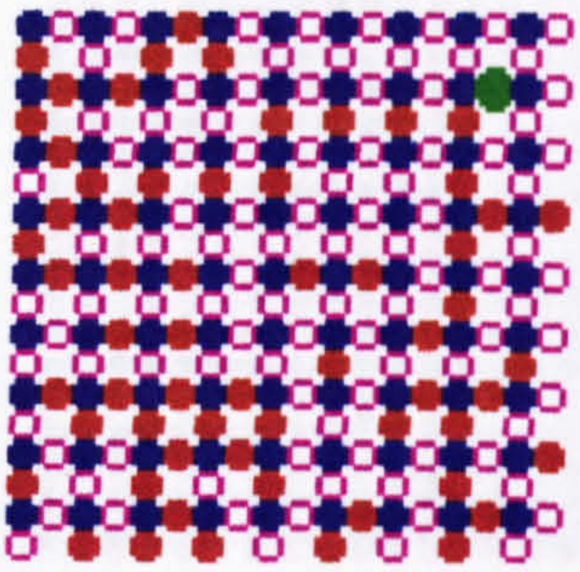

Fig.(A.5a) The initial state for a (18x18) lattice including 62 oxygen atoms (x = 0.8) which are distributed randomly between empty sites.

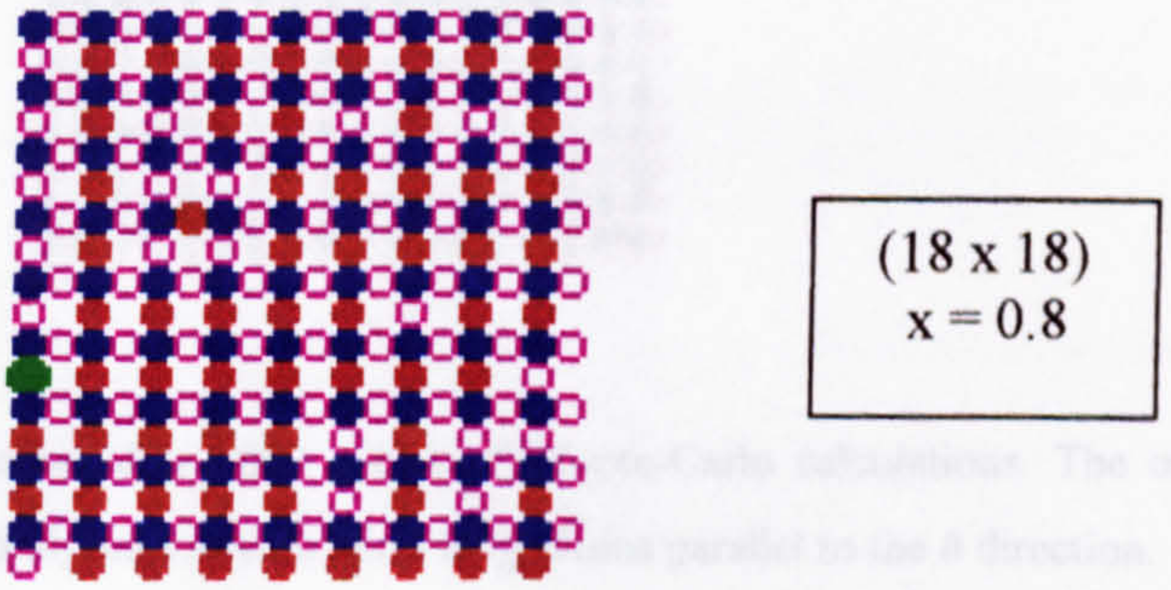

Fig.(A.5b) The final state for that lattice after 500 cycles of Monte-Carlo calculations. The oxygen atoms now show a long-range ordered configuration with fairly long chains parallel to the *b* direction.

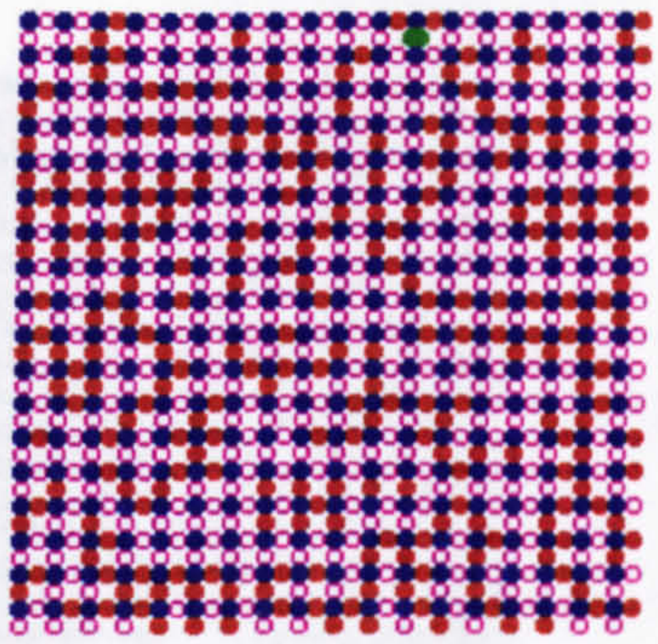

Fig.(A.6a) The initial state for a (32x32) lattice including 261 oxygen atoms (x = 0.8) which are distributed randomly between empty sites.

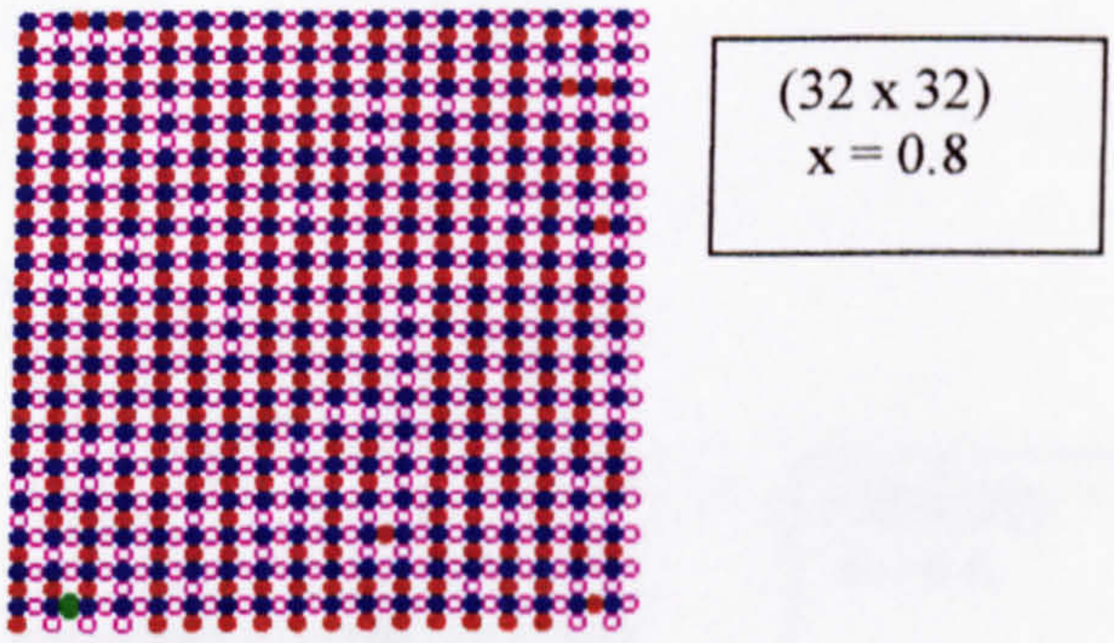

Fig.(A.6b) The final state for that lattice after 3000 cycles of Monte-Carlo calculations. The oxygen atoms now show a long range ordered configuration with fairly long chains parallel to the *b* direction.

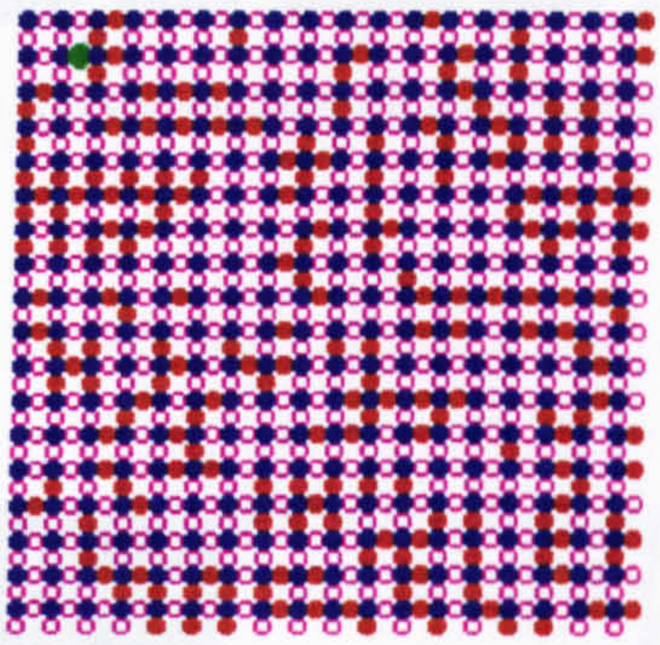

Fig.(A.7a) The initial state for a (32x32) lattice including 207 oxygen atoms (x = 0.6) which are distributed randomly between empty sites.

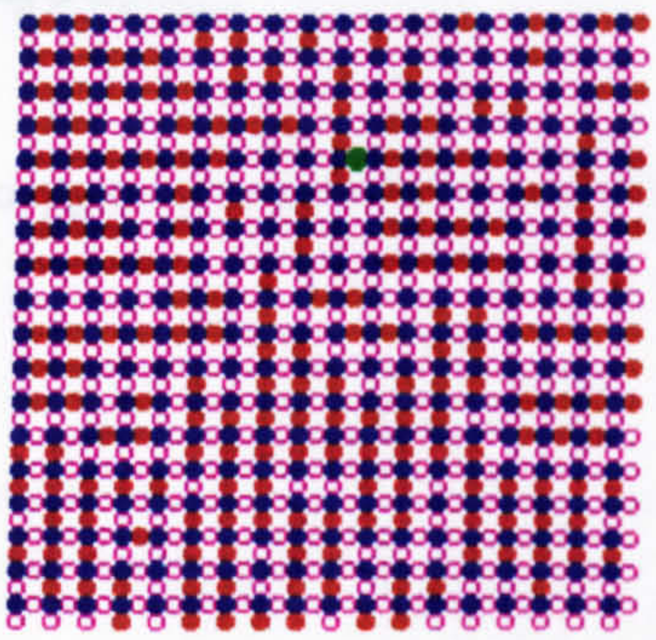

Fig.(A.7b) The final state for that lattice after 10000 cycles of Monte-Carlo calculations. The oxygen atoms ordering along the b direction is not very good and it needs more and more Monte-Carlo cycles.

Obviously for higher lattice dimension and lower oxygen concentration the model needs a large number of Monte-Carlo cycles to approach the expected order configuration (OI & OII). Because the improvement of the simulation techniques was not the main aim of

Evacuation of the system was initially a two-stages process, using a Leybold Trivac rotary pump to obtain a vacuum of around 10^{-2} mbar and then a Pfeiffer TCP121 turbo pump was used to get this down to 10^{-6} mbar.

The sample chamber was made of quartz, to allow it to be heated to high temperature (~1000°C). This meant that the range of available pressures was limited to about 1 bar. Fig.(B.2) shows a typical results of a adsorption process which the gas partial pressure increases exponentially while the sample released the absorbed gas, for gas absorption in the sample, the initial gas partial pressure decreases exponentially until the sample and the ambient gas approach to the thermodynamical equilibrium.

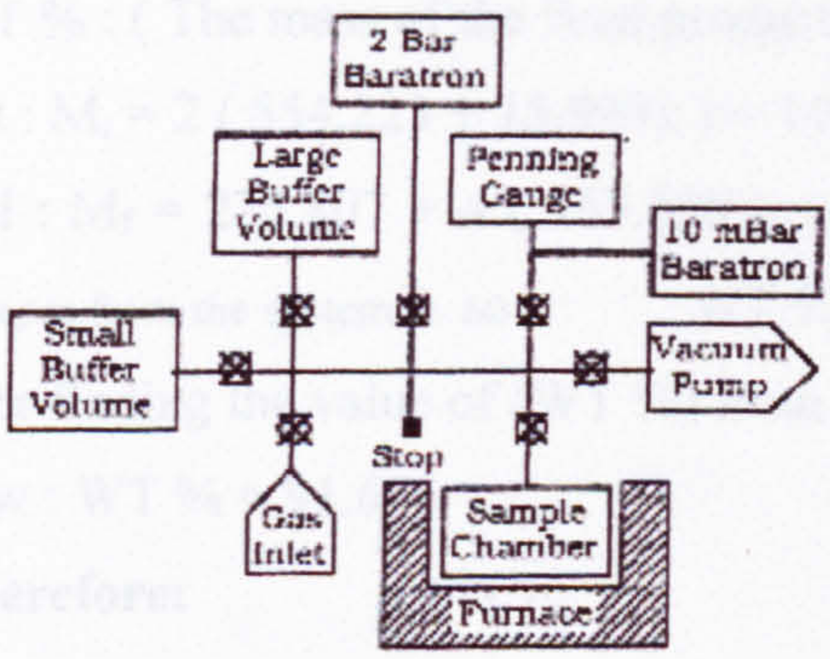

Fig.(B.1a) Schematic illustration of the volumetric rig

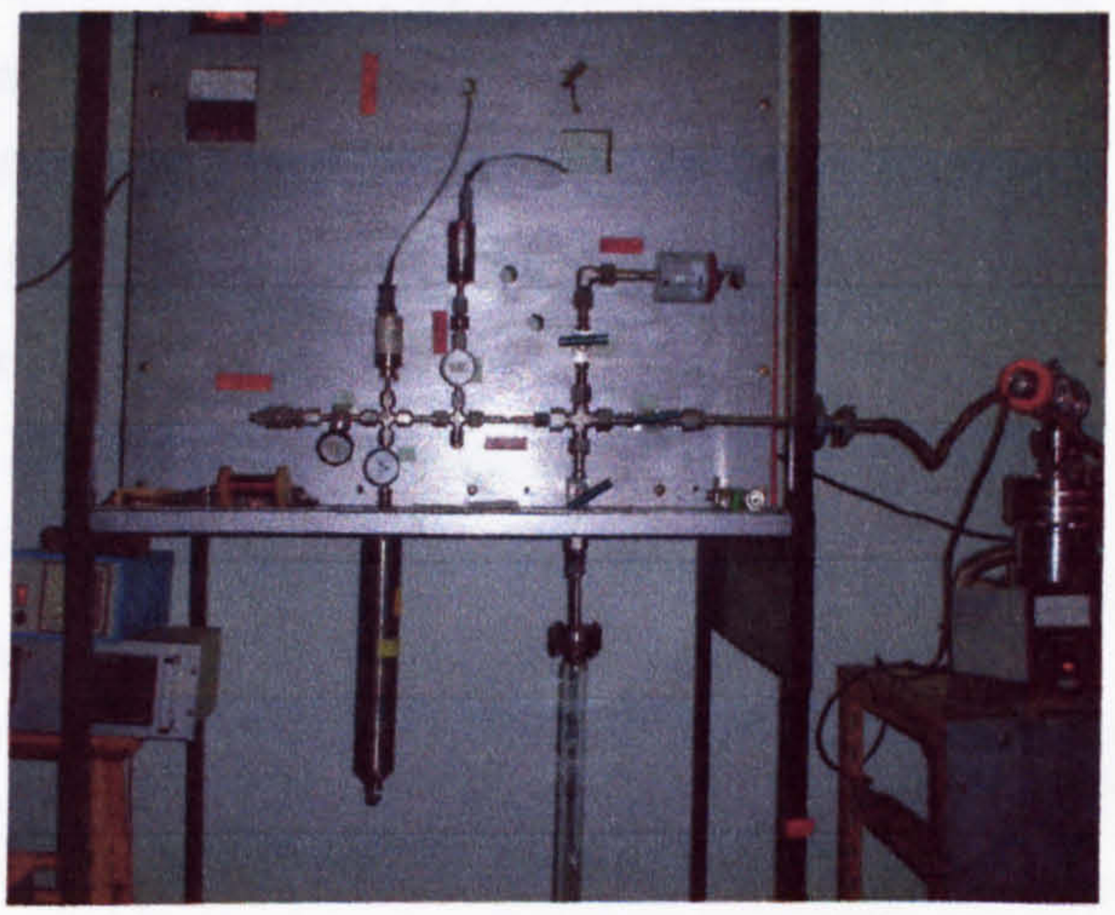

Fig.(B.1b) The volumetric apparatus

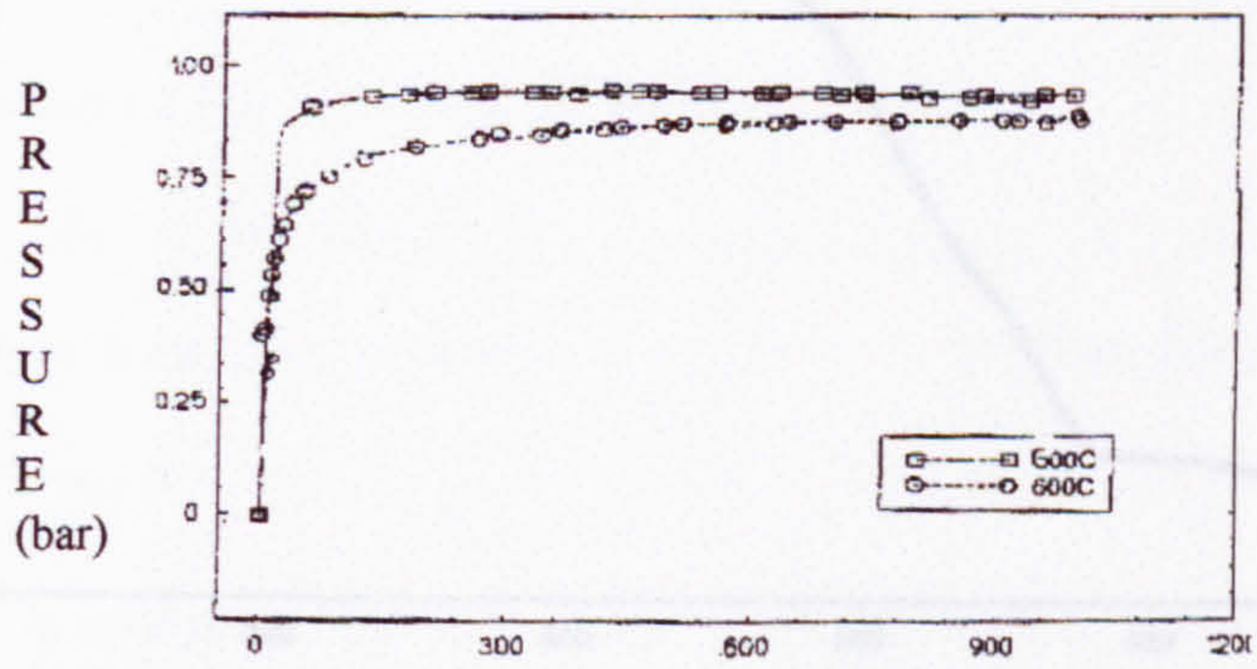

Fig.(B.2) Volumetric results for desorption at 500°C and 600°C

*Tolentonio H, Baundelet F, Fontane A, Gourieux T, Krill G, Henry J Y, Rossat-Mignod J; *Physica C* **192** (1992) 115

*Tarascon J M, McKinnon W R, Greene L H, Hull G W, Vogrl E M; *Phys Rev* B **36** (1987) 226

*Turchin V F, "Slow Neutron" (1965), out of print

*Van Tendeloo G, Zandbergen H W, Amelinkx S; *Solid State Communications* **63**, No 7 (1987) 603

*Von Dreele R B, Jorgensen J D, Windsor C G; Journal of Appllied Crystalgraphy **15** (1982) 581

*Welp U, Grimsditch M, You H, Kwok W K, Fang M M, Crabtree G W, Liu J Z; *Physica* C **161**(1989) 1

*Wong-Ng W, Gayle F W, Kaiser D L, Watkins S F, Fronczek F R; *Phys.Rev.*B **41** (1990) 4220

*Wille L T, Berera A, de Fontaine D; *Phys.Rev. Lett.* **60** (1988) 1065

*Warren B E; "X-ray Diffraction"; Addison-Wesley publishing company (1969)

*Wadhawan V K; *Phys. Rev.*B **38** (1988) 8936

*Xu Y, Suenga M, Tafto J, Sabatini R L, Moodenbaugh A R, Zolliker P *Phys. Rev.* B **39** (1989) 6667

*Young R A; "The Rietveld refinement method", *Oxford Univ. press* (1993)

*Zhang H, Zhang P, Chen X; J. Mat. Chem, 6 N°4 (1996) 615

*Zeiske T, Hohlwein D, Sonntag R, Kubanek F, Collin G; *Z. Phys. B- Condenced Matter* **86** (1992) 11

*Zeiske T, Hohlwein D, Sonntag R, Grybos J, Eichhorn K, Wolf T; *Physica* C **207** (1993) 333

*Zhu Y, Suenga M; "Interfaces in High-Tc Superconducting Systems"; Springer-Verlag, NewYork,1994

*Zhu Y, Suenga M, Tafto J *Phil.Mag.*A **67**(1993) 573

*Zhu Y, Suenaga M, Ji Ping, Wang Keguang, Wang Jingrong, Wu X; *Superconduct. Sci. Tech.* **3** (1990) 490